

ERCOFTAC

*Bulletin*

September 2014

100

---

## European Research Community on Flow, Turbulence and Combustion

---

ERCOFTAC is a leading European association of research, education and industry groups in the technology of flow, turbulence and combustion. The main objectives of ERCOFTAC are: To promote joint efforts of European research institutes and industries with the aim of **exchanging technical and scientific information**; to promote **Pilot Centres** for collaboration, stimulation and application of

research across Europe; to stimulate, through the creation of **Special Interest Groups**, wellcoordinated European-wide research efforts on specific topics; to stimulate the creation of advanced training activities; and to be influential on funding agencies, governments, the European Commission and the European Parliament.

[www.ercoftac.org](http://www.ercoftac.org)

### Honorary Presidents

Mathieu, J. Spalding, D.B.

### Executive Committee

#### Chairman

Tomboulides, A.  
University of Western  
Macedonia, Greece  
Tel: +30 246 105 6630  
atompoulidis@uowm.gr  
ananiast@auth.gr

#### First Deputy Chairman

Von Terzi, D.

#### Second Deputy Chairman

Hirsch, C.

#### Treasurer

Hämäläinen, J.

#### Deputy Treasurer

Ooms, G.

#### SPC Chairman

Geurts, B.J.

#### SPC Deputy Chairman

Sagaut, P.

#### KNC Chairman

Hutton, A. G.

#### KNC Deputy Chairman

Geuzaine, P.

#### Industrial Eng. Officer

Seoud, R.E.

#### Knowledge Base Editor

Rodi, W.

#### Bulletin Editor

Elsner, W.

### ERCOFTAC Seat of the Organisation

#### Director

Hirsch, C.  
Chaussée de la Hulpe 189  
Terhulpesteenweg  
B-1170 Brussels, Belgium  
Tel: +32 2 643 3572  
Fax: +32 2 647 9398  
ado@ercoftac.be

### Scientific Programme Committee

#### Chairman

Geurts, B.J.  
University of Twente  
Mathematical Sciences  
PO Box 217  
NL-7500 AE Enschede  
The Netherlands  
Tel: +31 53 489 4125  
b.j.geurts@utwente.nl

#### Deputy Chairman

Sagaut, P.

### Knowledge Network Committee

#### Chairman

Hutton, A. G.  
Airbus Operations Ltd.  
Building 07S  
Filton, Bristol, BS99 7AR  
United Kingdom  
Tel: +44 117 936 7 590  
anthony.hutton@airbus.com

#### Deputy Chairman

Geuzaine, P.

#### Engagement Officer

Seoud, R.E.  
richard.seoud-ieo@ercoftac.org

### ERCOFTAC Central Administration and Development Office (CADO)

#### Admin. Manager

Jakubczak, M.  
PO Box 53877  
London, SE27 7BR  
United Kingdom  
Tel: +44 203 602 8984  
magdalena.jakubczak@ercoftac.org  
Skype: Ercoftaccado

**TABLE OF CONTENTS**

<b>Introduction to Special Theme: Erosion Processes</b> <i>V. Armenio</i>	<b>3</b>
<b>Numerical Simulation of Coastal Flow And Sediment Transport Over Rippled Beds</b> <i>G. A. Kolokythas, G. A. Leftheriotis and A. A. Dimas</i>	<b>5</b>
<b>Two-phase Flow Modelling for Sediment Transport: Application to Gravity-Driven Flows of Subaqueous Granular Beds</b> <i>C. Varsakelis, D. Monsorno and M.V. Papalexandris</i>	<b>14</b>
<b>Mathematical Modelling of Discontinuous Open-Channel Flows Over Granular Beds</b> <i>R.M.L. Ferreira, S. Amaral and B. Spinewine</i>	<b>20</b>
<b>Quadrant Analysis of Shear Events in Open Channel Flows Over Mobile and Immobile Hydraulically Rough Beds</b> <i>M.J. Franca, B.O. Santos, F. Antico and R.M.L. Ferreira</i>	<b>29</b>
<b>Sediment Transport in Mountain Rivers</b> <i>C. Ancey, P. Bohorquez and E. Bardou</i>	<b>37</b>
<b>Experiments on the Erosion Rate in a Mixture of Incoherent and Cohesive Sediments</b> <i>R. Gaudio and F. Calomino</i>	<b>53</b>
<b>LES of Turbulent Flow with Suspended Particle Dynamics at High Volume Concentration</b> <i>B. J. Geurts</i>	<b>64</b>

<b>EDITOR</b>	Marek, M.
<b>TECHNICAL EDITOR</b>	Kuban, Ł.
<b>CHAIRMAN</b>	Elsner, W.
<b>EDITORIAL BOARD</b>	Armenio, V. Dick, E. Geurts, B.J.
<b>DESIGN &amp; LAYOUT</b>	Borhani, N. Nichita, B.A.
<b>COVER DESIGN</b>	Aniszewski, W.

**SUBMISSIONS**

ERCOFTAC Bulletin  
Institute of Thermal Machinery  
Częstochowa University of Technology  
Al. Armii Krajowej 21  
42-201 Częstochowa  
Poland  
Tel: +48 343 250 507  
Fax: +48 343 250 507  
Email: [ercoftac@imc.pcz.czest.pl](mailto:ercoftac@imc.pcz.czest.pl)

**HOSTED, PRINTED & DISTRIBUTED BY**



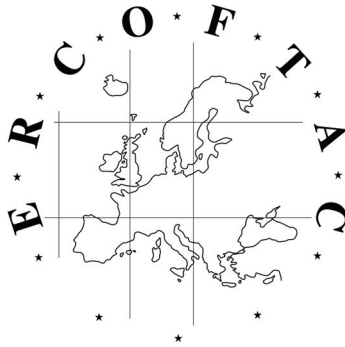
**CZĘSTOCHOWA UNIVERSITY OF TECHNOLOGY**

The reader should note that the Editorial Board cannot accept responsibility for the accuracy of statements made by any contributing authors

**NEXT ERCOFTAC EVENTS**

**ERCOFTAC Autumn Festival**  
October 15<sup>th</sup> 2014  
Saint Etienne du Rouvray, France

**ERCOFTAC Committee Meetings**  
October 16<sup>th</sup> 2014  
Saint Etienne du Rouvray, France



# The ERCOFTAC Best Practice Guidelines for Industrial Computational Fluid Dynamics

The Best Practice Guidelines (BPG) were commissioned by ERCOFTAC following an extensive consultation with European industry which revealed an urgent demand for such a document. The first edition was completed in January 2000 and constitutes generic advice on how to carry out quality CFD calculations. The BPG therefore address mesh design; construction of numerical boundary conditions where problem data is uncertain; mesh and model sensitivity checks; distinction between numerical and turbulence model inadequacy; preliminary information regarding the limitations of turbulence models etc. The aim is to encourage a common best practice by virtue of which separate analyses of the same problem, using the same model physics, should produce consistent results. Input and advice was sought from a wide cross-section of CFD specialists, eminent academics, end-users and, (particularly important) the leading commercial code vendors established in Europe. Thus, the final document can be considered to represent the consensus view of the European CFD community.

Inevitably, the Guidelines cannot cover every aspect of CFD in detail. They are intended to offer roughly those 20% of the most important general rules of advice that cover roughly 80% of the problems likely to be encountered. As such, they constitute essential information for the novice user and provide a basis for quality management and regulation of safety submissions which rely on CFD. Experience has also shown that they can often provide useful advice for the more experienced user. The technical content is limited to single-phase, compressible and incompressible, steady and unsteady, turbulent and laminar flow with and without heat transfer. Versions which are customised to other aspects of CFD (the remaining 20% of problems) are planned for the future.

The seven principle chapters of the document address numerical, convergence and round-off errors; turbulence modelling; application uncertainties; user errors; code errors; validation and sensitivity tests for CFD models and finally examples of the BPG applied in practice. In the first six of these, each of the different sources of error and uncertainty are examined and discussed, including references to important books, articles and reviews. Following the discussion sections, short simple bullet-point statements of advice are listed which provide clear guidance and are easily understandable without elaborate mathematics. As an illustrative example, an extract dealing with the use of turbulent wall functions is given below:

- Check that the correct form of the wall function is being used to take into account the wall roughness. An equivalent roughness height and a modified multiplier in the law of the wall must be used.
- Check the upper limit on  $y^+$ . In the case of moderate Reynolds number, where the boundary layer only extends to  $y^+$  of 300 to 500, there is no chance of accurately resolving the boundary layer if the first integration point is placed at a location with the value of  $y^+$  of 100.

- Check the lower limit of  $y^+$ . In the commonly used applications of wall functions, the meshing should be arranged so that the values of  $y^+$  at all the wall-adjacent integration points is only slightly above the recommended lower limit given by the code developers, typically between 20 and 30 (the form usually assumed for the wall functions is not valid much below these values). This procedure offers the best chances to resolve the turbulent portion of the boundary layer. It should be noted that this criterion is impossible to satisfy close to separation or reattachment zones unless  $y^+$  is based upon  $y^*$ .
- Exercise care when calculating the flow using different schemes or different codes with wall functions on the same mesh. Cell centred schemes have their integration points at different locations in a mesh cell than cell vertex schemes. Thus the  $y^+$  value associated with a wall-adjacent cell differs according to which scheme is being used on the mesh.
- Check the resolution of the boundary layer. If boundary layer effects are important, it is recommended that the resolution of the boundary layer is checked after the computation. This can be achieved by a plot of the ratio between the turbulent to the molecular viscosity, which is high inside the boundary layer. Adequate boundary layer resolution requires at least 8-10 points in the layer.

All such statements of advice are gathered together at the end of the document to provide a 'Best Practice Checklist'. The examples chapter provides detailed expositions of eight test cases each one calculated by a code vendor (viz FLUENT, AEA Technology, Computational Dynamics, NUMECA) or code developer (viz Electricité de France, CEA, British Energy) and each of which highlights one or more specific points of advice arising in the BPG. These test cases range from natural convection in a cavity through to flow in a low speed centrifugal compressor and in an internal combustion engine valve.

Copies of the Best Practice Guidelines can be acquired from:

ERCOFTAC (CADO)  
PO Box 53877  
London, SE27 7BR  
United Kingdom  
Tel: +44 203 602 8984  
Email: [magdalena.jakubczak@ercoftac.org](mailto:magdalena.jakubczak@ercoftac.org)

The price per copy (not including postage) is:

ERCOFTAC members		
First copy		<i>Free</i>
Subsequent copies		75 Euros
Students		75 Euros
Non-ERCOFTAC academics		
Non-ERCOFTAC industrial		140 Euros
EU/Non EU postage fee		230 Euros
		10/17 Euros

# INTRODUCTION TO SPECIAL THEME: EROSION PROCESSES

V. Armenio

*Dipartimento di Ingegneria ed Architettura,  
Universita' di Trieste, Piazzale Europa 1  
34127 Trieste, Italy*

ARMENIO@dicar.units.it

The Special Interest Group Environmental Fluid Mechanics (SIG5) is concerned with that part of fluid mechanics of interest for environmental processes in the low atmosphere and in water bodies. Among them, sediment transport in water basins and streams represents a traditional as well as relevant research topic. With sediment transport it is intended the movement of solid particles (sediment), in water bodies or streams. Although seminal studies of sediment transport date to more than 100 years ago, recently renewed interest is being paid to this field due to implications in river, coastal and marine engineering. Specifically, understanding and prediction of sediment motion processes is of paramount importance in coastal and river engineering due to implication for stability and preservation of anthropogenic structures placed at the bottom surface. Traditionally two main classes of sediment transport processes have been identified, depending on the way sediments are conveyed in the water current. With suspended sediment transport it is intended a process where fine sediments are transported within the water body. It may develop over distances of kilometers and may involve transport of contaminants and polluted matter from rivers to the sea. Heavy sediments are more likely transported in the bed-load mode, where particles move along the bed by rolling, sliding or saltation. The result is bed morphology changes such as ripple or dunes, which cause a complex interaction with the water current and anthropogenic structures placed therein. Sediment transport is among the most traditional research fields of classical hydraulic engineering. Theories based on analytical considerations and results from laboratory and field experiments have allowed determination of engineering simplified formulas for evaluation of quantities of interest for design purposes. With the development of high performance computers as well as novel experimental techniques, a renewed interest has raised in developing research aimed at understanding physical mechanisms of sediment transport at the grain scale from one side, and at developing new-generation numerical models where the mutual interaction between turbulence and sediments is parameterized based on physical considerations.

Worldwide, national and international research projects are being running, aimed at the analysis of interaction between water bodies and the bottom surface. These projects usually involve the Academia, research centers and private companies and are aimed at improving knowledge of sediment transport phenomena and at developing novel state-of-art prognostic models for the evaluation of variation of bed morphology at

sea, estuaries and rivers. Among them, it is worth of mention a Multipartners Network for Initial Training project (SEDITRANS), recently started under the Marie Curie Actions of the 7th Framework Programme. The project, led by Prof. T. Dimas (University of Patras, GR) is aimed at developing research for the analysis of sediment transport in the fluvial, estuarine and coastal environment. As posted in the webpage of the project: SEDITRANS consists of six academic and four industrial partners and provides an elaborate and interdisciplinary training-through-research program to 12 early stage and 4 experienced researchers. Some of the partners of SEDITRANS have kindly accepted to participate in the composition of the present volume.

The volume contains six contributions, spanning a wide variety of themes and methodological approaches within the general topic of sediment transport.

The paper by Kolokythas et al. is interested to flow developing in coastal regions and deals with numerical simulation of a free-surface flow, induced by the propagation of nonlinear water over a rippled bottom. The aim of the paper is understanding sediment transport processes over sand ripples for further parameterization of the phenomenon in large-scale operational models.

The paper by Varsakelis et al. is devoted to development of a two-phase flow model for sediment transport based on a mixture theory for fluid-saturated granular materials. The model is also applied to the analysis of erodible, subaqueous granular beds.

The paper by Ferreira et al. deals with the discontinuities occurring in geomorphic dam-break. The authors take advantage of the shallow-flow theory to identify its generation mechanism and to detect whether the phenomenon can be described as a Riemann problem or, processes beyond the shallow-flow theory control it. Experimental results are presented and compared with a theoretical solution of the governing equations.

The paper by Santos et al. describes the results of an experimental study aimed at understanding the interaction between near-bed turbulent structures and a rough bed, in two different configurations, namely immobile and mobile bed.

The paper by Ancey et al. is devoted to a review on the progresses achieved over the years by the authors, in modelization of bed load transport in mountain rivers. This is a problem of paramount importance for the

evaluation of the hydraulic risk in mountain areas. The authors highlight the significance of the fluctuations of the particle flux together with the propagation of bed forms.

The paper by Gaudio and Calomino reports on laboratory experiments of transport of incoherent and cohesive sediments. The experiments were aimed at detecting the main characteristics of the erosion process under variation of the bed slope and discharges for a mixture of sand, silt and clay.

Finally the paper by Geurts deals with a review of Lagrange-Euler modelization of sediment transport, a novel methodology well suited to study the phenomenon at the grain scale.

The authors of papers 1 to 4 co-participate to the SEDITRANS project together with the author of the present preface and actors from private companies.

The community of scientists and practitioners working in the field of sediment transport is wide and variegated worldwide. The present volume intends to give a contribution to establish a closer connection between the community of scientists operating in the field of theoretical and computational fluid mechanics, and that of hydraulic and coastal engineering. The aim is enhancing a forth-and-back transfer of knowledge and technologies for a rapid progress in the field of erosion processes.

# NUMERICAL SIMULATION OF COASTAL FLOW AND SEDIMENT TRANSPORT OVER RIPPLED BEDS

G. A. Kolokythas, G. A. Leftheriotis and A. A. Dimas

*Department of Civil Engineering, University of Patras, Greece,  
email: adimas@upatras.gr*

## Abstract

In this paper, numerical simulations of (a) free-surface flow, induced by the propagation of nonlinear water waves, and (b) oscillatory flow over a rippled bottom, coupled with bed and suspended sediment transport, are presented. The simulations are based on the numerical solution of the Navier-Stokes equations and the advection-diffusion equation for the suspended load, while empirical formulas are used for the bed load. For the wave propagation simulations, a  $\sigma$ -transformation is applied, while for the coupled oscillatory flow and suspended sediment transport simulations, the Immersed Boundary (IB) method is implemented for the imposition of fluid and sediment boundary conditions. Vortex shedding at the ripple crest generates alternating circulation regions over the ripple trough, while the amplitude of the bed shear stress increases with increasing ripple height. Furthermore, the vortices generated on the lee side of the ripples are highly correlated to the behavior of the suspended sediment. It is found that the mobility parameter affects directly both the bed load transport magnitude and the amount of sediment that is uplifted in suspension by the flow.

## 1 Introduction

Bed morphology evolution in the coastal zone is a direct result of sediment transport induced by the action of waves and currents. The nearshore, wave-induced flow interacts dynamically with sandy beaches resulting in the formation of small-scale bed patterns, called ripples. Their presence increases the effective seabed roughness, which in turn affects the near-bed boundary layer hydrodynamics, as well as the sediment transport in coastal areas. Consequently, accurate predictions of the flow structure and sediment transport rates over rippled beds are important elements in morphological studies in coastal marine environments.

### 1.1 Classification and Dimensions of Ripples

Coastal bed ripples are classified to rolling-grain ripples, appearing in flows with low bed shear stress, not much greater than the critical value for incipient motion, and vortex ripples, appearing in flows with higher bed shear stress [1]. In the latter flows, ripples evolve gradually from rolling-grain to vortex ones, which grow steeper until an equilibrium state is reached between bed load transport, ripple steepness ( $= h_r/L_r$  where  $h_r$  is the ripple height and  $L_r$  is the ripple length) and angle of repose of sand. Furthermore, it has been reported that rolling-grain ripples are not found with steepness greater than about 0.1, since exceeding this value implies separation

of the boundary layer and formation of vortices on either side of the ripple crest [2]. Vortex ripple dimensions are associated to the parameters of the oscillatory flow, induced by the wave propagation, near the bed. It has been reported [3] that ripple length and height depend on the amplitude of the near-bed wave orbital motion,  $a_o = U_o/\omega$ , where  $U_o$  is the amplitude of the near-bed wave orbital velocity,  $\omega = 2\pi/T$  is the wave radial frequency and  $T$  is the wave period. The corresponding amplitude Reynolds number is

$$Re = \frac{a_o U_o}{\nu} \quad (1)$$

where  $\nu$  is the water kinematic viscosity. For second order Stokes waves, it is deduced that  $a_o = (H/2)\sinh(kd)$  where  $H$  is the wave height,  $k = 2\pi/\lambda$  is the wavenumber,  $\lambda$  is the wavelength and  $d$  is the local water depth. Ripples are also classified as: orbital, suborbital or anorbital [4]. This classification is based on the relationship between ripple length,  $L_r$ , wave orbital amplitude,  $a_o$ , and median grain diameter of sand,  $D_g$ . Orbital are the ripples whose length is proportional to  $a_o$ , and occur for low values of the ratio  $a_o/D_g (< 500)$ . Anorbital are the ripples whose length is independent of  $a_o$  and in the range  $400 < L_r/D_g < 600$ , and occur for high values of  $a_o/D_g (> 2,500)$ . Suborbital are the ripples that occur between the orbital and anorbital regimes of  $a_o/D_g$ , and their length depends on both  $a_o$  and  $D_g$  but with an undefined relation. Vortex ripples are either orbital or suborbital [4]. The dimensionless parameters, which describe the ratio between disturbing (induced by the waves) and stabilizing (due to gravity) forces exerted on a sand grain of the bed sediment, are the mobility parameter

$$\Psi = \frac{U_o^2}{(S-1)gD_g} \quad (2)$$

and the Shields parameter

$$\theta = \frac{\tau_b}{\rho(S-1)gD_g} \quad (3)$$

where  $S$  is the sediment specific gravity,  $g$  is the gravitational acceleration,  $\tau_b$  is the bed shear stress and  $\rho$  is the water density. Ripple dimensions - relative length  $L_r/a_o$ , relative height  $h_r/a_o$  and steepness  $h_r/L_r$  - are correlated to the mobility and the Shields parameters via empirical formulas based on measurements for regular and irregular waves [3,5,6,7].

### 1.2 Flow Over Ripples

For oscillatory external flow, both the inviscid [8] and the viscous [9] dynamics of vortex shedding at the ripple crest and its effect on bed resistance were studied. For  $Re \approx 20,000$ ,  $kd = 0.57$ ,  $L_r/\alpha_o = 2.42$  and  $h_r/L_r = 0.159$ , it was demonstrated both experimentally and numerically in [10] that the lee-wake vortices,

after they are washed over the ripple crest, are convected opposite to the wave propagation direction. For  $0.5 \leq L_r/\alpha_o \leq 2$  and  $0.13 \leq h_r/L_r \leq 0.2$ , utilizing a discrete vortex method in [11], it was concluded that the thickness of the resulting oscillating boundary layer is considerably larger than the one over a flat bed. For  $Re = 1,005$ ,  $L_r/\alpha_o = 1.33$  and  $h_r/L_r = 0.14$ , the numerical study of the viscous, three-dimensional, instability and vorticity dynamics over two-dimensional ripples with smooth crests in [12] showed that vortex shedding at the ripple crest becomes three-dimensional and forms vorticity streaks that eject vorticity upwards. Finally, for  $Re = 15,600$ ,  $L_r/\alpha_o = 1.28$  and  $h_r/L_r = 0.18$ , the numerical study of the turbulent, three-dimensional, oscillatory flow over two-dimensional ripples with smooth crests and profiles of increasing steepness in [13] concluded that the wave boundary layer thickness over rippled bed increases, while the average wall shear stress decreases, with increasing ripple profile steepness.

### 1.3 Sediment Transport

The total sediment load transported in the coastal areas is divided in two main categories, i.e., bed load and suspended load. Bed load is defined as the part of the total load that is in more or less continuous contact with the bed during the transport. On the contrary, the suspended load is the part of the total load that is moving without continuous contact with the bed as a result of the agitation of fluid turbulence [14]. Empirical formulas for the calculation of bed load transport rates were developed a few decades ago for steady unidirectional flows [15,16]. These formulas are based on the concept that the sediment transport rate can be related to the shear stress exerted on the bed by the fluid flow. The initiation of bed sediment motion, in cases of ripple generation from a flat bed or morphology change of a rippled bed, occurs whenever the bed shear stress exceeds a critical value. Studies of ripples under oscillatory flow date back to the end of the 19<sup>th</sup> and the beginning of the 20<sup>th</sup> century, but it was not until the late 1950s that large-scale experimental studies started to take place. Measurements of sediment concentration near rippled beds in an oscillatory flow water tunnel were presented in [17]. The size of the facilities in more recent laboratory experiments has increased significantly compared to earlier works, as well as the quality and quantity of the data obtained. Since 1990, a series of new laboratory datasets with measured sediment transport rates in full-scale, wave-induced, oscillatory flows became available [18,19,20,21,22,23]. Furthermore, a number of relevant numerical studies have also been reported in the literature, employing either a Reynolds-averaged Navier-Stokes (RANS), or a large-eddy simulation (LES) approach for the fluid flow. Studies with oscillatory flow conditions, especially using LES, are not as frequent primarily due to computational cost considerations. For example, in [24] it is demonstrated the ability of LES to model the time evolution of sediment transport above idealized ripples. The focus was on oscillatory flow over 2D straight-crested, and 3D ripples for  $Re \approx 2,400$ , based on the channel height of 2.1 cm. In [25], the above work was expanded to ripples of larger scale, highly energetic flow with amplitude Reynolds numbers on the order of 650,000, and simulation of the suspended sediment concentration field. It was concluded that the correlation between sediment concentration and vertical velocity is instantaneous, establishing that coherent structures is an important entrainment mechanism.

### 1.4 Objectives of Present Study

First, numerical simulations of the free-surface flow, developing by the propagation of nonlinear waves over a rippled bed, are presented. The main objective is to investigate the spatio-temporal variation of the flow structure in the vicinity of a rigid rippled bed (consisting of parabolic ripples of various dimensions), and also study the effect of ripple height on the bed shear-stress. Next, the focus is on the bed load and suspended sediment transport induced by pure oscillatory flow over ripples of various dimensions. The objective is to investigate the correlation between the behavior of suspended sediment and the development of the coherent vortices, which characterize the oscillatory flow over ripples. Moreover, the influence of the mobility parameter,  $\Psi$ , on the distribution of both bed and suspended flux, is examined. In the following sections, the formulation, the implemented methodologies and results are presented for the simulated wave-induced and pure oscillatory flow cases.

## 2 Formulation

### 2.1 Wave Propagation

The two-dimensional, incompressible, viscous, free-surface flow induced by wave propagation in the coastal zone, is governed by the continuity

$$\frac{\partial u_i}{\partial x_i} = 0 \quad (4)$$

and the Navier-Stokes equations

$$\frac{\partial u_i}{\partial t} + u_j \frac{\partial u_i}{\partial x_j} = -\frac{\partial p}{\partial x_i} + \frac{1}{Re_d} \frac{\partial^2 u_i}{\partial x_i \partial x_i} \quad (5)$$

where  $i, j = 1, 2$ ,  $t$  is time,  $x_1$  is the horizontal coordinate,  $x_2$  is the vertical coordinate, positive in the direction opposite to gravity,  $u_1$  and  $u_2$  are the corresponding velocity components,  $p$  is the dynamic pressure and  $Re_d$  is the Reynolds number. Equations (4) and (5) are expressed in dimensionless form with respect to the inflow depth  $d_I$ , the gravity acceleration  $g$  and the water density  $\rho$ , therefore,  $Re_d = (gd_I)^{1/2} d_I/\nu$ . For viscous flow, the kinematic and dynamic (normal and tangential stress) boundary conditions at the free surface are

$$u_2 = \frac{d\eta}{dt} = \frac{\partial \eta}{\partial t} + u_1 \frac{\partial \eta}{\partial x_1} \quad (6)$$

$$p - \frac{\eta}{Fr^2} - \frac{2}{Re_d} \frac{1 + (\partial \eta / \partial x_1)^2}{1 - (\partial \eta / \partial x_1)^2} \frac{\partial u_2}{\partial x_2} = p_{air} = 0 \quad (7)$$

$$\frac{\partial u_1}{\partial x_2} + \frac{\partial u_2}{\partial x_1} - 4 \frac{\partial \eta / \partial x_1}{1 - (\partial \eta / \partial x_1)^2} \frac{\partial u_1}{\partial x_1} = \tau_{air} = 0 \quad (8)$$

respectively, where  $\eta$  is the free-surface elevation,  $Fr$  is the Froude number, which under the present dimensionless formulation is equal to one,  $p_{air}$  and  $\tau_{air}$  are pressure and shear stress on the air side, which can be set equal to zero in the absence of wind. In addition, the no-slip and non-penetration boundary conditions at the bottom are

$$u_1 - u_2 \frac{\partial d}{\partial x_1} = 0 \quad u_2 + u_1 \frac{\partial d}{\partial x_1} = 0 \quad (9)$$

respectively, where  $d$  is the local bottom depth measured from the still free surface level.

## 2.2 Oscillatory Flow

The governing flow equations are the continuity (4) and the Navier-Stokes (5) equations. Note that in the case of oscillatory flow, all variables are rendered dimensionless using the maximum velocity,  $U_o$ , and the amplitude of the orbital motion,  $\alpha_o$ , of the oscillatory flow. As a result, the corresponding amplitude Reynolds number, expressed by Eq. (1), appears in Eq. (5). At the bottom, the boundary conditions (9) are also imposed, while a zero Neumann condition (rigid-lid),  $\partial u_i/\partial x_2 = 0$ , is applied at the upper limit of the computational domain.

## 2.3 Sediment Transport

As mentioned before, both bed load and suspended sediment transport are considered for the case of pure oscillatory flow. The bed load transport rate,  $q_b$ , is expressed by the normalized variable

$$\Phi_B = \frac{q_b}{\sqrt{(S-1)gD_g^3}} \quad (10)$$

where  $S$  is the sediment specific gravity. Here,  $\Phi_b$  is computed by the following semi-empirical formula [26]

$$\Phi_b = \begin{cases} \frac{10\pi}{6} \left[ 1 + \left( \frac{1}{6} \frac{\pi\mu_d}{\theta - \theta_c} \right)^4 \right]^{-1/4} (\sqrt{|\theta|} - 0.7\sqrt{|\theta_c|}) & \text{for } |\theta| > |\theta_c| \\ 0 & \text{for } |\theta| \leq |\theta_c| \end{cases} \quad (11)$$

where  $\theta_c$  is the critical Shields parameter, the value of which, for a bed of local slope  $\partial h/\partial x$ , is obtained by the following expression [26]

$$\theta_c = \frac{\theta_{co}}{\sqrt{1 + (\partial h/\partial x)^2}} \left( \text{sgn}(\theta) + \frac{\partial h/\partial x}{\mu_d} \right) \quad (12)$$

where  $\theta_{co}$  is the critical Shields parameter for a horizontal bed,  $\mu_d$  is the dynamic friction coefficient of sand, and  $\text{sgn}(\theta) = \pm 1$  is the sign function of  $\theta$ . Here,  $\theta_{co}$  is obtained as a function of the dimensionless grain size,  $D_* = D_g[(S-1)g/\nu^2]^{1/3}$ , based on the Shields diagram [27]. The motion of sediment in suspension is computed using an advection-diffusion equation for the concentration,  $c$ , of the suspended sediment

$$\frac{\partial c}{\partial t} + u_1 \frac{\partial c}{\partial x_1} + (u_2 - w_s) \frac{\partial c}{\partial x_2} = \nu \left( \frac{\partial^2 c}{\partial x_1^2} + \frac{\partial^2 c}{\partial x_2^2} \right) + f_c \quad (13)$$

where  $w_s$  is the settling velocity, computed according to [28], and  $f_c$  is a source term associated with the implementation of the IB method for the enforcement of the bottom boundary conditions.

The bottom boundary condition for equation (13) is generally specified using a bed load model. From the physical point of view, the bed load provides the available sediment which may be suspended. The concentration of the sediment-water mixture at the top of the bed load layer is known as the reference concentration. Since it is a measure of the bed load, in the literature, it is commonly referred to as  $c_{bed}$  or  $c_b$ . Mathematically,  $c_b$  serves as the bed boundary condition for the suspended sediment concentration equation (13). In the present formulation, the model in [26] is used

$$c_b = \frac{c_o}{(1 + 1/\lambda_b)^3} \quad (14)$$

where  $\lambda_b$  is the linear concentration and  $c_o (= 0.65)$  is the bed concentration for firmly packed grains.

## 3 Methodologies

### 3.1 Wave Propagation: $\sigma$ -transformation

Given that the free surface of water during wave propagation is time-dependent, the Cartesian coordinates are transformed, in order for the computational domain to become time-independent, according to the following expressions

$$s_1 = x_1 \quad s_2 = \frac{2x_2 + d - \eta}{d + \eta} \quad (15)$$

where  $-1 \leq s_2 \leq 1$ . In the transformed domain,  $s_2 = 1$  corresponds to the free surface and  $s_2 = -1$  to the bottom. For the simplification of the transformed flow equations, the velocity components are also transformed in the following way

$$u_1 = v_1 \quad u_2 = v_2 + rv_1 = v_2 + v_\eta \quad (16)$$

where  $r = 0.5[(1 + s_2)\partial\eta/\partial s_1 - (1 - s_2)\partial d/\partial s_1]$ .

The continuity and Navier-Stokes equations (4) and (5), and the free-surface and bottom conditions, equations (6) to (9), are transformed accordingly by the application of equations (15) and (16). A detailed presentation of the transformed equations is given in [29].

The flow simulations are based on the numerical solution of the transformed Navier-Stokes equations, which are written in the form

$$\frac{\partial \vec{v}}{\partial t} = \vec{A} + \nabla_r \Pi + \frac{1}{Re_d} \Delta_r \vec{v} \quad (17)$$

where  $v = (v_1, v_2)$ ,  $\vec{A}$  includes all nonlinear terms,  $\nabla_r$  is the transformed gradient operator,  $\Pi = p + (\vec{v} \cdot \vec{v})/2$  is the pressure head and  $\Delta_r$  is the transformed Laplacian operator. A fractional time-step scheme, consisting of three stages, is used for the temporal discretization and a hybrid scheme for the spatial discretization. Central finite differences are applied, on a uniform grid with size  $\Delta s_1$ , for the discretization along the streamwise direction  $s_1$ , and a spectral approximation method with Chebyshev polynomials along the vertical direction  $s_2$ . According to the hybrid scheme for the spatial discretization, each flow variable  $F$  (velocity, pressure etc.), is approximated as

$$F(s_1, s_2, t) = \sum_{n=0}^{N_z} F_n(s_1, t) T_n(s_2) \quad (18)$$

where  $F_n$  is the Chebyshev transformation of  $F$  (in the spectral domain),  $T_n$  is the Chebyshev polynomial of order  $n$  and  $N_z$  is the highest order of Chebyshev polynomials. The transformations between  $F$  and  $F_n$  are performed by a Fast Fourier Transform algorithm. The velocity field is advanced in time by adding successively the corresponding corrections at each of the three stages of the time-step. At the first stage of each time-step, the nonlinear term,  $A$ , of equations (17) is treated explicitly by an Euler scheme. At the second stage, an implicit Euler scheme is used for the treatment of the pressure head term,  $\nabla_r \Pi$ , of equations (17), which results into a generalized Poisson's equation for  $\Pi$  by satisfying the transformed continuity equation as well. The transformed dynamic (normal stress) free-surface condition and non-penetration bottom condition are imposed at this stage. At the third stage, the viscous term,  $\Delta_r \vec{v}$ , of equations (17) is treated by an Euler implicit scheme satisfying the

transformed dynamic (tangential stress) free-surface and bottom conditions. The pressure field is obtained at the second stage of the time-step, as mentioned above, while the free-surface elevation is computed by satisfying the transformed kinematic boundary condition, at the end of each time-step.

### 3.2 Oscillatory Flow: Immersed Boundary (Ib) Method

For the pure oscillatory flow simulations, the introduction of the rippled bed in the computational domain, which is discretized with a structured Cartesian grid, is achieved by means of the so-called IB method. The implementation of our method follows the one in [30]. The main characteristic of the implementation of the IB method is that every wall surface within the computational domain is discretized using marker points with spacing approximately equal to the local grid size. In such cases, where the bed surface is not aligned with the grid, the solution is reconstructed, in the vicinity of the boundary, in order to enforce the no-slip condition. Here, the Navier-Stokes equations are discretized through a two-stage, time-splitting scheme, where an intermediate velocity field is computed by:

$$\frac{\hat{u}_i - u_i^n}{\Delta t} = \frac{3}{2}H_c(u_i^n) - \frac{1}{2}H_c(u_i^{n-1}) + \frac{\partial p^{n+1}}{\partial x_i} + f_i^{n+1} \quad (19)$$

where  $H_c$  is a spatial operator, including the convective and viscous terms, based on the explicit Adams-Bashforth scheme,  $p$  is the dynamic pressure of the external flow and  $f_i$  represents a source term associated with the implementation of the IB method for the enforcement of non-slip boundary conditions on the immersed bed surface. Eq. (19) is valid in the whole computational domain, which includes the ripple surface. The computation of the velocity at the next time-step is expressed by:

$$u_i^{n+1} = \hat{u}_i - \Delta t \frac{\partial \delta p}{\partial x_i} \quad (20)$$

where the dynamic pressure correction is computed by solving the Poisson equation:

$$\frac{\partial^2 \delta p}{\partial x_i \partial x_i} = -\frac{1}{\Delta t} \frac{\partial \hat{u}_j}{\partial x_j} \quad (21)$$

which enforces the satisfaction of the continuity equation for  $u^{n+1}$ .

## 4 Results

### 4.1 Wave Propagation

Two cases of incoming second-order Stokes waves, with dimensionless wavenumbers  $kd_I = 1.047$  and  $0.785$ , wave periods  $T(g/d_I)^{1/2} = 6.95$  and  $8.75$ , and the same wave height  $H/d_I = 0.3$ , propagating over a rigid rippled bed, are considered (extra parameters are included in Table 1). For both cases,  $Re_d = 250,000$  is considered, which corresponds to dimensionless Stokes length  $\delta_s/d_I = 0.003$ , while a third case with  $Re_d = 500,000$  ( $\delta_s/d_I = 0.002$ ) and wave parameters that coincide to those in Case 1, is also investigated. For each flow case, several combinations of ripple dimensions were considered for a total of 14 tests. Specifically, simulations were performed for ripple characteristics in the ranges of  $0.08 \leq h_r/L_r \leq 0.20$  and  $1.16 \leq L_r/a_o \leq 2.08$ , according

Table 1: Investigated cases of wave propagation over rippled bed

Case	1	2	3
$H/d_I$	0.3	0.3	0.3
$\lambda/d_I$	6	8	6
$T(g/d_I)^{1/2}$	6.95	8.75	6.95
$Re_d$	250,000	250,000	500,000
$kd_I$	1.047	0.785	1.047
$a_o/d_I$	0.120	0.173	0.120
$Re$	3.258	5.350	6.517

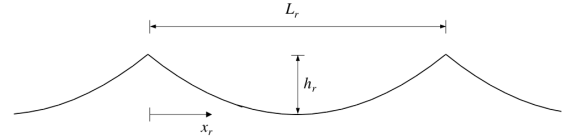


Figure 1: Sketch of a typical vortex ripple

to laboratory and field data in the orbital regime [14,31]. In all tests, the initial shape of the vortex ripples was assumed to be parabolic (Fig. 1).

As shown in the sketch of the computational domain (Fig. 2), a flat inflow region of length  $\lambda$  and constant depth  $d_I$ , is followed by the rippled bed region of length  $0.5\lambda$ , which in turn is followed by the flat outflow region of length  $5\lambda$  and constant depth  $d_I$ . An absorption zone of length  $4\lambda$  before outflow ensures that the reflection of waves at the outflow boundary is minimized [32]. The numerical parameters are  $\Delta s_1 = 0.0125$ ,  $N_z = 128$  and  $\Delta t = 0.002$ .

Typical snapshots of the velocity and vorticity field in the vicinity of two successive ripples, at four time instants during a wave period  $T$ , are presented in Fig. 3. The flow separates along the wave propagation direction at each ripple crest, and forms a recirculation region on the downslope side of the ripple, when a wave crest propagates above the ripple crest [Figs 3(a)-(b)]. Separation opposite to the wave propagation direction leads to the formation of a recirculation region on the upslope side of the ripple, when a wave trough propagates above the ripple crest [Figs 3(c)-(d)].

The spatial distribution of the friction coefficient,  $f = 2\tau_b/\rho U_o^2 = 2\theta/\Psi$ , at two time instants of a wave period is shown in Fig. 4, for relative ripple height  $h_r/a_o = 0.173$  and  $0.416$ . The amplitude of the friction coefficient variation increases substantially in the rippled region, especially near the ripple crests, and this increase is proportional to the ratio of ripple height to wave orbital amplitude,  $h_r/a_o$ . The wave friction factor,  $f_w$ , which is defined as the maximum absolute value of the fric-

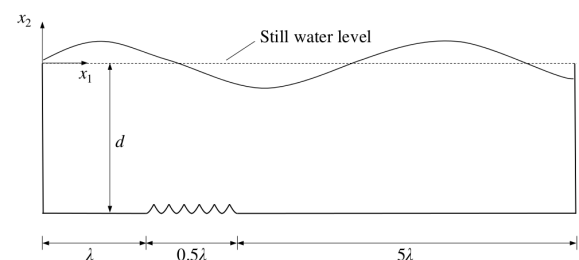


Figure 2: Computational domain for simulation of wave propagation over rippled bed

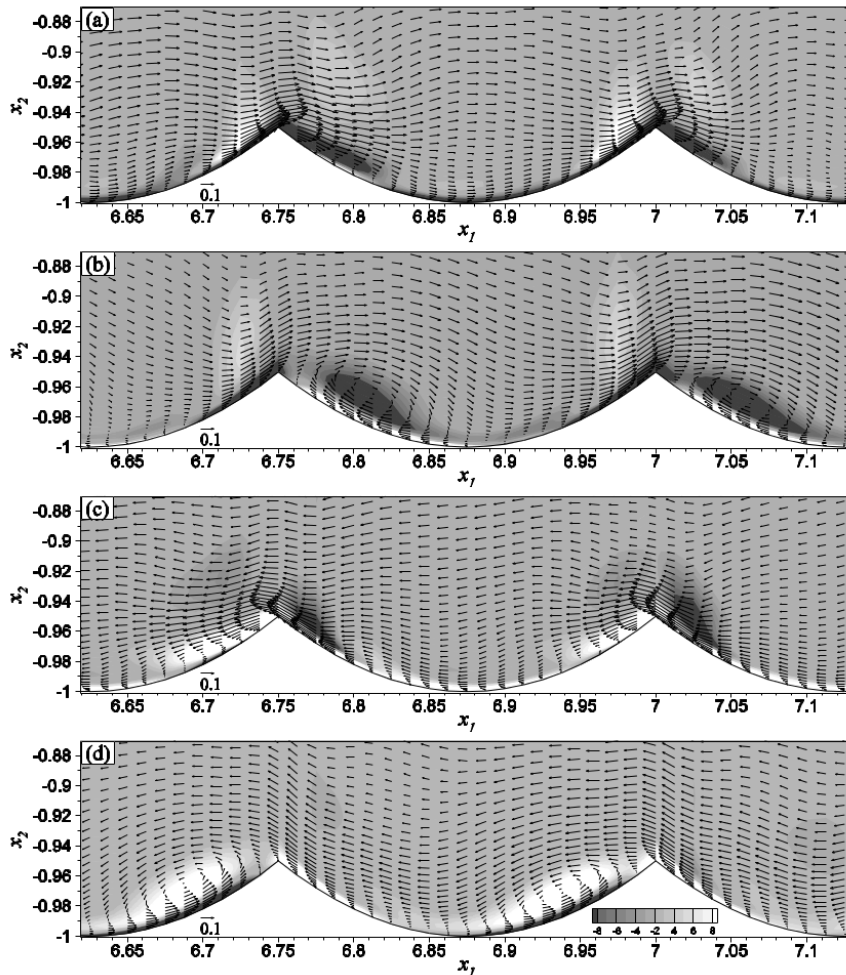


Figure 3: Snapshots of velocity (vectors) and vorticity (contours) field in the vicinity of two ripples of relative length  $L_r/a_o = 2.08$  and height  $h_r/a_o = 0.416$

tion coefficient during the wave period, near the ripple crests was  $f_w = 0.06$  for ripples of  $h_r/a_o = 0.173$  and  $f_w = 0.128$  for  $h_r/a_o = 0.416$ , while at the ripple troughs was  $f_w = 0.027$  and  $0.023$ , respectively. The values of  $f_w$  at the ripple trough are smaller than the one ( $f_w = 0.032$ ) at the flat bed upstream of the ripples (Fig. 2) due to the effect of the separated flow. This effect weakens with the decrease of the ripple steepness. It is noted here that the predicted value of the wave friction factor  $f_w = 0.032$ , at the flat bed, agrees well with the one ( $f_w = 0.035$ ) obtained for a flat bed for pure oscillatory flow at the same  $Re = 3,258$  [33].

Typical contours of the spatio-temporal evolution of  $f$  along one ripple and during one wave period are depicted in Fig. 5. It is indicated that the highest - positive and negative - values of  $f$  occur very close to the ripple crest during the first and third phase quarters,  $t/T = 13 - 13.25$  and  $13.5 - 13.75$ , respectively. During the second and fourth phase quarters,  $t/T = 13.25 - 13.5$  and  $13.75 - 14$ , respectively, which correspond to the formation of the recirculation regions (Fig. 4), the local maxima - negative and positive - of  $f$  occur at the downslope and upslope sides of the ripple, respectively.

## 4.2 Oscillatory Flow

The computational domain with the immersed ripple boundary is shown in Fig. 6. The length of the computational domain is equal to three ripple lengths ( $L_r$ ), while the height of the computational domain is equal

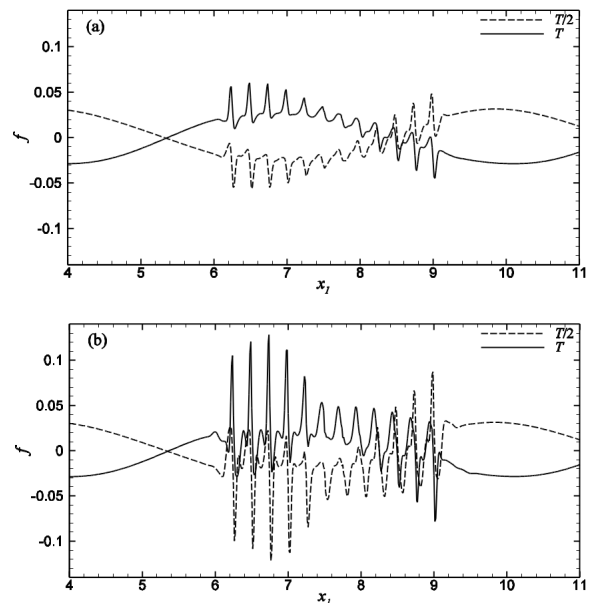


Figure 4: Friction coefficient distribution, at two time instants of a wave period, for ripples of relative height (a)  $h_r/a_o = 0.173$  and (b)  $h_r/a_o = 0.416$

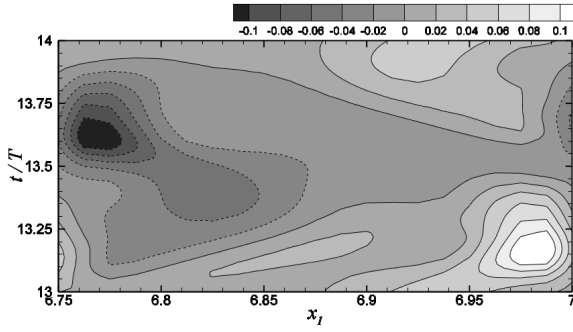


Figure 5: Spatio-temporal distribution of friction coefficient along a ripple during the 14<sup>th</sup> wave period for ripples of length  $L_r/a_o = 2.08$  and height  $h_r/a_o = 0.416$

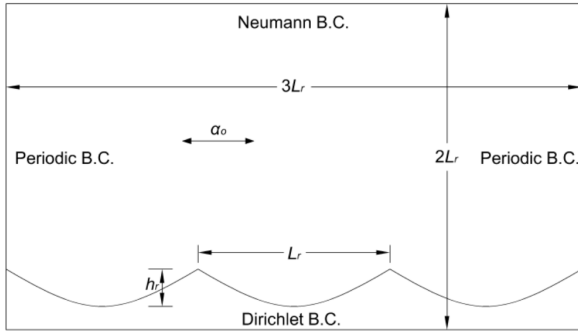


Figure 6: Sketch of the computational domain used in the simulations of oscillatory flow over ripples

to two ripple lengths. The grid spacing in the streamwise direction,  $\Delta x_1/a_o$ , is uniform and equal to 0.004, while the grid spacing in the vertical direction,  $\Delta x_2/a_o$ , varies from 0.001 to 0.002 and 0.004, as one moves away from the bottom. As a result, the domain has a maximum number of  $2472 \times 2750$  grid points. Considering that, in the present simulations the wall friction coefficient is  $|f| < 0.2$ , the grid spacing given in wall units is  $\Delta x_2^+ = \Delta x_2 u^*/\nu < 1.58$ , and  $\Delta x_1^+ = \Delta x_1 u^*/\nu < 6.32$ , where  $u^* = U_o(|f|/2)0.5$ . Therefore, the flow close to the wall is well resolved.

The flow is driven by a uniform pressure gradient at  $Re = 5,000$ , while again ripples of parabolic shape with sharp crests were examined (Fig. 1). The ripple characteristics, i.e., the ratio of the ripple length to the orbital motion amplitude,  $L_r/a_o$ , and the ratio of the ripple height to the orbital motion amplitude,  $h_r/a_o$  were calculated according to [31]

$$\begin{aligned} \frac{h_r}{a_o} &= 0.275 - 0.0022\Psi^{0.5} \\ \frac{L_r}{a_o} &= 2.2 - 0.345\Psi^{0.34} \end{aligned} \quad (22)$$

for three different values of the mobility parameter, ( $\Psi = 4, 10, 40$ ) and the results are presented in Table 2.

Results of coupled simulations of oscillatory flow, sediment transport (bed and suspended), are presented. Each simulation starts with the fluid and the sediment at rest. First, flow results are presented. Typical snapshots of the vorticity field over three successive ripples for mobility parameter,  $\Psi = 10$ , are presented at four time instants in Fig. 7. During each half-cycle, vortices are generated at the lee side of the ripple. At flow reversal, the lee vortex is ejected from the bed.

Table 2: Ripple characteristics determined according to mobility parameter

$\Psi$	$L_r/a_o$	$h_r/a_o$
4	1.647	0.231
10	1.445	0.205
40	0.991	0.136

### 4.3 Sediment Transport

Next, results of sediment transport are presented for sediment with relative median grain diameter,  $a_o/D_g$ , equal to 500, and specific gravity  $S = 2.65$ . The concentration of suspended sediment for oscillatory flow over ripples, for mobility parameter,  $\Psi = 10$ , is illustrated in Fig. 8 at the same time instants as in Fig. 7. Initially, bed sediment is set in motion and becomes eligible to be suspended near the crests where bed shear stress is high. The suspended sediment rise is correlated to the level reached by the vortices of the flow. Between flow reversals, sediment is carried up to the ripple crest and then hurled out over the lee vortices. At flow reversal, sediment is hurled up by the vortices ejected at the same time instant. These results are in agreement with measurements of sediment concentration near rippled beds in an oscillatory flow water tunnel [17]. Specifically, our results agree reasonably well with the observations in [17] about both vortex creation and ejection, as well as the variation of concentration during half-cycle and at flow reversal. Similar findings about vortex formation-ejection and sediment plume formation are presented in [25], which are in accordance to our results.

The bed flux,  $\Phi_B$ , and suspended flux,  $\Phi_S$ , [defined according to Eq. (10)] distribution in the region between two ripple crests during an oscillatory period for  $\Psi = 10$  is presented in Fig. 9. In this case, suspended load is the dominant transport mechanism. High negative values of suspended flux at  $t = 3T/4$  are due to the plume of sediment ejected at flow reversal, while high positive values at  $t = T$ , are due to the sediment which is hurled out over the lee vortices.

Next, comparison results are presented for different values of the mobility parameter  $\Psi$ . Fig. 10 and Fig. 11 show that the concentration and the uplift of the suspended sediment, as well as the bed load transport magnitude, are amplified, with increasing values of the mobility parameter. Obviously, this result is due to increase of the instantaneous Shields parameter, and the reduction of the settling velocity,  $w_s$ , which are directly coupled with the increase of the mobility parameter  $\Psi$ .

## 5 Conclusions

First, the free-surface flow, developing by wave propagation over a bed with ripples of parabolic shape and sharp crests, was considered. It was found that flow separation at the ripple crest generates alternating circulation regions and vortices in the ripple trough always carrying momentum upwards. The amplitude of the bed shear stress in the rippled region of the domain increases with increasing relative ripple height. Next, coupled simulations of pure oscillatory flow, sediment transport (bed and suspended) were performed. The IB method was employed for the imposition of the fluid and sediment boundary conditions at the rippled bed. It was found that the behaviour of suspended sediment is highly correlated to the development of the coherent vortices, which characterize the oscillatory flow over ripples. Sediment is

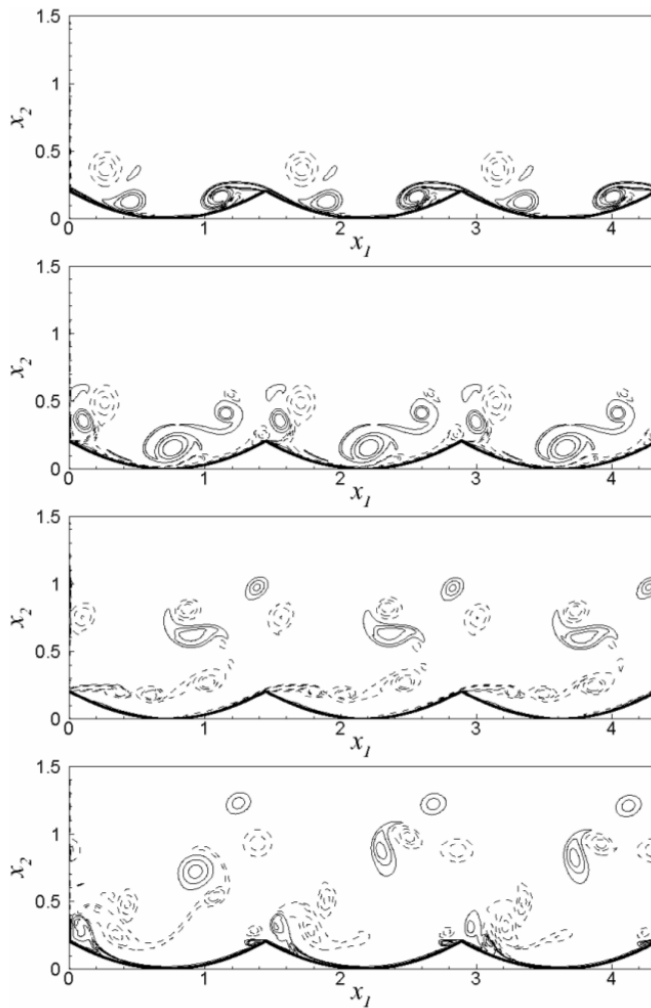


Figure 7: Vorticity field ( $3T/4 \leq t \leq 6T/4$  and  $\Psi = 10$ ) at  $T/4$  increments from top to bottom. Dashed lines correspond to negative vorticity values

hurled over these vortices until the end of each half-cycle of the period. At flow reversal, the lee vortex is ejected from the bed and throws up a plume of sediment. Finally, it was observed that when mobility parameter increases, the concentration and the uplift of the suspended sediment, as well as the bed load transport magnitude, are substantially enhanced.

### Acknowledgements

This paper is part of the research project "ARISTEIA I - 1718", implemented within the framework of the program "Education and Lifelong Learning", and co-financed by the European Union (European Social Fund) and Hellenic Republic funds.

### References

[1] Bagnold, R.A., "Motion of waves in shallow water: Interaction between waves and sand bottoms," Proc. R. Soc. Lond. A, 187, 1-15, 1946.

[2] Sleath, J.F.A., Sea bed mechanics. Wiley Interscience, New York, 1984.

[3] Nielsen, P, "Dynamics and geometry of wave-generated ripples," J. Geophys. Res., 86, 6467-6472, 1981.

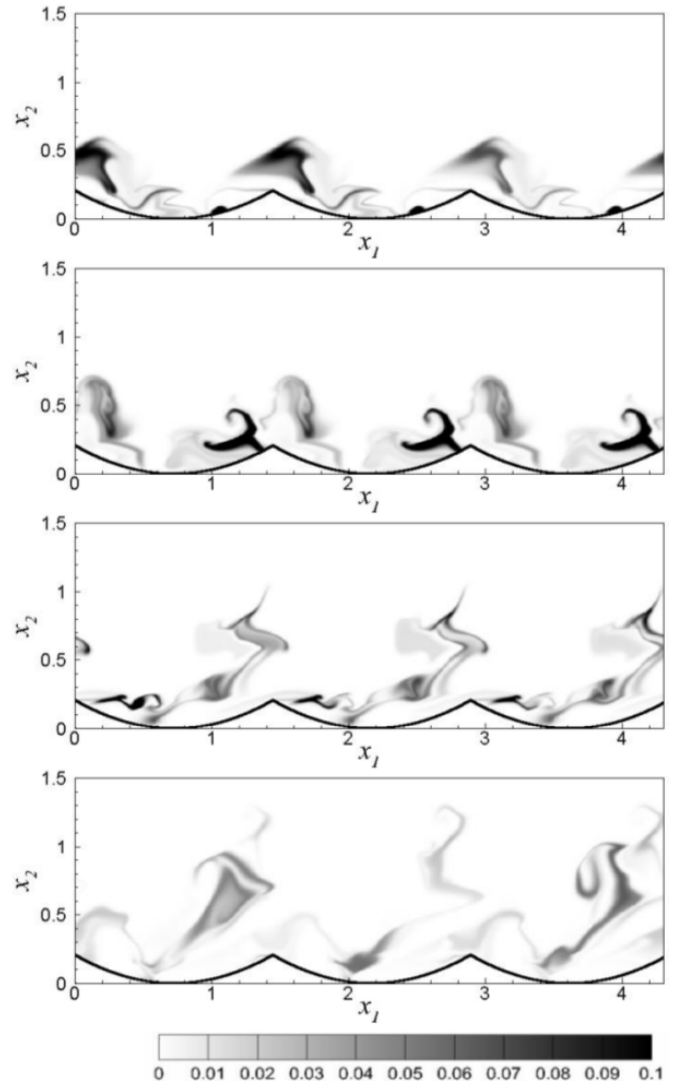


Figure 8: Suspended sediment concentration field ( $3T/4 \leq t \leq 6T/4$  and  $\Psi = 10$ ) at  $T/4$  increments from top to bottom

[4] Clifton, H.E., and Dingler, J.R., "Wave-formed structures and paleoenvironmental reconstruction," Marine Geol., 60, 165-198, 1984.

[5] Wiberg, P.L., and Harris, C.E., "Ripple geometry in wave-dominated environments," J. Geophys. Res., 99(C1), 775-789, 1994.

[6] Grant, W.D., and Madsen, O.S., "Movable bed roughness in unsteady oscillatory flow," J. Geophys. Res., 87, 469-481, 1982.

[7] Faraci, C., and Foti, E, "Geometry, migration and evolution of small-scale bedforms generated by regular and irregular waves," Coastal Eng., 47(1), 35-52, 2002.

[8] Longuet-Higgins, M.S., "Oscillating flow over steep sand ripples," J. Fluid Mech., 107, 1-35, 1981.

[9] Blondeaux, P. and Vittori, G., "Vorticity dynamics in an oscillatory flow over a rippled bed," J. Fluid Mech., 226, 257-289, 1991.

[10] Fredsoe, J., Anderson, K.H. and Sumer, B.M., "Wave plus current over a ripple-covered bed," Coastal Eng., 38, 177-221, 1999.

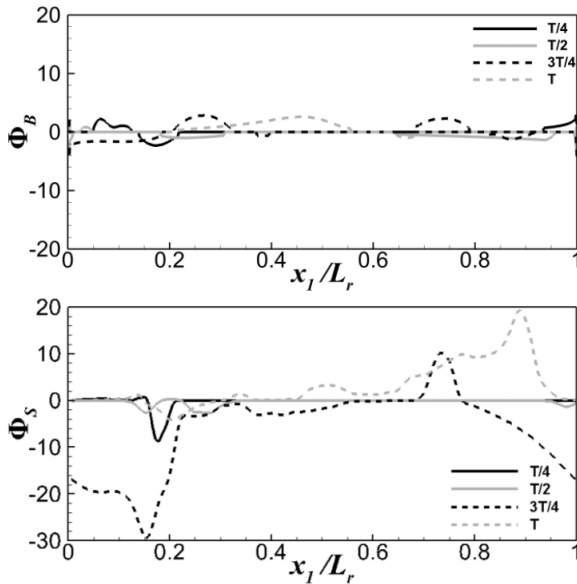


Figure 9: Bed flux,  $\Phi_B$ , and suspended flux,  $\Phi_S$ , distribution in the region between two ripple crests during an oscillatory period for  $\Psi = 10$

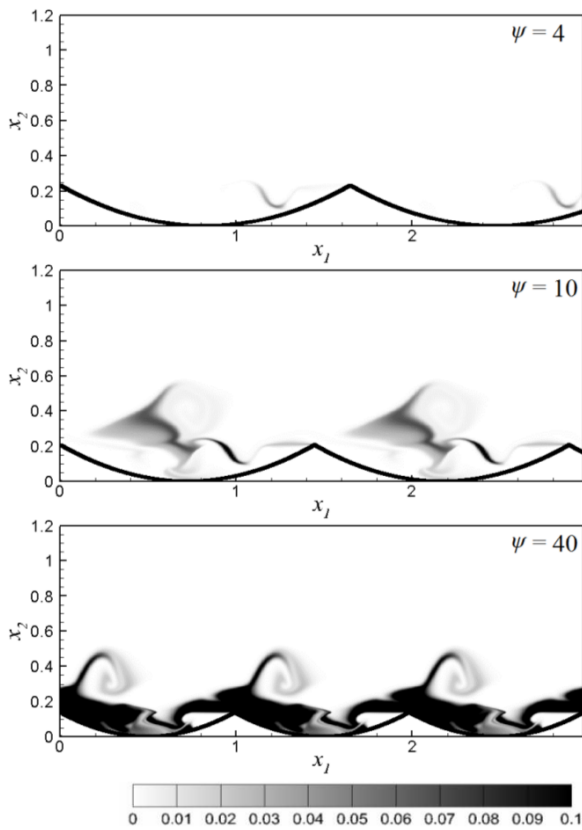


Figure 10: Suspended sediment concentration field ( $t = 11T/16$ ,  $\Psi = 4, 10, 40$ )

[11] Davies, A.G. and Villaret, C., "Eulerian drift induced by progressive waves above rippled and very rough bed," *J. Geophys. Res.*, 104(C1), 1465- 1488, 1999.

[12] Scandura, P., Blondeaux, P., and Vittori, G., "Three-dimensional oscillatory flow over steep ripples," *J. Fluid Mech.*, 412, 355-378, 2000.

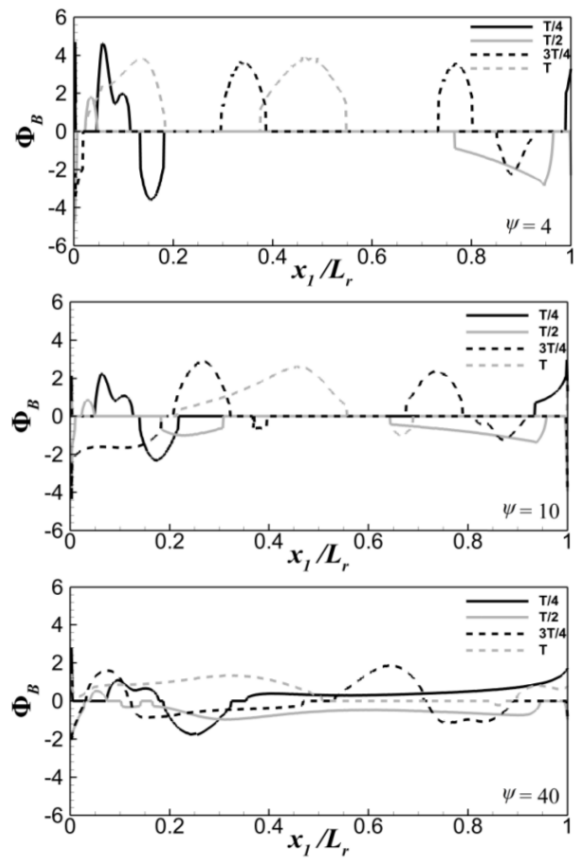


Figure 11: Bed flux,  $\Phi_B$ , distribution in the region between two ripple crests at  $T/4$  increments ( $0 \leq t \leq T$ ,  $\Psi = 4, 10, 40$ )

[13] Barr, B.C., Sinn, D.N., Pierro, T. and Winters, K.B., "Numerical simulation of turbulent, oscillatory flow over sand ripples," *J. Geophys. Res.*, 109, C09009, 2004.

[14] Fredsoe, J., and Deigaard, R., *Mechanics of coastal sediment transport*. World Scientific, Singapore, 1992.

[15] Meyer-Peter, E., and Müller, R., "Formulas for bed-load transport," *Proc. 2nd Meeting, Int. Assoc. for Hydraulic Structures, Assoc. for Hydr. Res.*, Madrid, 2, 39-64, 1948.

[16] Engelund, F., and Hansen, E., *A Monograph on Sediment Transport in Alluvial Streams*. Teknisk Forlag, Copenhagen, 1967. ERCOFTAC Bulletin xx

[17] Sleath, J.F.A., "The suspension of sand by waves," *J. Hydraul. Res.*, 20(5), 439-452, 1982.

[18] Al-Salem, A.A., *Sediment transport in oscillatory boundary layers under sheet flow conditions*. PhD Thesis, Delft University of Technology, 1993.

[19] Ribberink, J.S., and Al-Salem, A. A., "Sediment transport in oscillatory boundary layers in cases of rippled bed and sheet flow," *J. Geophys. Res.*, 99, C6, 12707-12727, 1994.

[20] O' Donoghue, T., and Clubb G., "Sand ripples generated by regular oscillatory flow," *Coastal Eng.*, 44(2), 101-115, 2001.

[21] Werf van der, J. J., Ribberink, J. S., O' Donoghue, T., and Doucette, J. C., "Modelling and measurement

- of sand transport processes over full-scale ripples in oscillatory flow," *Coastal Eng.*, 53 (8), 657-673, 2006.
- [22] Pedocchi, F., and Garcia, M. H., "Ripple morphology under oscillatory flow: 1. Prediction," *J. Geophys. Res.*, 114, C12014, 2009.
- [23] Pedocchi, F., and Garcia, M. H., "Ripple morphology under oscillatory flow: 2. Experiments," *J. Geophys. Res.*, 114, C12015, 2009.
- [24] Zedler, E. A., and Street, R. L., "Large-eddy simulation of sediment transport: Currents over ripples," *J. Hydraul. Eng.*, 127(6), 444-452, 2001.
- [25] Zedler, E. A., and Street, R. L., "Sediment transport over ripples in oscillatory flow," *J. Hydraul. Eng.*, 132(2), 1-14, 2006.
- [26] Engelund, F. and FredsÅye, J., "A sediment transport model for straight alluvial channels," *Nordic Hydrology*, 7, 293-306, 1976.
- [27] van Rijn, L.C., "Sediment transport, Part I: Bed load transport," *J. Hydraul. Eng.*, 110(10), 1431- 1456, 1984.
- [28] Hallermeier, R.J., "Terminal settling velocity of commonly occurring sand grains," *Sedimentology*, 28, 859-865, 1981.
- [29] Dimas, A.A., and Kolokythas, G.A., "Flow dynamics and bed resistance of wave propagation over bed ripples." *J. Waterway, Port, Coastal, Ocean Eng.*, 137(2), 64-74, 2011.
- [30] Balaras, E., "Modeling complex boundaries using an external force field on fixed Cartesian grids in large-eddy simulations," *Computers & Fluids*, 33, 375-404, 2004.
- [31] Nielsen, P., *Coastal Bottom Boundary Layers and Sediment Transport*. World Scientific, 324pp, 1992.
- [32] Dimas, A.A., and Dimakopoulos, A.S., "Surface roller model for the numerical simulation of spilling wave breaking over constant slope beach," *J. Waterway, Port, Coastal, Ocean Eng.*, 135(5), 235- 244, 2009.
- [33] Jensen, B.L., Sumer, B.M., and Fredsoe, J., "Turbulent oscillatory boundary layers at high Reynolds numbers," *J. Fluid Mech.*, 206, 265-297, 1989.

# TWO-PHASE FLOW MODELLING FOR SEDIMENT TRANSPORT: APPLICATION TO GRAVITY-DRIVEN FLOWS OF SUBAQUEOUS GRANULAR BEDS

C. Varsakelis<sup>1</sup>, D. Monsorno<sup>1</sup> and M.V. Papalexandris<sup>1</sup>

<sup>1</sup>*Institute of Mechanics, Materials, and Civil Engineering,  
Université catholique de Louvain  
B-1348, Louvain-la-Neuve, Belgium*

## Abstract

In the first part of this paper, a two-phase flow model for sediment transport is introduced, based on a mixture theory for fluid-saturated granular materials. This model consists of balance laws of mass and linear momentum for both the sediment and the interstitial fluid and an additional equation for the distribution of particle concentration. The second part of this paper is devoted to numerical aspects of the two-phase flow model in hand and, more specifically, we present a multi-phase projection method, endowed with an interface detection-and-treatment methodology, for its numerical integration. In the final part of this paper, results from numerical studies on gravity-driven flows of erodible, subaqueous granular beds down inclined planes are presented. These results constitute important sanity tests for the assessment of the predictive capacity of the two-phase flow model in hand.

## 1 Introduction

Sediment transport in coastal areas causes significant morphological changes that can amplify the effects of floods and related inundation hazards. Such unmitigated, and often undesirable, morphological changes increase the risk of failure of near-shore structures. Therefore, they can result in human and animal fatalities, substantial economic losses, and alteration of ecosystems.

Coastal sediment transport is induced by the interaction between turbulence and the solid particles that comprise the sediment. Due to the permeability of the sediment, the interstitial fluid (water) can penetrate it, thus forming a heterogeneous, immiscible mixture. As water flows through and over the sediment, it exerts both normal and shear stresses that engender its erosion.

Modelling of sediment transport is a challenging issue because of the complex interactions between water and sediment, the non-Newtonian behaviour of the latter, and the multitude of spatial and temporal scales that are associated with the flow. Traditionally, in sediment transport studies, the motion of the fluid is modelled either via the shallow water equations [1], or the Boussinesq equation [2], or the Navier-Stokes equations [3]. These equations are then coupled with (semi)empirical formulas for bed sediment transport [4] and an advection/diffusion equation for the suspended sediment [5]. In fact, as regards bed sediment transport, the employment of (semi)empirical formulas extends to both the incipient motion and the sediment flux [6].

Nonetheless, such single-phase flow models and their incarnations, cannot properly account for the interac-

tions between the solid particles and water. To overcome this difficulty, one has to resort to two-phase flow models. The compelling advantage of such models is that they take into consideration the dynamics of both phases and subsume mass and momentum balance laws that are valid both in and over the sediment. Typically, the derivation of two-phase models is based either on an averaging or on a mixture-theory approach. The averaging approach employs aspects from kinetic theories and is based on modifying the equations of motion of a single constituent to account for the presence of the other constituents and then averaging these equations over space and/or time. On the other hand, mixture theories treat the mixture as a multi-component continuum and adopt a non-equilibrium thermodynamic formalism for the derivation of the balance equations for each phase. This is achieved by employing the constraints imposed by the entropy inequality law in order to derive constitutive relations for the irreversible phenomena that take place, such as, viscosity, heat transfer, phase interactions, *etc.*

In this paper, we introduce a two-phase flow model for sediment transport derived from the continuum theory for fluid-saturated granular flows of Papalexandris [7]. This theory constitutes a generalization of the theory of irreversible processes; see, for example, Lebon et al. [8], to open and interacting subsystems with microstructure. The resulting model is valid for both compressible and incompressible flows while simultaneously taking into account the stresses that are developed in the granular medium due to its microstructure and the distribution of grains in space. The incompressible limit of this model has been formally derived by Varsakelis and Papalexandris in [9], upon generalization of low-Mach number asymptotics to multi-phase flows.

Following the presentation of the two-phase flow model, we shift our attention to its numerical integration and we delineate an algorithm for two-phase continua, that has been recently proposed by Varsakelis and Papalexandris [10]. This algorithm belongs to the class of projection-type methods, suitably extended to two velocity – two pressure models. One important aspect of this algorithm is its capacity to treat strong material interfaces associated with steep gradients of particle concentration. Finally, we assess the predictive capacity of the model of interest via numerically investigating the evolution of a subaqueous erodible bed in inclined configurations.

## 2 The Two-Phase Flow Model for Sediment Transport

We consider an isotropic granular material, saturated by a simple fluid, that occupies a domain  $\Omega$ . Further, we assume that both phases have constant density. Then, according to Varsakelis and Papalexandris [9], the governing equations of the mixture read, in non-dimensional form,

*Mass and momentum balance equations for the granular phase,*

$$\begin{aligned} \nabla \cdot \mathbf{u}_s &= 0, \\ \rho_s \phi_s \frac{d\mathbf{u}_s}{ds t} + \nabla(\phi_s p_s) &= \frac{1}{Re} \nabla \cdot (\mu_s \phi_s \mathbf{V}_s^v) \\ &\quad - \nabla \cdot (\Gamma_s \nabla \phi_s \otimes \nabla \phi_s) \\ &\quad + p_f \nabla \phi_s + \delta(\mathbf{u}_f - \mathbf{u}_s) \\ &\quad + \rho_s \phi_s \mathbf{g}. \end{aligned} \quad (1)$$

*Mass and momentum balance equations for the fluid phase,*

$$\begin{aligned} \nabla \cdot ((\mathbf{u}_s - \mathbf{u}_f) \phi_f) &= 0, \\ \rho_f \phi_f \frac{d\mathbf{u}_f}{df t} + \nabla(\phi_f p_f) &= \frac{1}{Re} \nabla \cdot (\mu_f \phi_f \mathbf{V}_f^v) \\ &\quad - (p_f \nabla \phi_s + \delta(\mathbf{u}_f - \mathbf{u}_s)) \\ &\quad + \rho_f \phi_f \mathbf{g}. \end{aligned} \quad (3)$$

*Compaction equation,*

$$\frac{d\phi_s}{ds t} = 0. \quad (5)$$

Here, the subscripts “ $s$ ” and “ $f$ ” denote the granular and fluid phase, respectively. Further,  $\rho_i$ ,  $\phi_i$  and  $\mathbf{u}_i = (u_{i1}, u_{i2}, u_{i3})$ ,  $i = s, f$  are the density, volume fraction and velocity vector of the phase  $i$ . Also,  $p_s$  and  $p_f$  are the “dynamic” pressures of the granular and fluid phase, respectively; they are completely equivalent to the pressure term that appears in the Navier-Stokes equations. Additionally,  $\mu_i$  is the viscosity coefficient of the phase  $i$  and  $\mathbf{g}$  is the gravity vector. We note that  $\mu_s$ , which describes the rheology of the granular material, is not constant but depends, among others, on the particle concentration.

The operators  $\frac{d}{ds t} = \frac{\partial}{\partial t} + \mathbf{u}_i \cdot \nabla$  and  $\mathbf{V}_i^v$  stand for the material derivative and the traceless deviatoric part of the deformation tensor of phase  $i$ ,  $i = s, f$ , respectively. The above governing equations are closed by the saturation condition,

$$\phi_s + \phi_f = 1. \quad (6)$$

The momentum exchange between the two phases is represented by the combined term  $p_f \nabla \phi_s + \delta(\mathbf{u}_f - \mathbf{u}_s)$ , appearing in the right-hand side of the momentum equations 2 and 4, albeit with opposite sign. More specifically, the term  $\delta(\mathbf{u}_f - \mathbf{u}_s)$  models the interphasial drag exerted on the solid particles by the fluid, with  $\delta$  being the interphasial drag coefficient. Further, the non-conservative product  $p_f \nabla \phi_s$  models nozzle effects and its presence is dictated by thermodynamic considerations.

The term  $\Gamma_s \nabla \phi_s \otimes \nabla \phi_s$ , whose divergence enters the momentum equation of the granular phase, 2, is the so-called *configuration stress tensor* and, accordingly,  $\Gamma_s$  is

the *configuration stress coefficient*. This tensor represents stresses developed from rearrangements in the distribution of the interfacial area density. Moreover, it constitutes the non-dissipative part of the Cauchy stress tensor of the granular material. At equilibrium, its off-diagonal components model shear stresses that such materials support due to their micro-structure.

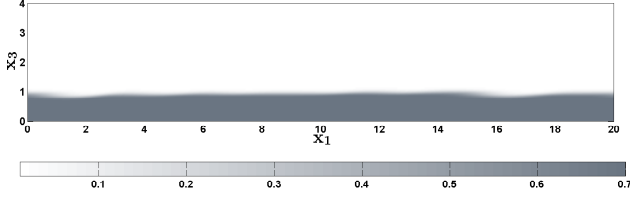
### 2.1 A Numerical Method for the Two-Phase Flow Model

Varsakelis and Papalexandris [10] proposed an algorithm for the integration of equations 1–5; see also the more recent article of Varsakelis et al. [11]. This algorithm constitutes a generalization of projection-type methods on collocated grids to two-phase flow models and employs a predictor–corrector scheme the integration in time. Due to the presence of two momentum equations, a double projection is employed; one for each velocity vector. Accordingly, a Poisson equation and a second-order elliptic PDE with variable coefficient are solved at both the prediction and the correction stages for the computation of the pressures of the granular and fluid phase, respectively. The generalized flux–interpolation method proposed in Lessani and Papalexandris [12] is employed for the integration of the convective terms to remedy the well-known odd–even decoupling phenomenon. Additionally, stiffness problems due to steep volume–fraction gradients in the vicinity of material interfaces are treated via a regularization method. Schematically, the flow-chart of the algorithm reads:

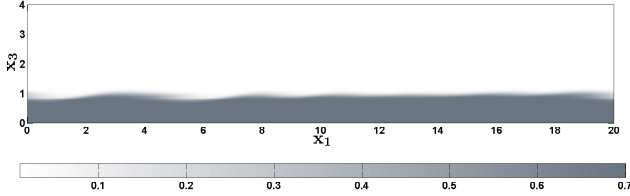
- i) The values of the volume fraction,  $\phi_s$  are computed by integrating the compaction equation 5 via the multi-dimensional upwind scheme of Colella [13].
- ii) The algorithm searches for interfaces by checking the magnitude of  $\nabla \phi_s$ . In the vicinity of the interface, the predicted values of  $\phi_s$  are replaced by those of smoother, compactly supported function obtained through a parabolic regularization.
- iii) A projection method is employed for the computation of the the granular pressure  $p_s$  and velocity  $\mathbf{u}_s$ . In particular, the pressure  $p_s$  is computed via solving numerically a Poisson equation. Once  $p_s$  has been computed,  $\mathbf{u}_s$  is calculated via the standard Helmholtz decomposition.
- iv) In our case,  $\mathbf{u}_f$  is not divergence free; see equation 3, which requires a generalization of the standard projection method. This results in a second order elliptic PDE with variable coefficients for the pressure  $p_f$ . Once  $p_f$  is computed, then  $\mathbf{u}_f$  is calculated via the Helmholtz-Marsden decomposition.

## 3 Numerical Results

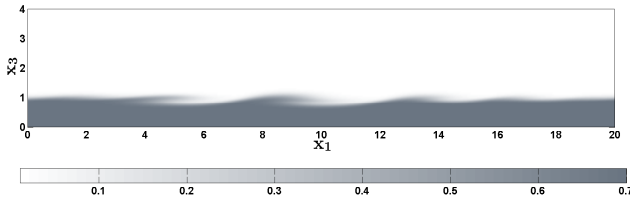
In this section, the two-phase flow model at hand is employed to investigate the motion of an subaqueous erodible granular bed down an inclined plane. The objective of this numerical study is twofold. First, to systematically study the properties of the flows of interest and gain physical insight on the mechanisms that drive their evolution. In this respect, emphasis is placed on the deformation of the material interface between the granular bed and the interstitial fluid lying above it. Second, to assess the predictive capacity of the model in hand for the flows of interest.



(a)



(b)



(c)

For clarity purposes, all dimensional variables are denoted with a hat symbol, “ $\hat{\cdot}$ ”.

### 3.1 Mixture Parameters and Computational Set-up

We consider a mixture of water with coarse sand. The sand is assumed to be monodisperse and its diameter  $\hat{d}_p$  is taken equal to  $1\text{ mm}$ . The densities of water and sand are  $\hat{\rho}_f = 1000\text{ kg/m}^3$  and  $\hat{\rho}_s = 2200\text{ kg/m}^3$ , respectively.

As regards the configuration stress coefficient  $\Gamma_s$ , we assume the following expression,

$$\hat{\Gamma}_s = \hat{k}_2 \hat{\rho}_s \phi_s. \quad (7)$$

Here,  $\hat{k}_2$  is a (strictly positive) material-dependent constant and its value should be obtained experimentally. However, systematic experimental measurements for  $\hat{k}_2$  have yet to appear in the literature. On the other hand, Varsakelis and Papalexandris [14] estimated numerically the value of  $\hat{k}_2$  by computing the equilibrium distributions of granular materials and the forces acting on them. On the basis of this study, we choose  $\hat{k}_2 = 4 \times 10^{-5}\text{ m}^4/\text{s}^2$ .

For the rheology of the granular material we opt for the experimental correlation derived by Savage [15],

$$\hat{\mu}_s = \frac{\hat{\mu}'_s \phi_s}{(\phi_c - \phi_s)^2}, \quad (8)$$

where the parameter  $\phi_c$  represents the maximum packing of grains. Following Passman et al. [16], the value of  $\hat{\mu}'_s$  is set equal to  $723\text{ kg/(m}\cdot\text{s)}$ . The blow-up of 8 at

$\phi_s = \phi_c$  is intended to represent the “jamming” effect that grains experience upon attaining their maximum packing. However, the effects of this singularity have not been explored, either theoretically or numerically. For this reason, we have assumed that  $\phi_c = 1$ , so that  $\mu_s$  remains bounded. On the other hand, the interstitial fluid, water, is assumed to be a simple Newtonian fluid at constant temperature. As such, its viscosity is taken to be constant and equal to  $\hat{\mu}_f = 1 \times 10^{-3}\text{ kg/(m}\cdot\text{s)}$ .

As regards the interphasial drag coefficient  $\hat{\delta}$ , the force density exerted by the fluid on the particles is approximated by the drag on a sphere moving at constant speed at low Reynolds numbers. This results in the following expression for  $\hat{\delta}$ ,

$$\hat{\delta} = \phi_s 18 \frac{\hat{\mu}_f}{\hat{d}_p^2} Q(Re_p). \quad (9)$$

For the function  $Q(Re_p)$ , the empirical relationship proposed by Rowe [17] is used,

$$Q(Re_p) = \begin{cases} 1 + 0.15 Re_p^{0.687}, & Re_p < 1000, \\ 0.01833 Re_p, & Re_p \geq 1000, \end{cases} \quad (10)$$

where  $Re_p$  is the particle Reynolds number, defined with respect to the relative grain velocity, *i.e.*,

$$Re_p = \frac{\hat{\rho}_f \hat{d}_p}{\hat{\mu}_f} |\hat{\mathbf{u}}_s - \hat{\mathbf{u}}_f|. \quad (11)$$

In our study, all physical parameters are non-dimensionalized as follows. The phasial densities and pressures have been non-dimensionalized with respect to the density of water,  $\hat{\rho}_{ref} = 1000\text{ kg/m}^3$ , and atmospheric pressure,  $p_{ref} = 10^5\text{ Pa}$ , respectively. Also, the initial thickness of the granular layer,  $\hat{h}$ , and the reference velocity  $u_{ref} = \sqrt{\hat{g} \hat{h}}$  have been used for the non-dimensionalization of lengths and velocities, respectively. Further, the viscosity coefficients have been non-dimensionalized with respect to the mixture’s viscosity  $\mu_{ref} = (\rho_s \phi_{s,in} \mu_s + \rho_f \phi_{f,in} \mu_f) / (\rho_s \phi_{s,in} + \rho_f \phi_{f,in})$ , where  $\phi_{s,in}$  stands for the initial distribution of particles. For the problem in hand,  $\mu_{ref} \equiv 608\text{ kg/(m}\cdot\text{s)}$  and, accordingly, the Reynolds number of the flow is equal to approximately 0.2.

### 3.2 Subaqueous Granular Bed Inclined at $30^\circ$ .

The unsteady, gravity-driven flow of a subaqueous erodible granular bed on a plane inclined at  $30^\circ$ , with the above mixture parameters, has been studied via direct numerical simulations in Varsakelis and Papalexandris [18]. Herein, we confine ourselves to a brief presentation of the the main findings and refer the reader to [18] for additional information. For the sake of completeness, we also discuss the computational set-up of the numerical experiments.

The mixture is placed on the surface of a plane inclined at an angle  $30^\circ$  to the streamwise direction. A Cartesian coordinate system is employed with  $x_1$  the streamwise and  $x_3$  the normal direction. The dimensions of the computational domain are  $l = 20$  and  $4$  in the streamwise and normal directions, respectively and an equidistant mesh of  $500 \times 100$  cells is used for its discretization. Finally, we set  $\Delta t = 0.005 \Delta x_3$ .

As regards boundary conditions, the flow is assumed to be periodic in the streamwise ( $x_1$ ) direction, with period

equal to  $l$ . At the bottom of the computational domain, which coincides with the inclined plane, the no-slip condition is prescribed for the phasial velocities and zero-Neumann conditions are prescribed for both the phasial pressures and the volume fraction. On the other hand, the top boundary of the computational domain is considerably far from the material interface. For this reason, at this boundary, the free-slip boundary condition is applied for the phasial velocities whereas zero-Neumann conditions are assigned to the phasial pressures and the volume fraction.

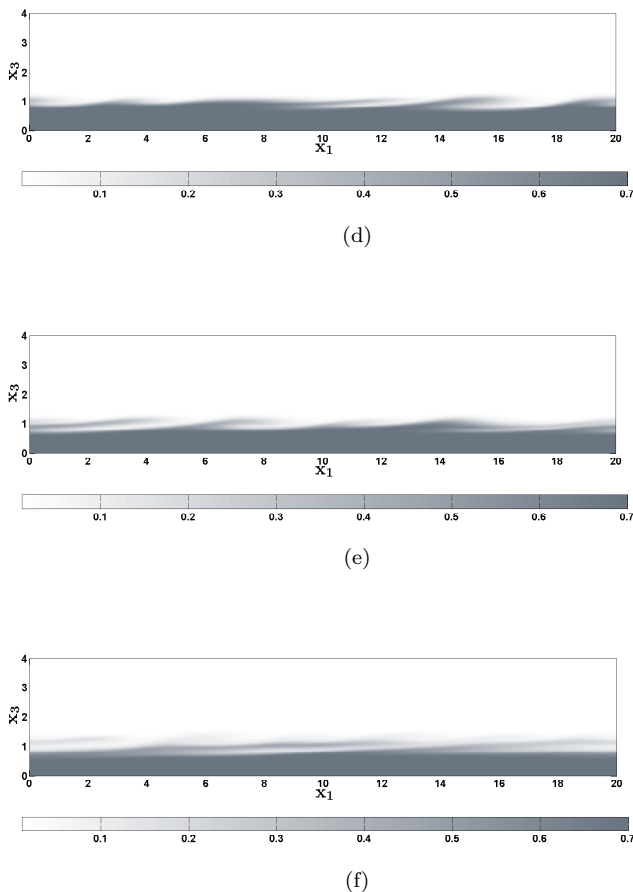


Figure 1: Iso-contours of particle concentration  $\phi_s$ . (a)  $t = 24.5$ , (b)  $t = 30$ , (c)  $t = 37$ , (d)  $t = 43$ , (e)  $t = 49$ , (f)  $t = 73$ . The material interface deforms into a series of long waves due to the onset of the Kapitza instability. The Kapitza waves are transformed into skewed, vortex ripples that grow in time and also coalesce. Eventually, the fluid velocity becomes large enough in the neighbourhood of the interface and the ripples are washed out

For the initial condition of the particle concentration, we consider a dense ( $\phi_s = 0.7$ ) granular layer of constant thickness  $h = 1$ , placed on the inclined plane. This profile is superimposed to a sinusoidal perturbation of period  $l$  and amplitude  $h/5$ , so as to trigger the erosion of the material interface. Outside the granular bed, the domain is filled with water. As regards the initial conditions for the other variables, we assume that the entire mixture is at rest so that the flow is induced by gravity.

Figures 1(a)–1(f) show the particle concentration at various time instances. Our simulations show that the evolution of the flow can be divided into three distinct phases. The first phase, which lasts until approximately  $t \simeq 36.7$ , is characterized by the onset of the Kapitza instability and the deformation of the material interface

into a series of long waves. In the second phase, which starts at  $t \simeq 36.7$  and lasts until  $t \simeq 62$ , the Kapitza waves transform into skewed vortex ripples. As the flow evolves, the ripples grow and eventually coalesce. In the third phase, which spans from  $t \simeq 61.2$  until the termination of the simulation, the high fluid velocities wash out these ripples and a layer of rapidly moving particles forms at the material interface.

Let  $\bar{u}_{s_1}$  denote the normalized, streamwise-averaged, granular velocity component, in the streamwise direction. 2 shows plots of  $\bar{u}_{s_1}$ , against depth  $x_3$ , at different time instances. The velocities are maximized at the material interface. Away from it they decrease to zero, however, no rigid body motion is observed, even close to the inclined plane. This result is in very good agreement with the analysis of Andreotti and Douady [19], which asserts that, for angles of inclination  $a \geq 25^\circ$ , the flowing height reaches the inclined plane.

2 additionally yields that the predicted velocity profiles collapse very well to a master linear curve that has small negative curvature at the vicinity of the material interface; this is evidence that the flow evolves in a self-similar manner. According to previous experimental and numerical studies on dry granular flows with large angles of inclination, the profiles of  $\bar{u}_{s_1}$  are approximately linear, with positive curvature at the upper part and negative curvature at the lower part; see, for example, Andreotti and Douady [19]. Further, these studies show that for  $a \geq 30^\circ$ , the profiles become predominantly linear. Self-similar behaviour has also been reported in the experiments of dry granular avalanches of Bonamy et al. [20]. Our simulations provide the first evidence that these properties extend over to unsteady flows of fluid-saturated granular materials as well. Finally, it is worth noting that the aforementioned similarity between the  $\bar{u}_{s_1}$  profiles in dry and fluid-saturated granular flows has already been confirmed experimentally for steady flows; see Jain et al. [21], Doppler et al. [22] and others.

The examination of the vorticity field of the fluid provides important information about the nature of the observed ripples. Figures 3(a)–3(c) depict iso-contours of the magnitude of the fluid phase vorticity field at times  $t = 30, 43$  and  $73$ , respectively. The shearing of the granular medium by the interstitial fluid engenders vortex shedding from the material interface. These vortices are skewed, with their streamwise-diameter being nearly ten times large than the normal one, and undergo streamwise elongation as the flow evolves. Moreover, since the observed vortices are located downstream each ripple's crest, in accordance with Bagnold's classical terminology, the ripples are actually *vortex* ripples.

## 4 Conclusions

In the present article, a two-phase model for sediment transport has been presented. This model is derived from a particular mixture theory for fluid-saturated granular materials and comprises balance laws for both the fluid and the granular phase plus an additional equation that governs the evolution of the volume fraction. Further, it properly accounts for the momentum exchanges between the two phases in a thermodynamically consistent manner. Also, the model of interest allows for non-zero shear stresses at zero shear rates, which constitutes an important characteristic of granular materials.

Following the exposition of the two-phase flow model, an algorithm for its numerical treatment has been presented. This is a predictor-corrector numerical method that employs a double projection for the computation

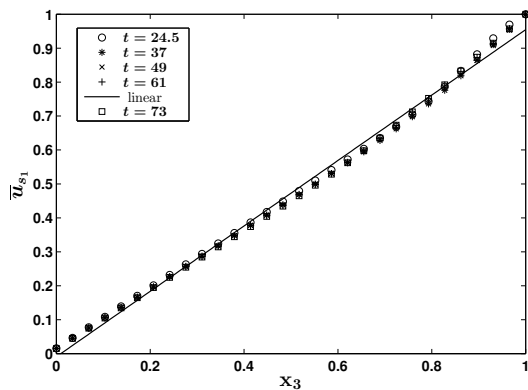
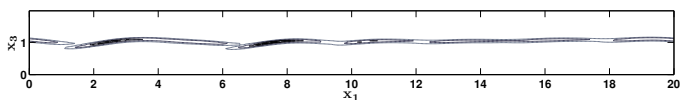
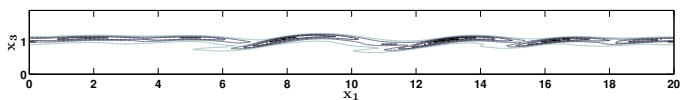


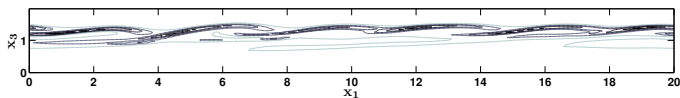
Figure 2: Granular velocity profiles  $\bar{u}_{s1}$  plotted against depth at various times. The predicted velocities collapse onto a master linear curve, with a slightly negative curvature close to the material interface. This collapse indicates that the flow evolves in a self-similar manner



(a)



(b)



(c)

Figure 3: Iso-contours of the vorticity field of the fluid phase at (a)  $t = 30.6$ , (b)  $t = 43$ , (c)  $t = 73$ . Vortical structures are observed over the material interface. At  $t = 43$ , when the ripples have been formed, lee vortices are formed downstream the crest of each ripple

of the phasial velocities and pressures; one for each velocity vector. For the numerical treatment of material interfaces, the algorithm is combined with an interface detection-and-treatment methodology which is based on a local regularization scheme.

The predictive capacity of the two-phase flow model of interest, has been assessed via direct numerical simulations of a gravity-driven flow of an erodible, subaqueous granular bed down an inclined plane. Overall, the

numerical predictions adduce that the two-phase flow model at hand can reproduce the important characteristics of the flows of interest.

## Acknowledgment

Financial support for the first author has been provided by the National Research Fund of Belgium (FNRS) under the GRANMIX Projet de Recherche. The second and third authors gratefully acknowledge the financial support of the European Union via SEDITRANS, a project funded by the Marie Curie Actions of the EU's 7th Framework Programme.

## References

- [1] M. J. Diaz, E. D. Fernandez-Nieto, and A. M. Ferreira, "Sediment transport models in shallow water equations and numerical approach by high order finite volume methods," *Comp. Fluids*, vol. 37, pp. 299–316, 2008.
- [2] H. A. Schäffer, P. A. Madsen, and R. Deigaard, "A boussinesq model for waves breaking in shallow water," *Coast. Eng.*, vol. 20, pp. 185–202, 1993.
- [3] A. S. Dimakopoulos and A. A. Dimas, "Large-wave simulation of three-dimensional, cross-shore and oblique, spilling breaking on constant slope beach," *Coast. Eng.*, vol. 58, pp. 790–801, 2011.
- [4] P. T. Nam, M. Larson, H. Hanson, and L. X. Hoan, "A turbulent and suspended sediment transport model for plunging breakers," *Coast. Eng.*, vol. 56, pp. 1084–1096, 2009.
- [5] B. Ontowirjo and A. Mano, "A turbulent and suspended sediment transport model for plunging breakers," *Coast. Eng. J.*, vol. 50, pp. 349–367, 2008.
- [6] B. Camenen and P. Larroude, "Comparison of sediment transport formulae for the coastal environment," *Coast. Eng.*, vol. 48, pp. 111–132, 2003.
- [7] M. V. Papalexandris, "A two-phase model for compressible granular flows based on the theory of irreversible processes," *J. Fluid Mech.*, vol. 517, pp. 103–112, 2004.
- [8] D. G. Lebon, D. Jou, and J. Casas-Vázquez, *Understanding Non-equilibrium Thermodynamics: Foundations, Applications, Frontiers*. Springer, 2008.
- [9] C. Varsakelis and M. V. Papalexandris, "Low-mach-number asymptotics for two-phase flows of granular materials," *J. Fluid Mech.*, vol. 669, pp. 472–497, 2011.
- [10] C. Varsakelis and M. V. Papalexandris, "A numerical method for two-phase flows of dense granular mixtures," *J. Comput. Phys.*, vol. 257, pp. 737–756, 2014.
- [11] C. Varsakelis, D. Monsorno, and M. V. Papalexandris, "Numerical aspects of two pressure – two velocity models." submitted for publication, 2014.
- [12] B. Lessani and M. V. Papalexandris, "Time-accurate calculation of variable density flows with strong temperature gradients and combustion," *J. Comput. Phys.*, vol. 212, pp. 218–246, 2006.

- [13] P. Colella, “Multidimensional upwind methods for hyperbolic conservation laws,” *J. Comput. Phys.*, vol. 87, pp. 171–200, 1990.
- [14] C. Varsakelis and M. V. Papalexandris, “The equilibrium limit of a constitutive model for two-phase granular mixtures and its numerical approximation,” *J. Comput. Phys.*, vol. 229, pp. 4183–4207, 2010.
- [15] S. B. Savage, “Gravity flow of cohesionless granular materials in chutes and channels,” *J. Fluid Mech.*, vol. 92, pp. 53–96, 1979.
- [16] S. L. Passman, J. W. Nunziato, and P. B. Bailey, “Shearing motion of a fluid-saturated granular material,” *J. Rheol.*, vol. 20, pp. 167–192, 1986.
- [17] P. N. Rowe, “Drag forces in a hydraulic model of a fluidised bed. part ii,” *Trans. Int. Chem. Engng.*, vol. 48, pp. 175–180, 1961.
- [18] C. Varsakelis and M. V. Papalexandris, “Numerical simulation of unsteady chute flows of fluid-saturated granular materials.” submitted for publication, 2014.
- [19] B. Andreotti and S. Douady, “Selection of velocity profile and flow depth in granular flows,” *Phys. Rev. E*, vol. 63, p. 031305, 2001.
- [20] D. Bonamy, F. Daviaud, and L. Laurent, “Experimental study of granular flows via a fast camera: a continuous description,” *Phys. Fluids*, vol. 14, pp. 1666–1673, 2002.
- [21] N. Jain, J. M. Ottino, and R. M. Lueptow, “Effect of interstitial fluid on a granular flow layer,” *J. Fluid Mech.*, vol. 508, pp. 23–44, 2004.
- [22] D. Doppler, P. Gondret, T. Loiseleux, S. Meyer, and M. Rabaud, “Relaxation dynamics of water-immersed granular avalanches,” *J. Fluid Mech.*, vol. 577, pp. 161–181, 2007.

# MATHEMATICAL MODELLING OF DISCONTINUOUS OPEN-CHANNEL FLOWS OVER GRANULAR BEDS

R.M.L. Ferreira<sup>1</sup>, S. Amaral<sup>2</sup> and B. Spinewine<sup>3</sup>

<sup>1</sup> *CEHIDRO, Instituto Superior Técnico, Universidade de Lisboa, Portugal, ruif@civil.ist.utl.pt*

<sup>2</sup> *Laboratório Nacional de Engenharia Civil (LNEC), Portugal, samaral@lnec.pt*

<sup>3</sup> *Université catholique de Louvain, Belgium, benoit.spinewine@uclouvain.be*

## Abstract

The flow resulting from an instantaneous removal of a vertical barrier initially separating different levels of fluid and granular material, extending indefinitely on both up- and downstream directions, constitutes a useful idealization of dam-break flows over mobile beds composed of cohesionless sediment. These herein called geomorphic dam-break flows, have been shown to exhibit discontinuities other than the downstream progressing wave-front. Of particular importance is the jump that forms, for some combinations of initial conditions and bed granular material, near the location of the vertical barrier. In this text, the discontinuities occurring in geomorphic dam-break flows are investigated in the framework of the shallow-flow theory. The main objective is to identify its generation mechanism, namely if they are susceptible to be described by Riemann waves or if they are flow features caused by momentum sources, namely friction, or by phenomena beyond the shallow-flow theory. Experimental results are presented and compared with a theoretical weak solution of the governing equations given initial discontinuous data conforming to a Riemann problem. The classification of the discontinuities follows the comparison between the observed and calculated flow features for the same initial conditions. Two types of discontinuities are found, one purely described by a nonlinear wave inherent to the solution of the Riemann problem and one generated by fluid-granular interactions not included in the shallow-flow idealisation.

## 1 Introduction

In this text, geomorphic dam-break flows are defined as shallow-flows resulting from the rapid release of stored water and sediment into a channel with a mobile granular bed, causing important morphological changes in the downstream valley. Such flows propagate in the form of a bore, a type of wave-front, often laden with sediment, which, given the involved length scales, can be considered a discontinuity [1]. The speed of this discontinuity, along with the maximum water depth associated to the dam-break flow, have been studied at length, as they constitute important elements for downstream risk assessment [2, 3, 4, 5].

The wave-front may not be the only discontinuity in geomorphic dam-break flows. A hydraulic jump occurring near the location of the dam was reported in the early mobile-bed experiments of Chen and Simonds [6]. More recently, Capart and Young [7] drew attention to an upstream-progressing jump seen to form at early times at the dam location. For some combinations of initial conditions and bed material, the experimental results of [4], [8] or [9] also exhibit discontinuities forming at

the vicinity of the dam and travelling at much smaller velocities than the wave-front. The experiments performed in these works may not provide a coherent body of data, since the shape, the dimensions of the flumes and the methods to remove the vertical barrier are too distinct. Thus, on safe grounds, only one observational result can be assertively uttered: on prismatic rectangular mobile-bed channels, geomorphic dam-break flows resulting from the instantaneous removal of a vertical dam exhibit, for some combinations of initial conditions and bed material, a jump that forms near the location of the dam at early times and whose velocity is slower than that of the wave-front. This discontinuity will be henceforth called a *2-jump*.

The characterization of the wave-front benefits from more than one hundred years of theoretical and experimental studies (for the review of early results, *cf.* Stoker (1957), [10], pp. 22-22). Quite on the contrary, the amount of empirical results concerning the 2-jump is much limited and theoretical results are almost non-existent Spinewine and Capar [9].

In this text, the discontinuities occurring in geomorphic dam-break flows are investigated. Special emphasis is placed on the quantification of the variables that describe the 2-jump. The thorough phenomenological characterization of these discontinuities will not be attempted. The main objective is to understand whether they are susceptible to be described by Riemann waves of the weak solution of the homogeneous part of the governing equations, based on the shallow-water theory, or if they are flow features whose mathematical description requires a formal treatment beyond the shallow-water theory, namely the introduction of vertical accelerations. Empirical evidence, experimental results described in Amaral (2004) [11], is compared with the solution of the governing equations, as presented by Ferreira (2005) [12], pp. 396-430.

The classification of the discontinuities follows the comparison between observed and calculated flow features for the same initial conditions. If the solution of the homogeneous conservation equations (based on the shallow-water theory) does not seem to describe occurring flow discontinuities, it is concluded that phenomena not included in the inertial and flux terms of the governing one-dimensional equations is responsible for the 2-jump.

## 2 Conceptual Model

The conservation laws of sediment and global mass and of global momentum describing flows over cohesionless granular beds can for shallow-flow as detailed in, e.g., [12, 13]. Such framework will be considered valid for the description of geomorphic dam-break flows (see

also [14, 9]). Following Ferreira et al. (2009), [13], the one-dimensional conceptual model employed in this study features a layered structure with i) a lowermost layer, the bed, composed of grains with no appreciable vertical or horizontal mean motion, ii) the contact-load layer, where sediment concentrations approach saturation and iii) an upper layer, essentially constituted of clear water.

In what concerns flow resistance and the interaction between the bed and the contact-load layer, Fraccarollo and Capart [1] showed that there is a time window where the effects of flow friction are negligible and were local equilibrium is a valid approximation for sediment transport. Although the results of Fraccarollo and Capart (2002) [1] are strictly valid for erosional flows and for a particular conception of a frictional time scale, it will be assumed that there is indeed a time window for which geomorphic dam-break flows feature equilibrium sediment transport and are only marginally affected by bed friction. The one-dimensional conservation equations become homogeneous and are susceptible to be written in the following quasi-conservative form

$$\partial_t (h + Y_b) + \partial_x (hu) = 0 \quad (1)$$

$$\partial_t (a_m hu) + \partial_x (a_c u_c^2 h_c + u_s^2 h_s + g (\frac{1}{2} h_s^2 + \frac{1}{2} a_c h_c^2 + h_s h_c)) + g (a_c h_c + h_s) \partial_x (Y_b) = 0 \quad (2)$$

$$\partial_t ((1-p)Y_b + C_c h_c) + \partial_x (Chu) = 0 \quad (3)$$

where  $t$  and  $x$  are the independent variables time and longitudinal coordinate, respectively,  $h$  is the water depth,  $u$  is the depth averaged flow velocity,  $Y_b$  is the bed elevation (the latter three are the primitive dependent variables),  $h_c$ ,  $u_c$  and  $C_c$  are, respectively, the thickness, the depth-averaged velocity and the flux-averaged concentration of the contact-load layer,  $h_s$  and  $u_s$  are, respectively, the thickness and the depth-averaged velocity of the upper flow layer,  $a_m = 1 + (s-1)C$ ,  $a_c = 1 + (s-1)C_c$ ,  $s$  is the specific gravity of the sediments,  $C$  is the flow-averaged sediment concentration,  $p$  is the bed porosity and  $g$  is the acceleration of gravity. The conservative variables of the system are  $h + Y_b$ ,  $a_m hu$  and  $(1-p)Y_b + C_c h_c$ .

In the stratified flow idealization of Ferreira et al. (2009) [13], the equilibrium bedload discharge is  $q_s = C_c u_c h_c$ . Assuming that  $h_c$  is related to the the flux of kinetic energy associated to the fluctuating motion of transported grains, its closure equation is

$$\frac{h_c}{d_s} = m_1 + m_2 \theta \quad (4)$$

where  $\theta$  is Shields number and  $m_1$  and  $m_2$  are parameters that should depend on the mechanical properties of the sediment particles, on its diameter and density and on the viscosity of the fluid. Ferreira (2005) [12], pp. 283–285 and Ferreira et al. (2009) [13] proposed that, for a given fluid, for a certain ranges of Shields numbers and grain diameters and for granular materials such as sand and plastic pellets,  $m_1$  and  $m_2$  may show little variation with particle properties and can be considered constants. In this text  $m_1 = 1.5$  and  $m_2 = 5.5$ . This is in accordance with the data of [15].

Shields number  $\theta$  is defined as  $C_f u^2 / (\rho^{(w)} g (s-1) d_s)$ , where  $C_f$  is the friction coefficient. Ferreira et al. (2009) [13] proposed that Sumer et al. (1996) [15] sheet-flow data could be used to express flow resistance in geomorphic flows such as those resulting from the collapse of a dam over mobile beds. Reorganising the data, they noted that, at the highest shear stresses, the friction coefficient could be fitted by  $\frac{u}{\omega_s} \frac{d_s}{h}$ , where  $\omega_s$  is the terminal

fall velocity of the particles and  $d_s$  is the particle diameter, and that the mean of the highest values were 0.02.

The velocity of the mixture in the contact layer is parametrized as in Ferreira et al. (2006) [16]:

$$u_c = u \left( \frac{h_c}{h} \right)^{1/6} \quad (5)$$

Should there be an imbalance between the actual and the capacity bedload discharges, there will be a vertical displacement of the bed. Ferreira et al. (2009) [13] argued that this would be a result of an imbalance between collisional and frictional stresses in a thin sub-layer at the base of the contact-load layer. If these stresses are in equilibrium, a formula for  $C_c$  can be derived:

$$C_c = \frac{\theta}{\tan(\varphi_b) (m_1 + m_2 \theta)} \quad (6)$$

where  $\tan(\varphi_b)$  is the dynamic friction angle of the granular material (the ratio between normal and shear granular stresses [17]).

Equations (4), (5) and (6), along with the equation for the friction coefficient, close the system of conservations laws (1), (2) and (3). Other choice of closures is likely to change quantitatively the solution of the system, as seen in Canelas et al. (2013) [18], but the structure of solution remains unchanged.

### 3 Solution of the Riemann Problem

Condensed in vector notation, the homogenous part of the conservation laws (1), (2) and (3) form the first order hyperbolic system

$$\partial_t (\mathbf{V}(\mathbf{U})) + \partial_x (\mathbf{F}(\mathbf{U})) + \mathbf{A} \partial_x (\mathbf{V}(\mathbf{U})) = \mathbf{0} \quad (7)$$

where  $\mathbf{V} : \mathbb{R}^3 \times ]0, +\infty[ \rightarrow \mathbb{R}^3$  is the vector of dependent primitive variables,  $\mathbf{F} : \mathbb{R}^3 \rightarrow \mathbb{R}^3$  is the vector of conservative variables,  $\mathbf{F} : \mathbb{R}^3 \rightarrow \mathbb{R}^3$  is the conservative flux vector,  $\mathbf{A} \partial_x (\mathbf{V}(\mathbf{U})) : \mathbb{R}^3 \rightarrow \mathbb{R}^3$  is the vector of non-conservative fluxes,  $\mathbf{A}$  is a matrix such that  $\mathbf{A}_{23} = g (a_c h_c + h_s)$  and  $\mathbf{A}_{ij} = 0$ ,  $(i, j) \neq (2, 3)$ .

Should the collapse of a dam be idealized as an instantaneous removal of a vertical barrier initially separating two constant states featuring given values of elevations of bed and free-surface, as seen in Figure 1, the mathematical expression of the geomorphic dam-break problem is a Riemann problem cast as equation (7) subjected to the initial condition

$$\mathbf{U}_0 \equiv \mathbf{U}(x, t=0) = \begin{cases} \mathbf{U}_L & \text{if } x < 0 \\ \mathbf{U}_R & \text{if } x \geq 0 \end{cases} \quad (8)$$

where subscripts L and R stand for left and right states, respectively, defined as in Figure 1.

There is no result guaranteeing the existence and unicity of the solution to the Cauchy problem represented by governing equations of the conceptual model and any complete set of initial conditions. However, under strict conditions, Glimm's theorem [19] can be employed to demonstrate the existence and unicity of weak solutions of Riemann problems. Ferreira (2005) [12], pp. 361–363, showed that weak solutions for the particular Riemann problem formed by equations (7) and (8) exist but they are not unique. This is so because equations (1) to (3) cannot be written in pure conservative form. Indeed,

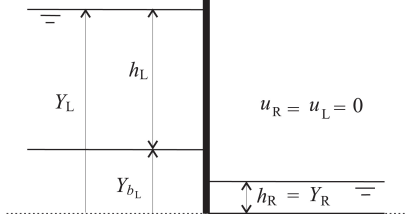


Figure 1: Initial conditions of the dam-break problem. The involved variables are:  $Y$ , the water elevation,  $h$  the water depth,  $Y_b$  the bed elevation and  $u$ , the depth-averaged flow velocity. The subscripts L and R stand for the initial left and right states, respectively

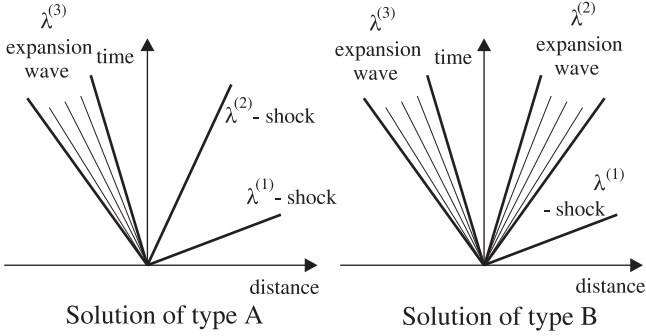


Figure 2: Wave structure of the weak solution of the Riemann problem constituted by system (7) subjected to the initial conditions (8). Left: solution of type A; right: solution of type B

term  $g(a_c h_c + h_s) \partial_x (Y_b)$  represents a source of momentum and is not reducible to a conservative flux (thus precluding the direct application of Glimm's theorem). In fact, existence can only be asserted if A is linearized across discontinuities. Thus, the solution depends on the specific linearization carried out. The Rankine-Hugoniot jump conditions derived from the integral form of equation (7) become

$$(\mathbf{U}_d - \mathbf{U}_u) S_j = (\mathbf{F}_d - \mathbf{F}_u) + \mathbf{A}^* (\mathbf{U}_d - \mathbf{U}_u) \quad (9)$$

where  $S_j$  is the velocity of the shock associated to the  $\lambda^{(j)}$ -characteristic field,  $\mathbf{A}^*$  is the linearized matrix A and the subscripts d and u stand for "downstream" and "upstream", respectively. A consistent linearization can be obtained by averaging the terms across the discontinuity.

The weak solution of system (7) subjected to (8), in which  $\mathbf{U}_0$  expresses the geometry seen in Figure 1, admits two types of self-similar solutions, A and B, depending on the values of  $h_L$ ,  $Y_{bL}$  and  $h_R$ . Their wave structure, represented in the  $x-t$  plane, can be seen in Figure 2. All characteristic fields are genuinely non-linear, as demonstrated in Ferreira (2005). In accordance to Lax theorem, both solutions comprise three non-linear waves separated by constant states. Herein, the eigenvalues associated to the eigenvectors of system (7) are ordered such that  $\lambda^{(1)} > \lambda^{(2)} > \lambda^{(3)}$ .

Solution of type A comprises one expansion wave associated to the  $\lambda^{(3)}$ -characteristic field and two shock waves, associated to the  $\lambda^{(2)}$ - and the  $\lambda^{(1)}$ -characteristic fields. Constant state 1 separates the waves associated to  $\lambda^{(2)}$ - and  $\lambda^{(1)}$ -characteristic fields. Constant state 2 separates the expansion wave associated to  $\lambda^{(3)}$ -characteristic field and the wave associated to  $\lambda^{(2)}$ -characteristic field. The celerity of the

shock associated to the  $\lambda^{(1)}$ -characteristic field is designated  $S_1$  and the velocity, flow depth and bed elevation in constant state 1 are, respectively  $u_1$ ,  $h_1$  and  $Y_{b1}$ . Concomitantly, the celerity of the shock associated to the  $\lambda^{(2)}$ -characteristic field is designated  $S_2$  and the velocity, flow depth and bed elevation in constant state 1 are, respectively  $u_2$ ,  $h_2$  and  $Y_{b2}$ .

Solution of type B comprises two expansion waves associated to the  $\lambda^{(3)}$ - and  $\lambda^{(2)}$ -characteristic fields, and one shock wave, associated to the  $\lambda^{(1)}$ -characteristic field. As in solution A, constant states 1 and 2 separate the non-linear waves, with the same definitions. The variables that characterize the constant states keep the same designations. Note that, in this solution, there is no definition of  $S_2$ .

The flow profiles corresponding to the wave structures of Figure 2 are shown in Figure 3.

Solution of type B, first studied by Fraccarollo and Capart (2002) [1] in the wake of Fraccarollo and Armanini (1999) [20], does not admit 2-jumps. On the contrary, in the solution of type A, the shock associated to  $\lambda^{(2)}$  is a flow feature that may be associated to the 2-jump.

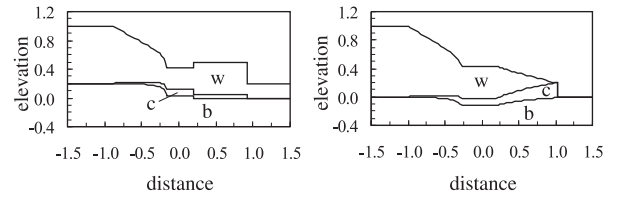


Figure 3: Flow profiles corresponding to the weak solution of the Riemann problem constituted by system (7) subjected to the initial conditions (8). Left: solution of type A; right: solution of type B. The flow regions are: w - clear water/suspended sediment layer; c - contact load layer and b - bed

It is noted that the shock associated to the  $\lambda^{(2)}$ -characteristic field in solution of type A represents a negative jump in the flow depth and a positive, aggradational, jump in the bed elevation. The direction of propagation and the type of morphological impacts featured by the observed jump provide the fundamental criteria to decide whether it is a flow structure describable by a Riemann shock or one that requires different conceptualization. The key result is the following: geomorphic hydraulic jumps that migrate upstream and that are associated to scour in the bed are clearly not described by the 2-jumps generated by the sediment dynamics included in equations (1) to (3).

The behaviour of the solution with the increase of the initial jump at  $x = 0$  is now assessed and compared with Stoker's (1957) classic solution. In particular, the velocity of the shock associated to the  $\lambda^{(1)}$ -characteristic field is compared with the value of the reference velocity represented by Ritter's solution for the velocity of the dam-break wave-front,  $2\sqrt{gh_0}$ .

Dimensional analysis reveals that the self-similar longitudinal profile of any flow variable  $U_i$  is determined by the following parameters

$$\Gamma_i = \Pi_i \left( \alpha', \delta', s, \tan(\varphi_b), \frac{d_s}{L_*} \right) \quad (10)$$

where

$$\alpha' \equiv \frac{h_R + |\min(0, Y_{bL})|}{h_L + \max(0, Y_{bL})} \quad (11)$$

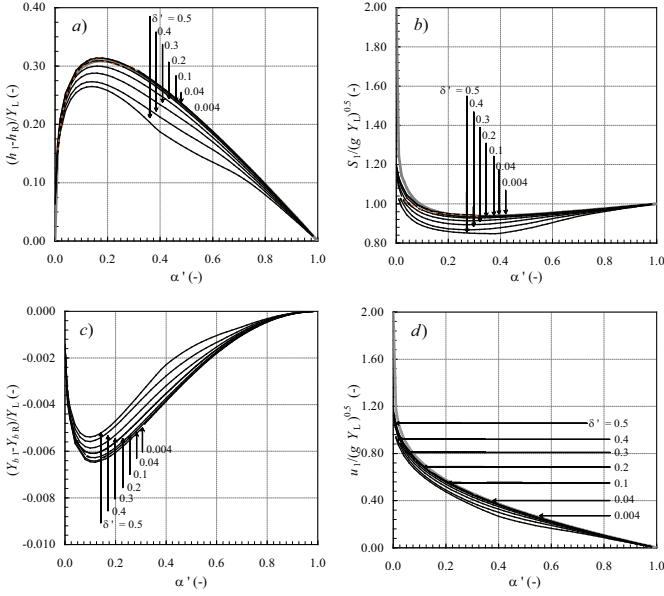


Figure 4: Geometric and cinematic features of the shock associated to the  $\lambda^{(1)}$ -characteristic field and of the first constant state. a) Strength of the shock expressed in terms of water depths; b) velocity of the shock  $S_1$ ; c) strength of the shock expressed in terms of bed elevation and d) velocity in the constant state,  $u_1$ . Grey thick line stands for the Stoker's (1957) solution. Orange dotted line signals the boundary between solutions of types A and B. Solution computed for PVC pellets with  $d_s = 0.001$  m,  $s - 1 = 0.58$  and  $\tan(\varphi_b) = 0.32$ . Initial conditions comprise  $Y_L = 0.25$  and  $Y_{bR} = 0.0$

and

$$\delta' \equiv \frac{Y_{bL}}{h_L + \max(0, Y_{bL})} \quad (12)$$

The length scale implicit in (11) and (12) is  $L_* = h_L + \max(0, Y_{bL})$ . From this length scale, time and velocity scales can be derived. It is obtained  $T_* = \sqrt{\frac{L_*}{g}}$  and  $U_* = \sqrt{gL_*}$ , respectively. Note that, for positive  $\delta'$ ,  $L_* = Y_L$ .

Hence, the for constant  $s$ ,  $\tan(\varphi_b)$  and relative submergence of the particles,  $d_s/L_*$ , the behaviour of the solution can be assessed in the  $\alpha'$ - $\delta'$  space, thus allowing for a direct comparison with the classic theoretical results of Stoker (1957) [10]. Figures 4 and 5 show the geometric and cinematic features of the waves associated to the  $\lambda^{(1)}$ - and  $\lambda^{(2)}$ -characteristic fields and adjacent constant states as a function of  $\alpha'$  and  $\delta'$ .

Figure 4(a) shows that the strength of the shock associated to the  $\lambda^{(1)}$ -characteristic field, expressed in terms of water depths, decreases as  $\delta'$  increases. The magnitude of the bed discontinuity (Figure 4c) associated to the same shock also decreases as  $\delta'$  becomes larger. As for the flow velocity in the first constant state,  $u_1$  (4b), and the shock velocity,  $S_1$  (4d), both cinematic variables decrease as the initial bed step increases. This fact is particularly obvious in the case of the dam-break wave-front velocity  $S_1$ .

It is also observed that, for small values of  $\delta'$  (less than, say, 0.04), the theoretical solution of the geomorphic shallow-water equations is only distinguishable from Stoker's solution only if  $\alpha'$  is small. In particular, for  $\alpha' = 0$ , it can be proved that the shock associated to the  $\lambda^{(1)}$ -characteristic field has a finite value [12], contrarily

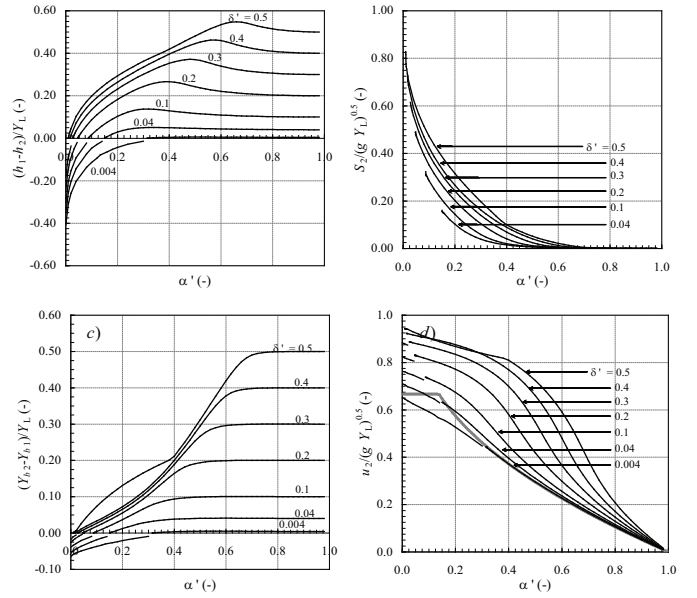


Figure 5: Geometric and cinematic features of the shock associated to the  $\lambda^{(2)}$ -characteristic field and of the first constant state. a) Strength of the shock expressed in terms of water depths; b) velocity of the shock  $S_2$ ; c) strength of the shock expressed in terms of bed elevation and d) velocity in the constant state,  $u_2$ . Grey thick line stands for the Stoker's (1957) solution. Orange dotted line signals the boundary between solutions of types A and B. Solution computed for PVC pellets with  $d_s = 0.001$  m,  $s - 1 = 0.58$  and  $\tan(\varphi_b) = 0.32$ . Initial conditions comprise  $Y_L = 0.25$  and  $Y_{bR} = 0.0$

to the fixed-smooth bed case, in which Ritter's solution features a wave-front of vanishing height. Indeed, it is observable in Figure 4 that, as  $\alpha' \rightarrow 0$ , both  $h_1$  and  $Z_1$  converge to finite values while the limits of  $u_1$  and  $S_1$  are different from Ritter's result for the velocity of the wave-front  $2\sqrt{gY_L}$ .

The influence of increasing the value of  $\delta'$  is thus to reduce the magnitude of the wave associated to the  $\lambda^{(1)}$ -characteristic field, slowing down its velocity and diminishing its strength. Two causes may be at the root of this behaviour: i) the dynamics of the wave associated to the  $\lambda^{(2)}$ -characteristic field may represent an energy loss for the overall flow and ii) the influence of inertia of the sediment, evermore important as  $\delta'$  increases, may add inertia to the overall flow. Hypothesis (i) may be validated, in its essential traits, by noting that a) it is only in the realm of solution of type A (that actually features a dissipative discontinuity, the geomorphic hydraulic jump) that the influence of  $\delta'$  in the reduction of the velocity of the bore is relevant and b) the strength and the celerity of the shock associated to the  $\lambda^{(2)}$ -characteristic field are increasing functions of  $\delta'$ .

This last aspect can be seen in Figures 5(a), (b) and (c). It is also seen that (Figure 5d) that the velocity in the second constant state also strongly increases as a function of  $\delta'$ , irrespectively of the type of solution.

Table 1: Summary of the initial data for experimental tests

Name	$h_L$ (m)	$Y_{b_L}$ (m)	$h_R$ (m)	$L_*$ (m)	$\alpha'$ (-)	$\delta'$ (-)
25_-05_00	0.30	-0.05	0.00	0.30	0.167	-0.167
35_-05_00	0.40	-0.05	0.00	0.40	0.125	-0.125
25_00_00	0.25	0.00	0.00	0.25	0.000	0.000
35_00_00	0.35	0.00	0.00	0.35	0.000	0.000
35_05_00	0.30	0.05	0.00	0.35	0.000	0.143
25_05_00	0.20	0.05	0.00	0.25	0.000	0.200
35_10_00	0.25	0.10	0.00	0.35	0.000	0.286
25_05_05	0.20	0.05	0.05	0.25	0.200	0.200
35_10_10	0.25	0.10	0.10	0.35	0.286	0.286

## 4 Comparison with experimental evidence and discussion

Experimental work took place in the laboratory of hydraulics of the Department of Civil and Environmental Engineering of the Université catholique de Louvain, Louvain-la-Neuve, Belgium. The experimental tests were performed in 6 m long and 25.1 cm wide horizontal channel. The dam was simulated by a vertical gate, placed at 3 m from the extremities, whose movement is directed downwards [3]. A manually activated trigger releases the pressure of 7 bar, generated in a compressor, required to open the gate at a speed of about  $5 \text{ ms}^{-1}$ . The maximum non-dimensional time necessary to open the gate is  $t_0^* = t_0 \sqrt{\frac{9.8}{\max(h_L)}} = 0.4$  where  $t_0$  is the maximum time necessary to open the gate and  $\max(h_L)$  is the maximum initial water depth behind the gate.

The experimental tests were recorded in digital video by a CCD camera acquiring 200 fps with the resolution of  $512 \times 1024$ . The flow was fully recorded in the downstream reach of the channel. Upstream the gate, only the first 0.8 m were recorded as explained in Amaral (2004) [11].

The sediment particles employed in the tests were PVC pellets with  $s = 1.56 \text{ kg m}^{-3}$ . The equivalent diameter of a PVC particle – the diameter of a sphere with the same volume – is 3.9 mm. The dimensions of the particles exhibited little variability. All tests featured a piecewise horizontal bed. In accordance with Figure 1, the datum was set to the level of the downstream bed. It is important to note that the downstream bed was saturated in all tests, even if  $h_R = 0$ . The initial conditions for the nine experimental tests shown here, described with the variables presented in Figure 1, are shown in table 1.

The raw video-footage data obtained from the tests allowed for the determination of longitudinal flow profiles (details in [11]) where three surfaces were identified: a) the free surface, b) the boundary between the transport layer and the clear water layer and c) the boundary between the bed and the transport layer. The profile of the water depth was computed as the difference between the free surface and the bed. From the water depth profiles, it was possible to estimate the location and the strength of the observed discontinuities at each instant.

The observed longitudinal flow profiles are shown in Figures 6 – solution of type B – and 7 – solution of type A. The theoretical profiles, calculated from the weak solution of system (7) given the initial conditions discriminated in table 1, are also shown in these Figures, superimposed to the flow profiles. Both the experimental profiles and the theoretical solutions are shown in self-

similar co-ordinates.

It is observed that the thickness of the contact load layer and the minimum bed elevation are correctly estimated in almost all tests. Naturally, phenomena pertaining to soil mechanics, namely slope stability and *en masse* bed movement, could not have been reproduced by the theoretical solution since the governing equations do not incorporate formulations for those phenomena. The steep slopes featured by the weak solutions at the end of the expansion wave associated to the  $\lambda^{(3)}$ -characteristic field in Figures 6e), f) and g) are the Riemann-wave idealisation of the gentler slopes featured by the observed profiles. The sharp bed step could not be maintained by the cohesionless bed material; a fracture surface was formed at the toe of the step with the inclination of the rest angle of the particles; finally the sediment above this fracture surface entered the contact load layer and was eventually deposited further downstream. A simple mechanism accounting for this mass failure was proposed and tested in numerical solutions by several researchers [9, 18, 21] but it is not relevant for the present discussion.

In the tests with a negative bed step (6a and b) the theoretical solution captures the bed profile reasonably well. It is observed that a steep positive slope results from the initial discontinuity. Presumably, it is the flow that provides the extra shear force to maintain the bed slope larger than the submerged rest slope.

The instability of the initial bed step in the experimental tests shown in Figure 7 obeyed same mechanisms already explained for the tests depicted in Figures 6e), f) and g). However, because of the presence of a layer of water downstream, the transport capacity is much lower and the flow does not evolve into a debris-flow-like wave-front. Hence, the bed material resulting from the initial bed step failure is deposited almost instantaneously at the toe of the step and, as the flow loses memory of the gate movement, becomes a bed discontinuity progressing downstream along with the jump in water surface. As a result, the bed profile calculated along the expansion wave associated to the  $\lambda^{(3)}$ -characteristic field is, in these tests, a better description of the observed profile.

The effect of flow resistance is perceived in the observed profiles inasmuch they are not truly self-similar. This is particularly true for the flows depicted in Figures 6. Furthermore, it is noticed that Froude similarity does not completely determine the flow profiles. If that was the case, parameters  $\alpha'$  and  $\delta'$  would suffice to determine the profiles. Instead, it is observed in Figures 6c) and d), whose profiles are both characterized by  $\alpha' = 0$  and  $\delta' = 0$ , that neither the velocity of the wave-front nor the overall shape of the profile are exactly the same for the two types of flows. The differences are, however, negligible in the time window under consideration.

In both solutions, the shock associated to the  $\lambda^{(1)}$ -characteristic field is physically identifiable with the wave-front (see Figures 6 and 7). As for the 2-jumps, their existence and the variables that characterize them were determined in accordance to the principles explained above. It is clear that tests 25\_-05\_00, 35\_-05\_00 and 35\_00\_00 (Figure 6a, b and d) develop 2-jumps that progress upstream. Tests 25\_05\_05 and 35\_10\_10 (Figure 7a and b) develop 2-jumps that move downstream. In other words, the 2-jump may not always be identifiable by the shock associated to the  $\lambda^{(2)}$ -characteristic field in the solution of type A. Indeed, it is clear from Figures 2 (left) and 7 that this is a downstream progressing shock, while the observed 2-jumps often migrate upstream.

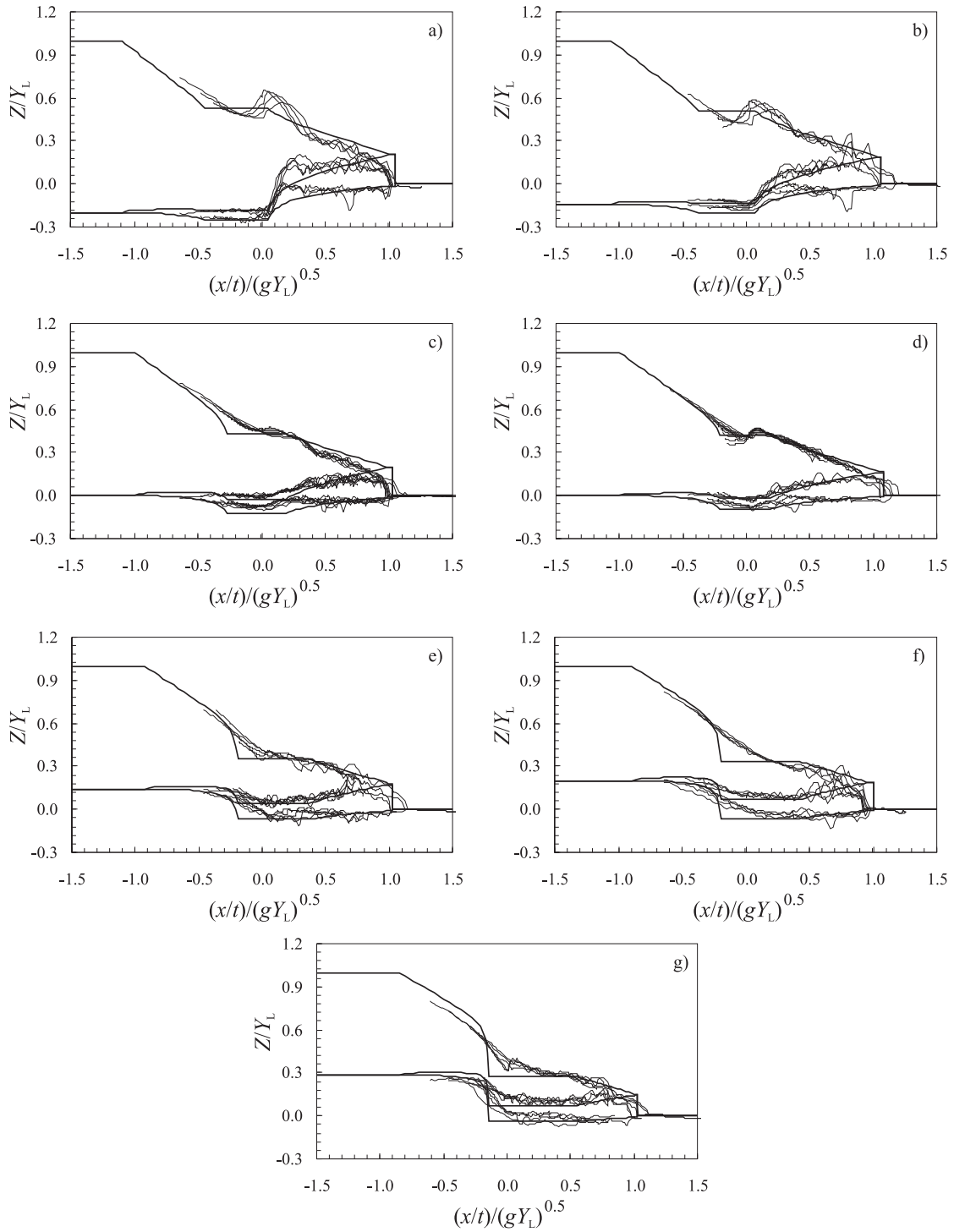


Figure 6: Flow profiles. Solution of type B. Profiles correspond to tests a) 25\_-05\_00; b) 35\_-05\_00; c) 25\_00\_00; d) 35\_00\_00; e) 35\_05\_00; f) 25\_05\_00; g) 35\_10\_00. Solid thick lines (—) stand for the theoretical solution while solid thin lines (—) stand for the observed profiles

The dynamics and the kinematics of the wave-front are sufficiently well described by the Rankine-Hugoniot jump conditions, equations (9) with  $j = 1$ . Indeed, the strength of the wave-front, defined as  $h_R - h_L$ , remains approximately constant throughout the duration of the experimental test (see Figure 7) which enables a meaningful comparison between the weak solutions and the experimental profiles.

The velocity of the wave-front, however, decreases over time, as seen in Figure 8, especially for the tests for which  $h_R = 0$  (Figure 8a to 8f). This fact prompted Leal et al. [2] to describe the path of the wave-front in

the  $xt$  plane as a 2<sup>nd</sup> order equation. There is no appreciable decrease in the velocity of the wave-front in the experiments for which  $h_R > 0$ . This suggests that bottom friction is the main responsible for the delay of the wave-front.

Since bottom friction is not included in the weak solution of 7, in order to delay the velocity of the wave-front in the theoretical solution it is necessary to increase the factors that affect  $S_1$  in 9. Such factors are related to the inertia of the contact load layer and are expressed by its thickness and the sediment concentration. Given that  $\tan(\varphi_b)$ ,  $m_1$  and  $m_2$  are constants, a good agreement

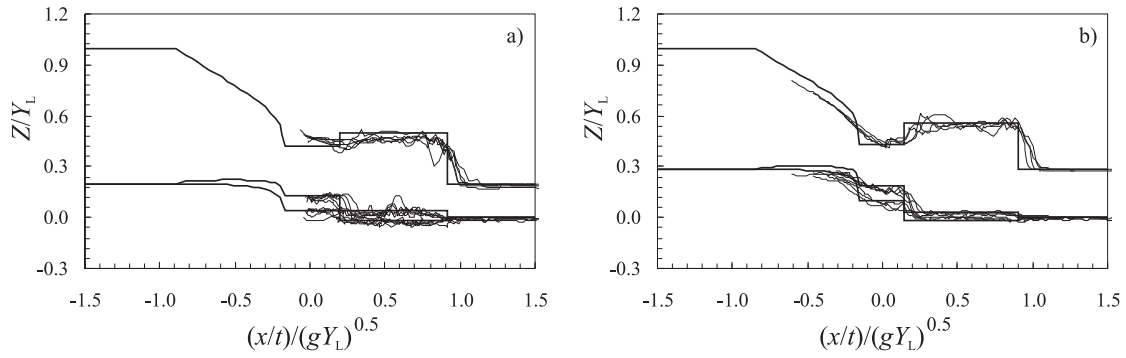


Figure 7: Flow profiles. Solution of type A. Profiles correspond to a) 25\_05\_05; b) 35\_10\_10. Solid thick lines (—) stand for the theoretical solution while solid thin lines (—) stand for the observed profiles

of the observed and the calculated wave-front velocity requires a good estimate for the friction coefficient  $C_f$ . The current formulation apparently leads to the increase of the flow depth in the first constant state (the state upstream the  $\lambda^{(2)}$ -shock). As seen in Figure 9, the theoretical shock strength is consistently overestimated, for the same initial conditions.

Fraccarollo and Capart [1] noticed that the wave-front propagates as an erosional shock. Since it is associated to the  $\lambda^{(1)}$ -characteristic field, it is fundamentally a hydrodynamically-driven shock: the bed jump is comparatively small. On the contrary, Ferreira [12], showed that the  $\lambda^{(2)}$ -shock is always an aggradational shock in which morphodynamics is of paramount importance. Since the influence of the variables that describe sediment dynamics is strong in the  $\lambda^{(2)}$ -characteristic field, the dynamics of the associated shock are fundamentally determined by the solid phase: the  $\lambda^{(2)}$ -shock progresses with the velocity of propagation of the jump in the bed, much slower than the wave-front.

The experimental work revealed that only the tests depicted in Figure 7 featured 2-jumps susceptible to be identified with the  $\lambda^{(2)}$ -shock. These downstream-progressing discontinuities are driven by the dune-like advancement of a sharp-edged bed wave. The strong coupling between hydrodynamic and morphodynamic variables in the  $\lambda^{(2)}$ -characteristic field is revealed by the fact that the strength of the shock is of the same magnitude in both types of variables.

Because of the correct coupling between hydrodynamic and morphodynamic variables, the results of the weak solution are a good reproduction of the observed behaviour, especially in what concerns the shock velocity (see 8g and h). The shock strength is less well reproduced. As seen in Figure 9, the shock strength is overestimated by the theoretical solution. This is mainly due to the fact that the weak solution overestimates the bed elevation in the 2<sup>nd</sup> constant state.

It is proposed that 2-jumps that occur in geomorphic dam-break flows whose mathematical description is a weak solution of type A are well described by the  $\lambda^{(2)}$ -shock. Its dynamics traduce the equilibrium of the flux and inertial terms across the shock, being the gravity-related term included in the flux terms, once linearized in accordance with equation 9.

Other types of 2-jump were found in the experimental tests whose profiles are depicted in Figures 6. The mathematical description of these tests is a weak solution of type B. When  $\alpha = 0$  the solution is necessarily of type B. If  $\alpha > 0$  and  $\delta < 0$ , the solution is also of type B. It

follows from the fact that type B solutions exhibit a continuous wave associated to the  $\lambda^{(2)}$ -characteristic field, that any 2-jump developing from such initial conditions can not be described by the jump conditions (9).

Alcrudo and Benkhaldoun [22] developed a theoretical solution for the dam-break flow over fixed bed with a discontinuity in the dam location. Their solution features an extra discontinuity, a jump born in the source term that describes the force of gravity. Such discontinuity is impossible in mobile bed problems, as the derivative of the bed elevation,  $\partial_x(Y_b)$ , ceases to be treated as a source. Thus, the origin of these 2-jumps must be searched in interaction between the bed and the flow in the first instants.

It is observed that these 2-jumps are associated with important scour at the vicinity of the dam. Capart and Young [7], working with almost neutrally buoyant particles ( $s = 1.05$ ), observed a 2-jump with these properties and whose upstream velocity is comparable to those shown in Figures 8a), b) and d). They proposed that bottom friction could be a cause of the jump, by slowing down the wave-front. Mathematically, the characteristics in the  $\lambda^{(2)}$ -characteristic field would fold backwards in the  $x - t$  plane until converging into a compressive shock. Capart and Young [7] backed these model with the early studies of Dressler [23] on the influence of bottom friction. Numerical experiments carried out for fixed and mobile beds [12] have shown that it is always possible to find continuous solutions even in the presence of very large bottom friction. It is thus unlikely that this 2-jump is mainly originated by the compressing of the  $\lambda^{(2)}$ -characteristic field under the effect of friction.

Chen and Simonds [6] report an upstream progressing 2-jump in a bed featuring an initial positive bed step. They believe that the jump is originated by the increased flow velocity over the bed discontinuity, as it would occur in a weir. Although their initial conditions are difficult to interpret, their results may be used to state the case for the influence of two-dimensional effects in the first stages of the flow. A highly accelerated parcel of flow directed downwards would originate an scour hole, not explainable by the shallow water theory. Once formed, this accelerated flow region would progress upstream, a process similar to the knickpoint migration. This would explain the 2-jump observed in test 35\_00\_00 (Figure 6d).

The jumps seen in the tests featuring an initial negative bed step, 25\_-05\_00 and 35\_-05\_00 (Figures 6a and b) may also owe to two-dimensional flow effects. An accelerated parcel of flow directed upwards would be susceptible to slow down the flow in the vicinity of the bed jump, thus provoking the free surface elevation seen in

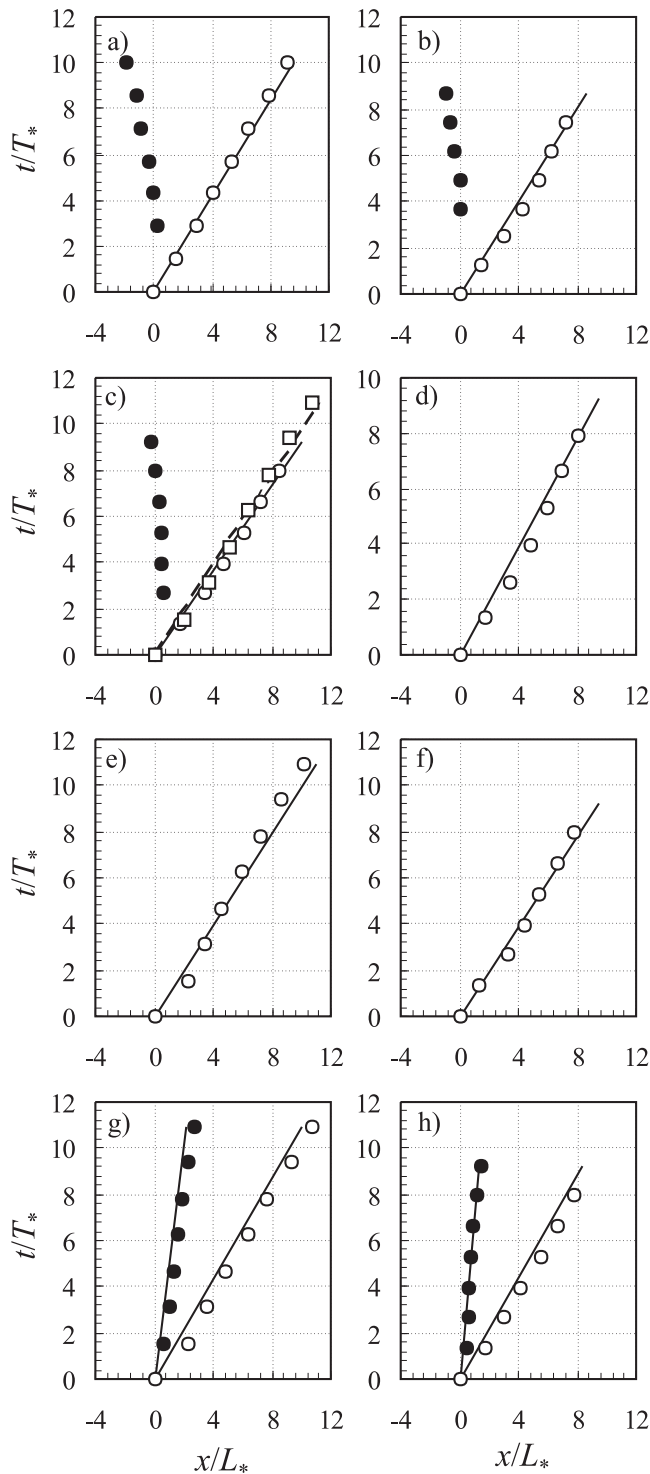


Figure 8: Calculated and measured non-dimensional shock paths. a)  $\alpha = 0.167$ ,  $\delta = -0.167$ ; b)  $\alpha = 0.125$ ,  $\delta = -0.125$ ; c)  $\alpha = 0.0$ ,  $\delta = 0.0$  (features tests with  $d_s/L_* = 0.0129$  and  $d_s/L_* = 0.0180$ ); d)  $\alpha = 0.0$ ,  $\delta = 0.143$ ; e)  $\alpha = 0.0$ ,  $\delta = 0.200$ ; f)  $\alpha = 0.0$ ,  $\delta = 0.286$ ; g)  $\alpha = 0.200$ ,  $\delta = 0.200$ ; h)  $\alpha = 0.286$ ,  $\delta = 0.286$ . Solid lines (—) stand for the calculated path of the  $\lambda^{(1)}$ - and the  $\lambda^{(2)}$ -shocks; open circles ( $\circ$ ) stand for the measured path of wave-front; solid circles ( $\bullet$ ) stand for the measured path of the 2-jump. In sub-Figure c), the convention is maintained for the test with  $d_s/L_* = 0.0129$ ; for the test with  $d_s/L_* = 0.0180$ , the dashed line (- - -) stands for the calculated path of the  $\lambda^{(1)}$ -shock and the open squares ( $\square$ ) stand for the measured path of the wave-front

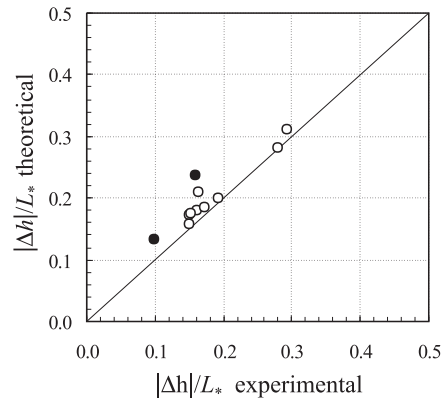


Figure 9: Calculated and measured non-dimensional shock strengths in terms of flow depths. Open circles ( $\circ$ ) stand for the wave-front; solid circles ( $\bullet$ ) stand for the 2-jump

Figures 6a) and b). The hydrodynamic response to compatibilize the supercritical and subcritical flow regimes thus created would be forming a jump. It would progress upstream in an antidune-like movement.

## 5 Conclusion

The present study attempted to contribute to the characterization of the discontinuities observed in geomorphic dam-break flows. Special attention was conceded to the often observed 2-jump that forms at early times at the location of the dam.

A comparison between experimental flow profiles and the weak solution of the dam-break Riemann revealed that there is a class of 2-jumps whose mechanics are susceptible to be described by the Rankine-Hugoniot conditions of the shock associated to the  $\lambda^{(2)}$ -characteristic field. The distinctive traits of these 2-jumps are its positive velocity of propagation and, in what concerns bed morphology, its aggradational nature.

When the weak solution features an expansion wave in the  $\lambda^{(2)}$ -characteristic field, the causes of the 2-jump must be searched outside the realm of phenomena described by the homogeneous one-dimensional governing equations. It is observed that these 2-jumps migrate upstream and are associated to scour holes. Possible explanations comprise: i) frictional effects combined with non-equilibrium sediment transport and; ii) two-dimensional flow effects. More likely, a combination of the preceding effects may be the cause of these 2-jumps.

## Acknowledgements

This research was partially funded by FEDER, program COMPETE, and by national funds through Portuguese Foundation for Science and Technology (FCT) project RECI/ECM-HID/0371/2012.

## References

- [1] L. Fraccarollo and H. Capart, “Riemann wave description of erosional dam-break flows,” *Journal of Fluid Mechanics*, vol. 461, pp. 183–228, 2002.

- [2] J. Leal, R. Ferreira, and A. Cardoso, "Dam-break wave front celerity," *Journal of Hydraulic Engineering*, vol. 132, no. 1, pp. 69–76, 2006.
- [3] B. Spinewine and Y. Zech, "Small-scale laboratory dam-break waves on movable beds," *J. Hydraul. Res.*, vol. extra issue, pp. 73–86, 2007.
- [4] J. Leal, R. Ferreira, and A. Cardoso, "Maximum level and time to peak of dam-break waves on mobile horizontal bed," *Journal of Hydraulic Engineering*, vol. 135, no. 1, pp. 995–999, 2009.
- [5] J. L. Carrivick, R. Jones, and G. Keevil, "Experimental insights on geomorphological processes within dam break outburst floods," *J. Hydrology*, vol. 408, pp. 151–163, 2011.
- [6] Y. Chen and D. Simonds, "An experimental study of hydraulic and geomorphic changes in an alluvial channel induced by failure of a dam," *Water Resources Research*, vol. 15, pp. 1183–1188, 1979.
- [7] H. Capart and D. Young, "Formation of a jump by the dam-break wave over a granular bed," *Journal of Fluid Mechanics*, vol. 372, pp. 165–187, 1998.
- [8] L. Goutière, S. Soares-Frazão, and Y. Zech, "Dam-break flow on mobile bed in abruptly widening channel: experimental data," *Journal of Hydraulic Research*, vol. 49, no. 3, pp. 367–371, 2011.
- [9] B. Spinewine and H. Capart, "Intense bed-load due to a sudden dam-break," *J. Fluid Mech.*, vol. 731, pp. 579–614, 2013.
- [10] J. Stoker, *Water Waves. The mathematical theory with applications*. Interscience Publishers, 1957.
- [11] S. R. C. Amaral, "Experimental Characterization of 1-D Dam-Break Waves over Cohesionless Sediment Beds." Final Project for the Graduation in Civil Engineering. Instituto Superior Técnico, Technical University of Lisbon., 2004.
- [12] R. M. L. Ferreira, *River Morphodynamics and Sediment Transport. Conceptual Model and Solutions*. PhD thesis, Instituto Superior Técnico - Technical University of Lisbon, Lisboa, 2005.
- [13] R. M. Ferreira, M. J. Franca, J. G. Leal, and A. H. Cardoso, "Mathematical modelling of shallow flows: Closure models drawn from grain-scale mechanics of sediment transport and flow hydrodynamics," *Canadian Journal of Civil Engineering*, vol. 36, pp. 1604–1621, 2009.
- [14] J. G. Leal, R. M. Ferreira, and A. H. Cardoso, "Geomorphic dam-break flows. part i. 1d conceptual model," *Water Management*, vol. 163, pp. 297–304, 2010.
- [15] B. M. Sumer, A. Kozakiewicz, J. Fresoe, and R. Deigard, "Velocity and concentration profiles in sheet-flow layer of movable bed," *J. Hydraul. Eng.*, vol. 122, pp. 549–558, 1996.
- [16] R. M. L. Ferreira, J. G. Leal, and A. H. Cardoso, "Conceptual model for the bedload layer of gravel bed stream based on laboratory observations," in *River Flow 2006* (E. A. R.M.L. Ferreira, J.G.B. Leal and A. Cardoso, eds.), vol. 1, pp. 947–956, Balkema, Taylor and Francis Group, 2006.
- [17] R. Bagnold, "Experiments on a gravity-free dispersion of large solid spheres in a newtonian fluid under shear," in *Proceedings of the Royal Society of London*, pp. 49–63, 1954.
- [18] R. Canelas, J. Murillo, and R. M. Ferreira, "Two-dimensional depth-averaged modelling of dambreak flows over mobile beds," *J. of Hydraul. Res.*, vol. 51, pp. 392–407, 2013.
- [19] J. Glimm, "Solutions in the large for nonlinear hyperbolic systems of equations.," *Comm. Pure Appl. Math.*, vol. 18, pp. 697–715, 1965.
- [20] L. Fraccarollo and A. Armanini, "A semi-analytical solution for the dam-break problem over a mobile bed," in *Proc. of 1<sup>st</sup> IAHR Symposium of River, Coastal and Estuarine Morphodynamics (RCEM)*, vol. 1, pp. 361–369, University of Genova, Genova, Italy, 1999.
- [21] C. Swartenbroekx, Y. Zech, and S. Soares-Frazão, "Two-dimensional two-layer shallow water model for dam break flows with significant bed load transport.," *Intl J. Numer. Meth. Fluids*, vol. 73, no. 5, p. 477?508, 2013.
- [22] F. Alcrudo and F. Benkhaldoun, "Exact solutions to the riemann problem of the shallow water equations with a bottom step," *Computers and Fluidsp*, vol. 30, pp. 643–671, 2001.
- [23] R. F. Dressler, "Comparison of theories and experiments for the hydraulic dambreak wave.," in *Assemblée General de Rome*, vol. 3, pp. 319–328, Intl. Assoc. of Hydrology, 1954.

# QUADRANT ANALYSIS OF COHERENT STRUCTURES IN OPEN CHANNEL FLOWS OVER MOBILE AND IMMOBILE HYDRAULICALLY ROUGH BEDS

M.J. Franca<sup>1</sup>, B.O. Santos<sup>2</sup>, F. Antico<sup>3</sup> and R.M.L. Ferreira<sup>4</sup>

<sup>1</sup> *Laboratoire de Constructions Hydrauliques, École Polytechnique Fédérale de Lausanne, Lausanne, Switzerland, email: mario.franca@epfl.ch*

<sup>2</sup> *Department of Civil Engineering & MARE - Marine and Environmental Sciences Centre, New University of Lisbon, Portugal, email: oliveirasantos@gmail.com*

<sup>3</sup> *Instituto Superior Técnico & CEHIDRO, University of Lisbon, Portugal, email: federica.antico@tecnico.ulisboa.pt*

<sup>4</sup> *Instituto Superior Técnico & CEHIDRO, University of Lisbon, Portugal, email: ruif@civil.ist.utl.pt*

## Abstract

Sediment overfeeding may induce important changes in the structure of the near-bed region of gravel-bed river flows, mainly in what concerns exchange of momentum and mass between the flow within the riverbed roughness elements and the flow in the upper regions. Although the turbulent structure of flows over gravel-bed rivers is object of several previous studies, it is not well-known how statistics characterizing coherent turbulence events responsible by the generation of turbulent shear stresses are affected by bed load transport in flows over hydraulically rough beds with low relative submergence. This study is aimed at bridging this research gap. It is based on two-dimensional instantaneous velocity data, in the stream-wise and vertical directions, acquired with Particle Image Velocimetry in a laboratory flume. Two tests simulated framework gravel beds with sand matrixes, one of which fed with sand at near capacity conditions. The framework, immobile under the imposed flow conditions, consists of coarse gravel whose diameters range between 0.5 cm and 7 cm. Matrix and imposed sand feature a median diameter of 0.9 mm. For both tests, the quadrant threshold analysis technique was employed and transported momentum were analyzed and discussed in what concerns their intensity distribution for events in the four quadrants, and for several positions within the flow. It is shown that under mobile bed conditions, sweeps are dominant in the turbulence production in the pythemic region of the flow. In the outer region of the flow, this is independent from the channel bed; in the overlapping intermediate layer, between the inner region and the pythemic region, the flow characteristics depend on the position in relation to the crests and troughs of the bed.

## 1 Introduction

Sediment mechanics, in particular the processes involved in erosion, transport and deposition of sediment particles, greatly depend on local flow hydrodynamics. Sediment transport rates determine river morphodynamics at a wide range of scales and, closing the loop, river morphology influences hydrodynamics, also at a wide range of scales. In spite of the existence of a large body of research on this looping chain of phenomena, fundamental questions remain unsolved in what concerns turbulent flow organization under sediment

transport conditions. In particular, the effects of sediment transport on the coherent structures of turbulence that develop on boundary layers, frequently designated as the bursting cycle [24], are still poorly known. Initial interest on coherent structures in wall-bounded flows has been sparked by the desire to understand the structure of near-wall turbulence and how it determines Reynolds shear stresses and turbulence production ([3], [19], [18], [13], [2]). Following [3], [30] and [20], these coherent structures have been frequently interpreted as events organized periodically in the time domain that imprint its signature on the time series of Reynolds shear stresses, hence the designation of bursting cycle. Conditional sampling techniques, namely quadrant threshold analysis [24], allow for detecting the events of the cycle as interactions of two orthogonal components of the instantaneous velocity,  $(u'_1, u'_3)$  for instance, in the four quadrants of a 2D Cartesian referential. Usual terms are: outward interaction (Q1,  $u'_1 > 0, u'_3 > 0$ ), ejection (Q2,  $u'_1 < 0, u'_3 > 0$ ), inward interaction (Q3,  $u'_1 < 0, u'_3 < 0$ ) and sweep (Q4,  $u'_1 > 0, u'_3 < 0$ ). Ejections and sweeps entail quite different flow kinematics but both contribute to the increase of the absolute magnitude of Reynolds shear stresses.

A considerable body of research has been dedicated to understand the formation of coherent structures in wall-bounded flows, mostly from the study of the dynamics of hairpin vortexes (see [31] and reviews in [22]), and to provide comprehensive experimental and theoretically characterizations [26], [14], including new taxonomies [21], [9].

Specific advances have been achieved in the experimental characterization of flows over hydraulically rough beds, employing Acoustic Doppler Velocimetry (ADV, ADVP), Laser Doppler Anemometry (LDA) or Particle Image Velocimetry (PIV). Investigating flow over gravel beds under moderate relative submergence with ADVP, [23] found out that sweeps are produced dominantly within the interfacial region centered on the plane of the crests of roughness elements, in which the velocity profiles are inflectional. They also found that space-averaged value of mean momentum carried by ejections becomes less relevant towards the bed, relatively to that of sweeps. Analyzing ADV measurements of flows over gravel beds with  $k_s/h = 18$  (where  $k_s$  is the length scale of roughness elements), [4] conformed the result that ejections become less relevant near the

bed, relatively to sweeps; however, contrarily to [23] they found that the momentum transported by ejections decreases fast below the plane of the crests.

Less information is available for hydraulically rough flows with small relative submergence. PIV data of [16] seems to indicate that, in these flows, larger-scale flow structures are formed by superimposition and coalescence of numerous smaller structures, which confirms the generality of the model of [31]. Performing a Galilean decomposition [1], [16] and [17] observe that shear layers from flow separation in individual roughness elements are the forcing responsible for the instabilities that will ultimately generate coherent structures, which is compatible with the findings of [23] for larger relative submergences.

The link between sediment transport and coherent structures associated to a bursting cycle was pointed out early in the study of [13]. Concerning this issue, advances were accomplished by [15], employing LDA to measure flow statistics over a smooth sand bed. They observed that the presence of intense intermittent sediment transport increases the extreme values of shear stress while the flow becomes more organized in the second and fourth quadrants, mainly increasing the importance of sweep events to turbulence production. The period between events of the second and fourth quadrants (shear stress producing events) decreases considerably in the presence of sediment transport, producing more frequent ejection and sweep events.

More recently, [8], explored an LDA database of flows hydraulically over hydraulically rough beds, mobile and immobile, under moderate relative submergences enough to exhibit a logarithmic layer. They found that the momentum transported by very strong sweeps and also by extreme ejections increase in the mobile bed case. However they found no important differences in the duration and frequency of the events. A general trend of increase of relative importance of sweep events towards the bed was registered. Studying flows over hydraulically rough beds at threshold conditions with ADV, [5] confirm that in the near-bed flow region sweeps become the dominant mechanism for sediment entrainment. They also confirm that the duration and frequency of Q2 and Q4 is smaller in mobile beds in is the smooth-bed case of [15].

The purpose of this work is to contribute to the understanding of coherent structures that develop in gravel-bed channels with low relative submergence and to assess the influence of sand transport on the dynamics of these structures. The study is dedicated to all four types of events in the bursting cycle that contribute to the of Reynolds shear stresses. The joint study of flows over framework-supported gravel beds with low relative submergence and sand transport constitutes the key novelty. Under these conditions Townsend's wall similarity [29] is not likely to hold, indicating that shear stress producing mechanisms may differ from those of high relative submergence. This research addresses also the effect of sand transport within the random array of surface roughness elements, namely its potential to disrupt the mechanisms triggering instabilities.

To accomplish the proposed objective, laboratory flume tests were conducted and 2D instantaneous velocity fields (streamwise and vertical directions) were mea-

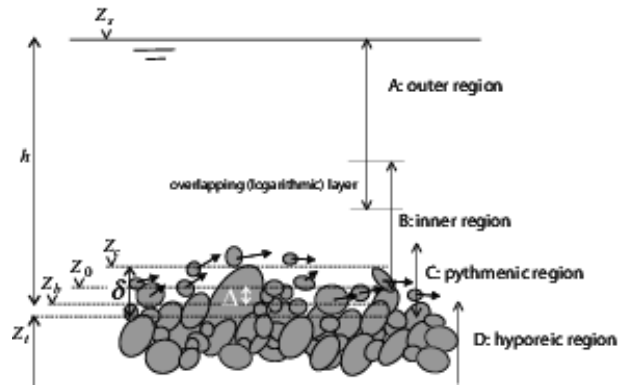


Figure 1: Flow structure proposed for permeable rough porous poorly sorted gravel-sand beds with sediment bed load.  $h$  stands for the flow depth,  $Z_b$  stands for the boundary zero elevation,  $Z_c$  stands for the highest crest elevation,  $Z_s$  stands for the elevation of the free-surface and  $Z_t$  is the elevation of the deepest trough

sured with PIV. The flow is studied based on a quadrant threshold analysis described by [24] and modified by [8]. Mean values and histograms of event duration, maximum shear stress, transported momentum and period of occurrence of all the four types of events were quantified. The sensitivity of the transported momentum to the sampling threshold the events is herein presented and discussed, allowing a physical insight on the influence of the occurrence of sediment transport on the turbulence organization of flows over gravel-bed beds. Further and complementary results on the statistical analysis of shear stress events, ensuing from the very same experiments, may be found in [28], and further details on the experimental tests and data analysis can be found in [27].

## 2 Characterization of the Physical System

The model proposed in [6] for the vertical flow structure of permeable, rough porous poorly sorted, gravel-sand beds with sediment load is herein considered (Figure 1). It features a flow layer, the pythmenic region, where the flow is determined by the particular geometry of bed roughness elements and, possibly, the amount and size of moving particles. Different flow regions overlap as the phenomena that characterizes them does not cease to exist abruptly. The overlapping layer between the pythmenic and inner regions, near the crests of the roughness elements, is assimilable to the “jet layer“, as described by [11] or the layer where instabilities leading to coherent structures are generated [16]. Also, interaction of characteristics from both pythmenic and inner regions generates strong momentum fluxes in vertical and spanwise directions [7].

In the inner region, the flow is directly governed by the bed roughness in its lowermost region and indirectly in its uppermost region. It is assumed that the friction velocity is the velocity scale responsible for the momentum transfer from the outer to the inner layer, thus valid for both flow regions [25], [8].

### 3 Experimental Setup and Methods

#### 3.1 Laboratory Facilities

Experimental tests were performed recurring to the Recirculating Tilting Flume (CRIV), at the Laboratory of Hydraulics and Environment of Instituto Superior Técnico, Universidade de Lisboa. The flume has a rectangular cross section 408 mm wide, 500 mm height, and effective length of 12.5 m. It is composed of ten 0.5 m height glass panels, in each sidewall, that allow acquiring experimental data recurring to flow visualization. The flume slope is adjustable between  $-1/200$  and  $+1/40$ , by means of a motorized system.

The recirculation is made through a pressure circuit, incorporating a centrifugal pump with a maximum discharge of  $220 \text{ m}^3/\text{h}$ . Free surface oscillations are eliminated at the inlet by means of a wooden board. The water level and uniform flow conditions in the subcritical regime were set and controlled by a venetian blind gate at the outlet which is tuned using a screw pole.

At a distance of 2.5 m downstream from the inlet, a conveyor belt imposed a constant sediment feed. The belt was equipped with a structure that allowed controlling the sediment discharge by regulating its velocity and the thickness and width of the sediment streak. A polystyrene board was used to eliminate any free surface disturbance resulting from the introduction of sediments in the stream.

#### 3.2 Measuring Instrumentation

The experimental tests required measurements of free surface elevation, bed topography and instantaneous flow velocity maps in both longitudinal and vertical directions. The free surface elevation and bed topography profiles were obtained with a point gauge with 0.1 mm of precision. Flow discharge in the system was measured by an electromagnetic flow-meter inserted in the recirculating circuit. Instantaneous flow velocity maps were acquired non-intrusively by means of a PIV system. The PIV encompasses a 30 mJ Nd:YAG 532 mm double-cavity (pulsed) laser, a CCD camera with a resolution of  $1600 \times 1200$  pixel and an acquisition system. The laser is shaped through cylindrical lenses providing a 2 mm thick light sheet. The system operation is performed with time between pulses and sampling frequency controlled by the user. Spurious velocity data were despiked using the phase-space thresholding method [12], adapted for PIV data.

#### 3.3 Characterization of the Tests

Two tests were performed, for which instantaneous flow velocity maps were collected under uniform subcritical flow conditions. The tests were named S3 and S4, respectively in mobile bed and immobile bed conditions, and their main defining parameters are shown in Table 1.

In Table 1,  $Q$  stands for flow discharge,  $i$  is the bed slope and  $q_b$  is the volumetric sediment discharge. The bed is composed of gravel and sand with mean diameter and the geometric standard deviation respectively,  $d_{50}^g = 28 \text{ mm}$ ,  $\sigma_D^g = 1.4$  for gravel ( $^g$ ) and  $d_{50}^s = 0.9 \text{ mm}$ ,  $\sigma_D^s = 1.6$  for sand ( $^s$ ). In both tests the coarse-gravel elements forming a stable framework whose interstices

Table 1: Main characteristics of the experimental tests

Test	$Q(\text{l/s})$	$i(-)$	$q_b(\text{l/s})$	$h(\text{m})$
S3	23.3	0.0044	$4.77 \times 10^{-3}$	0.127
S4	16.7	0.0044	$2.08 \times 10^{-3}$	0.156

Table 2: Main characteristics of the experimental tests

Test	$Z_t(\text{m})$	$Z_c(\text{m})$	$\delta(\text{m})$	$\varphi_m(-)$	$\lambda_b(-)$
S3	0.107	0.146	0.039	0.7197	0.22
S4	0.090	0.144	0.053	0.6570	0.34

were filled with a sand matrix. This was achieved by water-working the bed for 30 hours to completely assure armoring conditions. By filling the interstices, the thickness of the pythmenic layer is reduced and consequently the porosity in the substratum is reduced too. In test S4 the filling sand is well stored below crests ensuring that sediment transport is completely inexistent under the imposed flow conditions, while in test S3 the sand presence in the bed was slightly increased, until the sand discharge achieves transport capacity.

The channel bed is characterized by the parameters shown in Table 2, namely the elevations of the planes of the lowest troughs,  $Z_t$ , and highest crests,  $Z_c$ , the thickness of the pythmenic layer,  $\delta = z_c - z_t$ , the bed porosity,  $\lambda_b$  and the depth-averaged value of the void function (between  $Z_t$ , and  $Z_c$ ),  $\varphi_m$ , which characterizes the fraction of space that is occupied by the fluid between  $Z_t$ , and  $Z_c$ .

Variables in Table 3 are  $Z_s$  the free surface elevation, while  $h^*$  is a reference flow depth for shear stress calculation purposes and is calculated as  $h^* = h - \delta(1 - \varphi_m)$  (details in [7]),  $U$  is the depth averaged mean flow velocity in the stream direction, calculated by  $U = \frac{Q}{B(Z_s - Z_c)}$ , where  $B$  is the flume width. The value of  $\tau_0$  stands for total shear stress and it is estimated from total shear stress profile. This profile is subjected to a liner regression in the linear segment and then extrapolated to the level of the mean void function, estimating total shear stress of the flow,  $\tau_0$ , while  $u^* = \sqrt{\frac{\tau_0}{\rho^w}}$ , where  $\rho^w$  is the water density.

Non-dimensional parameters Froude, Reynolds and Shields numbers are presented in Table 4. Froude number is calculated by  $Fr = \frac{U}{\sqrt{gh}}$ , where  $g$  is the acceleration of gravity. The Reynolds number is  $Re = \frac{Uh}{\nu}$ , where  $\nu$  is the kinematic viscosity of the water. The Shields parameter is calculated for both gravel and sand sizes by  $\theta^i = \frac{u^{*2}}{(\rho^i/\rho^w - 1)gd_{50}^i}$ , where  $u^*$  stands for friction velocity,  $\rho^w$  is the water density,  $\rho^i$  is sand or gravel density, and  $d_{50}^i$  is the mean diameter of sand or gravel.

Table 3: Flow characteristics

Test	$Z_s(\text{m})$	$h^*(\text{m})$	$U(\text{m/s})$	$\tau_0(\text{Pa})$	$u^*(\text{m/s})$
S3	0.234	0.116	0.648	3.060	0.057
S4	0.246	0.137	0.557	3.924	0.062

Table 4: Non-dimensional parameters

Test	$Fr$	$Re$	$\theta^g$	$\theta^s$
S3	0.61	76606	0.008	0.223
S4	0.45	86843	0.009	0.269

Table 5: Criteria for the detection of shear events

Outward interactions:

$$Q_{out} = \{u', w' \in \mathbb{R} : u' > 0 \wedge w' > \frac{\sigma_h}{u'} \wedge u' < \sigma^+\}$$

Ejections:

$$Q_{ej} = \{u', w' \in \mathbb{R} : u' < 0 \wedge \{w' > \frac{\sigma_h}{|u'|} \vee u' < \sigma^-\}\}$$

Inward interactions:

$$Q_{in} = \left\{ \begin{array}{l} u', w' \in \mathbb{R} : \\ \{u' < 0 \wedge w' < 0 \wedge |w'| > \frac{\sigma_h}{|u'|} \wedge u' > \sigma^-\} \end{array} \right.$$

Sweeps:

$$Q_{sw} = \left\{ \begin{array}{l} u', w' \in \mathbb{R} : \\ \{u' > 0 \wedge \{w' < 0 \wedge |w'| > \frac{\sigma_h}{u'}\} \vee u' > \sigma^+\} \end{array} \right.$$

## 4 Data Analysis

### 4.1 Event Detection

Conditional sampling organizes the shear stresses and helps in the identification of events occurring in the bursting cycle. The quadrant threshold method [24] was chosen as the detection criteria in the modified version proposed by [8]. It involves thresholding  $u'w'(t)$  data accordingly to each quadrant, where  $u' = u'_1$  and  $w' = u'_3$  are the longitudinal and vertical velocity fluctuations, respectively. The thresholds are controlled by the constants

$$\sigma_h = H \times u_{rms} \times w_{rms} \quad (1)$$

$$\sigma^\pm = \pm 2.5 \times u_{rms} \quad (2)$$

where  $H$  represents the hole size and,  $u_{rms}$  and  $w_{rms}$  are the root mean square of the instantaneous flow velocity, respectively in longitudinal and vertical directions. The thresholds  $\sigma^+$  and  $\sigma^-$  depend on the values of the fluctuation of the instantaneous flow velocities and are kept constant for each of the experiments. Outward interactions, ejections, inward interactions and sweeps are identified based on the domains of occurrence described in Table 5.

An example of the distribution of instantaneous velocity fluctuations over the four quadrants with the threshold criteria superimposed is shown in Figure 2. Treating consecutive events of smaller scale as independent events may result in an incorrect approach. To avoid that in the boundary regions, a consecutive set of smaller scale events is eligible as a single major event if the persistence of  $u'$  is well correlated with the persistence of the event, as proposed in [8]. This is the justification for the introduction of the additional criterion employing constants  $\sigma^+$  and  $\sigma^-$ .

### 4.2 Event statistics

After performing the event detection, the following statistical parameters can be calculated as presented in Fig-

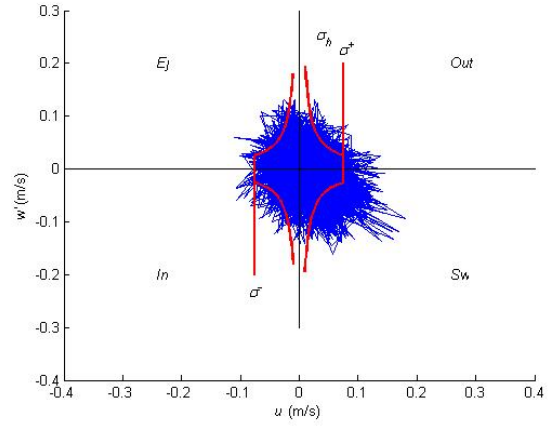


Figure 2: Location of the reference points considered in test S3, in mobile bed conditions

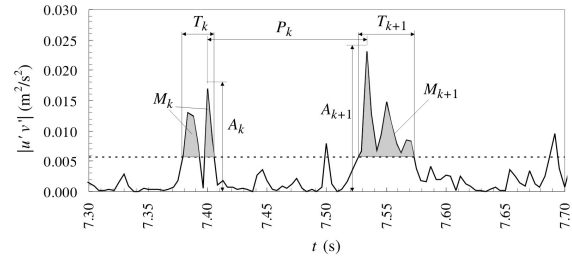


Figure 3: Detailed shear stress time series with parameters that characterize events

Figure 3: maximum shear stress (A), transported momentum (M), duration (T) and period (Pc), the time between consecutive events, measured between centroids of the regions representing transported momentum.

Hereinafter, the ensemble-average, over the detected events, of the transported momentum (M) relative to the four types of events will be analysed as a function of the threshold hole for the event detection. A discussion of the remainder statistical parameters is made in [28].

Event detection and calculation of  $M_k$  of each event are made inside a loop that goes through a continuous increase of the hole size value,  $H$ , starting in zero and ending in 3 with a step of 0.1

### 4.3 Analyzed positions

The cumulative values of the transported momentum are normalised by the total transported momentum of the correspondent spatial position (m:n) which was produced during the entire experiment. This approach compares the persistence of each kind of event in the experiment sample. The analysis was made at several positions of the flow velocity longitudinal maps as represented in Figure 4. The points considered were chosen accordingly to the physical system proposed by [6], presented earlier in Section 2. Five positions are herein presented in detail: (1,4), (3,2), (3,3), (5,3) and (5,4). These five points stand in different regions of the flow and are representative of these.

The point marked as (1,4) was adopted because it is far enough from the bed. Point (3,2) and (3,3) are standing at the crest level at the interface between inner and pythemic layers, over the crest level in the overlapping

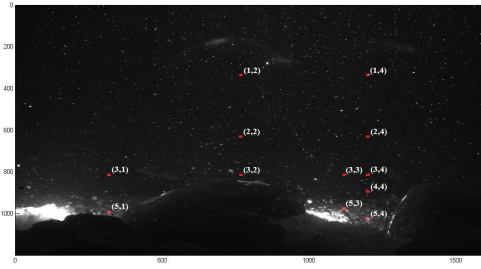


Figure 4: Location of the reference points considered in test S3, in mobile bed conditions

between inner and pythmenic regions the former, and over the trough position the latter. They allow for evaluating the influence over the flow, caused by the crest itself and by the mobile bed effects. The behaviour in the lower pythmenic region is assessed by investigating points (5,3) and (5,4).

## 5 Presentation and Discussion of Results

### 5.1 In the Outer Region, Position (1,4)

In the outer region, the evaluation of the hole size shows that the flow is mainly governed by ejection events. The sweep events also stand out but those are not as important as ejection events in the turbulence production processes. Comparing Figure 5(a), without bed load, to Figure 5(b), where bed load is present, one finds that there is no effect sediment movement at this upper flow region. Although wall similarity is not expected with this low relative submergence, one must assume that the mechanisms that govern coalescence of smaller vortices should be the same at these flow elevations.

### 5.2 Over the crest, in the overlapping between inner and pythmenic regions, position (3,2)

Figure 6(a) and Figure 6(b) show the shear stress over the crest in the nearest measured point, respectively, for immobile and mobile bed conditions. According to [23] or [16], it is in this layer that instabilities leading to coherent structures are formed. Figure 6(a) and Figure 6(b) show that the importance in the shear stress production processes is transferred from ejection and sweep events to outward and inward events, which expresses a tendency to turbulence isotropy. This is the situation for both cases of immobile and mobile bed conditions.

### 5.3 At the crest level but over the trough, position (3,3)

This reference point stands in the overlapping between inner and pythmenic regions but over a trough where a shear layer is seen to develop [7]. The quadrant threshold analysis at this point highlights a clear reorganization of the flow, with ejection and sweep events equally responsible for the production of Reynolds shear stresses. The mobile bed does not seem to affect the flow organization at this level, over the trough as it is presented in Figure 7(a) and Figure 7(b), respectively for immobile bed and mobile bed conditions.

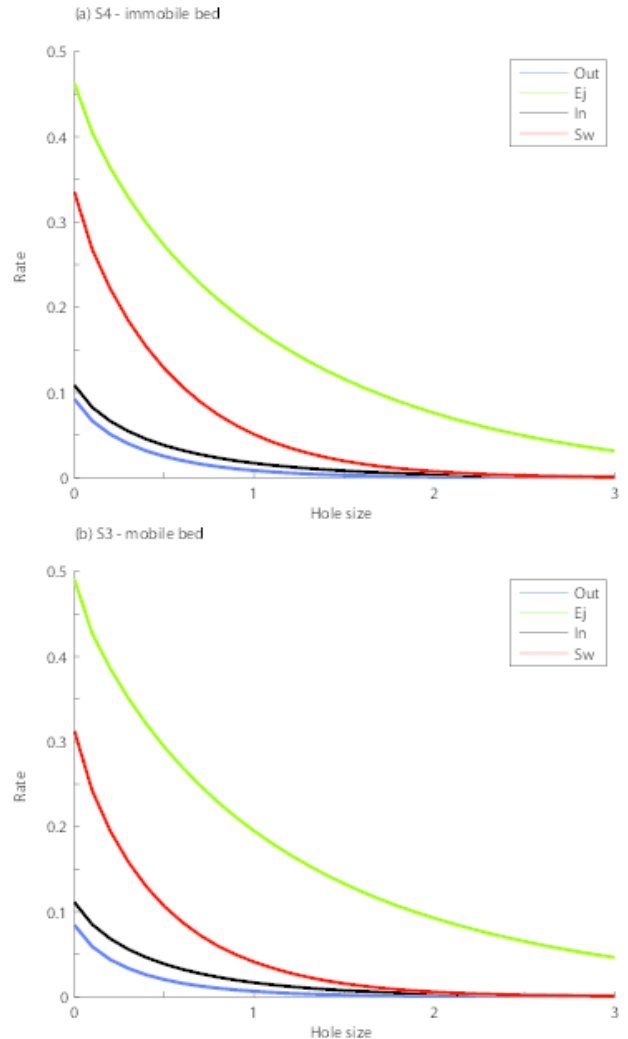


Figure 5: Distribution of transported momentum through the hole size in position (1,4)

### 5.4 In the pythmenic region, position (5,3)

At this point, standing in the pythmenic region, considering immobile bed conditions, the ejection and sweep events share importance in shear stress production processes. However, when in mobile bed conditions, the ejection events decrease its contribution to the shear stress production processes while sweep events stand out and assume a main role in the same processes as shown in Figure 8(a) and Figure 8(b), respectively for immobile bed and mobile bed. For the immobile bed test (S4) there is relative tendency to isotropy when compared to the mobile bed situation (S3).

### 5.5 In the lower pythmenic region, position (5,4)

Figure 9(a) and Figure 9(b), respectively standing for immobile and mobile bed conditions, show the sensitivity analysis of the transported momentum to the hole size in the deepest trough. At this (relatively deep) level, the flow exhibits characteristics of both the hyporheic and pythmenic regions. Figure 9(a) shows that in immobile bed conditions, the sweep events assume the major contributions to the shear stress production processes, and they even increase their contribution in the mobile bed case, as shown in Figure 9(b). However, in immobile

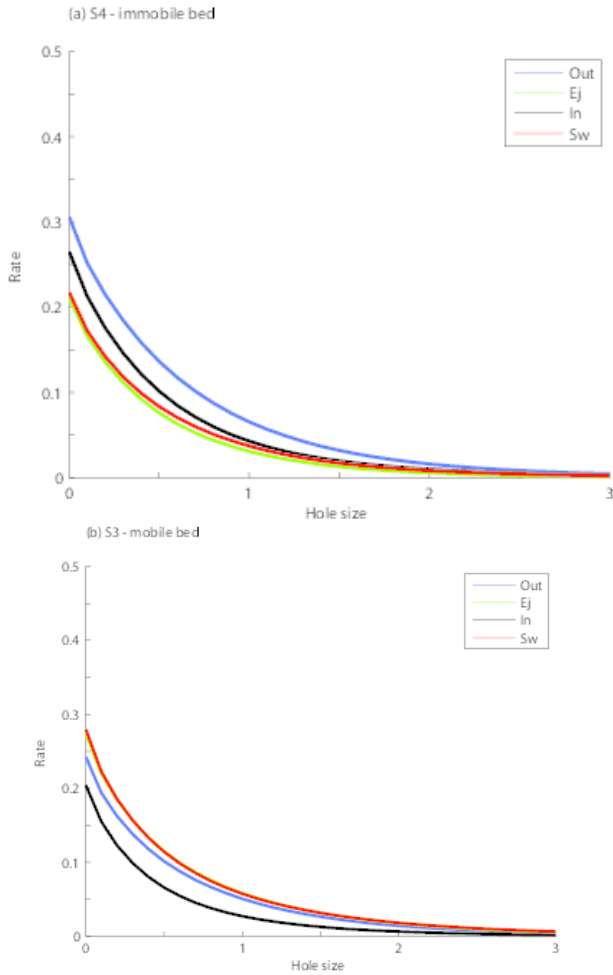


Figure 6: Distribution of transported momentum through the hole size in position (3,2)

bed conditions, contributions from ejection and inward events cannot be neglected at all as they stand out from the outward events. Despite that this reference point is placed in front of a pebble, the flow presents characteristics similar to those found at other reference points placed in the trough, however it is clearer at this reference point, if it is compared for instance with the reference point shown previously in Figure 8(b), where sweep events assume clearly the main contribution to the shear stress production, when in mobile bed conditions.

## 6 Conclusions

The analysis of laboratorial data, based on instantaneous flow velocity fields, permitted the evaluation of the effect of sediment transport in the near-bed region on the bursting cycle. The two tests were performed in conditions of open-channel flow with porous rough bed and poorly sorted gravel-sand mixture. After the application of a modified quadrant analysis method to sample shear events, statistics of these latter were computed. An analysis of the sensitivity of the transported momentum to the hole size defined to sample the events allowed an inner insight to the shear activity within the flow column.

In the outer layer of the flow, as expected (cf. [5]), the flow is controlled by near-surface conditions and is independent of the channel bed. In the overlapping layer, between inner and pythmenic regions, standing over a

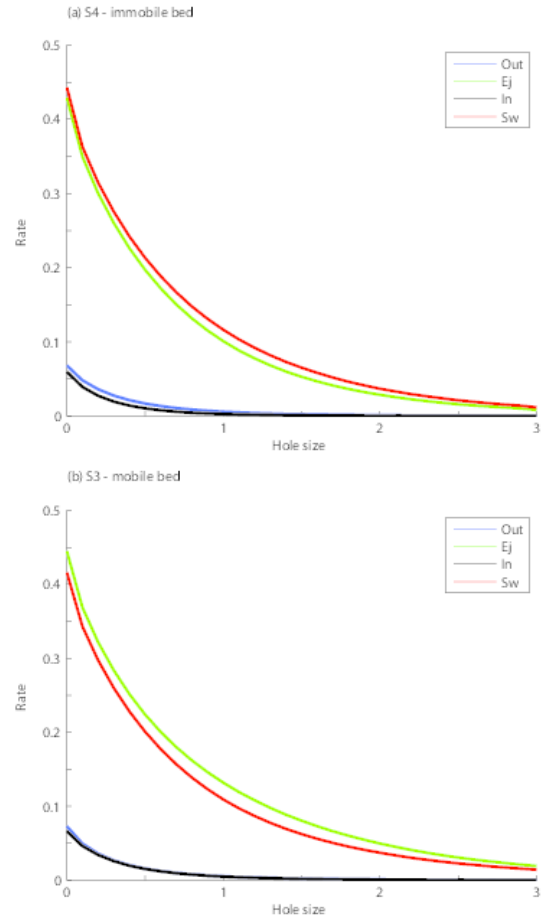


Figure 7: Distribution of transported momentum through the hole size in position (3,3)

crest, the turbulent flow tends to isotropy. The events are equally distributed between the four quadrants and exhibit an equal share in the processes of shear stress production. In the pythmenic region, standing over a trough, mobile bed conditions lead to a situation where ejection and sweep events are responsible for the shear stress production processes with sweep events assuming the main role (cf. [23]), in opposition to the situation in the upper regions of the flow. The mobile bed does not seem to affect the flow organization at this level, for both situations, standing over a crest or over a trough. Ejection events suffer the most important decrease due to sediment transport in the near bed region, more specifically in the pythmenic region. Here, the immobile bed showed a relative tendency to isotropy when compared to the mobile bed situation. In the overlap between hyporheic and pythmenic regions, in mobile bed conditions the sweep events assume the major production of shear stress as pointed out by [5]. In immobile bed conditions, contributions from ejection and inward events cannot be neglected at all as they stand out from the outward events. Although the results here are not conclusive for all positions in the lowest layer, sweeps tend to be here the dominant shear event confirming the observations by [11].

Complementary results, obtained for the same experiments, are shown in [28]. Here it is shown that, generally, the sediment transport of sand decreases the transported momentum and maximum shear stress values (as observed by [5]) but increases their frequency of occurrence in time. The analysis of the probability distri-

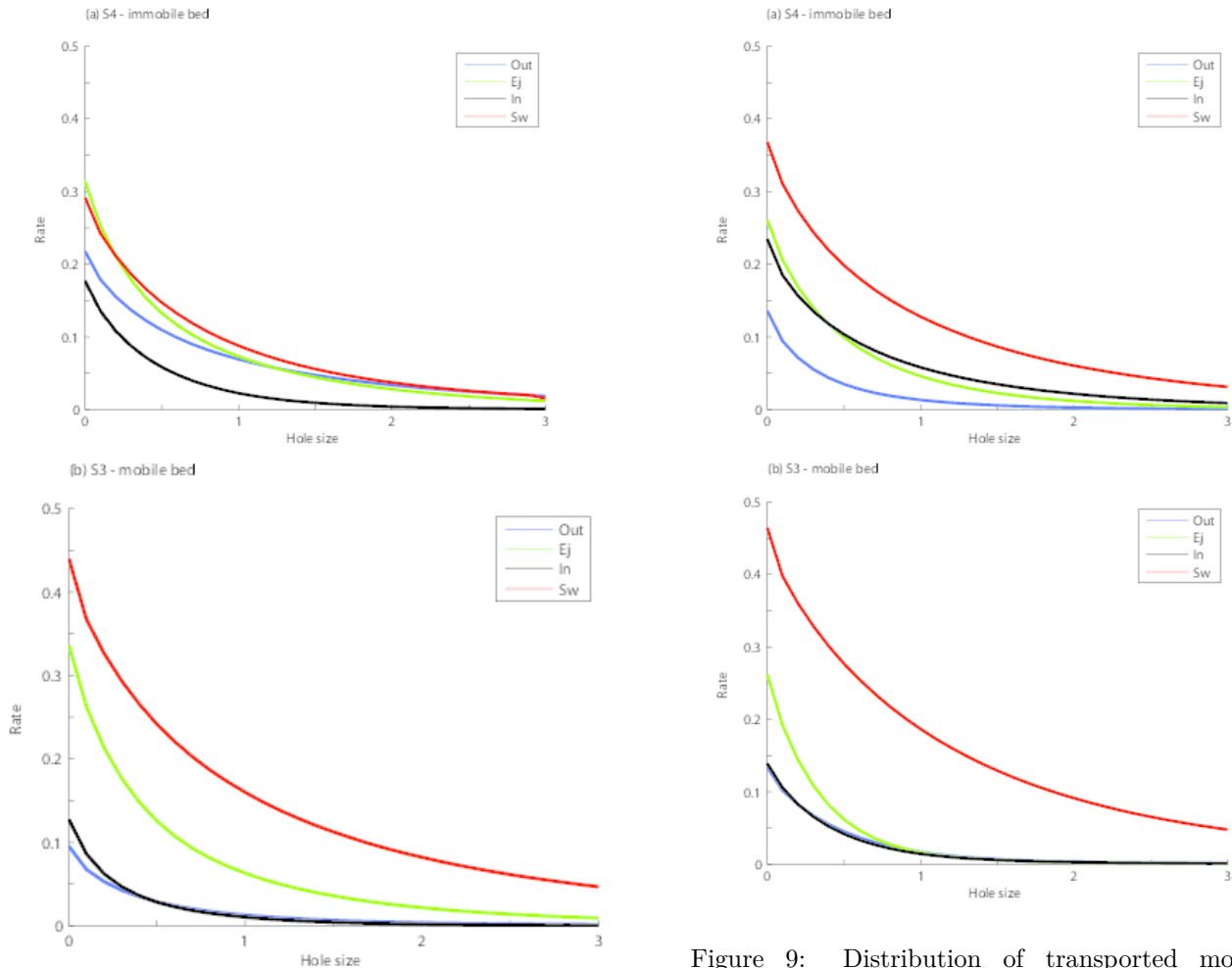


Figure 8: Distribution of transported momentum through the hole size in position (5,3)

bution function of both ejections and sweeps, shows an effect of sediment transport in the reduction of the frequency of large events and in the increase of the frequency of small events. This may be due to breaking of eddy coherence by sediment motion and is especially observed in the pythmenic region.

## Acknowledgements

This work was funded by FEDER, program COMPETE, and by national funds through Portuguese Foundation for Science and Technology (FCT) project RECI/ECM-HID/0371/2012 and by the People Programme (Marie Curie Actions) of the European Union's Seventh Framework Programme FP7/2007-2013/ under REA grant agreement  $n^{\circ}$  607394-SEDITRANS.

## References

[1] Adrian, R.J., Christensen, K.T. and Liu, Z.C. 2000. Analysis and interpretation of instantaneous turbulent velocity fields. *Exp. Fluids* 29: 275-290.

[2] Antonia, R.A. & Atkinson, J.D. (1973). High-order moments of Reynolds shear stress fluctuations in a turbulent boundary layer. *J. Fluid Mech.* 58(3): 581-593.

[3] Corino, E. R. and R. S. Brodkey (1969). A visual investigation of the wall region in turbulent flow. *Journal of Fluid Mechanics*, 37(01), 1-30.

Figure 9: Distribution of transported momentum through the hole size in position (5,4)

[4] Dey, S. and Das, R. (2012) Gravel-Bed Hydrodynamics: Double-Averaging Approach. *J. Hydraul. Eng.* 138(8): 707-725.

[5] Dey, S., Sarkar, S., Solari, L. (2011). Near-Bed Turbulence Characteristics at the Entrainment Threshold of Sediment Beds. *J. Hydr. Engng.* 137(9): 945-958.

[6] Ferreira, R. M. L., M. J. Franca, J. G. A. B. Leal, & A. H. Cardoso (2012). Flow over rough mobile beds: Friction factor and vertical distribution of the longitudinal mean velocity. *Water Resources Research* 48(5):W011126.

[7] Ferreira, R.M.L., Ferreira, L.M.; Ricardo, A.M.; and Franca, M.J. (2010) Impacts of sand transport on flow variables and dissolved oxygen in gravel- bed streams suitable for Salmonid spawning. *River Research and Applications* 26(4): 414-438.

[8] Ferreira, R.M.L., Franca, M.J.; Leal, J.G.B. and Cardoso, A.H. (2009). Organized turbulence over mobile and immobile hydraulically rough boundaries. In *proc. 35 rd IAHR Congress, Vancouver, British Columbia, Canada*, pp. 36-43.

[9] Franca, M. J. & Lemmin, U. (2014). Detection and reconstruction of large - scale coherent flow structures in gravel - bed rivers. *Earth Surface Processes and Landforms*, DOI: 10.1002/esp.3626.

[10] Franca, M. J., Ferreira, R. M., & Lemmin, U. (2008). Parameterization of the logarithmic layer of

- double-averaged streamwise velocity profiles in gravel-bed river flows. *Advances in Water Resources*, 31(6): 915-925.
- [11] Gimenez-Curto and Corniero Lera (1996) Oscillating turbulent flow over rough surfaces. *J. Geoph. Res.* 101(C9): 20745-20758.
- [12] Goring, D. G. and Nikora, V.I. (2002). Despiking acoustic doppler velocimeter data. *Journal of Hydraulic Engineering* 28(1): 117-126.
- [13] Grass, A. J. (1971). Structural features of turbulent flow over smooth and rough boundaries. *Journal of Fluid Mechanics* 50(02): 233-255.
- [14] Green, M.A.; Rowley, C.W. Haller, G. (2007) Detection of Lagrangian coherent structures in three-dimensional turbulence. *J. Fluid. Mech.*, 572:111- 120.
- [15] Gyr, A. and Schmid, A. (1997). Turbulent flows over smooth erodible sand beds in flumes. *Journal of Hydraulic Research* 35(4), 525-544.
- [16] Hardy, R.J. Best, J.L.; Lane, S.N. and Carbonneau, P.E. (2010) Coherent flow structures in a depth-limited flow over a gravel surface: The influence of surface roughness *J. Geophysical Research: Earth Surface*, 115(F3006)
- [17] Hardy, R.J.; Best, J.L.; Marjoribanks, T.I.; Parsons, D.R.; Rosser, N.J. (2013) Detection and analysis of coherent flow structures in a depth-limited flow over a gravel surface. In "Coherent Flow Structures at Earth's Surface" Ed. by Jeremy G. Venditti, James L. Best, Michael Church and Richard J. Hardy. Wiley-Blackwell. ISBN-13:978-1119962779.
- [18] Kim, H. T., Kline, S.T., and Reynolds W.C. (1971). The production of turbulence near a smooth wall in a turbulent boundary layer. *Journal of Fluid Mechanics* 50(01): 133-160.
- [19] Kline, S. J.; Reynolds, W.C.; Schraub, F.A. and Runstadler, P.W. (1967) The structure of turbulent boundary layers. *Journal of Fluid Mechanics* 30(04): 741-773.
- [20] Lu, S.S. and Willmarth W.W. (1973). Measurements of the structure of the reynolds stress in a turbulent boundary layer. *Journal of Fluid Mechanics* 60(03): 481-511.
- [21] Marquis, G.A. and Roy, A.G. (2011) Bridging the gap between turbulence and larger scales of flow motions in rivers. *Earth Surface Processes and Landforms* 36(4), 563-568.
- [22] Marusic, I.; McKeon, B.J.; Monkewitz, P.A.; Nagib, H.M.; Smits, A.J. and Sreenivasan, K.R. (2010) Wall-bounded turbulent flows at high Reynolds numbers: Recent advances and key issues. *Phys. Fluids* 22, 065103.
- [23] Mignot, E.; Hurther, D.; and Barthelemy, E. (2009) On the structure of shear stress and turbulent kinetic energy flux across the roughness layer of a gravel- bed channel flow. *J. Fluid Mech.*, 638(11), 423- 452.
- [24] Nakagawa, H. and Nezu, I. (1977). Prediction of the contributions to the Reynolds stress from bursting events in open-channel flows. *Journal of Fluid Mechanics* 80(01): 99-128.
- [25] Pokrajac D.; Finnigan J.J.; Manes, C., McEwan I., Nikora V.I. (2006) On the definition of the shear velocity in rough bed open channel flows. *River Flow*, vol. 1. Eds R.M.L. Ferreira, E. Alves, J.G.A.B. Leal and A.H. Cardoso. London: Taylor & Francis, p. 89-98.
- [26] Porporato, A. and Ridolfi, L. (2002) Some dynamical properties of a differential model for the bursting cycle in the near-wall turbulence. *Phys. Fluids* 14, 4278.
- [27] Santos, B.O. (2013). Coherent structures in open channel flows with bed load transport over an hydraulically rough bed. MSc. Thesis. Faculdade de Ciências e Tecnologia, Universidade Nova de Lisboa: <http://hdl.handle.net/10362/11204>
- [28] Santos, B.O., Franca M.J., and Ferreira R.M.L. (2014). Coherent structures in open channel flows with bed load transport over an hydraulically rough bed. In *River Flow 2014*. Eds. A.J. Schleiss, G. de Cesare, M.J. Franca, M. Pfister.
- [29] Townsend A. A. (1976) *The structure of Turbulent Shear Flows*, 2nd edition. Cambridge University Press, Cambridge, UK.
- [30] Willmarth, W.W. and Lu, S.S. (1972). Structure of the reynolds stress near the wall. *Journal of Fluid Mechanics* 55(01): 65-92.
- [31] Zhou, J.; Adrian, R.J.; Balachandar, S. and Kendall, T.M. (1999) Mechanisms for generating coherent packets of hairpin vortices in channel flow. *J. Fluid Mech.*, vol. 387: 353-396.

# SEDIMENT TRANSPORT IN MOUNTAIN RIVERS

C. Ancey<sup>1</sup>, P. Bohorquez<sup>2</sup> and E. Bardou<sup>3</sup>

<sup>1</sup>*EPFL, Lausanne, Switzerland*

<sup>2</sup>*CEACTierra, University of Jaén, Spain*

<sup>3</sup>*CREALP, Sion, Switzerland*

## Abstract

The paper reviews our recent attempts at modelling bed load transport in mountain rivers. This is a longstanding issue that has attracted considerable attention over the last century. While a number of field and laboratory studies have been instrumental in getting the big picture, there is a clear lack of efficient methods for predicting bed evolution and particle flux. Most approaches to bed load transport have emphasized the existence of a one-to-one relationship between the particle flux and water discharge, but this result conflicts with the spread of data, which often spans over several orders of magnitude.

A possible interpretation lies in the significance of the fluctuations of the particle flux together with the propagation of bed forms. We have therefore developed a theoretical model based on birth-death Markov processes to describe the random exchanges between the stream and bed, which then allows us to derive a governing equation for the particle flux fluctuations. We end up with the probability distribution function of the sediment transport rate. A striking feature is the existence of large fluctuations even under steady flow conditions.

Numerical simulations have been carried out to compute the flow features, for the moment with no sediment transport. These simulations have shown that the kinematic wave approximation (which leads to a significant simplification of the Saint-Venant equation into a non-linear advection equation) performs well for a wide range of water discharges. Remarkably, it has been found that under steady flow conditions, the local flow variables (wetted section and water discharge, or flow depth and mean velocity) exhibit a Froude similarity, i.e. regardless of the water discharge, the Froude number remains fairly constant at a given place of the river. Future work will consider the inclusion of a stochastic sediment transport equation in the Saint-Venant equations.

## 1 Introduction

The objective of this paper is to present an innovative approach to sediment transport. The work is done within the framework of a joint project involving EPFL, a research institute of the Wallis canton CREALP, and the University of Jaén (Spain). This project aims to provide a better quantitative picture of sediment transport in gravel-bed rivers, with a particular focus on mountain rivers.

In spite of decades of research, sediment transport, in particular in gravel-bed rivers, is still a difficult issue. For instance, 1 shows the bed load transport rates measured in the Navisence River in Zinal from 2011 to 2013 (1-min averaged flux rates) and the empirical trend given by Meunier's bed load rating curve, which relates the bed load transport rate  $Q_s$  (in kg/s) to the water discharge

$Q_w$  (in m<sup>3</sup>/s) and bed slope  $i$  as follows:  $Q_s = 9450i^2Q_w$  [1]. More sophisticated equations lead to similar or larger errors. At low flow rates, the deviation between the empirical equation and measurements exceeds three orders of magnitude and even at the highest transport rates (for the 8 Aug. 2013 flood, the period of return was  $\sim 50$  yr), there is a conspicuous deviation. This example shows how poor our predictive capacity of bed load transport rate is when empirical equations are used.

This shortcoming has been known for ages although most textbooks on the topic barely mention the tremendous uncertainty associated with bed load transport equations (not to mention the systematic use of log-log plots that minimize the perception of errors and deviations). Each generation of scientists has tackled this issue by arguing that more physics is needed to properly address the problem at hand.

In the 1950s, Hans Einstein proposed a model of bed load transport in which transport results from the difference between the entrainment and deposition rates,  $E$  and  $D$ , respectively, which depend on the flow conditions and bed geometry [2]. This amounts to writing that on a small interval  $\Delta x$ , the particle flux variation is  $\delta q_s = (E - D)\Delta x$ , and so the particle flux at bed equilibrium is the implicit solution to the equation  $E = D$ . The originality of Einstein's treatment lies in the introduction of probabilistic concepts to quantify the probability of entrainment of one particle lying on the bed.

In the 1960s, Ralph Bagnold considered sediment transport as the result of momentum transfers between solid and liquid phases [3]. Bed load transport is essentially a two-phase flow whose dynamics are controlled by the momentum transfers between the water and solid phases.

Needless to say that after decades of investigations, the debate is still open. To advance our understanding of sediment transport, we need to identify the blackspots when building theories of sediment transport. In this paper, we present some of the major difficulties in the current developments. We also refer the reader to recent review papers, which give an comprehensive summary of the state of the art regarding steep gravel-bed rivers, e.g [4]. We then outline a theoretical approach under construction, whose originality lies in its capacity to calculate not only the mean particle flux, but also its probability distribution. We do not claim that this approach solves all of the problems. In fact, laboratory experiments have just provided the proof of concept. Applications to the field require substantial adaptations of the theoretical framework, which is too idealized to be of practical interest (e.g., particles are spherical and of identical size in the current version of the model). Yet, this approach has the potential to elucidate a number of issues arising in the study of bed load transport. The last part of the paper concerns the numerical treatment of the water flow. This is achieved within the framework

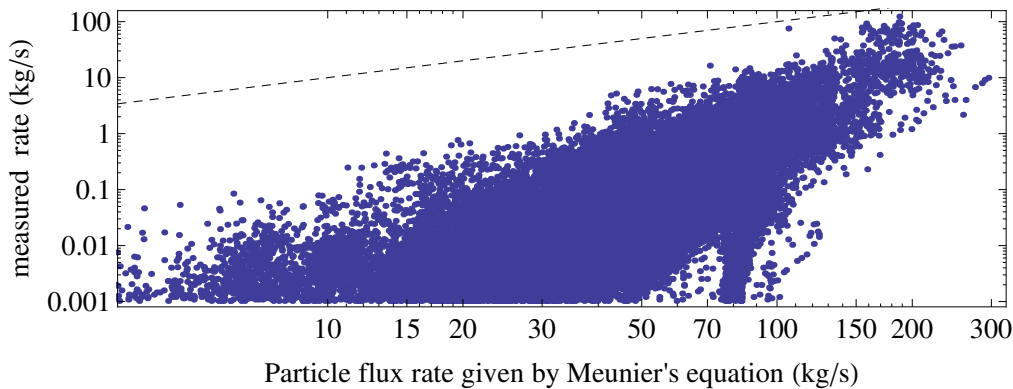


Figure 1: Comparison between bed load transport rates measurements and Meunier's equation for the Navisence river (Zinal, VS). Here the local slope upstream of the station is  $i = 3.2\%$

of the Saint-Venant equations. Here we present the numerical framework and results related to water flow (with no sediment transport). The coupling between the water stream and bed leads to a multitude of challenges that go beyond the scope of this paper. These challenges include the theoretical stochastic framework, which has to be extended to deal with non-uniform flow conditions, and the formulation and numerical resolution of a stochastic Exner equation.

## 2 Scientific and Technical Hurdles

This year marks the 100 years anniversary of the report by Gilbert (1914), which is credited with the first comprehensive experimental investigation into bed load transport in inclined flumes [5]. Empirical equations were proposed earlier than Gilbert. For instance, from his observations of the Rhone River south to Tournon (France) in 1879, the French civil engineer Paul du Boys introduced a bed load transport equation from consideration of the bottom shear stress on a granular bed [6]. An analysis of the current literature on bed load transport models shows that there has been no major breakthrough between the earlier attempts by Gilbert or du Boys and the models still used by scientists and engineers today. This does not mean that the state of art is mature (and thus progress is incremental), but on the opposite, there are still many problems to sort out before a new generation of models can be proposed. In this section, we review of the major obstacles to quantitative description of bed load transport.

### 2.1 Definition of the Sediment Transport Rate

Surprisingly, there is no unique way to define the sediment transport rate. Randomness, intermittency, and rapid changes in the transport rate measurements raise the problem of a suitable procedure that enables calculation and description of sediment flux for both theoretical and practical purposes. In spite of valuable efforts in recent years to gain insight into this issue, it is still unclear whether the different transport rate equations lead to compatible results in terms of statistical properties [7, 8].

An intuitive definition of the particle transport rate is to regard it as the flux of particles through a cross-section

$S$  of unit width:

$$q_s = \int_S \mathbf{u}_p \cdot \mathbf{k} dS, \quad (1)$$

with  $\mathbf{u}_p$  the particle velocity field and  $\mathbf{k}$  the unit normal to  $S$ . This definition is rarely used in practice as it is more suited to continuous fields than discrete elements. Therefore, different forms of the sediment transport rate have been proposed. They all assume bed load transport at equilibrium or near equilibrium. On average, they may provide the same values, but the statistical properties of  $q_s$  are influenced a great deal. Here are three examples.

A variant of 1 is to count the number of particles that pass through  $S$  over a short time increment  $\delta t$ . The main problem is that  $q_s$  is a step function, which takes zero values except at the times of arrival of individual particles; the resulting signal is then very noisy.

Another related form is to count the number of particles that arrive up to time  $t$  or to integrate  $q_s$  over a short period of time. In the laboratory, this is done by weighting the material accumulated in a basket located at the flume outlet while in the field, sediment traps and bed load samplers are used. These techniques do not provide  $q_s$  directly, but the sediment volume per unit width  $V(t) = \int q_s(t) dt$ . In principle, it should be possible to differentiate  $V$  to derive  $q_s$ , but in practice, fluctuations in the  $V(t)$  records make this operation delicate, which explains why sampling time is a key issue when trying to properly evaluate the solid discharge.

The use of tracer stones in gravel-bed rivers has given rise to a third relationship. From the observation that particles can be moving, lying at rest on the bed surface, or buried in the bed, one can define a virtual velocity, which is the time-averaged velocity  $U_p$  of a single particle regardless of its state. Only the upper bed layer participates in bed load transport and is therefore termed the *active layer*; the thickness of this layer is  $L_a$ . It represents the depth down to which the bed is continuously reworked by fill and scour. Mass conservation then implies that

$$q_s = U_p L_a. \quad (2)$$

This equation has been used for natural rivers and flume experiments. The statistical properties of  $q_s(t)$  depend on the fluctuations of  $U_p$  and  $L_a$ , which are little known in practice.

So what can we do? From a theoretical perspective, more suitable definitions of the particle transport rate can be borrowed from microstructural models used in

the rheology of particle suspensions. Yet, these models rely on ensemble averages, which lead to numerous difficulties in the calculations or in practical applications. To make the problem more tractable, we can substitute ensemble averages with volume averages. This makes sense when the entire flow is homogeneous, i.e., when the particles are homogeneously distributed in the streamwise direction. For two-phase flows over mobile beds, bed forms usually affect the distribution of moving particles, which makes the assumption of homogeneity dubious. One solution is to introduce a local particle transport rate defined on a control volume ( $\mathcal{V} = L \times S$ ) of length  $L$  [9, 10]

$$\bar{q}_s = \frac{S}{V} \sum_{i=1}^N u_i v_p = \frac{v_p}{L} \sum_{i=1}^N u_i, \quad (3)$$

where  $v_p$  is the particle volume (per unit width) and  $u_i = \mathbf{u}_p \cdot \mathbf{k}$  denotes the streamwise velocity component of particle  $i$ . Like the *representative elementary volume* in microstructural theories, the control volume must be sufficiently long to contain a number of particles, but short enough compared to the scale of variation of  $\bar{q}_s$  on the macroscopic scale.

The introduction of a finite-size volume in 3 leads to additional problems: how can we distinguish fluctuations that are intrinsic to the phenomenon and those that are induced by the average process? To illustrate this issue, let us consider that we would like to calculate the solids fraction of an ordered packing of cylinders by taking the average over a control volume of length  $L$ . See 2. Volume-averaged solids fractions can be calculated as a function of  $L$ . When  $L \rightarrow 0$ , we get  $\bar{\phi} \rightarrow 1$  while for  $L \rightarrow \infty$ ,  $\bar{\phi} \rightarrow \pi/4$ . Although there is no randomness in the particle arrangement, the volume-averaged solids fraction exhibits fluctuations, whose amplitude decreases with increasing  $L$  as  $2\pi a/L$ . This clearly shows in that case that the observed fluctuations of  $\bar{\phi}$  are not intrinsic, but depend on the control volume. For more complicated situations, e.g. with random particle arrangements, it is more complicated to untangle intrinsic and induced fluctuations. The problem is made even more intricate owing to other processes such as the propagation of bed forms, whose typical length often matches that used for defining the control volume.

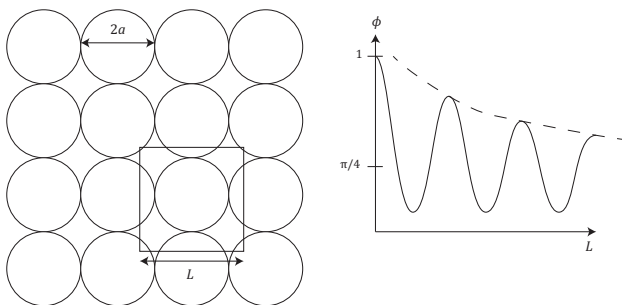


Figure 2: Calculation of the volume-averaged solids fraction

## 2.2 Bed Structures

A major challenge in fluid mechanics is to understand the origins and mechanisms that lead to the formation of macroscopic structures in systems characterized by apparent disorder. Waterways do not escape the rule. They offer a wide range of bed morphologies exhibiting regular patterns depending on the grain size distribution,

bed slope, water flow rate, etc. [11, 12]. Planform structures (e.g., bars and meanders) as well as bed forms (e.g. ripples, dunes, steps and pools) have attracted considerable attention from geomorphologists and hydraulicians. 3 shows the upper reach of the Navisence River at Zinal (Wallis, Switzerland), whose main channel can split into two arms or more (braiding) and exhibits significant sinuosity.



Figure 3: View of the upper reach of the Navisence River, with the stream wandering through its alluvium. The longitudinal profile is given in 11

A remarkable feature of bed structures is that they emerge quite rapidly at fairly low discharge rates [13]. During intense floods, most bed structures are destroyed and sediment transport occurs in the form of thick layers of grains, a mode of transport called *hyperconcentrated flow* [14]. In many practical situations, gravel beds exhibit undulations, which evolve permanently. Bed structures are thus more the rule than the exception. This is, however, poorly addressed in most laboratory experiments used to derive bed load equations.

The mainstream view is that that bed structures arise from a loss of stability of the bed due to the coupling between the turbulent water stream, sediment transport, and bed topography [15]. The main difficulty is that depth-averaged equations such as the Saint-Venant-Exner equations (see §3.1) are linearly stable for Froude numbers as large as 2. The calculation of bed form initiation and propagation then requires a more elaborate framework [16].

An alternative approach to pattern formation highlights the part played by random fluctuations of the particle transport rate  $q_s$  in the development of bed forms [17]. Analogies can be drawn with many nonlinear physical systems, in which fluctuations can produce spatially regular structures as a result of noise-induced transitions between different states of the system [18]. In the absence of a more fundamental understanding of bed load transport fluctuations, the simplest idea has been to add a noise term to the governing equations. For instance, Jerolmack and Mohrig showed that the growth and steady-state dimensions of sand dunes can be successfully captured using white noise in the Exner equation [19].

Regardless of the precise mechanism that rules their dynamics, it is clear that bed structures markedly affect the water flow, which in turn influences bed form initiation and propagation. Field surveys, laboratory experiments and numerical simulations have provided clear evidence that flow resistance is controlled to a large extent by bed forms [20]. For instance, in the absence of bed

forms, there is a one-to-one smooth relationship between the water discharge  $q$  and flow depth  $h$ , but when these bed forms develop, this relationship exhibits a more complicated pattern (non-uniqueness, hysteretic behaviour). Bedforms are also often regarded as the main source of particle flux fluctuations [21, 22, 23]: for instance, as bed slope is locally quite different between the stoss and lee sides of dunes, there is a significant change in the water flow conditions (thus particle transport) and particle entrainment.

## 2.3 Separation of Scales

The advent of modern science is tightly tied to the *reductionist* approach (i.e., any system can be broken down into individual elements, whose understanding helps us to get to grips with the whole system) [24]. Part of the success of this approach lies in the separation of length and time scales for many problems. For instance, for monoatomic gases, starting from the description of collisions at the particle scale (kinetic theory), we can derive macroscopic equations of conservation (Navier-Stokes equations) on the macroscopic scale. In that case, the large difference between the atom size and the typical length scale of continuum mechanics makes it possible to treat each problem separately. The linkage between the micro- and macro-descriptions is ensured through averaging. This procedure works at coarser scales (typical examples in computational fluid mechanics include large eddy simulations, in which averaging is replaced by low-pass filtering).

A hierarchical decomposition of the fluvial system into nested components (from watershed to particle) has been proposed [11], but a striking detail of the decomposition is the overlap of scales and the varying nature of the elements involved: while for Newtonian fluids, there is a clear separation between the molecular scale, Kolmogorov’ microscales of turbulence, and flow length scale, it is no longer the case for instance, between bed components such as boulders and the flow depth (mountain streams are mostly characterized by low submergence, i.e. the flow depth is just a few times larger than the typical bed roughness). 4 shows the Navisence River upstream of the measurement station: the typical flow depth is 50 cm while the mean diameter is  $d_{50} = 10$  cm. Note also the presence of vegetation, which plays a role often overlooked, e.g., jamming wood debris during floods [25] and consolidating effects of root systems on the long run [26].



Figure 4: View of the Navisence River near the measurement station of Zinal

## 2.4 Particular Realization Vs. Mean Trend

Field surveys have shown that the sediment transport rate seems to closely follow the time variations in the water discharge. 5 shows a typical example of evolution for the Navisence River. In this mountain stream, sediment transport is highly intermittent: it occurs primarily in spring and summer as a result of snowmelt, glacier runoff, and rainstorms, and tapers off during the cold season. Yet, as shown by 4, there is no one-to-one relationship between the water discharge and sediment transport rate: for a given water discharge, the sediment flux spans often over two to three orders of magnitude, which shows that under similar flow conditions, the actual sediment flux can be quite different from the mean trend. This spread of data has significant implications. First, most theoretical models are only concerned with mean fluxes and so, it is extremely difficult to test models against field and laboratory data when these data span over several orders of magnitude. Then, in many practical applications, focus is on different variables related to sediment transport. For instance, for calculating the time associated with reservoir filling, one is interested in determining the volume of sediment as a function of time. Owing to the random variation of the sediment flux, this volume is a stochastic integral. The actual value of the sediment volume at a given time is also quite different from the mean trend  $V(t) = \int Q_s dt$ . Strikingly, most—if not all—models developed so far ignore this problem of bed load transport variability whereas it should be at the heart of the concerns.

## 3 Outline of the Theoretical Framework

Here we outline the model under development. In the construction of this model we have tried to tackle the different issues presented in § 2. To date, we have essentially focused on the determination of the particle transport rate. The water phase is assumed to be properly described using the Saint-Venant equations (see § 3.1). The coupling between bed load transport and water flow is achieved primarily through the Exner equation, which expresses the conservation of mass for the bed. This framework implies that turbulence is roughly described by simple scalar relationships (e.g., the Manning-Strickler equation for flow resistance). As turbulence is key in the entrainment of particles from the bed and their subsequent motion, averaged equations such as the Saint-Venant equations may be too crude to capture the flow dynamics in all its various aspects, but in a first stab at modelling sediment transport, we assume that they are sufficient to provide the main features of the water flow. More attention is paid to the Exner equation, which is useful not only to compute the mean particle flux (or more precisely, the gradient of the particle flux), but also particle exchanges between the bed and stream. To that end, we take inspiration from other approaches taken in kinetic chemistry or population dynamics, which lead to evolution equations for the chemical components or the species (see § 3.2). For the particle velocity fluctuations, we use a simple analogy with Brownian motion of particles in a potential to derive the probability distribution function of the particle velocity. We eventually end up with the probability distribution of the particle transport rate.

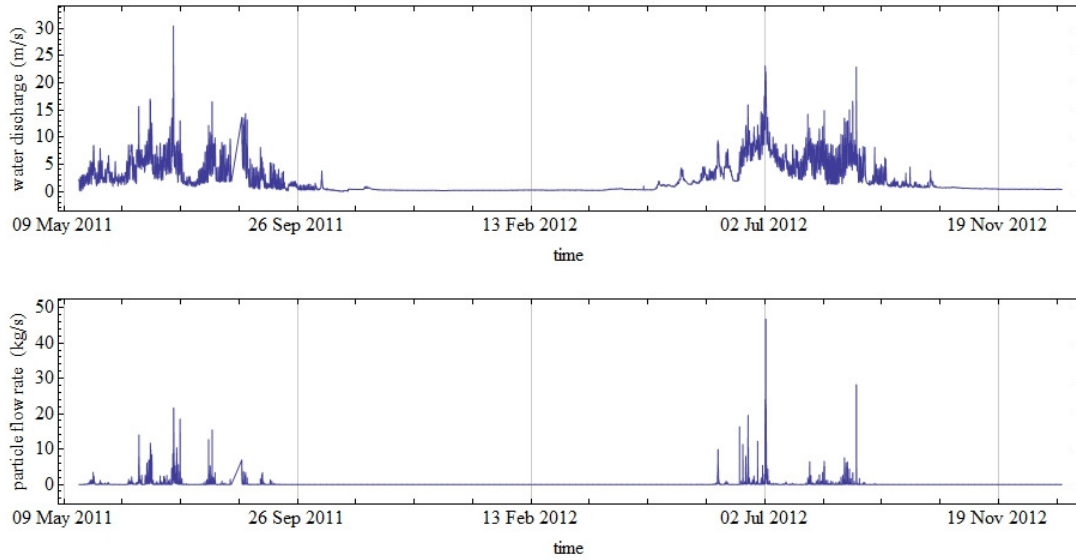


Figure 5: Time series showing the water discharge and the sediment transport rate from May 2011 to Dec. 2012 in the Navisence River, Zinal

### 3.1 Saint-Venant-Exner Equations

For one-space variable problems, the simplest morphodynamic model comprises the shallow-water (Saint-Venant) equations for the conservation of mass and momentum of the water phase and the Exner equation for the continuity equation of the bed [27]:

$$\frac{\partial h}{\partial t} + \frac{\partial h\bar{v}}{\partial x} = 0, \quad (4)$$

$$\frac{\partial h\bar{v}}{\partial t} + \frac{\partial h\bar{v}^2}{\partial x} + gh \cos \theta \frac{\partial h}{\partial x} = gh \sin \theta - \frac{\tau_b}{\rho}, \quad (5)$$

$$(1 - \zeta_b) \frac{\partial y_b}{\partial t} = -\frac{\partial \bar{q}_s}{\partial x} = D - E, \quad (6)$$

in which  $h(x, t) = y_s - y_b$  denotes the flow depth,  $y_b(x, t)$  and  $y_s(x, t)$  the positions of the bed and free surfaces,  $\bar{v}$  the depth-averaged velocity,  $x$  the downstream position,  $t$  time,  $\rho$  the water density,  $\tau_b$  is the bottom shear stress,  $\zeta_b$  the bed porosity,  $\bar{q}_s$  the average bed load transport rate, and  $D$  and  $E$  represent the deposition and entrainment rates, respectively. The bed slope is defined as  $\tan \theta = -\partial_x y_b$ . In most models based on 4–6, the governing equations are closed by empirical relationships for the flow resistance  $\tau_b$  and sediment transport rate  $\bar{q}_s$ , both being functions of the flow variables  $\bar{v}$  and  $h$ , and additional parameters (e.g., bed roughness and slope).

Whereas the Saint-Venant equations are classical and their physics is seldom called into question, the coupling with the Exner equation leads to numerous difficulties both physically and mathematically [28, 29]. Several derivations of the Exner equation have been proposed for different situations including variations in sediment properties or changes in the boundary conditions (e.g, tectonic uplift for landscape dynamics problems) [30, 19, 7, 31, 8]. A central theme in all of these derivations is that the Exner model is an averaged equation that specifies the rate of buildup/erosion of the bed surface as a function of the sediment flux through the surfaces defining the control volume over which the averaging has been done. The average sediment transport rate has nontrivial effects on the flow dynamics owing to the strong nonlinearities and coupling in the governing equations 4–6. Indeed, the sediment flux affects the bed

surface  $y_b(x, t)$  (thus its slope angle  $\theta$ ) through the Exner equation 6, and it may also influence flow resistance depending on the empirical parametrization chosen for the bottom shear stress  $\tau_b$  [32].

Our guess is that, if fluctuations are relevant to the macroscopic description of bed load transport, then the mean-field Exner equation 6 cannot properly account for the bed evolution or particle flux, or at least, as is the case for algebraic closure equations used in turbulence, this equation is a gross approximation of reality. To clarify this point, we need to take a closer look at the microdynamics of the bed evolution as a result of entrainment and deposition of particles.

### 3.2 Evolution of the Number of Moving Particle

The idea is to count the number of moving particles in a control volume or in an array of adjacent volumes of length  $\Delta x$ . In each elementary volume, the number of moving particles varies with time as a result of transport and exchanges with the bed (see 6). We do not discriminate between rolling and saltation and treat both motions as a single species which we call the moving particles. A convenient framework for the investigation of the statistics of these exchanges is the theory of birth-death Markov processes, widely used in population-dynamics models or chemical kinetics [33].

As for any idealized formulation, a tradeoff between physical scope and mathematical tractability has had to be found. To achieve analytical results, we introduce a number of simplifications:

- The sediment comprises spherical particles of equal diameter  $d$  and density  $\rho_p$ .
- We consider a two-dimensional steady water stream flowing down a sloping bed composed of particles identical to those transported. The bed breadth  $B$  is assumed to be indefinitely large.
- The water flow is characterized by its depth-averaged velocity  $\bar{v}(x, t)$  and flow depth  $h(x, t)$ , which are assumed to be prescribed and independent of the sediment transport. The water flow is

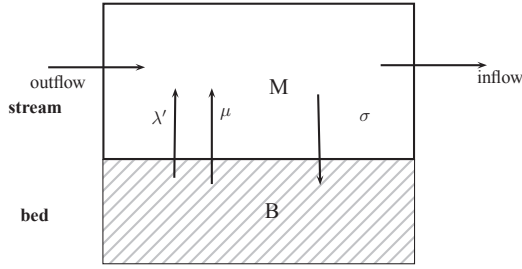


Figure 6: Sketch showing the processes considered for calculating the evolution of the number  $N$  of moving particles  $M$  within an observation window of length  $\Delta x$ . This number can be increased when particles enter the volume or are entrained as a result of individual and collective entrainments from the bed  $B$  (with a respective rate  $\lambda'$  and  $\mu$ );  $N$  decreases when particles leave the volume or are deposited (with a rate  $\sigma$ )

turbulent, but the details of the turbulence and velocity field are ignored. Turbulence dissipation and flow resistance due to the particles are entirely encoded in the  $\tau_b(\bar{v}, h)$  expression, which will not be studied here.

- The concentration of moving particles is small and so particle interactions may be neglected. In terms of the bed load transport regime, this also means that the bed shear stress narrowly exceeds the threshold for incipient sediment motion.
- The water stream drives the sediment phase: the particle phase is subordinate to the water phase in that the mean particle velocity  $\bar{u}_s$  is controlled by the water flow conditions, but due to particle exchanges (entrainment/deposition) between the bed and stream as well as particle velocity fluctuations, the instantaneous particle flux  $q_s$  undergoes variations of different magnitudes.
- The bed is initially flat and here we do not consider the development of bed forms, even though after a finite time such bed forms are likely to develop and affect water flow and sediment transport.
- We assume that the number of particles making up the bed is infinite, i.e., whenever a particle at the bed interface is set in motion, the shape of the interface is altered, but not the number of particles available to entrainment at the bed interface.
- As we study steady uniform flows over flat beds (free of patterns), we do not address the dependence of the model coefficients on the Shields stress or any other parameterization of the flow conditions. These coefficients (e.g., entrainment and deposition rate coefficient) are thus constant in the following developments. Note that the final structure of the governing equations will not be affected by this assumption.

If there are  $N$  moving particles within the control window, the probability of deposition within the time increment  $\delta t$  is  $\sigma N \delta t$ , with  $\sigma$  the deposition rate. For entrainment, we assume that there are two processes referred to as individual and collective entrainment resulting in a probability of entrainment  $P = (\lambda' + \mu N) \delta t$ , where  $\lambda'$  and  $\mu$  denote the individual and collective entrainment rates, respectively. *Collective entrainment* acts as

a feedback loop: as will be shown later,  $\mu$  is a key parameter, which controls the development and strength of wide fluctuations. A caveat is in order: here, *collective entrainment* implies that the probability of entrainment depends not only on the flow conditions (through  $\lambda'$ ), but also on the number of moving particles (through  $\mu$ ) as these can impact the bed and impart momentum to the bed particles, favouring their entrainment. In contrast with the physics of phase transition, it does not mean that there are massive departures of particles (avalanches) within short time spans. For subsequent use, we also introduce a volumetric particle entrainment rate per unit length  $\lambda = \lambda' \varpi_p / \Delta x$  and the differential rate  $\kappa = \sigma - \mu$  between deposition and collective entrainment.

The evolution of the number of moving particles could be described using the following forward master equation:

$$\begin{aligned} \frac{\partial}{\partial t} P_n(n, t) &= (n+1)\sigma P_n(n+1, t) \\ &+ (\lambda' + (n-1)\mu) P_n(n-1, t) \\ &- (\lambda' + n(\sigma + \mu)) P_n(n, t). \end{aligned} \quad (7)$$

Steady-state solutions to this equation can be obtained using the probability generating function. A stumbling block in this approach is that the governing equation for  $N$  involves discrete probabilities. To generalize the model and derive a continuum formulation, we wish to replace the discrete variable  $N$  with a continuous variable. A classical strategy is to introduce the density number  $c = N/\Delta x$ . The governing equation for the density number can be obtained from 7 by using the Kramers-Moyal or system-size expansion. This technique was used in a former paper [7]. The problem is that the resulting governing equation involves an infinite series of terms. Even if the objective is to find an approximation of the probability distribution, the number of terms required in the truncated series increases significantly when  $\Delta x \rightarrow 0$ , which makes the analytical approximation of little interest.

Exact solutions can be determined by using the equivalent of a Fourier transform, called the Poisson representation [34]

$$P(n, t) = \int_{\mathcal{C}} \frac{e^{-a} a^n}{n!} f(a, t) da, \quad (8)$$

where integration is made over a certain domain  $\mathcal{C}$  and  $f(a, t)$  is a positive real-valued function. Fourier transforms are reversible operations that map the time and frequency domains in spectral theory of signals. On many occasions when working with times series, it is easier to work in the frequency domain than the original time domain. Similarly here, the Poisson transform can be introduced to map the discrete and continuous probability domains. Using this transform, we have shown that the master equation 7 can be transformed into a second-order nonlinear parabolic diffusion equation, which has the same structure as that of a Fokker-Planck equation

$$\frac{\partial f}{\partial t} = \mu \frac{\partial^2 a f}{\partial a^2} - \frac{\partial}{\partial a} [(\lambda' - a(\sigma - \mu)) f], \quad (9)$$

with  $f(a)$  the transform of  $P$  in the  $a$ -space. This equation also arises in economics to model short-term interest rates [35].

The decisive advantage of this formulation is that we can readily obtain exact solutions in the  $a$ -space for

steady-state or time-dependent flow conditions. Further information such as the autocorrelation function and moments can also be derived straightforwardly. Algorithms simulating the process are also available to study time-dependent flow problems [36].

This formulation has, however, disadvantages: while analytical calculations are easier in the  $a$ -space, it is difficult to return to the physical variables. As a consequence, if we are able to compute the probability density function  $f$  in the  $a$ -space or to provide its governing equation, the back-transformation is uneasy. It is possible to relate the moments of  $f$  and  $N$ , but hardly possible to provide more information on the stochastic variation of  $N$ , which hinders, for the moment, the development of a stochastic Exner equation.

Under steady state conditions and in the absence of bed forms, it is possible to calculate the probability of finding  $n$  moving particles within the control volume. When the collective entrainment  $\mu$  is nonzero, the solution to 7 is the negative binomial distribution

$$P_s(n) = \text{NegBin}(n; r_{nb}, p) = \frac{\Gamma(r_{nb} + n)}{\Gamma(r_{nb})n!} p^{r_{nb}} (1-p)^n, \quad (10)$$

with  $r_{nb} = \lambda'/\mu$  and  $p = 1 - \mu/\sigma$ , and where  $\Gamma$  denotes the gamma function. The mean is

$$\langle N \rangle = \frac{\lambda'}{\sigma - \mu}, \quad (11)$$

and the variance is

$$\text{var } N = \frac{\lambda' \sigma}{(\sigma - \mu)^2}. \quad (12)$$

For  $\mu = 0$ , we obtain the Poisson distribution of rate  $r_p = \lambda'/\sigma$ ,

$$P_s(n) = \frac{(r_p)^n}{n!} e^{-r_p}, \quad n = 0, 1, \dots \quad (13)$$

### 3.3 Velocity Fluctuations

Many models have been proposed to compute the mean particle velocity, but the probability distribution of the velocity for a single particle has not been well investigated until very recently [37, 38, 39, 40]. We have developed a very simple model, in which, making the analogy with Brownian particles in a potential, we end up with the probability distribution in the form of a truncated Gaussian distribution:

$$P_u^{eq}(u) = \sqrt{\frac{2t_r}{\pi D_u}} F(u), \quad (14)$$

with

$$F(u) = \frac{\exp\left(-\frac{t_r(u - \bar{u}_s)^2}{2D_u}\right)}{1 + \text{erf}(\bar{u}_s \sqrt{t_r}/\sqrt{2D_u})} \quad (15)$$

where  $t_r$  is a relaxation time,  $D_u$  is the equivalent of a particle diffusivity, and  $\bar{u}_s$  is the mean particle velocity imposed by the water stream, i.e. the asymptotic value to which the particle velocity tends at long times in the absence of fluctuations.

We tested 14 against experimental data. The detail can be found in an earlier paper [10]. The bed was composed of gravel characterized by a narrow size distribution around a mean diameter 8 mm. The particle density was 2650 kg m<sup>-3</sup>. Particle motion was tracked

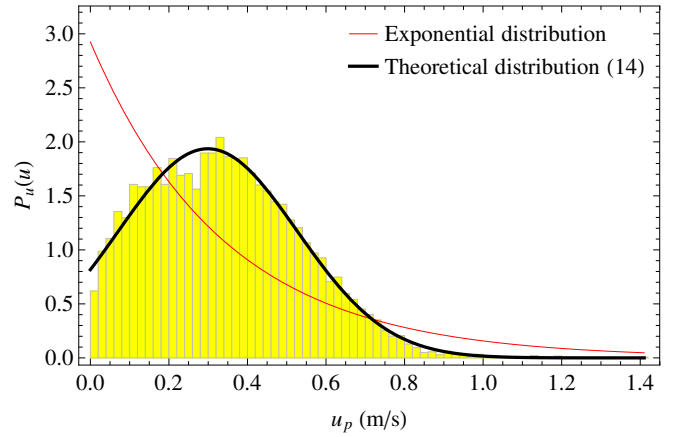


Figure 7: Probability distribution for the particle velocity. The histogram represents the empirical probability density function of  $u_p$ . The thick black solid line is the theoretical distribution 14 with  $\bar{u}_s = 29.9 \text{ cm s}^{-1}$  and  $\zeta = 5.7$ . The thin red line shows the exponential probability distribution  $P_u(u) = e^{-u/\bar{u}_s}/\bar{u}_s$ , still with  $\bar{u}_s = 29.9 \text{ cm s}^{-1}$ . The dimensionless parameter  $\zeta$  is defined as  $\zeta = \bar{u}_s/\sqrt{D_u/t_r}$

using a high-speed camera over a 40 cm length. 7 shows the probability density function of the particle velocity up computed from 755 trajectories. The flow conditions were the following: depth-averaged velocity of water  $\bar{v} = 92.5 \text{ cm s}^{-1}$ , mean flow depth  $h = 2 \text{ cm}$ , Froude number  $\text{Fr} = 2.1$ , flow Reynolds number  $\text{Re} = 18 \times 10^3$ , Shields number  $\text{Sh} = \rho h \sin \theta / [(\rho_p - \rho)d] = 0.042$ . For these flow conditions, long wavelength bed forms developed.

There is a fairly good agreement between these data and the truncated Gaussian distribution 14. This result compares well with the observations made by Martin *et al.* [38] with similar flow conditions. Our results contrast with those obtained by Fan *et al.* [40], Robeseberry *et al.* [41], and Lajeunesse *et al.* [37], who found that the empirical probability distribution of particle velocity  $u_p$  was well captured by an exponential distribution. This discrepancy may originate from the differences in the experimental set-up.

Although there is experimental evidence for the theoretical velocity distribution 14, the diversity of experimental data shows that its range of application is unlikely to cover all sediment sizes. We note, however, that in either case, the truncated Gaussian and exponential laws are thin-tailed, a result that can be anticipated as it is uncommon for the highest particle velocities to exceed fluid velocities. Therefore, the high fluctuations of sediment transport rates are unlikely to stem from a thick tail of the velocity distribution.

### 3.4 Particle Flux Fluctuations

As a matter of convenience, we express the instantaneous particle flux as the number of moving particles per unit time within the control volume rather than their volume

$$\dot{n}(t; \mathcal{V}) = \frac{1}{\Delta x} \sum_{i=1}^{N(t)} U_{p,i}, \quad (16)$$

where both  $N$  and  $U_{p,i}$  are random variables. For a stationary process, their probability distributions are given by 10—or 13 if  $\mu = 0$ —and 14, respectively. The probability density function of the sum of random variables

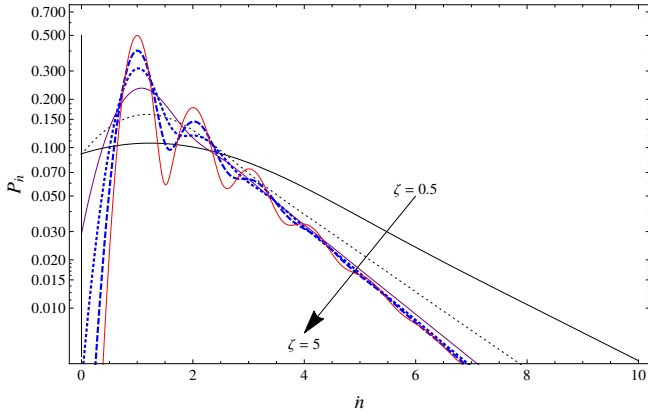


Figure 8: Shape of the probability density function  $P_{\dot{n}}(\dot{n})$  given by 17 in a log-linear plot for different values of  $\zeta$  (the arrow shows increasing  $\zeta$  values):  $\zeta = 0.5$  (black solid line),  $\zeta = 1$  (black dotted line),  $\zeta = 2$  (purple solid line),  $\zeta = 3$  (blue dotted line),  $\zeta = 4$  (blue dashed line), and  $\zeta = 5$  (red solid line). All of the other parameters are kept constant:  $\Delta x = 1$  m,  $\bar{u}_s = 1$  m s $^{-1}$ ,  $r = 1$  ( $\lambda' = \mu$ ) and  $p = 0.5$  ( $\sigma = 2\lambda'$ ). The mean particle flux  $\langle \dot{n} \rangle$  is 1.541, 1.115, 1.007, 1.000, 1.000, 1.000 beads s $^{-1}$  when  $\zeta$  is increased from 0.5 to 5. The square coefficient of variation  $\text{var } \dot{n} / \langle \dot{n} \rangle^2$  is 2.410, 2.362, 2.209, 2.109, 2.062, and 2.040 beads $^2$  s $^{-2}$  when  $\zeta$  is increased from 0.5 to 5

drawn from the same distribution can be calculated by taking the Fourier transform of the convolution product, then inverting the result. After a little bit of work, we eventually find that

$$P_{\dot{n}}(\dot{n}) = P_s(0)\delta(\dot{n}) + \frac{\zeta \Delta x}{\bar{u}_s} \sqrt{\frac{2}{\pi}} \sum_{k=1}^{\infty} P_s(k) G(\dot{n}), \quad (17)$$

with

$$G(\dot{n}) = \frac{\exp\left[-\zeta^2 \frac{(\dot{n}\Delta x - k\bar{u}_s)^2}{2k\bar{u}_s^2}\right]}{\sqrt{k}(1 + \text{erf}(\sqrt{k}\zeta/\sqrt{2}))} \quad (18)$$

where  $P_s(k)$  is given by 10 if  $\mu > 0$  and 13 if  $\mu = 0$ . We have also introduced the dimensionless number  $\bar{u}_s/\sqrt{D_u/t_r}$ . The probability density function of  $\dot{n}$  is discontinuous at  $\dot{n} = 0$ : there is a finite probability  $P_s(0) = (1 - \mu/\sigma)^{\lambda'/\mu}$  for  $\mu > 0$  ( $P_s(0) = \exp(-\lambda'/\sigma)$  for  $\mu = 0$ ) that there is no moving particle within the window, in other words, that the particle flux is zero (intermittent sediment transport).

Some remarkable features can be deduced from numerical evaluations of 17. 8 shows examples of variations of  $P_{\dot{n}}(\dot{n})$  for  $\zeta$  ranging from 0.5 to 5. For low  $\zeta$  values, the probability density function varies smoothly and slowly except for the point of discontinuity  $\dot{n} = 0$ , as explained above. Increasing  $\zeta$  leads to (i) a faster (but still exponential-like) decay at larger values of  $\dot{n}$ , which is little influenced by the actual value of  $\zeta$ , and (ii) the development of sharp peaks of probability for the lowest values of  $\dot{n}$ : in a dilute flow much of the flux is carried by a couple of particles and, in the absence of velocity fluctuations, the particle flux exhibits this bumpy landscape in which each peak corresponds to the crossing of one particle.

Although Einstein used probabilistic concepts to derive his bed load equation, he did not end up with a probability distribution for the sediment transport rate. His arguments lead to a binomial variation of the number of moving particles, thus a Poisson distribution in

the limit  $p \rightarrow 0$  (i.e.  $\mu \rightarrow \sigma$ ) and  $N \gg 1$  [2]. This means that intense sediment transport exhibits bounded Poissonian fluctuations, with the coefficient of variation  $\text{var}^{1/2} q_s / \langle q_s \rangle = r_p^{-1/2}$  given by the steady-state Poisson distribution 13. Hamamori is credited with the first attempt to derive the probability distribution for the sediment transport rate. He considered that bed load transport rate fluctuations arise from the migration of bed forms [42]. He obtained a nonparametric density distribution function of the bed load transport rate

$$P(q_s) = \frac{1}{4\langle q_s \rangle} \log\left(4 \frac{\langle q_s \rangle}{q_s}\right), \quad (19)$$

which implies that the fluctuations are bounded:  $0 < q_s < 4\langle q_s \rangle$ , and that the square coefficient of variation is constant:  $\text{var } q_s / \langle q_s \rangle^2 = 7/9$ . More recently, Turowski used a two-parameter distribution derived from the normal distribution, called the Birnbaum-Saunders distribution

$$P(q_s) = \frac{q_s + \alpha}{2\beta q_s \sqrt{2\pi\alpha q_s}} \exp\left[-\frac{(q_s - \alpha)^2}{2\alpha\beta^2 q_s}\right], \quad (20)$$

with  $\alpha$  and  $\beta$  two calibration parameters [43]. The mean value is  $\langle q_s \rangle = \alpha(1 + \beta^2/2)$  and the coefficient of variation is found to range from 0 to  $\sqrt{5}$ . 9 shows the comparison of the probability distributions 17, 19, 20 for a particular case. As the fluctuations are bounded, Hamamori's relation is unable to capture the exponential tail of the distribution and tends to overestimate the bed load transport rate significantly (compared with what 17 predicts) in the limit of  $\dot{n} \rightarrow 0$ . This latter shortcoming is also observed for the Birnbaum-Saunders distribution, but the tail behaviour is consistent with that predicted by our model 17. On the whole, the general impression one gets from 8 is that the Birnbaum-Saunders distribution smooths out the ups and downs in the probability distribution 17. Although the point of this paper is not to discuss the agreement with field and experimental data, note that that high-resolution data confirm (i) the significant proportion of zero values of the particle flux and (ii) the highly fluctuating nature of time series, two features that are consistently described by 17 and 9 [9, 44, 45].

Comparison with experimental data usually shows a decent agreement between theory and experiment. Systematic comparison was done with an idealized setup, in which sediment was replaced by 6-mm glass beads free to move in a narrow flume [9]. 10 shows the empirical and theoretical probability density functions  $P_{\dot{n}}(\dot{n})$  for a slope of 5°. One possible reason for the discrepancy between theory and experiment is the existence of two populations of moving particles with two distinctive mean velocities. Indeed, there is a size factor of about 5 between the velocities in the rolling and saltating regimes. Comparing the different runs also shows that the larger the number of moving particles, the better the agreement. This may be an indication either that theory performs less well in the limit  $N \rightarrow 0$  or the calculation of the sediment transport rate is biased as we assumed that the probabilities  $P_n(n)$  and  $P_u(u_p)$  were independent in order to obtain  $P_{\dot{n}}(\dot{n})$  by taking the Fourier transform of the convolution product. This requires further work. A more thorough experimental investigation is still needed to test the model.

### 3.5 Local and Macroscopic Forms of the Exner Equation

The last building block is to make a link between the Exner equation 6 and the local conservation of mass.

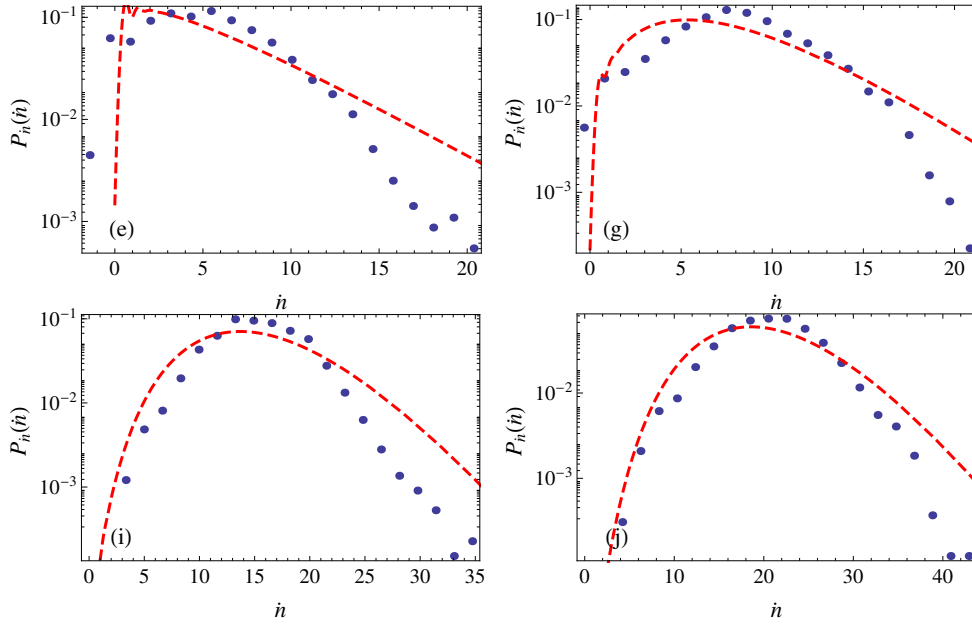


Figure 10: Probability density functions for the particle flux compared to experimental data collected by Tobias Böhmer [9]. The dots represent the empirical probability density function while the dashed curves are the theoretical distributions 17 with  $\zeta = 4$ . This parameter was fixed arbitrarily, but provided that  $\zeta > 3$ , we found that altering  $\zeta$  did not change the shape of  $P_{\dot{n}}(\dot{n})$  significantly for these runs. Run (e)  $\bar{n} = 5.3$  beads/s,  $h = 10.2$  mm,  $\bar{u}_s = 0.41$  m/s. Run (g)  $\bar{n} = 8.0$  beads/s,  $\bar{u}_s = 0.44$  m/s,  $h = 12.2$  mm. Run (i)  $\bar{n} = 15.4$  beads/s,  $h = 16.9$  mm,  $\bar{u}_s = 0.48$  m/s. Run (j)  $\bar{n} = 20.0$  beads/s,  $h = 19.4$  mm,  $\bar{u}_s = 0.53$  m/s. See [10] for further information

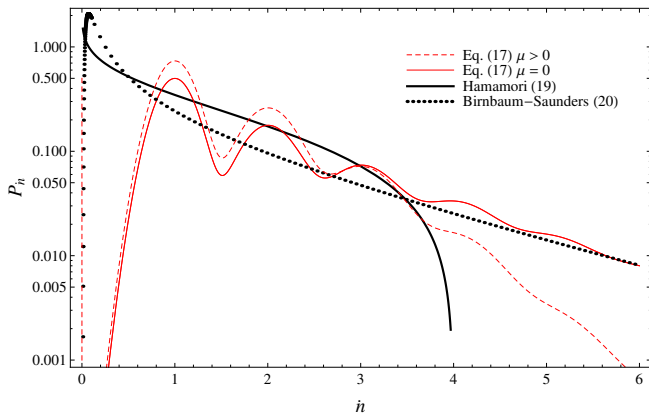


Figure 9: Comparison of the probability density function  $P(\dot{n})$  in a log-linear plot: Hamamori's equation 19 (with  $\langle \dot{n} \rangle = 1$  beads  $s^{-1}$ ) and Birnbaum-Saunders distribution 20 (with  $\alpha = 0.451$  and  $\beta = 1.556$ ). We also report the probability density function  $P_{\dot{n}}(\dot{n})$  for  $\zeta = 5$  ( $\Delta x = 1$  m,  $\bar{u}_s = 1$   $m s^{-1}$ ): when the number of moving particles follows the negative binomial distribution 10 (solid red line) with  $r = 1$  ( $\lambda' = \mu$ ) and  $p = 0.5$  ( $\sigma = 2\lambda'$ ) or the Poisson distribution 13 (dashed red line) with  $r_p = 1$  beads  $s^{-1}$ . Except for the Poisson distribution (whose variance equals the mean), the coefficient of variation is  $\sqrt{2}$  and all of the distributions have the same mean ( $\langle \dot{n} \rangle = 1$  beads  $s^{-1}$ )

By integrating the velocity probability equation, we obtain an equation for the particle concentration or, equivalently, the particle activity (the volume of particles per unit bed length)  $\gamma(x, t) = N\varpi_p/\Delta x$

$$\frac{\partial}{\partial t} \langle \gamma(x, t) \rangle + \frac{\partial}{\partial x} (\bar{u}_s \langle \gamma(x, t) \rangle) = \frac{\partial^2}{\partial x^2} (D_u \langle \gamma(x, t) \rangle) + \lambda - \kappa \langle \gamma(x, t) \rangle, \quad (21)$$

with  $\kappa = \sigma - \mu$  and  $\lambda = \lambda' \varpi_p / \Delta x$ . This is a linear advection diffusion equation with a source term. Albeit of very common structure, this equation yields many interesting insights into the physics of sediment transport. Note that 21 can also be cast in the following form

$$\frac{\partial}{\partial x} \mathcal{Q}(x, t) = E(x, t) - D(x, t) - \frac{\partial}{\partial t} \langle \gamma \rangle, \quad (22)$$

with  $\mathcal{Q} = \bar{u}_s \langle \gamma \rangle - \partial_x (D_u \langle \gamma \rangle)$ ,  $E = \lambda + \mu \langle \gamma \rangle$ , and  $D = \sigma \langle \gamma \rangle$ . Interestingly, if we borrow the definition of the sediment flux rate from David Furbish [31] and refer to  $\mathcal{Q}$  as the *macroscopic sediment transport rate*, then 22 is the generalized Exner equation established by a number of authors [46, 47, 30]. Note that the standard equation 6 does not usually include the time variation in the particle activity  $\partial_t \langle \gamma \rangle$  as this term is vanishingly small. Indeed, using dimensional analysis, [48] showed that provided that the ratio  $\epsilon = \bar{q}_s / q_w$  (with  $q_w$  the water discharge) remains small, the time variation  $\partial_t \langle \gamma \rangle$  is second order. Thus to leading order, the bed evolution  $\partial_t y_b$  is controlled by the gradient  $\partial_x \bar{q}_s$ .

The existence of diffusive effects in the Exner equation may lead to the conclusion that by smoothing out particle activity variations  $\langle \gamma(x, t) \rangle$  along the bed, particle fluctuations dissipate short wavelength perturbations and so make the bed more stable. Yet, as exemplified by Turing patterns in certain reaction-diffusion systems [49], diffusion may amplify instabilities instead of dampening them under a slight perturbation by noise.

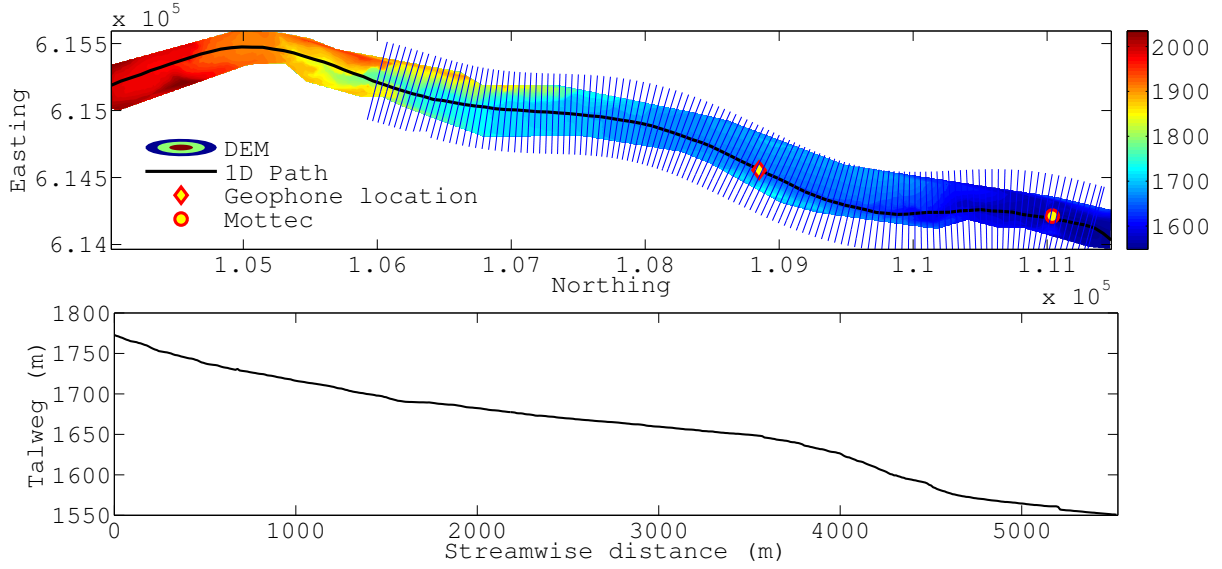


Figure 11: Digital elevation model of the study site (top) and talweg profile along northing (bottom). Blue lines represent the cross sections employed in the simulations (only 1 of every 5 are shown for the sake of clarity)

## 4 Numerical Modelling

In this section we present numerical results to describe the flow hydrodynamics in the upper reach of the gravel bed Navisence river between Mottec and Zinal glacier (5.5 km in length), see 11. The mean bed gradient is 4.1%, which is regarded as steep according to geomorphological criteria, but this mean slope is shallow in the mathematical sense (i.e.  $\cos\theta \approx 1$ ), with the important consequence that the pressure distribution (across the depth) is hydrostatic and the Saint-Venant equations are well-suited.

The river exhibits a rich collection of geomorphological features such as steps and pools sequences, meanders, multi-channels and slosh dynamics that increase flow resistance with respect to regions of quasi-uniform flow because of mechanical losses due to flow expansion/contraction, dead zones and channel geometry variations. This pushes us to use cross sectionally averaged formulations of the Saint-Venant equations as these better accounts for streamwise variations of water flow conditions along the river.

### 4.1 Cross-sectionally Averaged Saint-Venant Equations

The one-dimensional version of Saint-Venant equations 4-6 can be extended to account for cross sectional variations as described by Cunge et al. [50]:

$$\frac{\partial \mathbf{U}}{\partial t} + \frac{\partial \mathbf{F}}{\partial x}(x, \mathbf{U}) = \mathbf{S}(x, \mathbf{U}), \quad (23)$$

with

$$\mathbf{U} = (A, Q)^T, \quad (24)$$

$$\mathbf{F} = \left( Q, \frac{Q^2}{A} + gI_1 \right)^T, \quad (25)$$

$$\mathbf{S} = [0, gI_2 + gA(S_0 - S_f)]^T, \quad (26)$$

in which  $A$  is the wetted cross-sectional area and  $Q \equiv \bar{v}A$  is the water flow rate. The term  $I_1$  represents a cross-sectional hydrostatic pressure force,

$$I_1(x, A) = \int_0^{h(x,A)} [h(x, A) - \eta] \sigma(x, \eta) d\eta, \quad (27)$$

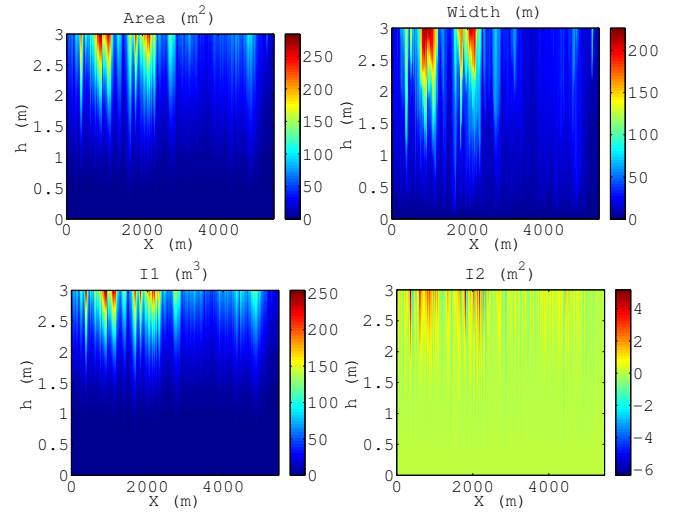


Figure 12: Dependence of channel area  $A$ , width  $b$ , pressure force terms  $I_1$  and  $I_2$  on the streamwise coordinate  $x$  and flow depth  $h$

in which the surface water level is denoted by  $h(x, A)$  and the local width  $\sigma(x, \eta)$  at a given depth is

$$\sigma(x, \eta) = \frac{\partial A(x, t)}{\partial \eta}, \quad (28)$$

In 26,  $I_2$  is the component of the pressure force in the main stream direction due to the reaction of the walls arising from shape variations

$$I_2(x, A) = \int_0^{h(x,A)} [h(x, A) - \eta] \frac{\partial \sigma(x, \eta)}{\partial x} d\eta. \quad (29)$$

The magnitude of this force depends on the cross-sectional variation for a constant depth. Note that (i) this approach is underpinned by the hypothesis of gradual variation in flow variables and bed geometry and (ii) the streamwise gradient of the width is central to the accurate computation of the total pressure.

In 26, the one-dimensional friction slope term required to close the model is taken in the form of the Darcy-

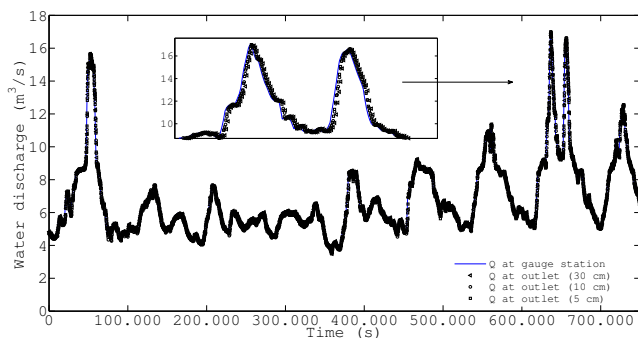


Figure 13: Comparison between inlet and outlet hydrographs for several grain sizes in Ferguson's equation [53, 54]

Weisbach friction law

$$S_f = \frac{f}{8g} \frac{|\bar{v}|\bar{v}}{R_h}, \quad (30)$$

where  $f$  is the friction factor and  $R_h$  is the hydraulic radius of the channel. The last term 26 is the bed slope  $S_0 \equiv -\partial y_b / \partial x$ .

A numerical code was written in Matlab to automatically compute  $A(x, h)$ ,  $R_h(x, h)$ ,  $b(x, h)$ ,  $I_1(x, h)$  and  $I_2(x, h)$  for a given digital elevation model (DEM) and path. Tabulated data were used in an in-house finite volume code [51], second-order accurate in space and time, as follows: unknowns  $A$  and  $Q$  at every time step were obtained by solving for 23-30; a bidimensional searching algorithm was then employed to obtain the value of  $h$  associated with  $A$ ; next, the terms  $I_1(x, h)$ ,  $I_2(x, h)$  and  $R_h(x, h)$  were updated using quadratic interpolation.

Geometrical inputs give us useful information about the uniformity of the river channel. For instance, on inspection of the channel area  $A$ , width  $b$  and pressure force terms,  $I_1$  and  $I_2$ , for a fixed water flow depth  $h$  along the streamwise coordinate  $x$ , see 12, it is readily observed that  $b$  and  $A$  remain nearly constant over  $3 \leq x \leq 4.5$  km, whilst there are substantial variations in the upstream reach for  $x \leq 3$  km.  $I_1$  and  $I_2$  exhibit a similar trend as well as other variables such as  $R_h$  (not shown here for brevity). The channel in the lower reach indeed corresponds to a narrow, deep, confined, and, entrenched single thread stream with steep, cascading, step/pool features and low sinuosity [52]. Conversely, the upper reach is a braided channel with frequently spaced scour/depositional bed forms. The complex stream pattern found upstream also exhibits numerous expansions and contractions, as seen in 12 with the width variations, which are influenced by gravel pit and anthropogenic structures.

Taking into account the previous considerations, all of the terms in 23-30 were included in the simulations. In doing so, their relative importance can be evaluated *a posteriori* to discuss further simplifications.

## 4.2 Unsteady Simulation of Circadian Water Discharge Variations

Unsteady numerical results were obtained for a synoptic hydrograph measured at the Zinal gauge station (equipped with geophones to record bed load transport rates). The water flow discharge was set as an upstream boundary condition placed at this station. The inlet cross-section area was determined to impose a critical Froude number, i.e.  $A$  was given by the solution to the

equation  $Q = A^{3/2} \sqrt{g/b}$ . The characteristic variable extrapolation method was employed at the outlet.

The sensitivity of the numerical results to grain size was evaluated using Ferguson's friction factor [53], which is particularly well suited for uniform regimes in gravel-bed rivers with constant cross section [54]. 13 shows the outlet hydrograph obtained for a given inlet discharge (blue solid line) and characteristic grain sizes of  $d_{84} = 5$ , 10 and 30 cm. Surprisingly the outlet hydrograph preserves the same shape as that fixed at the inlet regardless of the diameter  $d_{84}$ . In a long temporal scale the inlet and outlet hydrographs nearly collapse. Looking into the details, we found out a small delay between them, see the inset of 13, that amounts to a different lag time ranging from 473 s ( $d_{84} = 5$  cm) to 931 s ( $d_{84} = 30$  cm). An additional numerical simulation was performed using the Colebrook-White equation [55] with  $d_{84} = 10$  cm. It agreed very well with the previous one, showing a lag time of about 720 s.

Field works were done on 14th October 2012 to measure the velocity field *in situ*. It was measured for moderate water discharges between 2 and 8 m<sup>3</sup>/s at five points along the reach upstream of the geophones station. On average, the standard deviation of the mean velocity considered at each cross section was quite high (typically 0.8 m/s) compared to the mean flow velocity (approximately 2.7 m/s). This could be interpreted as the occurrence of non-uniform velocity profiles in the cross section and unsteady turbulent spots. The best agreement between prediction and mean experimental values was found with grain diameter values of about 10 cm. Maximum discrepancies were lower than 30 % when computing  $f$  using Colebrook-White's equation or Ferguson's law.

Previous results have important consequences for the hydraulic modelling of mountain rivers as it sets the validity of the kinematic wave approximation [56] and frictional laws in non-uniform quasi-steady regimes. We postulate that the propagation of a hydrograph wave form in mountain rivers can be computed as the solution to the first order wave equation (the so-called kinematic wave equation)

$$\frac{\partial Q}{\partial t} + c \frac{\partial Q}{\partial x} = 0, \quad (31)$$

where the wave speed  $c$  has to be estimated for a particular river reach and flow conditions. In addition, taking into account that the characteristic period of 24 h associated with circadian oscillations is much longer than the characteristic lag time of about 15 min for a reach of 2 km length, one can further assume a local quasi-steady regime. So, the water flow depth and the velocity corresponding to a given discharge  $Q$  can be obtained from the steady state solution of the momentum balance equation neglecting the gradients of  $Q$ , i.e. solving for

$$\bar{v} \frac{\partial \bar{v}}{\partial x} = g \left( S_0 - \frac{\partial h}{\partial x} \right) - \frac{f}{8} \frac{|\bar{v}|\bar{v}}{R_h}, \quad (32)$$

in which [50]

$$\frac{\partial h}{\partial x} = \frac{1}{A} \left( \frac{\partial I_1}{\partial x} - I_2 \right). \quad (33)$$

Note that the spatial variations of the velocity  $\bar{v}$  and flow depth  $h$  induced by cross section variations in non-uniform channels may play as important role as the bed slope  $S_0$  and the bottom friction as will be shown in the next section.

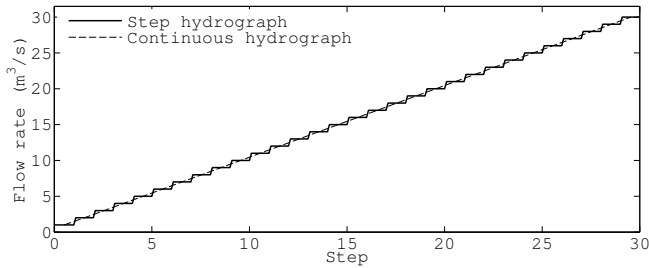


Figure 14: Step hydrograph imposed as boundary condition at the inlet. Results from step computations can be employed to mimic a continuous increase of the flow rate according to § 4.2

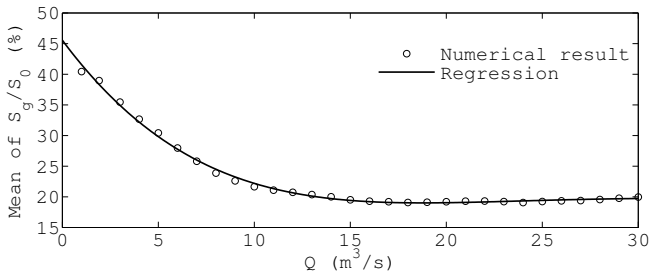


Figure 15: Relative local head variation  $S_g/S_0$

### 4.3 Steady State Computations

Steady state numerical simulations were performed for a realistic range of water discharges from 1 to 30 m<sup>3</sup>/s. The water discharge was fixed as an upstream boundary condition together with the area corresponding to a critical Froude number, similarly to the unsteady case. A sensitivity study, not shown here for the sake of the brevity, has proven that the numerical solution taken a few meters downstream of the inflow is insensitive to the water depth at the inlet. Hence, in the present case, flow hydrodynamics only depend on the river geometry, frictional resistance and discharge.

Numerical simulations were performed sequentially to save computational time. To this end the step hydrograph shown in 14 was set at the inlet. A constant value of the discharge was maintained during the integration of 23-30 until a steady state is reached throughout the whole computational domain. Subsequently, it was monotonously increased by steps of 1 m<sup>3</sup>/s ensuring steady state solutions at every discharge. The numerical solution obviously satisfies the steady state equation, 32-33, and allow us to evaluate the relative importance of the bed slope and momentum transfer to the bed (i.e. hydraulic resistance in uniform channels) relative to the terms, which can be interpreted as local resistance arising from the non-uniformity of the channel geometry.

In this context, we sought to evaluate the local energy variation caused by the non-uniformity of the river channel, denoted hereafter by  $S_g$  and defined as the deviation of the friction slope  $S_f$  with respect to the bed slope  $S_0$ :

$$S_g \equiv \left| \frac{\bar{v}}{g} \frac{\partial \bar{v}}{\partial x} + \frac{\partial h}{\partial x} \right| = |S_0 - S_f|. \quad (34)$$

15 shows the percentage value of the geometric slope  $S_g$  scaled by  $S_0$  obtained in the numerical simulations as a function of the water discharge. To make the description easier, we plotted the average value in the whole river. The average geometric slope induced by streamwise variations in the hydraulic variables amount

to more than twenty percent of the bed slope, with a maximum reached at low stages at which average head loss approaches 45%. It monotonously decreases as the flow discharge raises, attaining a minimum asymptotic value (which is above 20%) for flow discharges exceeding 15 m<sup>3</sup>/s. This result highlights the clear hydraulic control exerted by the river channel, which turns out to be significant at the lowest flow rates. This feature has to be accounted for in the hydraulic modelling if the objective is to be accurate.

The Froude number  $Fr \equiv Q/\sqrt{A^3g/b}$  follows a well-defined trend at all flow discharges, as shown in 16. Three hydraulic regimes are visible. The flow is supercritical upstream ( $x < 1600$  m), becomes nearly critical approximately along the next 2 km and finally returns to the supercritical regime further downstream ( $x > 3550$  m). The average value of the ratio between the standard deviation and the mean Froude number is lower than 14% when  $Q$  ranges from 1 to 30 m<sup>3</sup>/s at any  $x$ . A similar behaviour is observed if we use the one-dimensional definition of the Froude number  $Fr_{1d} = \bar{v}/\sqrt{gh}$  (whereas its value differs markedly from the cross-sectionally averaged one  $Fr$ ).

This remarkable result demonstrates that the solution exhibits Froude similarity at leading order. This property simplifies and tremendously speeds up the computation of flow depth and velocity for a given flow discharge. As a matter of fact, assuming that the Froude number  $Fr^*$  is known at a given location  $x$ , for instance calculating it from field data or by means of numerical simulations just at one discharge  $Q^*$ , the flow depth  $h$  at an arbitrary discharge  $Q$  can be obtained by solving the equation

$$\frac{A^3}{b}(x, h) = \frac{1}{g} \left( \frac{Q}{Fr^*} \right)^2. \quad (35)$$

Alternatively, one can solve  $h$  and  $\bar{v}$  along the thalweg from

$$\frac{\bar{v}}{\sqrt{gh}} = Fr_{1d}^* \quad \text{with} \quad \bar{v} = \frac{Q}{A(x, h)}. \quad (36)$$

## 5 Concluding Remarks

Our project (which started five years ago) has made steady progress, with some interesting achievements regarding the stochastic modelling of sediment transport and the numerical simulations. Here we summarize the main findings, speak of the future work, and highlight some of limitations in our current framework.

### 5.1 Stochastic Model of Sediment Transport

Our Markov-process-based approach has addressed at least two issues in the list of problems enumerated in § 2:

- Existence of large non-Gaussian fluctuations and sediment rating curve: in the absence of collective entrainment ( $\mu = 0$ ), the fluctuations of  $N$  are Poissonian, which leads to a rather simple macroscopic behaviour [9]. In contrast, for  $\mu > 0$ , fluctuations are non-Poissonian and may vary significantly over time, affecting the macroscopic behaviour by the growth of spatial correlations, which reflects local increases in the particle activity. Even for steady uniform flow conditions (with no bed forms), the variance of the particle flux may become very large. For time-dependent flow conditions and especially

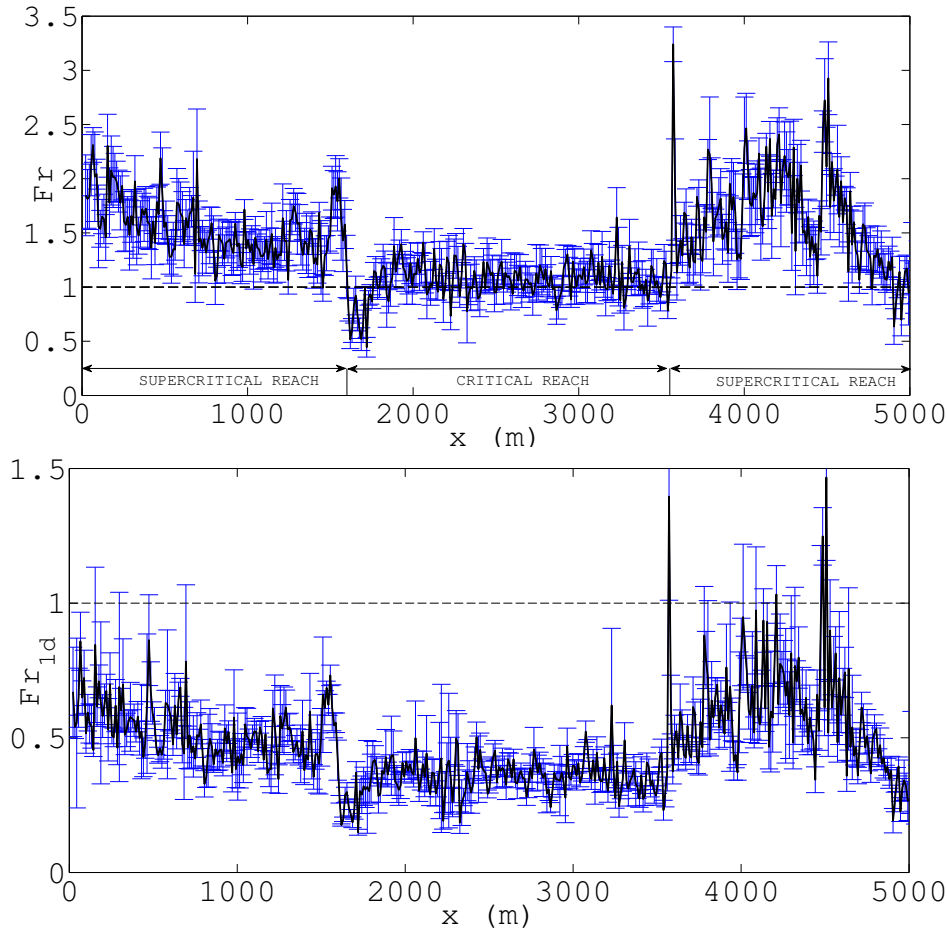


Figure 16: Mean value (black solid line) and standard deviation of the cross section (top) and 1d (bottom) Froude number for water discharges between 1 and 30 m<sup>3</sup>/s

when bed forms migrate, the expected behaviour of fluctuations is quite complicated. The Langevin equation associated with the Fokker-Planck equation 9 reveals that the noise structure, characterized by a square multiplicative noise term, differs significantly from the white noise term used by Jerolmack and Mohrig [19] to model the stochastic development of bed forms [10]. Altogether, this provides us with little reason to believe that in real flow conditions, marked by time dependence and bed form migration, one can obtain consistent time averages of the particle activity and sediment transport rates. In our opinion, this explains the failure in both the laboratory [45] and the field [57, 58] to arrive at robust estimates of transport rates when the sampling rate is changed. As a consequence, the idea of a unique bed load rating curve seems dubious.

- Existence of long correlation lengths and bed forms: when collective entrainment occurs ( $\mu > 0$ ), the spatial correlation function is nonzero and decays exponentially; the detail is given in [10]. From the combined action of the water stream (through  $D_u$ ) and sediment transport (through the deposition and entrainment rate difference  $\kappa$ ), emerges the correlation length scale  $\ell_c = \sqrt{D_u/\kappa}$ . Similarly, the auto-correlation time of the number of moving particles is  $t_c = 1/\kappa$  can be quite long (compared to flow characteristic times). Collective entrainment is consistent with the incipient phase of dune formation: for  $\mu > 0$ , there are areas characterized by high correlations in the particle activity, whose strength is

dictated by the ratio  $\mu/\kappa$ . This is likely to cause nonhomogeneous sediment transport, which in turn promotes bed form development. From this perspective, the initiation of bed structure is the consequence of collective entrainment. The subsequent development of bed patterns is, however, beyond the scope of our analytical application as it requires calculating the coupling between the stream and topography, and more specifically the effects of turbulence on particle entrainment.

Another particularly interesting result is related to the difference between the definition of the sediment transport rate at the micro- and macroscales. We come to conclusions similar to those drawn by Furbish *et al.* [31] about the form that the particle flux should take. The governing equation of the particle activity 21, derived from the microscopic description of particle transport, matches the Exner equation 6 provided that (i) the particle transport rate is defined at the macroscopic scale as

$$\bar{q}_s = Q(x, t) = \langle \gamma \rangle \bar{u}_s - \frac{\partial}{\partial x} (D_u \langle \gamma \rangle), \quad (37)$$

and (ii) the term  $\partial_t \langle \gamma \rangle$  is negligible relative to entrainment and deposition rates. The latter assumption is well-established [48]. This definition of  $\bar{q}_s$  differs from the local definition 3. The interpretation of the present stochastic analysis closely follows those obtained by Furbish *et al.*: at the macroscopic scale, diffusive effects are present in the Exner equation, which modulate, to a varying degree, the advection term. The significance of this modulation can be estimated using a dimensionless Péclet number [10].

In the coming years, the main tasks concern the extension of the model to deal with non-uniform flow conditions, which involves studying the difficult question of the coupling between bed topography, turbulence, and particle entrainment. Two stumbling blocks remain the definition of the particle flux and the dependence of the entrainment and deposition parameter under time-dependent flow conditions.

In the current framework, there are different possibilities of modelling the particle flux between cells. Here, we have presented one variant based on the decomposition of the particle flux into advection and diffusion [10]. Thanks to a Poisson transform, we can simulate the probability distribution of the particle activity in a continuous probably space (referred to the  $a$ -space above) and obtain results that should be valid independently of the cell size. The drawback of this formulation is the difficulty to get the back-transformation of the particle activity probability. So, for the moment, we can calculate the moments of the number of moving particles  $N$  (or particle activity  $\gamma$ ), but the full probability distribution (in the physical space) is more difficult to calculate.

Another possibility is to use a system-size expansion of the discrete probabilities [7]. In that case, the governing equation of the particle activity can be approximated as a Fokker-Planck equation (but directly in the physical space contrary to the previous formulation). The advantage is that the formalism is simpler, with no recourse to transform. The disadvantage is that this approximation holds true only for sufficiently large cell sizes.

## 5.2 Water Flow

A one-dimensional, cross-sectional-averaged Saint-Venant model has been adopted in order to analyse the hydraulics of a mountain river (La Navisence, Swiss Alps) at moderate water flow discharges in which bed load transport is weak.

The detailed study of circadian variations of the water discharge has shown that the flow regime is quasi-steady to leading order. The propagation of an arbitrary discharge wave along the river can be readily computed from the one-dimensional wave equation 31 in which the wave speed  $c$  is fixed by the bed roughness or grain size  $d_{85}$  and by the main channel geometry.

Strikingly, the thorough analysis of the steady state solution to the cross-sectionally averaged Saint-Venant equations 23-30 for a wide range of water flow discharges have proven the existence of Froude similarity in the flow processes. This feature is of paramount importance to the subsequent developments as it allows us to reconstruct the hydraulic conditions in a river section at any state  $Q$  by simply solving an algebraical system of equations, given by 35-36, where the input parameters are the channel bathymetry and the Froude number  $Fr^*$  (or  $Fr_{1d}^*$ ) at some discharge  $Q^*$ . The Froude number can be measured experimentally or computed from numerical simulations.

The value of the Froude number depends greatly on the definition used: it can be computed using the cross-section ( $Fr$ ) or the flow variables along the thalweg ( $Fr_{1d}$ ). As shown by 16, the differences between  $Fr$  and  $Fr_{1d}$  result from the channel geometry influence on the fluvial hydraulics since local head variations  $S_g$  are of the same order of magnitude as the bed slope  $S_0$ , as shown by 15.

## Acknowledgment

The work summarized here was supported by the Swiss National Science Foundation under grants No. 200021-129538 (a project called “The Stochastic Torrent: stochastic model for bed load transport on steep slope”) and No. 200021-105193/1 (a project called “Transient free-surface flows of concentrated suspensions—Application to geophysical flows,” funded by an R’Equip grant). P.B. thanks CEACTierra (University of Jaén) for partial financial support. The project is part of a longer programme spanning several years and which has benefited from feedback and many discussions. We are indebted to our colleagues Eric Travaglini from CREALP (Sion, Switzerland), Prof. Anthony Davison (EPFL), and Dr. Philippe Frey (IRSTEA, France). Most of the data presented here was obtained by Tobias Böhm during his thesis.

## References

- [1] V. Koulinski, *Étude de la formation d’un lit torrentiel par confrontation d’essais sur modèle réduit et d’observations sur le terrain*. Ph.D. Thesis, Grenoble, 1993.
- [2] H. A. Einstein, “The bed-load function for sediment transportation in open channel flows,” Technical Report No. 1026, United States Department of Agriculture, 1950.
- [3] R. A. Bagnold, “An approach to the sediment transport problem from general physics,” professional paper 422-I, United States Geological Survey, 1966.
- [4] F. Comiti and L. Mao, “Recent advances in the dynamics of steep channels,” in *Gravel-bed rivers: Processes, tools, environments* (M. Church, P. M. Baron, and A. G. Roy, eds.), pp. 351–377, 2012.
- [5] G. K. Gilbert and E. C. Murphy, “The transportation of debris by running water,” US Government Printing Office, 1914.
- [6] M. P. du Boys, “Etudes du régime du Rhône et de l’action exercée par les eaux sur un lit à fond de graviers indéfiniment affouillable,” *Annales des Ponts et Chaussées*, Série 5, No. 18, pp. 141–95, 1879.
- [7] C. Ancey, “Stochastic approximation of the Exner equation under lower-regime conditions,” *J. Geophys. Res.*, vol. 115, p. F00A11, 2010.
- [8] F. Ballio, V. Nikora, and S. E. Coleman, “On the definition of solid discharge in hydro-environment research and applications,” *J. Hydraul. Res.*, vol. 52, pp. 173–184, 2014.
- [9] C. Ancey, A. C. Davison, T. Böhm, M. Jodeau, and P. Frey, “Entrainment and motion of coarse particles in a shallow water stream down a steep slope,” *J. Fluid Mech.*, vol. 595, pp. 83–114, 2008.
- [10] C. Ancey and J. Heyman, “A microstructural approach to bed load transport: mean behaviour and fluctuations of particle transport rates,” *J. Fluid Mech.*, vol. 744, pp. 129–168, 2014.
- [11] S. A. Schumm, *River Variability and Complexity*. Cambridge: Cambridge University Press, 2005.

- [12] M. Church, “Bed material transport and the morphology of alluvial river channels,” *Annu. Rev. Earth. Planet. Sci.*, vol. 34, pp. 325–354, 2006.
- [13] S. E. Coleman and V. I. Nikora, “Fluvial dunes: initiation, characterization, flow structure,” *Earth Surf. Process. Landforms*, vol. 36, pp. 39–57, 2011.
- [14] D. Rickenmann, “Hyperconcentrated flow and sediment transport at steep slopes,” *J. Hydraul. Eng.*, vol. 117, pp. 1419–1439, 1992.
- [15] G. Seminara, “Fluvial sedimentary patterns,” *Annu. Rev. Fluid Mech.*, vol. 42, pp. 43–66, 2010.
- [16] M. Colombini and A. Stocchino, “Ripple and dune formation in rivers,” *J. Fluid Mech.*, vol. 673, pp. 121–131, 2011.
- [17] Y. Niño, A. Atala, M. Barahona, and D. Aracena, “Discrete particle model for analyzing bed form development,” *J. Hydraul. Eng.*, vol. 128, pp. 381–389, 2002.
- [18] F. Sagués, J. M. Sancho, and J. García-Ojalvo, “Spatiotemporal order out of noise,” *Rev. Mod. Phys.*, vol. 79, pp. 829–882, 2007.
- [19] D. Jerolmack and D. Mohrig, “A unified model for subaqueous bed form dynamics,” *Water Resour. Res.*, vol. 41, W12421, 2005.
- [20] Y. Shimizu, S. Giri, S. Yamaguchi, and J. Nelson, “Numerical simulation of dune-flat bed transition and stage-discharge relationship with hysteresis effect,” *Water Resour. Res.*, vol. 45, W04429, 2009.
- [21] R. A. Kuhnle and J. B. Southard, “Bed load transport fluctuations in a gravel bed laboratory channel,” *Water Resour. Res.*, vol. 24, pp. 247–260, 1988.
- [22] B. Gomez, R. L. Naff, and D. W. Hubbell, “Temporal variations in bed load transport rates associated with the migration of bed forms,” *Earth Surf. Process. Landforms*, vol. 14, pp. 135–156, 1989.
- [23] T. B. Hoey, “Temporal variations in bed load transport rates and sediment storage in gravel-bed rivers,” *Prog. Phys. Geog.*, vol. 16, pp. 319–338, 1992.
- [24] M. Esfeld, *Holism in Philosophy of Mind and Philosophy of Physics*, vol. 298. Springer, 2001.
- [25] B. C. Eaton and M. A. Hassan, “Scale-dependent interactions between wood and channel dynamics: Modeling jam formation and sediment storage in gravel-bed streams,” *J. Geophys. Res.*, vol. 118, pp. 2500–2508, 2013.
- [26] M. Tal and C. Paola, “Dynamic single-thread channels maintained by the interaction of flow and vegetation,” *Geology*, vol. 35, pp. 347–350, 2007.
- [27] M. H. García, “Sediment transport and morphodynamics,” in *Sedimentation Engineering* (M. H. García, ed.), vol. ASCE Manuals and Reports on Engineering Practice 110, pp. 21–164, Reston: American Society of Civil Engineers, 2007.
- [28] C. Parés, “Numerical methods for nonconservative hyperbolic systems: a theoretical framework,” *SIAM J. Numer. Anal.*, vol. 44, pp. 300–321, 2006.
- [29] G. Fasolato, P. Ronco, E. J. Langendoen, and G. Di Silvio, “Validity of uniform flow hypothesis in one-dimensional morphodynamic models,” *J. Hydraul. Eng.*, vol. 137, pp. 183–195, 2011.
- [30] C. Paola and V. R. Voller, “A generalized Exner equation for sediment mass balance,” *J. Geophys. Res.*, vol. 110, F04014, 2005.
- [31] D. J. Furbish, P. K. Haff, J. C. Roseberry, and M. W. Schmeeckle, “A probabilistic description of the bed load sediment flux: 1. Theory,” *J. Geophys. Res.*, vol. 117, F03031, 2012.
- [32] A. Recking, P. Frey, A. Paquier, P. Belleudy, and J. Y. Champagne, “Feedback between bed load transport and flow resistance in gravel and cobble bed rivers,” *Water Resour. Res.*, vol. 44, W05412, 2008.
- [33] D. T. Gillespie, *Markov Processes: An Introduction for Physical Scientists*. San Diego: Academic Press, 1992.
- [34] C. W. Gardiner, *Handbook of Stochastic Methods*. Berlin: Springer Verlag, 1983.
- [35] J. C. Cox, J. E. Ingersoll, and S. A. Ross, “A theory of the term structure of interest rates,” *Econometrica*, vol. 53, pp. 385–407, 1985.
- [36] S. M. Iacus, *Simulation and Inference for Stochastic Differential Equations*. New York: Springer, 2008.
- [37] E. Lajeunesse, L. Malverti, and F. Charru, “Bed load transport in turbulent flow at the grain scale: Experiments and modeling,” *J. Geophys. Res.*, vol. 115, F04001, 2010.
- [38] R. L. Martin, D. J. Jerolmack, and R. Schumer, “The physical basis for anomalous diffusion in bed load transport,” *J. Geophys. Res.*, vol. 117, F01018, 2012.
- [39] D. J. Furbish and M. W. Schmeeckle, “A probabilistic derivation of the exponential-like distribution of bed load particle velocities,” *Water Resour. Res.*, vol. 49, pp. 1537–1551, 2013.
- [40] N. Fan, D. Zhong, B. Wu, E. Foufoula-Georgiou, and M. Guala, “A mechanistic-stochastic formulation of bed load particle motions: From individual particle forces to the Fokker-Planck equation under low transport rates,” *J. Geophys. Res.: Earth Surface*, vol. 119, pp. 464–482, 2014.
- [41] J. C. Roseberry, M. W. Schmeeckle, and D. J. Furbish, “A probabilistic description of the bed load sediment flux: 2. Particle activity and motions,” *J. Geophys. Res.*, vol. 117, F03032, 2012.
- [42] A. Hamamori, “A theoretical investigation on the fluctuations of bed load transport,” Tech. Rep. Report R4, Delft Hydraulics Laboratory, 1962.
- [43] J. M. Turowski, “Probability distributions of bed load transport rates: A new derivation and comparison with field data,” *Water Resour. Res.*, vol. 46, W08501, 2010.
- [44] A. Radice, “Use of the Lorenz curve to quantify statistical nonuniformity of sediment transport rate,” *J. Hydraul. Eng.*, vol. 135, pp. 320–326, 2009.

- [45] A. Singh, K. Fienberg, D. J. Jerolmack, J. Marr, and E. Foufoula-Georgiou, “Experimental evidence for statistical scaling and intermittency in sediment transport rates,” *J. Geophys. Res.*, vol. 114, doi: 2007JF000963, 2009.
- [46] G. Parker, C. Paola, and S. Leclair, “Probabilistic Exner sediment continuity equation for mixtures with no active layer,” *J. Hydraul. Eng.*, vol. 126, pp. 818–826, 2000.
- [47] Z. Cao, R. Day, and S. Egashira, “Coupled and decoupled numerical modeling of flow and morphological evolution in alluvial rivers,” *J. Hydraul. Eng.*, vol. 128, pp. 306–321, 2002.
- [48] Y. Cui, G. Parker, T. E. Lisle, J. E. Pizzuto, and A. M. Dodd, “More on the evolution of bed material waves in alluvial rivers,” *Earth Surf. Process. Landforms*, vol. 30, pp. 107–114, 2005.
- [49] R. Hoyle, *Pattern Formation*. Cambridge: Cambridge University Press, 2006.
- [50] J. A. Cunge, F. M. Holly, and A. Verwey, *Practical aspects of computational river hydraulics*. Pitman: London, UK, 1980.
- [51] P. Bohorquez and S. E. Darby, “The use of one- and two-dimensional hydraulic modelling to reconstruct a glacial outburst flood in a steep Alpine valley,” *J. Hydrol.*, vol. 361, pp. 240–261, 2008.
- [52] D. L. Rosgen, “A classification of natural rivers,” *Catena*, vol. 22, pp. 169–199, 1994.
- [53] R. I. Ferguson, “Flow resistance equations for gravel- and boulder-bed streams,” *Water Resour. Res.*, vol. 43, W05427, 2007.
- [54] D. Rickenmann and A. Recking, “Evaluation of flow resistance in gravel-bed rivers through a large field data set,” *Water Resour. Res.*, vol. 47, W07538, 2011.
- [55] C. F. Colebrook and C. M. White, “Experiments with fluid friction in roughened pipes,” *Proc. R. Soc. London ser. A*, vol. 161, No. 906, pp. 367–381, 1937.
- [56] M. J. Lighthill and G. B. Whitham, “On kinematic waves. I. Flood movement in long rivers,” *Proc. R. Soc. London ser. A*, vol. 229, pp. 281–316, 1955.
- [57] K. Bunte and S. Abt, “Effect of sampling time on measured gravel bed load transport rates in a coarse-bedded stream,” *Water Resour. Res.*, vol. 41, W11405, 2005.
- [58] A. Recking, F. Liébault, C. Peteuil, and T. Jolimet, “Testing bed load transport equations with consideration of time scales,” *Earth Surf. Process. Landforms*, vol. 37, pp. 774–789, 2012.

# EXPERIMENTS ON THE EROSION RATE IN A MIXTURE OF INCOHERENT AND COHESIVE SEDIMENTS

R. Gaudio and F. Calomino

*Dipartimento di Ingegneria Civile, Università della Calabria, Ponte P. Bucci, Cubo 42B,  
Rende (CS), Italy, gaudio@unical.it, francesco.calomino@unical.it*

## Abstract

The erosion of mixtures of cohesive and incoherent sediments still constitutes an open problem. Many variables affect the erosion rate and, therefore, mathematical modeling is quite difficult, so that experimental evidence is necessary. Original laboratory results are presented and commented on for a mixture of sand, silt and a small amount of clay. The eroded surfaces were acquired with a 3D Laser Scanner and the time evolutions of the eroded volume and the cumulated volumetric erosion rate were studied, showing different kinds of behavior. The influence of bed slope and discharge was also observed.

## Keywords:

erosion, cohesive sediments, mixtures, erosion rate.

## 1 Introduction

### 1.1 Forces Acting in Cohesive Beds

Despite the great number of studies on fluvial erosion of cohesive beds, scientific knowledge on the subject is still not satisfactory, especially about mixtures of cohesive and incoherent sediments (hereafter mixtures). As detailed by Greco *et al.* (2010) [1], a deep comprehension of the factors influencing erosion is not achieved, nor complete models are available for the prediction of local scour depths, erosion rates and sediment discharges. The use of models deduced for incoherent sediments generally leads to uneconomical overestimations in the case of cohesive beds or mixtures. In cohesive beds, resistance is due not only to gravitational forces, but also to cohesive forces, which are forces acting on the particle surfaces, having physical-chemical, organic and biological origin. The erosion phenomenon presents an increasing complexity when the mobile bed is a mixture with a given percentage of cohesive sediment. Two sediment particles with size less than a few tens of  $\mu\text{m}$  experience a series of attractive and repulsive surface forces when immersed in an aqueous solution at a certain mutual distance. The origin of these forces is due to the presence of some chemical processes which allow the occurrence of electrostatic forces [2] [3] [4] [5] [6] [7] [8]. The force entity depends on certain physical-chemical characteristics of the sediment particles and of the solution and reduce with distance. Repulsive forces include the electric double layer forces, the forces of repulsion between two bodies with the same charge (Born's forces) and the forces of hydration; attractive forces include the van der Waals forces and the Coulomb force (for details, see, e.g., [9] [10] [2] [4]). Repulsive forces become negligible when the separation distance is greater than some tens of Å.

The total force acting on a particle can be computed with a volume integral. For silt and large size clay, the spherical shape can be considered as a first approximation, using shape coefficients as corrective factors. In this case, the intensity of repulsive actions is generally negligible with respect to the van der Waals force, which constitutes practically the unique contribution to cohesion forces. For clays with size not greater than a few  $\mu\text{m}$ , Mahmood *et al.* (2001) [3] showed that the real particle shape is to be considered, proposing some relationships for the assessments of repulsive forces in phyllosilicates of a flat hexagonal shape and thickness less than  $0.2 \mu\text{m}$ . In the case of sediment layers, the cohesive action depends also on the texture and structure of the bed; hence, the intensity of the cohesive forces is expressed as a function of the bulk density, the water content and the Atterberg limits. In the mixtures, cohesion is produced by the fine sediment fraction around the incoherent particles (which are described only with their density and grain size distribution curve). Winterwerp *et al.* (1990) [11] and Berlamont *et al.* (1993) [12] provided a list of 28 parameters influencing cohesion, among which the following relate to mixtures: percentage of the different sediment fractions; mean or median diameter of fine fraction, incoherent fraction and mixture; threshold value of the fraction of fine of coarse material, beyond which the cohesive forces are not negligible; optimal fraction of fine of coarse material at which resistance to erosion attains its maximum value; density of the incoherent fraction. For mixtures, van Rijn (2007) [13] proposes the classifications of Table 1.

In the classification by van Ledden *et al.* (2004) [14] also the water content is taken into account. Experimentally, the Authors observed the effects of cohesion for percentages by weight of clay not less than 7.5%, *ceteris paribus*. The above classifications are difficult to generalize, owing to the fact that they were deduced from specific experimental evidence.

### 1.2 Critical Shear Stress

Mehta *et al.* (1989) [15] identified three modalities of erosion: 1) surface erosion; 2) mass erosion; 3) fluidization. In the first type, single particles of little flocs are eroded, whereas in the second type masses larger than flocs are removed, with shear stresses greater than in the previous case. In the third type, solid material not completely deposited on the bed is transported by flow. With reference to first two erosion modalities, two threshold (or critical) values of the shear stress can be considered:  $\tau_s$  for surface erosion and  $\tau_m$  for mass erosion. Hence, surface erosion occurs for  $\tau_s < \tau < \tau_m$  (where  $\tau$  is the actual shear stress), whereas mass erosion for  $\tau > \tau_m$ . In dense beds, often the critical value is:  $\tau_c \equiv \tau_s < \tau_m$ ; in soft beds, on the contrary,  $\tau_c \equiv \tau_m$ . The direct observation of the critical condition of cohesive sediment

Table 1: Classification of mixture (from van Rijn, 2007 [13])

Mixture	Percentage of organic material (%)	Percentage of clay and fine silt (< 8 $\mu\text{m}$ ) (%)	Percentage of silt (8 $\div$ 62 $\mu\text{m}$ ) (%)	Percentage of sand (62 $\mu\text{m}$ $\div$ 2 mm) (%)
Muddy sand (slightly cohesive)	0 $\div$ 10	0 $\div$ 5	20 $\div$ 40	60 $\div$ 80
Sandy mud	0 $\div$ 10	5 $\div$ 10	30 $\div$ 60	60 $\div$ 30
Mud	0 $\div$ 20	10 $\div$ 20	50 $\div$ 70	0 $\div$ 10
Silty mud	0 $\div$ 20	10 $\div$ 40	60 $\div$ 80	0
Clayey mud	0 $\div$ 20	40 $\div$ 60	40 $\div$ 60	0

motion was firstly performed by many authors [16] [17] [18] [19] [20] [21]. Partheniades (1965) [22] related the amount of eroded material to  $\tau$  under steady flow conditions and obtained  $\tau_c$  through an extrapolation (as the value of  $\tau$  at which erosion is zero). Arulanandan (1975) [23] analyzed the influence of Cation Exchange Capacity (CSC) and Sodium Adsorption Ratio (SAR). Ariathurai and Arulanandan (1978) [24] studied the effect of pH and temperature  $T$ , observing a decrease of  $\tau_c$  as  $T$  increased. Other Authors correlated  $\tau_c$  to the sediment density [25] [26] [27] [28] [29] [30]. Mehta and Lee (1994) [31] tried to extend the Shields (1936) [32] diagram to cohesive sediments. Parchure and Mehta (1985) [33] and Zreik *et al.* (1998) [34] studied the  $\tau_s$  distribution in stratified cohesive deposits. As to mixtures, many other parameters influence the resistance to erosion. Kamphuis and Hall (1983) [35] obtained a linear relationship between  $\tau_c$  and, respectively, the resistance to compression and shear of mixtures. According to Mitchener and Torfs (1996) [36] and Berlamont and Torfs (1996) [37], the introduction of silt and clay (in a percentage greater than 5 $\div$ 20 %) in a sand deposits acts as to increase the resistance to erosion, due to the space filling process. Panagiotopoulos *et al.* (1997) [38] observed an increase of  $\tau_c$  for percentages of fine material greater than 30%, with a percentage of clay of about 11%. De Sutter *et al.* (2000) [39] observed a maximum increase of  $\tau_c$  for percentages of clay between 20% and 30%, with a decrease for higher percentages. Lick *et al.* (2004) [40] proposed the following relationship to assess the critical value of the shear stress for surface erosion:

$$\tau_s = \left[ 1 + \frac{c}{\pi/6 \cdot (\rho_s - \rho) \cdot g \cdot d^2} \right] \cdot 414 \cdot d \quad (1)$$

where  $c$  is an empirical coefficient,  $\rho$  the water density,  $\rho_s$  the sediment grain density,  $g$  the gravitational acceleration and  $d$  the sediment diameter. Kothyari *et al.* (2006) [41] proposed an empirical relationship to assess  $\tau_c$  in mixtures of sand and clay, considering the influence of different parameters. Julian and Torres (2006) [42] expressed  $\tau_c$  as a function of the percentage of silt and clay. Righetti and Lucarelli (2007) [43] tried to determine  $\tau_c$  by extending the Shields (1936) [32] abacus to cohesive sediments. In the same year, van Rijn (2007) [13] proposed some formulae for the assessment of  $\tau_c$  as a function of the Shields critical shear stress. Mostafa *et al.* (2008) [44] adopted the dimensional analysis to find a relationship among  $\tau_c$  and different influencing factors, identifying an optimal water content at which  $\tau_c$  attained its maximum value. Kothyari and Jain (2008) [45] determined  $\tau_c$  in mixtures of fine sand (median diameter  $d_{50} = 0.23$  mm), fine gravel ( $d_{50} = 3.1$  mm) and clay ( $d_{50} = 3.9$   $\mu\text{m}$ ). The estimates of  $\tau_c$  obtained from all the

above formulations differ notably from each other, also for an order of magnitude, confirming that the problem of predicting the critical condition of sediment motion in cohesive sediments and mixtures is still open.

### 1.3 Erosion Rate

The assessment of the amount of eroded material is usually performed through the quantification of the erosion rate,  $E$ , defined as the mass or volume of eroded sediment per unit surface and time. It is determined in an area  $A_E$ , on which the shear stress  $\tau$  is spatially constant. The erosion rate is the average velocity with which erosion occurs and can be related directly to the average scour depth. In the literature, many expressions are available for the computation of the erosion rate as a function of the shear stress excess,  $\tau - \tau_c$ . Partheniades (1965) [22] adopted a model based on probabilistic considerations. Ariathurai (1974) [46] proposed the following relationship for uniform cohesive deposits:

$$E = M \cdot \tau^{a_1} \cdot \rho_{d,b}^{a_2} \quad (2)$$

where  $M$  is the constant of erosion, the dimensional structure of which varies with the type of mathematical relation adopted. According to Roberts *et al.* (1998) [30]:

$$E = M \cdot \frac{\tau - \tau_c}{\tau_c} \quad (3)$$

where the exponents  $a_1$  and  $a_2$  are depend on the sediment characteristics and  $\rho_{d,b}$  is the density in undrained conditions. The Authors carried out laboratory tests by varying medium diameter,  $d_m$ , and  $\rho_{d,b}$  (between 1650 and 1950 kg/m<sup>3</sup>), obtaining the values reported in Table 2.

The results show an evident increase of  $a_1$  and  $a_2$  as  $d_m$  increases, but do not allow any conclusion on the behavior of  $M$ . For  $d_m \geq 222$   $\mu\text{m}$ , the erosion rate does not depend on  $\rho_{d,b}$  ( $a_2 = 0$ ). For stratified cohesive deposits and surface erosion, Thorn and Parsons (1980) [25] considered the erosion rate as a function of depth,  $z$ , as follows:

$$E = M(z) \cdot [\tau - \tau_s(z)]^n \quad (4)$$

where  $n$  is an exponent, whereas Parchure and Mehta (1985) [33] derived:

$$\ln\left(\frac{E}{E_f}\right) = M \cdot [\tau - \tau_s(z)]^{1/2} \quad (5)$$

Table 2: Experimental values of the coefficient and the exponents of Eq. (3) (from Roberts *et al.*, 1998 [30])

$d_m$ ( $\mu\text{m}$ )	$a_1$	$a_2$	$M$ $\left( \frac{\text{cm/s}}{Pa^{a_1} \cdot (g/\text{cm}^3)^{a_2}} \right)$
5.7	1.90	-29.0	$3.28 \cdot 10^3$
14.8	2.27	-27.4	$2.68 \cdot 10^4$
18.3	2.31	-25.6	$1.49 \cdot 10^4$
48	2.23	-23.8	$8.27 \cdot 10^3$
75	2.10	-22.3	$4.70 \cdot 10^3$
125	2.82	-20.6	$4.23 \cdot 10^3$
222	3.32	0	$1.25 \cdot 10^{-2}$
432	2.56	0	$2.25 \cdot 10^{-2}$
1020	2.51	0	$1.14 \cdot 10^{-2}$
1350	2.92	0	$6.74 \cdot 10^{-3}$

where  $E_f$  is the floc erosion rate referred to the amount of surface solid material removed in incipient motion condition ( $\tau = \tau_s$ ). Sandford and Maa (2001) [47] developed a unifying semi-empirical model, valid for both uniform and stratified deposits, which describes the evolution of the erosion rate over time,  $t$ , as follows:

$$E = M[z(t)] \cdot \beta \cdot (\tau - \tau_c) \cdot \exp[-\beta \cdot \xi \cdot (\tau - \tau_0)] \quad (6)$$

where  $\beta$  is a coefficient constant over time and space,  $\xi$  the gradient of the function  $\tau_s(z)$  and  $\tau_0$  the initial time instant. According to Aberle *et al.* (2004 and 2006) [48] [49] and Debnath *et al.* (2007) [50], on the contrary, parameter  $\beta$  of Eq. (6) varies as the local density varies. The attempt, highly diffused in the literature, to include all the factors which influence cohesion in the only parameter represented by the constant of erosion leads to results often in contrast to each other and of difficult physical interpretation. In addition, in the experimental determination of  $M$  the erosion is assumed to be uniform and is characterized with  $E$ . As discussed above, the knowledge on the erosion rate is not satisfactory yet; in particular about its time evolution. Hence, in the next sections, original laboratory results on the erosion rate of a mixture are presented and commented on.

## 2 Experiment

### 2.1 Installation

Experiments were carried out in the *Laboratorio di Grandi Modelli Idraulici, Università della Calabria*, Italy [51]. A 10 m-long, 48.5 cm-wide, 50 cm-high tilting flume with rectangular cross-section was used. The right and left wall were made of glass and PVC, respectively. A PVC false floor was mounted 30 cm above the flume bottom, in order to create a sediment recess box in which the mixture was positioned. The box with the mobile bed started 6 m downstream of the flume inlet and was 50 cm long and as wide as the cross-section. Sand with median diameter of 1 mm was glued on the top face of the PVC false floor, both upstream to and downstream of the recess box, in order to make the fixed bed as rough as the mobile one. A tailgate was set at the flume outlet to regulate the flow depth, which was measured with a  $\pm 0.1$  mm-accurate digital point gauge, mounted on a gantry moving on rails installed on the flume walls. The eroded surface of the mobile bed was acquired with a

3D Laser Scanner (model Vivid 300/VI-300, produced by Minolta) mounted on another gantry. Discharge was measured with a Thomson weir mounted in an outlet metallic caisson.

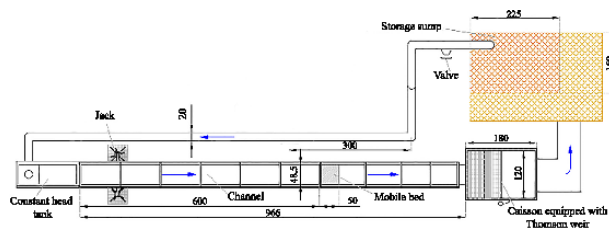


Figure 1: Plan view of the laboratory installation (unit:cm)

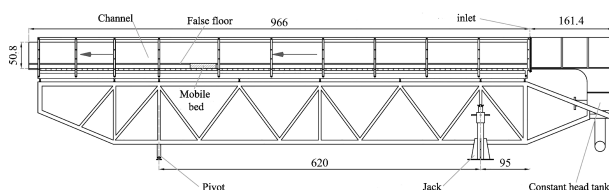


Figure 2: Side view of the laboratory installation (unit:cm)

The 3D Laser Scanner works in the range of distances from 0.55 to 1.2 m with respect to its base. The acquisition area is square, with side size varying from 185 mm (at the minimum distance) and 395 mm (at the maximum distance). The maximum measurable depth is 395 mm. The accuracy ranges from 0.95 mm (at the minimum distance) and 1.91 mm (at the maximum distance) along the  $x$ -streamwise and  $y$ -spanwise axes, whereas it varies from 0.45 mm to 1 mm along the  $z$ -axis orthogonal to the bed. The number of points acquired ranges from about 20000 (at the minimum distance) to 400 (at the maximum distance). The data elaboration was performed with the software Polygon Editing Tool. In the experiments, the following parameters were selected: distance of 70 cm; side size of the square area of 23.5 cm; accuracy in  $x$  and  $y$  directions of 1.2 mm; accuracy in  $z$  direction of 0.6 mm; number of points acquired 15500. The mixture was made of sand, silt and clay. The grain size distribution curves are shown in Figures 3, 4 and 5 for the sand, the fine material and the mixture, respectively. The mixture had median diameter  $d_{50}=0.35$  mm; the diameter for which 90% of the material was finer was  $d_{90}=1.5$  mm.

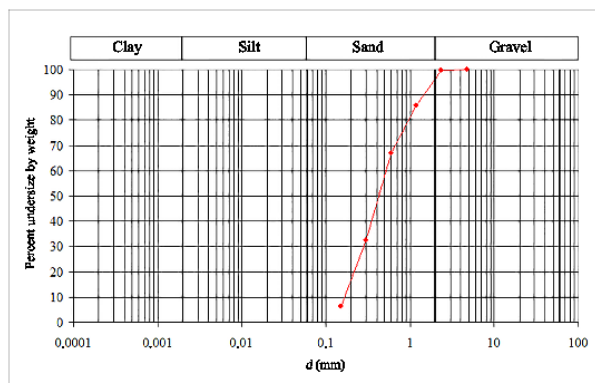


Figure 3: Grain size distribution curve of the sand used in the tests

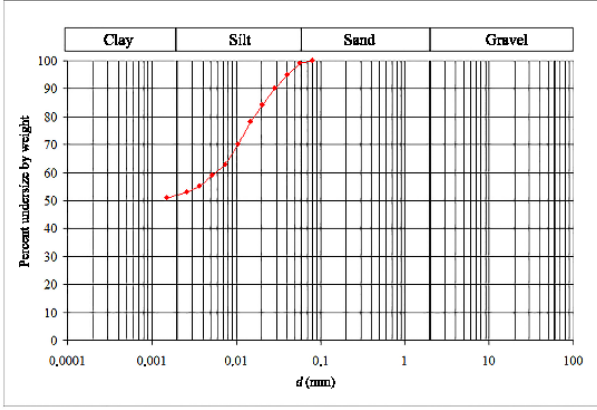


Figure 4: Grain size distribution curve of the fine material used in the tests

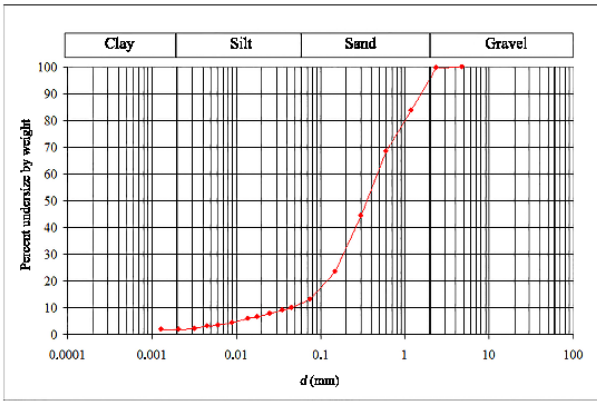


Figure 5: Grain size distribution curve of the mixture used in the tests

## 2.2 Tests

Two series of tests were carried out (Table 3): series A, with longitudinal bed slope  $S_0=0.5\%$ , and series B, with  $S_0=5\%$ . In the first series, four values of the average discharge over time,  $Q$ , were considered, whereas in the second series two values. Many test durations,  $t$ , were investigated for each discharge, in order to study the time evolution of erosion. Table 3 shows also the average flow depth over time,  $h$ , for each one of the 31 runs.

Before starting a run, the flume was slowly fed with a submerged pump; the tailgate was raised up, in order to reach an hydrostatic condition with a flow depth of 5 cm. The mixture was then kept in this condition (under water) for 1 h and was saturated. After that, the mobile bed surface was flattened, in continuity with the upstream and downstream fixed beds. The origin of the spatial reference system ( $x, y, z$ ) was conventionally positioned in the middle of the initial cross-section of the mobile bed (Figure 6).

For each test, the following variables were computed (see, e.g., Table 4 for test A1): the ratio  $B/h$ , the wetted area,  $A$ , the hydraulic radius,  $R$ , the mean flow velocity,  $V=Q/A$ , the Strickler coefficient,  $k_s = V/(R^{2/3}S_0^{1/2})$ , the Froude number,  $F_r = V/(gh)^{1/2}$ , the Reynolds number,  $Re=4VR/\nu$  ( $\nu=1.31\cdot 10^{-6} \text{ m}^2/\text{s}$  being the water kinematic viscosity at temperature  $T=10^\circ\text{C}$ ), the shear velocity,  $u_*=(gRS_0)^{1/2}$ , the shear Reynolds number,  $Re^*=u_*d_{90}/\nu$ , the average shear stress,  $\tau=\rho u_*^2$ , and the bed shear stress,  $\tau_b$ , obtained with the well-known Vanoni and Brooks (1957) side wall correction procedure.

Table 3: Characteristics of the tests

Dataset	Slope $S_0$ (‰)	Discharge $Q$ (l/s)	Duration $t$ (h)	Flow depth $h$ (mm)				
A	A1	0.5	12.7	1	65			
				2	65			
				4	65			
				8	64			
				10	64			
				12	64			
	A2	0.5	24.5	1	106			
				2	107			
				4	109			
				8	110			
				A3	0.5	17.0	1	96
							2	90.3
4	71.6							
8	74.6							
12	66							
A4	0.5	40.1	1				143	
			2	142				
			4	143				
			8	143				
			12	143				
			B	B1	5	25.1	1	86
2	84.52							
8	88.08							
15	90.93							
B2	5	40.1		1	112			
				2	117.3			
				4	119.4			
				8	125.4			
				12	125.4			
				18	129.7			

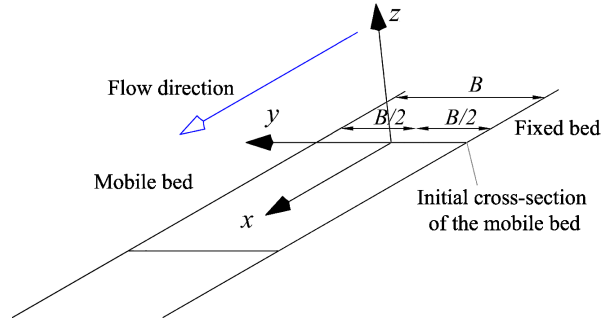


Figure 6: Cartesian coordinate system

The results showed that the flume behaved as “narrow” ( $B/h<3.5$ ) only in test A4; the flow was always subcritical ( $F_r<1$ ); the flow was transitional turbulent ( $4<Re_*<70$ ) except in the runs of test B2 in which it was fully turbulent.

## 3 Results

### 3.1 3D Eroded Surfaces

The datasets acquired with the 3D Laser Scanner were analyzed with a step of 0.5 mm in the  $x$  and  $y$  directions in a square window of side size 30 cm centred in the mobile bed. As examples, Figures 7 to 11 show the 3D eroded surface for all the runs of test A4, whereas Figures 12 to 15 for all the runs of test B1.

The 3D eroded surfaces show that the erosion process in the mixture is strongly three-dimensional; therefore, the centreline profile cannot be representative of the scouring process, since it is different from the lateral profiles. The scour depths increase over time, as expected.

Table 4: Hydraulic variables and results of the separation method (test A1)

$t$	(h)	1	2	4	8	10	12	15
$Q$	( $m^3/s$ )	0.0126	0.0127	0.0127	0.0126	0.0131	0.0129	0.0127
$h$	(m)	0.0653	0.0656	0.0659	0.0645	0.0645	0.0643	0.0719
$B/h$		7.4	7.4	7.4	7.5	7.5	7.5	6.7
$A$	( $m^2$ )	0.032	0.032	0.032	0.031	0.031	0.031	0.035
$R$	(m)	0.051	0.052	0.052	0.051	0.051	0.051	0.055
$V$	(m/s)	0.40	0.40	0.40	0.40	0.42	0.41	0.36
$k_s$	( $m^{1/3}/s$ )	129	129	128	131	136	135	112
$u_*$	(m/s)	0.0159	0.0159	0.0159	0.0158	0.0158	0.0158	0.0165
$Re$		$6.3 \cdot 10^4$	$6.3 \cdot 10^4$	$6.3 \cdot 10^4$	$6.3 \cdot 10^4$	$6.5 \cdot 10^4$	$6.4 \cdot 10^4$	$6.2 \cdot 10^4$
$Re_*$		18.22	18.26	18.29	18.14	18.14	18.12	18.93
$F_\tau$		0.50	0.50	0.50	0.51	0.53	0.52	0.43
$\tau$	(Pa)	0.252	0.253	0.254	0.250	0.250	0.249	0.272
$\tau_b$	(Pa)	0.307	0.308	0.310	0.303	0.302	0.301	0.340

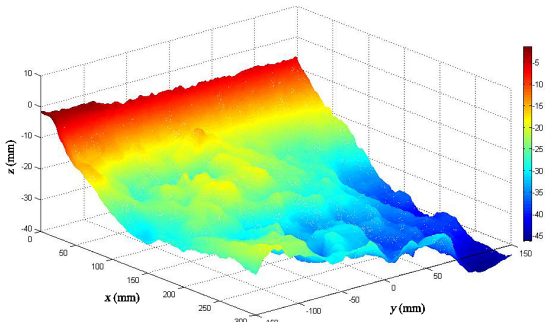


Figure 7: 3D eroded surface (test A4,  $t = 1$  h)

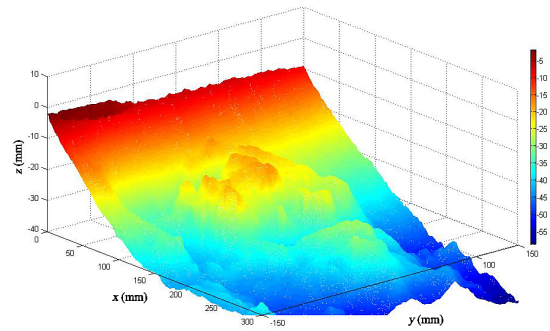


Figure 10: 3D eroded surface (test A4,  $t = 8$  h)

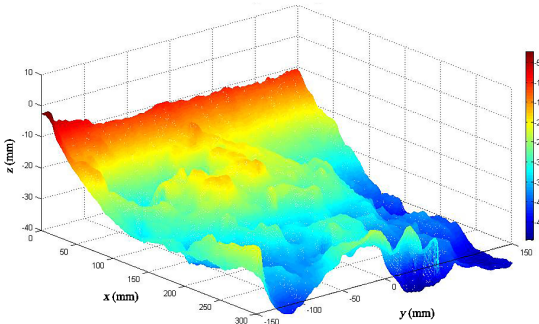


Figure 8: 3D eroded surface (test A4,  $t = 2$  h)

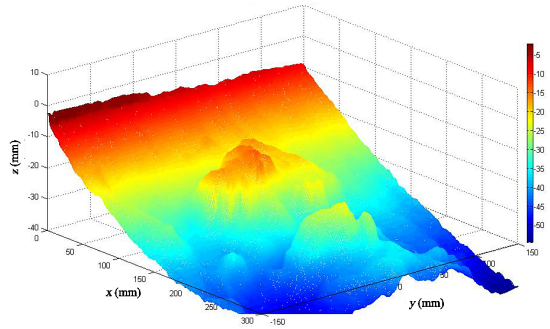


Figure 11: 3D eroded surface (test A4,  $t = 12$  h)

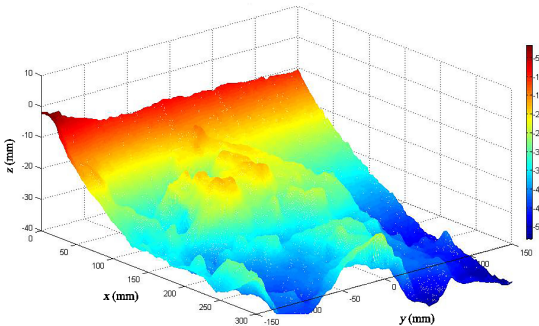


Figure 9: 3D eroded surface (test A4,  $t = 4$  h)

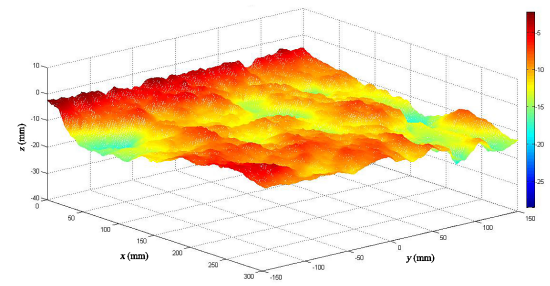


Figure 12: 3D eroded surface (test B1,  $t = 1$  h)

### 3.2 Eroded Cross-Sections and Longitudinal Profiles

The mean elevations,  $z_m$ , of the eroded surfaces were determined in discrete cross-sections with step  $\Delta x=0.5$  mm, as follows:

$$z_m(x) = \frac{\sum_{i=1}^{N_y} z(x, y_i)}{N_y} \quad (7)$$

where  $N_y$  is the number of points acquired in the cross-section at the abscissa  $x$ . Assuming  $z_0=0$  as the elevation of the initial mobile bed, the mean scour depth in the cross-section at the abscissa  $x$ ,  $d_{sm}$ , was obtained as follows:

$$d_{sm}(x) = z_0 - z_m(x) \quad (8)$$

It was used to describe to mean longitudinal profiles, whereas the maximum longitudinal profiles were computed according to the following formula:

$$d_{smax}(x) = \left| \min_{i=1}^{N_y} \{z(x, y_i)\} \right| \quad (9)$$

As examples, Figures 16 to 19 show respectively an eroded cross-section at a given time with the mean elevation line, the time evolution of an eroded cross-section, the time evolution of the mean longitudinal profiles and the time evolution of the maximum longitudinal profiles in test A1.

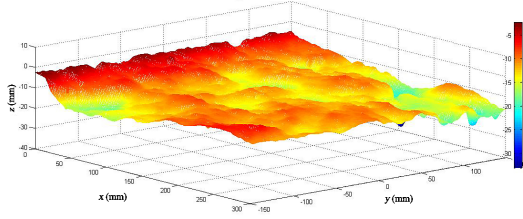


Figure 13: 3D eroded surface (test B1,  $t = 2$  h)

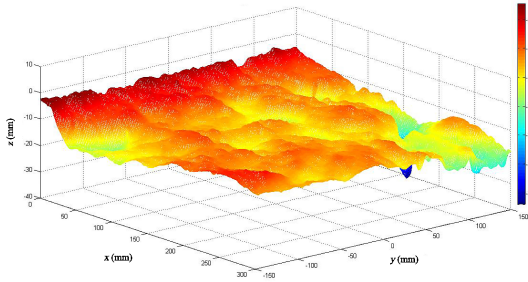


Figure 14: 3D eroded surface (test B1,  $t = 8$  h)

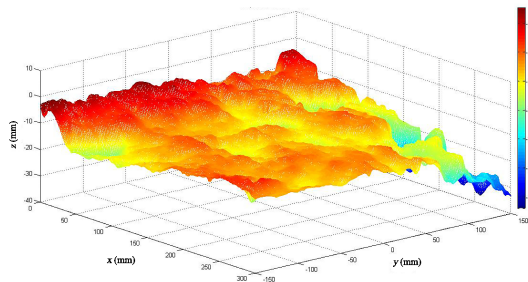


Figure 15: 3D eroded surface (test B1,  $t = 15$  h)

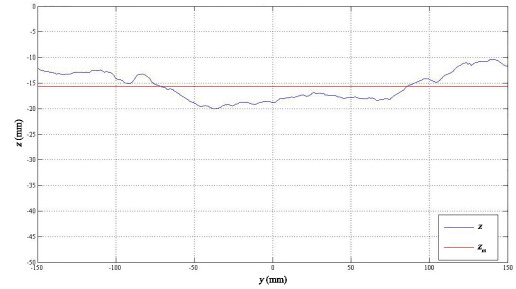


Figure 16: Eroded cross-section at  $x = 200$  mm (test A1,  $t = 1$  h)

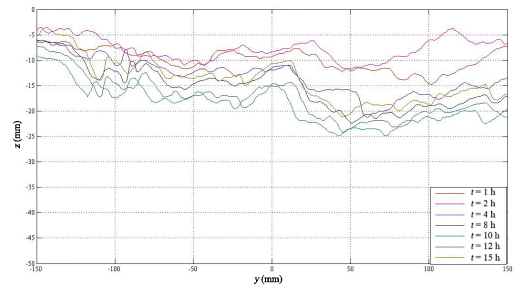


Figure 17: Time evolution of the eroded cross-section at  $x = 100$  mm (test A1)

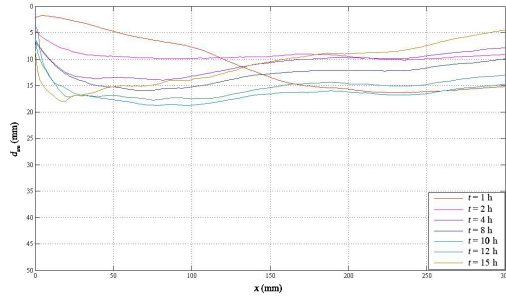


Figure 18: Time evolution of mean longitudinal profiles (test A1)

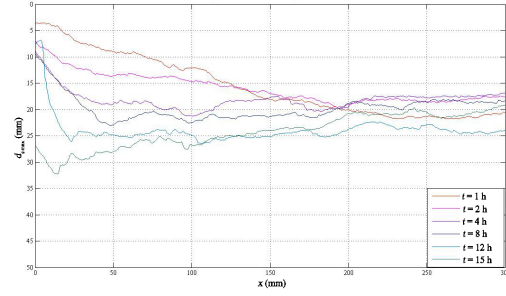


Figure 19: Time evolution of maximum longitudinal profiles (test A1)

### 3.3 Eroded Volumes and Erosion Rates

The volume at time  $t$  of the  $k^{th}$  discrete eroded element delimited at the top face with the plane  $z=0$  and below with a 3D surface of vertexes  $P_{i,j}$ ,  $P_{i+1,j}$ ,  $P_{i,j+1}$  and  $P_{i+1,j+1}$  is given by:

$$\Delta V_{E,k}(t) = \Delta x \cdot \Delta y \cdot \bar{z}_k(t) \quad (10)$$

where:

$$\bar{z}_k(t) = \frac{|z_{i,j}(t)| + |z_{i+1,j}(t)| + |z_{i,j+1}(t)| + |z_{i+1,j+1}(t)|}{4} \quad (11)$$

Hence, the eroded volume at time  $t$  is:

$$V_E(t) = \sum_{k=1}^{N_k} \Delta V_{E,k}(t) \quad (12)$$

where  $N_k$  is the number of elements in the acquired window.

The variation of eroded volume in the time interval  $\Delta t = t_i - t_{i-1}$  is:

$$\Delta V_E = V_E(t_i) - V_E(t_{i-1}) \quad (13)$$

The cumulated volumetric erosion rate,  $E_v(t)$ , is therefore:

$$E_v(t) = \frac{V_E(t)}{A_E \cdot t} \quad (14)$$

where  $A_E = 900 \text{ cm}^2$  is the area of acquisition window projected on the initial bed plane. The partial volumetric erosion rate,  $E_{v,p}(t_i)$ , is:

$$E_{v,p}(t_i) = \frac{\Delta V_E}{A_E \cdot \Delta t} \quad (15)$$

The average scour depth in the whole domain at time  $t$  is:

$$d_s(t) = \frac{V_E(t)}{A_E} \quad (16)$$

Tables 5 to 10 and Figures 20 to 24 show the results of the computations and the regression lines with the coefficients of determination,  $R^2$ .

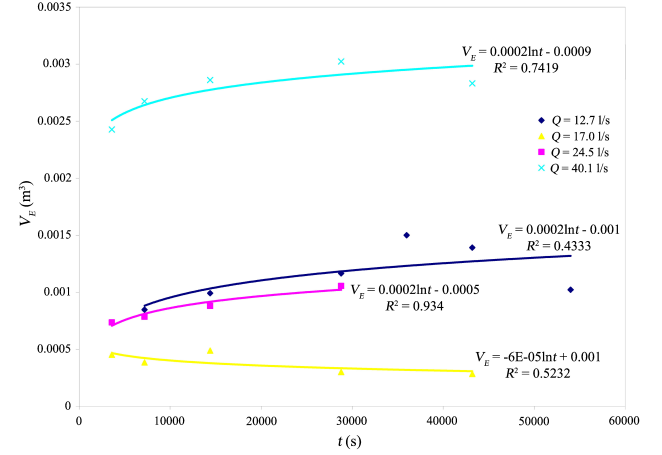


Figure 20: Time evolution of the eroded volumes (series A)

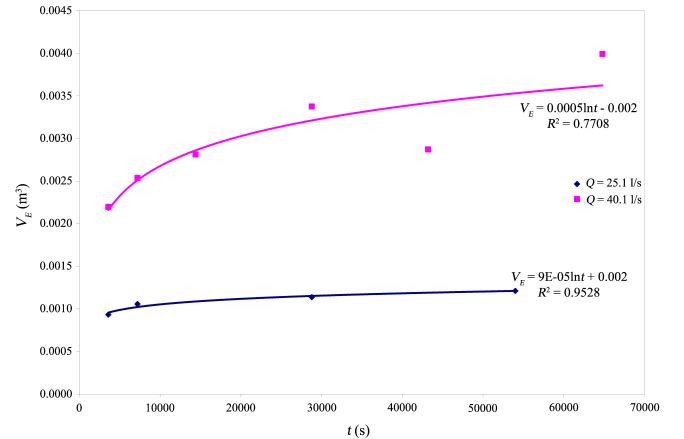


Figure 21: Time evolution of the eroded volumes (series B)

The results show that:

- the time evolution of the eroded volume has a logarithmic behavior;
- the time evolution of the partial volumetric erosion rate is not monotonic, owing to temporary phenomena of deposit;
- the time evolution of the cumulated volumetric erosion rate has a power law behavior;
- for a given slope, the cumulated volumetric erosion rate varies sensibly with the discharge;
- for a given discharge, the cumulated volumetric erosion rate does not vary sensibly with the bed slope.

Table 5: Eroded volume and erosion rate (test A1)

$t$ (h)	$\Delta t$ (h)	$V_E(t)$ ( $cm^3$ )	$\Delta V_E$ ( $cm^3$ )	$E_{v,p}(t)$ (m/s)	$E_v(t)$ (m/s)	$d_s(t)=V_E(t)/A_E$ (cm)
1	1	1000.9	1000.9	$3.1 \cdot 10^{-6}$	$3.1 \cdot 10^{-6}$	1.11
2	1	846.7	-154.2	$-4.8 \cdot 10^{-7}$	$1.3 \cdot 10^{-6}$	0.94
4	2	991.5	144.8	$2.2 \cdot 10^{-7}$	$7.7 \cdot 10^{-7}$	1.10
8	4	1164.7	173.2	$1.3 \cdot 10^{-7}$	$4.5 \cdot 10^{-7}$	1.29
10	2	1499.1	334.4	$5.2 \cdot 10^{-7}$	$4.6 \cdot 10^{-7}$	1.67
12	2	1391.0	-108.1	$-1.7 \cdot 10^{-7}$	$3.6 \cdot 10^{-7}$	1.55
15	3	1022.1	-368.9	$-3.8 \cdot 10^{-7}$	$2.1 \cdot 10^{-7}$	1.14

Table 6: Eroded volume and erosion rate (test A2)

$t$ (h)	$\Delta t$ (h)	$V_E(t)$ ( $cm^3$ )	$\Delta V_E$ ( $cm^3$ )	$E_{v,p}(t)$ (m/s)	$E_v(t)$ (m/s)	$d_s(t)=V_E(t)/A_E$ (cm)
1	1	734.7	734.7	$2.3 \cdot 10^{-6}$	$2.3 \cdot 10^{-6}$	0.82
2	1	785.1	50.3	$1.6 \cdot 10^{-7}$	$1.2 \cdot 10^{-6}$	0.87
4	2	879.6	94.5	$1.5 \cdot 10^{-7}$	$6.8 \cdot 10^{-7}$	0.98
8	4	1054.0	174.4	$1.3 \cdot 10^{-7}$	$4.1 \cdot 10^{-7}$	1.17

Table 7: Eroded volume and erosion rate (test A3)

$t$ (h)	$\Delta t$ (h)	$V_E(t)$ ( $cm^3$ )	$\Delta V_E$ ( $cm^3$ )	$E_{v,p}(t)$ (m/s)	$E_v(t)$ (m/s)	$d_s(t)=V_E(t)/A_E$ (cm)
1	1	451.6	451.6	$1.4 \cdot 10^{-6}$	$1.4 \cdot 10^{-6}$	0.50
2	1	383.6	-68.0	$-2.1 \cdot 10^{-7}$	$5.9 \cdot 10^{-7}$	0.43
4	2	487.7	104.1	$1.6 \cdot 10^{-7}$	$3.8 \cdot 10^{-7}$	0.54
8	4	300.7	-187.0	$-1.4 \cdot 10^{-7}$	$1.2 \cdot 10^{-7}$	0.33
12	4	283.2	-17.5	$-1.3 \cdot 10^{-8}$	$7.3 \cdot 10^{-8}$	0.31

Table 8: Eroded volume and erosion rate (test A4)

$t$ (h)	$\Delta t$ (h)	$V_E(t)$ ( $cm^3$ )	$\Delta V_E$ ( $cm^3$ )	$E_{v,p}(t)$ (m/s)	$E_v(t)$ (m/s)	$d_s(t)=V_E(t)/A_E$ (cm)
1	1	2426.1	2426.1	$7.5 \cdot 10^{-6}$	$7.5 \cdot 10^{-6}$	2.70
2	1	2673.4	247.3	$7.6 \cdot 10^{-7}$	$4.1 \cdot 10^{-6}$	2.97
4	2	2860.3	186.9	$2.9 \cdot 10^{-7}$	$2.2 \cdot 10^{-6}$	3.18
8	4	3022.6	162.3	$1.3 \cdot 10^{-7}$	$1.2 \cdot 10^{-6}$	3.36
12	4	2830.5	-192.1	$-1.5 \cdot 10^{-7}$	$7.3 \cdot 10^{-7}$	3.15

Table 9: Eroded volume and erosion rate (test B1)

$t$ (h)	$\Delta t$ (h)	$V_E(t)$ ( $cm^3$ )	$\Delta V_E$ ( $cm^3$ )	$E_{v,p}(t)$ (m/s)	$E_v(t)$ (m/s)	$d_s(t)=V_E(t)/A_E$ (cm)
1	1	932.6	932.6	$2.9 \cdot 10^{-6}$	$2.9 \cdot 10^{-6}$	1.04
2	1	1056.9	124.3	$3.8 \cdot 10^{-7}$	$1.6 \cdot 10^{-6}$	1.17
8	6	1137.9	81.0	$4.2 \cdot 10^{-8}$	$4.4 \cdot 10^{-7}$	1.26
15	7	1210.6	72.7	$3.2 \cdot 10^{-8}$	$2.5 \cdot 10^{-7}$	1.35

Table 10: Eroded volume and erosion rate (test B2)

$t$ (h)	$\Delta t$ (h)	$V_E(t)$ ( $cm^3$ )	$\Delta V_E$ ( $cm^3$ )	$E_{v,p}(t)$ (m/s)	$E_v(t)$ (m/s)	$d_s(t)=V_E(t)/A_E$ (cm)
1	1	2194.8	2194.8	$6.8 \cdot 10^{-6}$	$6.8 \cdot 10^{-6}$	2.44
2	1	2535.7	340.9	$1.1 \cdot 10^{-6}$	$3.9 \cdot 10^{-6}$	2.82
4	2	2811.0	275.3	$4.2 \cdot 10^{-7}$	$2.2 \cdot 10^{-6}$	3.12
8	4	3374.8	563.8	$4.4 \cdot 10^{-7}$	$1.3 \cdot 10^{-6}$	3.75
12	4	2870.6	-504.2	$-3.9 \cdot 10^{-7}$	$7.4 \cdot 10^{-7}$	3.19
18	6	3991.0	1120.4	$5.8 \cdot 10^{-7}$	$6.8 \cdot 10^{-7}$	4.43

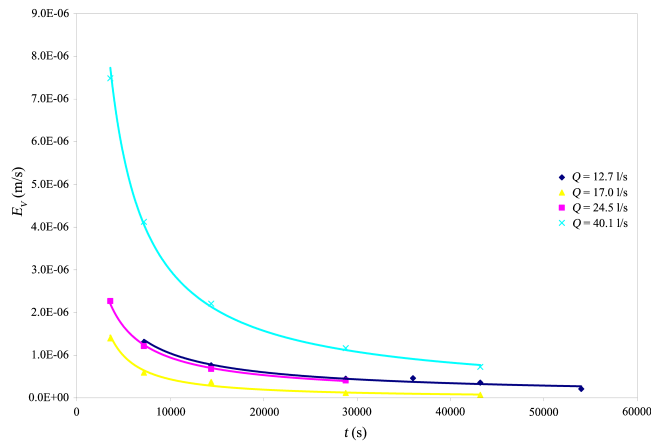


Figure 22: Time evolution of the cumulated volumetric erosion rate (series A)

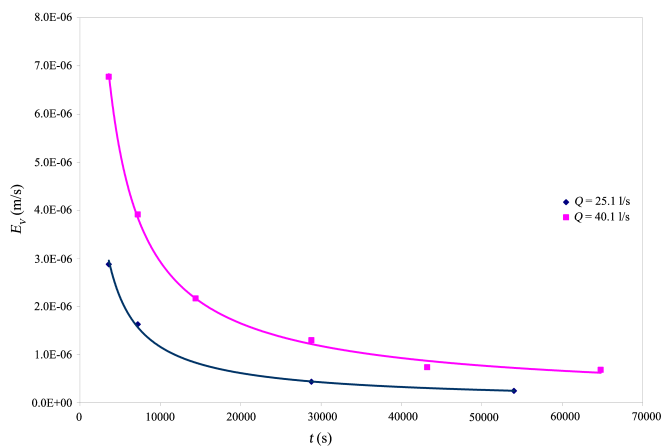


Figure 23: Time evolution of the cumulated volumetric erosion rate (series B)

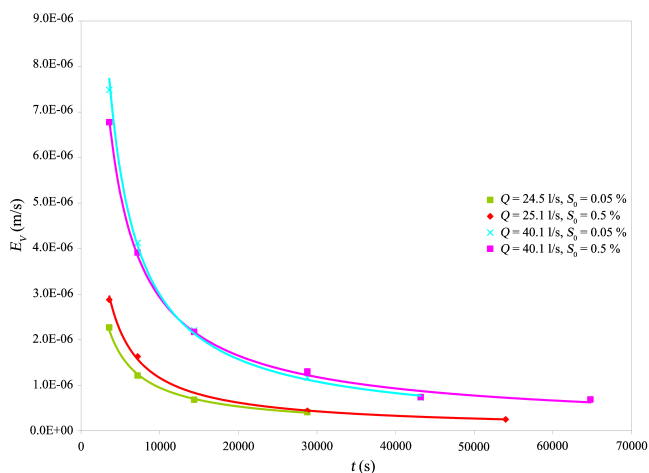


Figure 24: Comparison between the time evolutions of the cumulated volumetric erosion rate (tests A2-B1 and A4-B2)

## 4 Conclusion

The experiments carried out with different bed slopes and discharges on a mixture of sand, silt and clay showed that:

- 1) the erosion process is strongly three-dimensional;
- 2) the time evolutions of the eroded volume and of the cumulated volumetric erosion rate have a logarithmic and a power law behavior, respectively;
- 3) the cumulated volumetric erosion rate depends on the discharge more than on the bed slope, in the ranges investigated;
- 4) the partial volumetric erosion rate is influenced by transitory phenomena.

Further research is needed to extend the knowledge to different mixtures, especially at varying percentages of fine materials.

## References

- [1] F. Greco, R. Gaudio, and A. Miglio, "Erosione fluviale in alvei coesivi. stato dell'arte.," *L'Acqua*, vol. 5, pp. 11–28, 2010 (in italian).
- [2] J. N. Israelachvili, "Intermolecular and surface forces," *Academic Press Limited, London*, 1998.
- [3] T. Mahmood, A. Amirtharajah, T. W. Sturm, and K. E. Dennett, "A micromechanics approach for attachment and detachment of asymmetric colloidal particles," *Colloid Surface*, vol. 177, pp. 99–110, 2001.
- [4] J. C. Santamarina, K. A. Klein, and M. A. Fam, "Soils and Waves: Particulate Materials Behaviour, Characterization and Process Monitoring," *John Wiley & sons, LTD*, 2001.
- [5] K. S. Black, T. J. Tolhurst, D. M. Paterson, and S. E. Hagerthey, "Working with natural cohesive sediments," *J. Hydraul. Eng., Forum*, pp. 2–8, January 2002.
- [6] H. Bungartz and S. C. Wanner, "Significance of particle interaction to the modelling of cohesive sediment transport in rivers," *Hydrol. Process.*, vol. 18, pp. 1685–1702, 2004.
- [7] V. Ravisangar, T. W. Sturm, and A. Amirtharajah, "Influence of sediment structure on erosional strength and density of kaolinite sediment beds," *J. Hydraul. Eng.*, vol. 131, no. 5, pp. 356–365, 2005.
- [8] R. Banasiak and R. Verhoeven, "Quantification of the erosion resistance of undisturbed and remoulded cohesive sediments," *Water Air Soil Poll.: Focus*, vol. 6, pp. 381–391, 2006.
- [9] H. D. Foth and L. M. Turk, "Fundamentals of soil science," *John Wiley & Sons Inc.*, 1972.
- [10] K. Mitchell, "Fundamentals of soil behavior," *John Wiley & sons, Inc.*, 1976.
- [11] J. C. Winterwerp, J. M. Cornelisse, and C. Kuijper, "Parameters to characterize natural muds," *Int. Workshop on Cohesive Sediments, Abstract Volume, Brussels, KBIN, Brussels*, pp. 103–105, 1990.

- [12] J. E. Berlamont, M. C. Ockenden, E. A. Toorman, and J. C. Winterwerp, "The characterisation of cohesive sediment properties," *Coast. Eng.*, vol. 21, pp. 105–128, 1993.
- [13] L. C. van Rijn, "Unified view of sediment transport by currents and waves. i: initiation of motion, bed roughness, and bed-load transport," *J. Hydraul. Eng.*, vol. 133, no. 6, pp. 649–667, 2007.
- [14] M. van Ledden, W. G. M. van Kesteren, and J. C. Winterwerp, "A conceptual framework for the erosion behaviour of sand-mud mixtures," *Cont. Shelf Res.*, vol. 24, pp. 1–11, 2004.
- [15] A. J. Mehta, E. J. Hayter, W. R. Parker, R. B. Krone, and A. M. Teeter, "Cohesive sediment transport. part i: Process description," *J. Hydraul. Eng.*, vol. 115, no. 8, pp. 1076–1093, 1989.
- [16] A. Sundborg, "The river klaralven – a study of fluvial processes," *Meddelanden fram Uppsalg Universitetets Geografiska Institute, Series A, 115, Sartryck ur Geografiska Annalen Hafte 2-3*, 1956.
- [17] I. S. Dunn, "Tractive resistance of cohesive channels," *J. Soil Mech. Found., ASCE*, vol. 85, no. SM3, Proc. Paper 2062, June 1959.
- [18] E. T. Smerdon and R. P. Beasley, "The tractive force theory applied to stability of open channel in cohesive soils," *Res. Bull. 715, Agric. Exp. Stat. Univ. of Mo., Columbia*, 1959.
- [19] J. M. Laflen and R. P. Beasley, "Effect of compaction on critical tractive forces in cohesive soils," *Res. Bull. 749, Agric. Exp. Stat. Univ. of Mo., Columbia*, 1960.
- [20] E. M. Flaxman, "Channel stability in undisturbed cohesive soils," *J. Hydraul. Div., ASCE*, vol. 89, pp. 87–96, 1963.
- [21] W. M. Lyle and E. T. Smerdon, "Relation of compaction and other soil properties to the erosion resistance of soils," *Trans. Am. Soc. Civ. Eng.*, vol. 8, pp. 419–422, 1965.
- [22] E. Partheniades, "Erosion and deposition of cohesive soils," *J. Hydraul. Div., ASCE*, vol. 91, no. 1, pp. 105–139, 1965.
- [23] K. Arulanandan, "Fundamentals aspects of erosion of cohesive soils," *J. Hydraul. Div., ASCE*, vol. 101, no. 5, pp. 635–639, 1975.
- [24] R. Ariathurai and K. Arulanandan, "Erosion rates of cohesive soils," *J. Hydraul. Div., ASCE*, vol. 104, no. HY2, pp. 279–283, 1978.
- [25] M. F. C. Thorn and J. G. Parsons, "Erosion of cohesive sediments in estuaries," *Third Int. Symp. on Dredging Technology, Bordeaux, France*, 1980.
- [26] K. N. Hwang and A. J. Mehta, "Fine sediment erodibility in lake okeechobee," *Report UFLICOEL-891019, Coastal and Oceanographic Engineering Dept., Univ. of Florida, Gainesville, Florida*, 1989.
- [27] T. N. Burt, "Cohesive sediment and physical models," *Int. Conf. on Phys. Modeling of Transport, MIT, Cambridge, Massachusetts*, 1990.
- [28] L. C. van Rijn, "Principles of sediment transport in rivers, estuaries, and coastal seas," *Aqua Publications, Blokzijl, The Netherlands*, 1993.
- [29] R. Jepsen, J. Roberts, and W. Lick, "Effects of bulk density on sediment erosion rates," *Water Air Soil Poll.*, vol. 99, pp. 21–31, 1997.
- [30] J. Roberts, J. Jepsen, D. Gotthard, and W. Lick, "Effects of particle size and bulk density on erosion of quartz particles," *J. Hydraul. Eng.*, vol. 124, no. 12, pp. 1261–1267, 1998.
- [31] A. J. Mehta and S. I. Lee, "Problems in linking the threshold condition for the transport of cohesionless and cohesive sediment grain," *J. Coastal Res.*, vol. 10, pp. 170–177, 1994.
- [32] A. Shields, "Application of similarity principles and turbulence research to bed-load movement", translated from "anwendung der aehnlichkeitsmechanik und der turbulenzforschung auf die geschiebebewegung," *Mitteilungen der Preussischen Versuchsanstalt fur Wasserbau und Schiffbau, Berlin, by W.P. Ott and J.C. van Uchelen, Soil Conserv. Serv., Cooperative Lab., California Inst. of Tech., Pasadena, California*, 1936.
- [33] T. M. Parchure and A. J. Mehta, "Erosion of soft cohesive sediment deposits," *J. Hydraul. Eng.*, vol. 111, no. 10, pp. 1308–1326, 1985.
- [34] D. A. Zreik, B. G. Krishnappan, J. T. Germaine, O. S. Madsen, and C. C. Ladd, "Erosional and mechanical strengths of deposited cohesive sediments," *J. Hydraul. Eng.*, vol. 124, no. 11, pp. 1076–1085, 1998.
- [35] J. W. Kamphuis and K. R. Hall, "Cohesive material erosion by unidirectional current," *J. Hydraul. Eng.*, vol. 109, no. 1, pp. 49–60, 1983.
- [36] H. Mitchener and H. Torfs, "Erosion of mud-sand mixtures," *J. Coastal Eng.*, vol. 29, pp. 1–25, 1996.
- [37] J. E. Berlamont and H. M. Torfs, "Modelling (partly) cohesive sediment transport in sewer systems," *Water Sci. Technol.*, vol. 33, no. 9, pp. 171–178, 1996.
- [38] I. Panagiotopoulos, G. Voulgaris, and M. B. Collins, "The influence of clay on the threshold of movement of fine sandy bed," *Coast. Eng.*, vol. 32, pp. 19–43, 1997.
- [39] R. DeSutter, P. J. Rushforth, S. J. Tait, M. Huygens, R. Verhoeven, and A. J. Saul, "The erosion of cohesive mixed deposits: implication for sewer flow quality modelling," *Urban Water 2*, pp. 285–294, 2000.
- [40] W. Lick, L. Jin, and J. Gailani, "Initiation of movement of quartz particle," *J. Hydraul. Eng.*, vol. 130, no. 8, pp. 755–761, 2004.
- [41] U. C. Kothiyari, S. A. Ansari, and K. G. R. Raju, "Influence of cohesion on incipient motion of fine sediments," *Proc. 15th Congress of ADP-IAHR, IIT Madras, Chennai, India*, pp. 7–10, Aug. 2006.
- [42] J. P. Julian and R. Torres, "Hydraulic erosion of cohesive riverbanks," *Geomorphology*, vol. 76, pp. 193–206, 2006.

- [43] M. Righetti and C. Lucarelli, "May the shields theory be extended to cohesive and adhesive benthic sediments?," *J. Geophys. Res.*, vol. 112, no. C05039, p. 14, 2007.
- [44] T. S. Mostafa, J. Imran, M. H. Chaudhry, and I. B. Kahn, "Erosion resistance of cohesive soils," *J. Hydraul. Res.*, vol. 46, no. 6, pp. 777–787, 2008.
- [45] U. C. Kothyari and R. K. Jain, "Influence of cohesion on the incipient motion condition of sediment mixtures," *Water Resour. Res.*, vol. 44, no. W04410, p. 15, 2008.
- [46] R. Ariathurai, *A finite element model for sediment transport in estuaries*. Ph.d. thesis, Univ. of California, Davis, California, 1974.
- [47] L. P. Sandford and J. P. Y. Maa, "A unified erosion formulation for fine sediments," *Mar. Geol.*, vol. 179, pp. 9–23, 2001.
- [48] J. Aberle, V. Nikora, and R. Walters, "Effects of bed material properties on cohesive sediment erosion," *Mar. Geol.*, vol. 207, no. 1-4, pp. 83–93, 2004.
- [49] J. Aberle, V. Nikora, and R. Walters, "Data interpretation for in situ measurements of cohesive sediment erosion," *J. Hydraul. Eng.*, vol. 132, no. 6, pp. 581–588, 2006.
- [50] K. Debnath, V. Nikora, J. Aberle, B. Westrich, and M. Muste, "Erosion of cohesive sediments: resuspension, bed load, and erosion patterns from field experiments," *J. Hydraul. Eng.*, vol. 133, no. 5, pp. 508–520, 2007.
- [51] A. Ricca, *Studio sperimentale sul tasso erosivo in una miscela di sedimenti coesivi e non coesivi in canale a superficie libera*. Tesi di laurea specialistica in ingegneria civile, Università della Calabria, Facoltà di Ingegneria, Dipartimento di Difesa del Suolo "V. Marone", Rende (CS), Italy, Academic Year 2008-2009, 2009 (in Italian).

# LES OF TURBULENT FLOW WITH SUSPENDED PARTICLE DYNAMICS AT HIGH VOLUME CONCENTRATION

B. J. Geurts<sup>1,2</sup>

<sup>1</sup>*Multiscale Modeling and Simulation, J.M. Burgers Center, University of Twente, P.O. Box 217  
7500 AE Enschede, The Netherlands*

<sup>2</sup>*Anisotropic Turbulence, Fluid Dynamics Laboratory, Eindhoven University of Technology, P.O. Box 513  
5600 MB Eindhoven, The Netherlands*

## Abstract

Large-eddy simulations (LES) of a turbulent flow laden with a large number of solid point particles are discussed. The particle volume fraction is chosen to be high, it equals about 1.3%. This necessitates the use of a four-way coupling model for the discrete particle dynamics. The Euler-Lagrangian method is adopted, which means that the fluid dynamics is governed by the Navier-Stokes equations and that the motion of individual particles is tracked by solving their equation of motion, taking both the particle-fluid and particle-particle interactions into account. LES results of particle-laden turbulent channel flow are compared to single-phase flow to investigate the effect of the particles on turbulent statistics. Due to particle-fluid interactions the mean fluid profile is flattened and the boundary layer is thinner. Compared to single-phase turbulent flow, the streamwise turbulence intensity of the fluid phase is increased, while the normal and spanwise turbulence intensities are reduced, as is also observed in experimental data. The four-way coupled simulations are also compared with two-way coupled simulations, in which the inelastic collisions between particles are neglected. The latter comparison demonstrates that the collisions have a large influence on the main statistics of both phases, expressed for example by the stronger coherent particle structures observed in four-way coupling.

## 1 Introduction

Many flows of relevance to large-scale environmental sediment transport involve suspended solid particles at significant concentrations embedded in a carrying flow. Understanding the spatial distribution of these particles is essential in order to, e.g., predict long-term morphodynamics of the bottom topology in the near-shore surf-zone. This provides the main context for this study which is directed toward understanding the fundamental aspects of the dynamics of the embedded, interacting particles, and to develop a simulation strategy with which the central up-scaling of laboratory-scale experiments to realistic environmental settings can be supported.

The dynamics of the embedded particle-ensemble is quite complex and interacts nonlinearly with the carrying fluid-flow. The particles are dragged along by this carrying fluid-flow and exchange momentum with it. Moreover, the solid particles interact among each other, e.g., through inelastic particle-particle collisions. In case only particle-fluid interactions are incorporated the description is referred to as ‘two-way coupled’ while a ‘four-

way coupled’ formulation arises when also the particle-particle interactions are included (Elghobashi and Truesdell, 1993). At sufficiently low particle volume fraction  $\psi$  two-way coupling is adequate. However, with increasing  $\psi$  the collisions will become dynamically significant and the computationally more involved four-way coupling will be required. We will show that these collisions strongly influence the main statistical fluid properties and amplify the ‘self-organization’ of the embedded particles in coherent swarms.

The two-phase flow is governed by an interplay between the convective flow nonlinearity, the particle-fluid and the particle-particle interactions. These effects may accumulate and significantly change basic turbulence properties such as mean flow and turbulence intensities. A large-scale dynamic flow-structuring may arise affecting the flow-statistics compared to the case with no or only weak interactions. These flow-alterations constitute the so-called modulation of turbulence (see Gore & Crone 1989) which, e.g., seriously complicates the prediction of the up-scaling of flow-phenomena from laboratory-scale experiments to environmental-scale settings.

Turbulent particle-laden flows have been studied experimentally (e.g., Tsuji, Morikawa & Shiomi 1984; Kulick, Fessler & Eaton 1994; Nieuwland 1995; Moran & Glicksman 2003) and with simulations. Simulations can be performed using a two-fluid model in which the solid phase is modeled as a fluid using continuous variables (e.g., Nieuwland 1995, Mathiesen, Solberg & Hjertager 2000, Goldschmidt *et al.* 2002). This approach is quite well established and may be used to investigate statistical properties of multi-phase flows (Ferry & Balachandrar 2001). A promising, more recent, direction to solve two-phase flows is to enforce the no-slip condition on the boundary of each particle using front tracking methods (see e.g., Tryggvason *et al.* 2001, Feng & Michaelides 2004). No additional modeling assumptions are required, but the amount of particles that can be calculated is currently on the order of 1000s. In this paper we consider a third approach, the discrete particle method in which the Navier-Stokes equations which govern the fluid in a Eulerian framework are combined with a Lagrangian tracking of the motion of each individual particle. The forces between the fluid and each particle are modeled with a drag law and all collisions between particles are treated with a deterDNS), but models the effect of the small scales with a subgrid-model (see the reviews by Pope (2000), Sagaut (2001) and Geurts (2003)). It is considerably more efficient than Direct numerical simulation (DNS), which resolves all turbulent scales in the flow. These techniques are able to give proper detailed descriptions of the turbulence in a channel flow. LES/DNS of channel flows

supplemented with a discrete particle model have been reported a number of times (e.g., Wang & Squires 1996, Armenio, Piomelli & Fiorotto 1999, Armenio & Fiorotto 2001, Yamamoto *et al.* 2001, Squires & Simonin 2002, Marchioli *et al.* 2003). However, the total solids volume fraction in these studies remains rather small (0.01%) and most of these works employ one- or two-way coupling. An exception is Yamamoto *et al.* (2001) who started to investigate the influence of particle-particle interactions in LES of channel flow with particle volume fractions up to 0.014%. They found that even in such dilute regimes the effects of collisions are significant.

The purpose of this paper is to present LES of a channel flow in which the particle volume concentration is one or two orders of magnitude higher than existing Euler-Lagrangian studies in literature and hence closer to realistic applications. The discrete particle module developed by Hoomans *et al.* (1996) will be used, in which the spherical particles have a finite size and all (inelastic) collisions are taken into account. A subgrid closure needs to be adopted for the LES-equations of the fluid phase for which we will mainly adopt the model by Vreman (2004).

The organization of this paper is as follows. In section 2 we present the simulation method. Results of a large number of channel flow simulations are presented in section 3, focusing on turbulence modulation, the differences between two- and four-way coupling and coherent particle structures. Finally, concluding remarks are collected in section 4 (This paper is based on ‘Two-and four-way coupled Euler-Lagrangian large-eddy simulation of turbulent particle-laden channel flow’, Vreman, Geurts, Deen, Kuipers and Kuerten, *Flow, Turbulence and Combustion* **82**, 2009.)

## 2 Mathematical Formulation

In this section we specify the mathematical formulation of the simulation model for the turbulent fluid-solids flow. In subsection 2.1 the equations governing the fluid-phase are described. The treatment of the solids-phase is specified in subsection 2.2. The subgrid modeling for the turbulent stresses that arise in the large-eddy simulation is introduced in subsection 2.3 and, finally, the numerical method is discussed in subsection 2.4.

### 2.1 The Fluid Phase

The computational model distinguishes a fluid phase and a solids phase. The embedded solid particles are considered to be small compared to convective turbulent length-scales. This allows to effectively approximate the equations for the fluid phase in terms of flow through a (time- and position-dependent) porous medium (Hoomans *et al.* 1996; Zhang & Prosperetti 1997; Lakehal, Smith & Milleli 2002; Powers 2004). The local, instantaneous particle concentration determines the fluid-volume-fraction that is accessible to the fluid phase. At particle-volume-fractions around 1-2 % we may restrict to the standard Navier-Stokes equations that govern a compressible flow with appropriate forcing terms:

$$\partial_t \rho + \partial_j (\rho u_j) = 0, \quad (1)$$

$$\partial_t (\rho u_i) + \partial_j (\rho u_i u_j) = -\partial_i p + \partial_j \sigma_{ij} + \rho a_{ext} \delta_{i3} + f_i, \quad (2)$$

$$\begin{aligned} \partial_t e + \partial_j ((e + p) u_j) &= \partial_j (\sigma_{ij} u_i) + \rho a_{ext} u_3 \\ &+ f_i u_i - \partial_j q_j. \end{aligned} \quad (3)$$

where the symbols  $\partial_t$  and  $\partial_j$  denote the partial differential operators  $\partial/\partial t$  and  $\partial/\partial x_j$  respectively. Furthermore,  $\rho$  is the density,  $\mathbf{u}$  the velocity,  $p$  the pressure and  $e = p/(\gamma - 1) + \frac{1}{2} \rho u_k u_k$  the total energy per volume unit. The constant  $\gamma$  denotes the ratio of specific heats  $C_p/C_v = 1.4$ . The coordinate  $x_3$  denotes the streamwise direction of the channel flow,  $x_2$  is the normal and  $x_1$  is the spanwise direction. Throughout, we will frequently interchange the symbols  $x_1, x_2$  and  $x_3$  by  $x, y$  and  $z$  and  $u_1, u_2$  and  $u_3$  by  $u, v$  and  $w$  respectively. The domain is rectangular and the channel width, height and depth equal  $L_2 = 0.05m$ ,  $L_3 = 0.30m$  and  $L_1 = 0.075m$  respectively. Periodic boundary conditions are assumed for the stream- and spanwise directions.

The viscous stress  $\sigma_{ij}$  equals  $2\rho\nu S_{ij}$  where  $\nu$  is the fluid viscosity and the strain-rate is defined by

$$S_{ij}(u) = \frac{1}{2} \partial_i u_j + \frac{1}{2} \partial_j u_i - \frac{1}{3} \delta_{ij} \partial_k u_k. \quad (4)$$

The heat-flux  $q_j$  is defined as  $-\kappa \partial_j T$  where  $T$  is the temperature and  $\kappa$  the heat-conductivity coefficient. Pressure, density and temperature are related to each other by the equation of state for an ideal fluid  $\rho R_{fluid} T = M_{fluid} p$ , where  $R_{fluid} = 8.314 J/(molK)$  is the universal fluid constant and  $M_{fluid} = 0.0288 kg/mol$  is the molar mass of the fluid.

The symbol  $a_{ext}$  represents the acceleration caused by external forces on the fluid phase. It corresponds to a mean pressure gradient over the channel that is needed to maintain a desired mass flux. The forcing term  $f_i$  denotes the contributions due to the momentum-exchange of the particles to the flow. The external acceleration  $a_{ext}$  is a function of time only and its level is such that the total fluid mass flow is constant. In all cases the average mean fluid velocity is identical,  $U_m = 3.92 m/s$ . The sink-terms  $f_i$  are induced by an effective relative motion of the particles with respect to the fluid which gives rise to drag forces on the fluid (see next subsection).

We are interested in a section of a riser flow with a vertical centerline velocity  $U_c$  of about  $4m/s$ . The parameters of the fluid in the riser are close to those for air. The initial fluid density is uniform and equals  $\rho_g = 1.0 kg/m^3$ . The viscosity equals  $\nu = 3.47 \cdot 10^{-5} m^2/s$  and the heat-conductivity is obtained from the assumption that the Prandtl number equals one. The value of the viscosity is chosen such that  $Re_\tau = 180$  for channel flow without particles and  $U_c = 4.5 m/s$ . The Kolmogorov length-scale in channel flow equals about  $\eta^+ \approx 1.5$  in wall-units (Pope 2000), which implies  $\eta \approx 0.2 mm$ .

### 2.2 The Solids Phase

The number of solid particles in the channel flow equals  $N_p \approx 4 \cdot 10^5$ . During the simulations the motion of all these particles was tracked, starting from an initially uniform distribution of particles throughout the flow-domain. The initial velocity of each particle was taken equal to the local initial velocity of the fluid-phase. The particle diameter and density are  $d_p = 0.4 mm$  and  $\rho_p = 1500 kg/m^3$ , respectively. With the parameters above the average volume fraction of the particles equals 0.013. The Stokes response-time, defined as

$$\tau_p = \frac{\rho_p d_p^2}{18\mu}, \quad (5)$$

equals 0.4 s. The Stokes number equals 10, based on the Kolmogorov time derived from the average dissipation of the unladen flow. In this paper only a single, rather

high, value of the Stokes response-time will be adopted in order to emphasize the dynamic effects of the embedded particles. This provides a characteristic, demanding case of turbulent fluid-solid flow which is used to assess the feasibility and accuracy of Euler-Lagrangian LES.

The motion of every individual particle  $i$  in the system is calculated from Newton's second law:

$$m_i \frac{d\mathbf{v}_i}{dt} = V_i \beta (\mathbf{u} - \mathbf{v}_i) + m_i g \mathbf{e}_z + \mathbf{f}_i^{pp} + \mathbf{f}_i^{pw}, \quad (6)$$

where  $m_i$  denotes the mass,  $\mathbf{v}_i$  the velocity,  $V_i$  the volume of the  $i$ -th particle and  $\mathbf{e}_z$  is the unit vector in the  $z$ -direction. The gravitational acceleration equals  $g = -9.81 \text{ m/s}^2$ , which is opposite to the mean flow direction. The forces on the right hand side of the equation represent standard drag, gravity, particle-particle interaction ( $\mathbf{f}_i^{pp}$ ) and particle-wall interaction ( $\mathbf{f}_i^{pw}$ ), respectively. We return to this momentarily. The general equation of motion for a single particle derived by Maxey & Riley (1983) contains additional forces, such as added mass and history terms. However, the comparison with DNS results performed by Bagchi & Balachandar (2003) did not show improvements when these forces were included. In the present case, the particle density is much larger than the fluid density. Correspondingly, these additional forces, including buoyancy effects are relatively small and can be neglected (Armenio & Fiorotti 2001).

The symbol  $\beta$  in the drag term is the inter-phase momentum transfer coefficient. The flow is sufficiently dilute to employ the correlation of Wen & Yu (1966):

$$\frac{\beta d_p^2}{\mu} = \frac{3}{4} C_D \text{Re} \quad (7)$$

where

$$C_D = \begin{cases} 24(1 + 0.15 \text{Re}^{0.687})/\text{Re}; & \text{Re} < 10^3 \\ 0.44 & \text{Re} > 10^3, \end{cases} \quad (8)$$

in which  $\text{Re} = \rho |\mathbf{u} - \mathbf{v}_p| d_p / \mu$  is the particle Reynolds number, which is evaluated at the particle position.

Bagchi & Balachandar (2003) investigated the validity of the standard drag law for particles with a diameter  $1.5\eta < d < 10\eta$ , where  $\eta$  is the Kolmogorov length-scale. They found that the time-averaged drag is accurately predicted and insensitive to whether the fluid velocity is measured at the particle center, or obtained by averaging over a fluid volume of the order of the particle size. Instantaneous drag is reasonably well predicted for moderate particle sizes, e.g.,  $d < 4\eta$ . The diameter of the particles in the present study equals  $2\eta$  and is within this region. Hence, we will assume the drag law to be adequately representative of the dominant particle-motion physics, as far as the single particle dynamics is concerned. Since we consider volume fractions in the 1% range we treat collisional effects separate from the standard drag dynamics and ignore corrections from the average proximity of neighboring particles.

The collision model used in this work is based on the hard-sphere model developed by Hoomans *et al.* (1996) and Hoomans, (1999). The original formulation of this model was developed for two-dimensional flow. Here, we extend it to be applicable to turbulent flow in three spatial dimensions. As the particles are assumed small compared to the convective turbulent length-scales, this extension involves no principal changes but only some technical complications associated with the transition from two - to three spatial dimensions. This model has also been validated and frequently applied to three-dimensional flows (e.g., Delnoij *et al.* 1999, van der Hoef

Symbol	Value	Description
$d_p$	$4 \cdot 10^{-4} \text{ m}$	particle diameter
$\rho_p$	$1.5 \cdot 10^3 \text{ kg m}^{-3}$	particle density
$N_p$	419904	number of particles
$e$	0.97	normal restitution coeff
$\beta_0$	0.33	tangential restitution coeff
$\mu_f$	0.1	friction coefficient

Table 1: Parameters used in the treatment of the discrete particles. Each particle is spherical, corresponds to a Stokes response-time  $\tau_p = 0.4 \text{ s}$ , associated with a viscosity of the fluid phase of  $\mu = 3.47 \cdot 10^{-5} \text{ kg m}^{-1} \text{ s}^{-1}$ . The solids phase has an average volume fraction  $\langle \psi \rangle = 0.013$  and the mass-load is given by  $\langle \psi \rangle \rho_p / \rho_g = 19.5$ .

*et al.* 2008 and references therein). In the collision model it is assumed that the interaction forces are impulsive and therefore all other finite forces are negligible during collision.

The particle collision characteristics play an important role in the overall system behavior as was shown by Hoomans *et al.* 1996 and Goldschmidt *et al.* 2002. For this reason realistic collision properties of the particles are supplied to the model. The parameters used in the treatment of the discrete particles are summarized in table 1. Here  $\psi$  is the local solid volume fraction, which does not occur in the present model equations, but is computed for evaluation purposes (see section 3.3). Collisions between particles are monitored as follows. For each particle, say A, a neighbor-list is kept. This includes all particles that are located within a certain radius of particle 'A'. Particles nearer the top of the list are closer to 'A', while particles that are further separated are stored lower on the list. After each collision among the entire particle swarm, the neighbor lists are updated when necessary.

## 2.3 Subgrid-Modeling

In order to make large-scale turbulent flow simulations at high particle volume fractions feasible, the fluid phase is described using large-eddy simulation. This is obtained by applying spatial filtering to the flow equations in order to reduce their dynamical complexity. The filter is defined by

$$\bar{a} = \int G(x, \xi) a(\xi) d\xi \quad (9)$$

where  $\bar{a}$  denotes a filtered flow variable and  $G$  the filter-kernel. For the compressible equations we use a density-weighted filter,

$$\tilde{a} = \bar{a} / \bar{\rho}, \quad (10)$$

the so-called Favre filter and originally proposed by O. Reynolds (1895). If the convolution filter is applied to the governing equations the result may be expressed in terms of the LES-template (Geurts, 2003):  $\text{NS}(\bar{U}) = R(U, \bar{U})$  where the original and filtered variables are defined by  $U = [\rho, u_j, p, T]$ ;  $\bar{U} = [\bar{\rho}, \tilde{u}_j, \bar{p}, \tilde{T}]$ . The spatial filtering yields a 'closure-residual'  $R(U, \bar{U})$  which contains, e.g., the filtered forcing term  $\bar{f}_i$  and the divergence of the turbulent stress tensor

$$\tau_{ij} = \bar{\rho} \tilde{u}_i \tilde{u}_j - \bar{\rho} \tilde{u}_i \bar{\rho} \tilde{u}_j / \bar{\rho} = \bar{\rho} \{ \tilde{u}_i \tilde{u}_j - \tilde{u}_i \tilde{u}_j \} \quad (11)$$

The only closure term modeled in this paper is this turbulent stress tensor. The subgrid terms that result from the filtering of the diffusive viscous fluxes are neglected.

Likewise, subgrid contributions arising from filtering the momentum exchange between the discrete particles and the fluid as represented by the drag law are also neglected. This is a reasonable assumption for the present application, as we consider relatively coarse particles. The particles are slightly larger than the Kolmogorov length-scale and the Stokes response time is an order of magnitude larger than the Kolmogorov time. Therefore the motion of the particles is mainly influenced by the large-scale eddies in the flow (Armenio *et al.* 1999; Kuerten & Vreman 2005; Kuerten 2006).

Simulations were performed using different subgrid-models for the turbulent stress tensor  $\tau_{ij}$ . As the results were found to be quite insensitive of the adopted subgrid model, compared to the dynamic effects of the particles, we only include the eddy-viscosity model as described in Vreman (2004) and Geurts & Vreman (2006), Vreman *et al.* (2009). This model employs the following positive invariant of the gradient model  $m_{ij}$ ,

$$B = m_{11}m_{22} - m_{12}^2 + m_{11}m_{33} - m_{13}^2 + m_{22}m_{33} - m_{23}^2, \quad (12)$$

and defines the eddy-viscosity

$$\nu_e = c \sqrt{\frac{B}{(\partial_j \tilde{u}_i)(\partial_j \tilde{u}_i)}} \quad (13)$$

where  $c = 0.07$ . The dissipation of this eddy-viscosity and the exact subgrid dissipation were shown to vanish for precisely the same class of flows (Vreman 2004). This model was proposed independently of the work of Nicoud & Ducros (1999), who constructed a similar eddy-viscosity. That eddy-viscosity is not based on the gradient model, but on the square of the velocity gradient matrix.

## 2.4 The Numerical Method

The equations for the fluid phase are solved with a second-order finite volume method, based on central differencing on a collocated grid. For details we refer to Geurts & Kuerten (1993) and Vreman, Geurts & Kuerten (1996). In the latter work, the second-order numerical method was found to be sufficiently accurate in LES, also with respect to the dissipation of kinetic energy.

The channel flow is solved on the domain  $3H \times 2H \times 12H$ . The length of the domain in the spanwise ( $x_1$ ) direction is 1.5 times smaller than for most DNS/LES of single-phase channel flow in order to limit the amount of carried particles and their collisions to a manageable number. As a point of reference, we also performed a single-phase DNS for this computational domain. Specifically, we used an incompressible Fourier/Chebyshev method with  $64 \times 128 \times 128$  modes. The mean and rms profiles (shown in the next subsection) were verified to be identical to those of standard DNS-databases for  $Re_\tau = 180$  (*e.g.*, Moin & Kim 1982; Moser, Kim & Mansour 1999; Howard & Sandham 2000; Verstappen & Veldman 2003).

The large-eddy simulations presented in this paper involve  $32 \times 64 \times 64$  grid cells. The grid is only nonuniform in the normal direction and symmetric with respect to the plane  $x_2 = 0$ . The grid-points in the left-half of the channel are defined by

$$x_{2,j}/H = -1 + \frac{\sinh(aj/N_2)}{\sinh(a/2)} \quad ; \quad j = 0, \dots, N_2/2, \quad a = 6.5 \quad (14)$$

(Verstappen & Veldman 2003). The first grid point of the wall is at  $x_{2,1} = 0.2mm$ , corresponding to  $y^+ = 1.5$ .

The grid is sufficiently fine to have a well-resolved LES of channel flow at  $Re_\tau = 180$ , according to common criteria (see Piomelli & Balaras 2002).

The discretization in time is explicit: forward Euler for the particles, and a four-stage Runge-Kutta scheme for the fluid convective, viscous and pressure terms, using coefficients  $\frac{1}{4}$ ,  $\frac{1}{3}$ ,  $\frac{1}{2}$  and 1. The most costly part of the simulation method is the discrete particle model, which requires about 80% of the computation time in case of four-way coupled simulations. The Euler forward method was adopted in combination with first-order accurate tri-linear interpolation to obtain the Eulerian velocity field at the particle location. It is combined with sufficiently small time-steps to yield adequate accuracy for the particle trajectories. The particle time-step is about  $1/5$  of that of the fluid time-step. The simulations run until at least  $t = 5s$ , while statistics are accumulated between  $t = 3s$  and  $t = 5s$ . The averaging time of  $2s$  corresponds to  $20H/u_\tau$  in terms of the wall shear-velocity  $u_\tau$ , twice as large as a typical averaging time in single-phase channel flow. With a Stokes response-time of  $\tau_p = 0.4 s$ , the particles are evolved for  $12.5 \tau_p$  and the accumulation of the statistics is over  $5\tau_p$ .

## 3 Results

In this section we will compare results obtained in ‘clean’ riser-flow with the particle-laden case, using four different subgrid models. First we will consider the clean and four-way coupled cases and quantify the turbulence modulation of the fluid phase arising from the presence of the particles (subsection 3.1). In subsection 3.2 we will isolate the effects of the particle collisions and compare the four-way coupled results with two-way coupled simulations. Finally we will show the occurrence of coherent particle structures in our simulations (subsection 3.3).

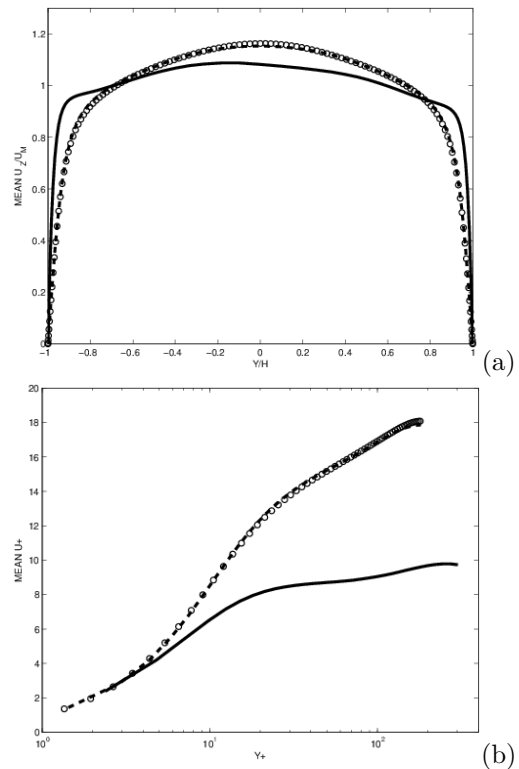


Figure 1: Mean streamwise fluid velocity  $\langle u_z \rangle$ : linear (a) and logarithmic (b) for a particle-laden flow, comparing clean flow (dashed) with four-way coupling (solid). DNS results of clean flow are indicated by circles.

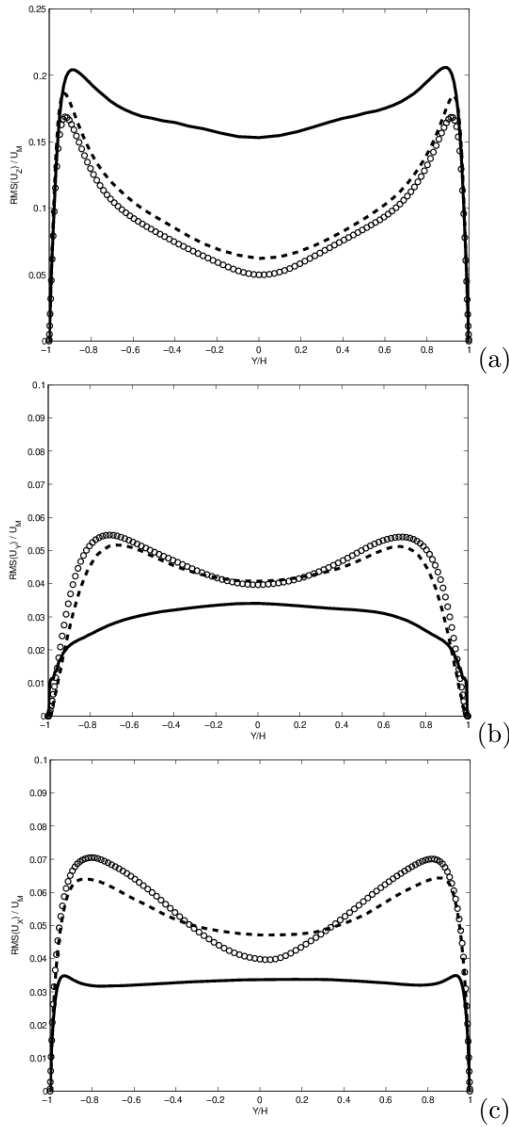


Figure 2: Turbulence intensities of the fluid phase; streamwise (a), normal (b) and spanwise direction (c), comparing clean flow (dashed) with four-way coupling (solid). DNS results of clean flow are indicated by circles.

### 3.1 Turbulence Modulation

The particle-phase strongly alters the fluid mean flow. 1 shows the fluid mean flow profile normalized with the maximum  $U_m$  (a) and the wall shear velocity  $u_\tau$  (b), based on the four-way coupled formulation. Relative to the clean channel we observe that the particles give rise to a strongly reduced boundary layer thickness and a flatter velocity profile. It corresponds to a larger skin-friction coefficient and, consequently, a larger  $Re_\tau$  based on the fluid velocity, which increases from 180 to 300. The effects of the embedded particles on the developing flow are also reflected by the profile in the logarithmic region. Compared to the clean case an approximately logarithmic velocity profile develops for  $10^{-3} < x_2 < 10^{-2}$ , i.e., corresponding to  $20 < y^+ < 200$ , but at a much larger Von Kármán ‘constant’ (Hinze 1975). In the following all velocity statistics are normalized with  $U_m$ , which is the same for all calculations.

2 shows the turbulence intensities of the fluid phase. The turbulence modulation by coarse particles leads to an increased streamwise turbulence intensity and de-

creased transverse and spanwise intensities. This observation appears generally in line with existing experimental data. Although a direct comparison with physical experiments faces important difficulties in view of differences in flow-conditions, volume fractions and particle properties, an interesting analogy with the simulation findings may be drawn. The experiments by Kulick *et al.* (1994) adopt smaller particles at lower volume fraction. In this regime a *decrease* in all components of the turbulence intensity was noted. This appears to contrast the present simulation findings. However, in a study by Tsuji *et al.* (1984) larger particles at higher volume fraction were studied including particles of 0.5 mm in diameter, with Stokes response-time  $\tau_p \approx 0.6$  s. This situation is close to our simulation setting in a number of respects. In such cases an *increase* in streamwise intensities in the core region of the channel was reported. For still coarser particles Tsuji *et al.* (1984) found an even stronger increase of turbulence intensity across the entire diameter of the pipe.

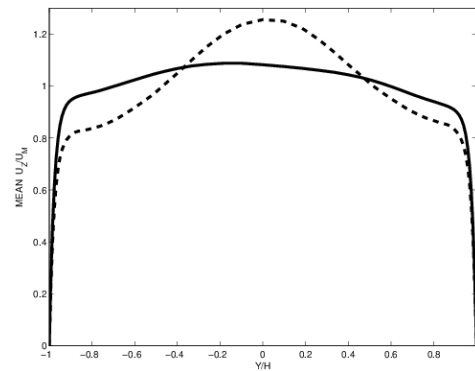


Figure 3: Mean fluid velocity comparing two-way (dashed) with four-way coupling (solid) using LES.

### 3.2 Effects of Collisions

In 3 we collected the mean streamwise fluid and solids velocity profiles. Considering the mean flow, both the two- and four-way coupling cause a higher skin-friction coefficient and results in a near-wall profile quite similar to the four-way coupled case. The correspondence of the near-wall fluid velocity profiles in the two- and four-way coupled descriptions reflects the interaction of the particles with the solid channel walls which were treated identically in both the two-way coupled and the four-way coupled cases. The inelastic collisions with the walls create a low-velocity-layer directly adjacent, which effectively acts analogous to an increased wall-roughness and hence yields an increased skin-friction coefficient. The absence of inelastic particle-particle collisions in the bulk of the flow is responsible for the absence of a flattening of the fluid velocity profile. The prediction of the bulk flow away from the boundary layers is quite different when comparing the two-way and the four-way approaches. The two-way description is seen to give rise to a somewhat localized ‘center-jet’ in which the fluid velocity is up to about 60% larger than the velocity at the edge of the boundary layer. In contrast, the four-way coupling gives rise to a slightly flatter velocity profile compared to the clean channel; the particle-particle collisions evidently allow to avoid the ‘center-jet’ as discussed above. The striking differences between the resulting dynamics in the two-way and the four-way coupled descriptions of the solids-phase are directly related to the inter-particle collisions. These collisions diffuse kinetic energy of the

solids in the normal direction. As a consequence the mean solids velocity profile flattens. Due to the coupling between phases through the drag force, this collisional diffusion also flattens the fluid mean velocity profile.

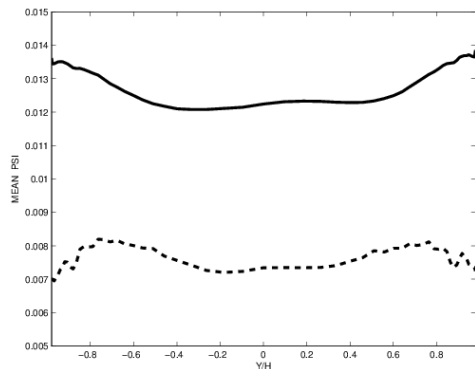


Figure 4: Solid volume fraction  $\langle\psi\rangle$  obtained with LES: two-way (dashed) compared with four-way coupling (solid). Notice that  $\langle\psi\rangle$  is shifted downward by 0.005 for the two-way results for clarity.

The particle volume fraction distribution is shown in 4. A characteristic turbophoresis effect is visible in terms of an approximately 15 % higher concentration near the solid walls. Turbophoresis has been observed in many experiments (Young and Leeming, 1997) and simulations. However the factor by which the particle concentration near the wall is increased, relative to the average bulk-value, depends strongly on the precise flow-regime that is considered. The relatively small turbophoresis effect observed in the present simulations may be attributed to the fact that the particles are coarse and the mass load is high. To verify this, we performed a four-way coupled simulation with particles with a much smaller diameter ( $d_p = 0.04mm$ ) and, consequently, a lower particle concentration ( $\psi = 1.3 \cdot 10^{-5}$ ). In that case strong turbophoresis was observed; the particle concentration near the walls increased with a factor of 30 relative to the mean bulk-concentration. When two-way coupling is used in combination with coarse, slowly responsive particles, no appreciable turbophoresis remains as is seen in 4.

### 3.3 Coherent Particle Structures

In this subsection we will consider the dynamic self-organization that arises due to the ‘competition’ between the structuring associated with the inelastic particle collisions and the bursting of particle-clusters due to the underlying tendency of the clean flow to develop strong turbulence. The observed flow-structuring displays an interesting dynamic behavior which will be illustrated in terms of characteristic instantaneous snapshots of the particle concentration. These display qualitatively the sequence of formation and destruction of quite large coherent regions of considerably increased particle densities. We will also show that the four-way coupling model gives rise to large-scale coherent particle swarms which are much weaker when the two-way coupling model is used.

In order to characterize the flow-structuring we concentrate on visualizing the instantaneous particle volume fraction  $\psi$ . at different times in 5. A contour value of  $\psi = 0.03$  is selected, while the solid volume fraction attains a maximum of approximately 0.1 and an average of 0.013. From these snapshots one may infer the for-

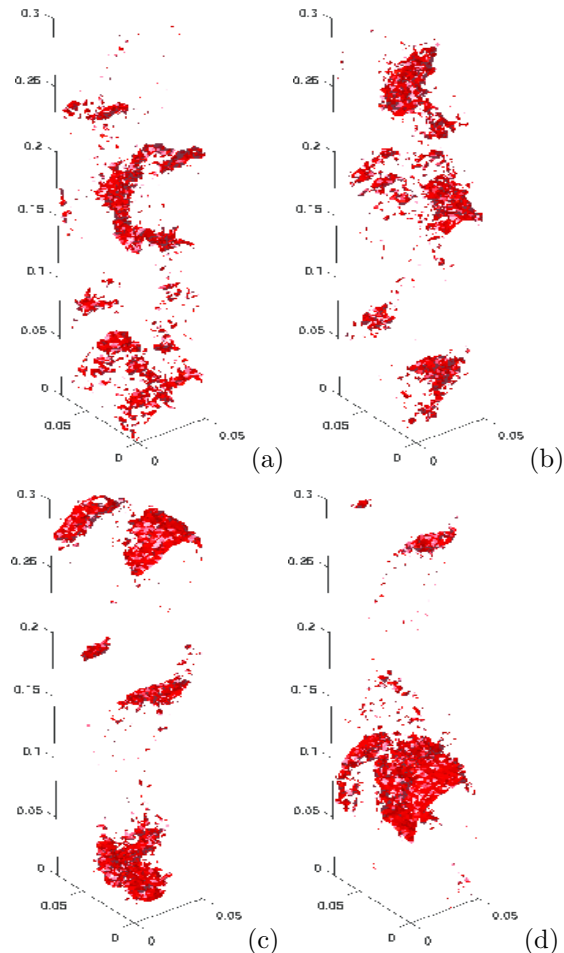


Figure 5: Snapshots of the particle volume fraction showing iso-surfaces at  $\psi = 0.03$  for four-way coupling;  $t = 3.1 s$  (a) with steps of 0.05 s.

mation of large-scale coherent structures in the particle concentration.

At the particle volume fractions considered here, the use of the full four-way coupling is essential. This is illustrated in 6 in which we compare a structured particle field associated with four-way coupling, with a structureless field arising in the two-way coupling model. The particle-particle interactions play a crucial role in the formation of coherent particle structures. These qualitative impressions further establish that four-way coupling can not be replaced by the computationally more appealing two-way coupling.

## 4 Concluding Remarks

In this paper we presented large-eddy simulation results of particle-laden turbulent flow in a vertical riser. This flow is relevant, e.g., to chemical processing and an understanding of the fundamental dynamics of this flow is essential in order to properly predict up-scaling of processes from a laboratory scale to settings which are of industrial importance. We showed that already at a modest particle volume fraction of about 1.5 % the particle-particle interactions play an important role in the development of the flow. The computationally more accessible two-way coupling model proved to give rise to predictions, which for slowly responsive particles and the present particle volume fraction, lack a turbophoresis effect and show the occurrence of a fairly strong ‘center-jet’ which was not recorded in experimental studies. The

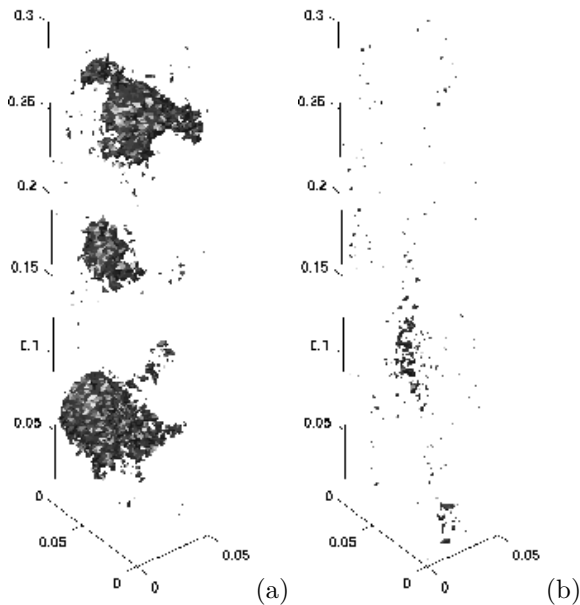


Figure 6: Granular clustering in coherent particle-swarms is strongly associated with the four-way coupling description. Snapshot of the particle volume fraction at  $t = 4$  s compare the four-way coupling (a) with the two-way coupling (b). The iso-surfaces shown correspond to  $\psi = 0.03$ .

present particle volume fraction is much larger than in previous studies of plane channel flow, and the effects of inter-particle collisions found in the present work are much larger than the collisional effects reported by Yamamoto *et al.* (2001), who found a mild effect of collisions in their case.

The presence of a large number of interacting particles leads to a strong modulation of the turbulence in the channel. Relative to a clean channel the coupling between particles and fluid and between particles with other particles and walls through inelastic collisions is mainly responsible for the reduction in the thickness of the boundary layer and the corresponding strong increase in the skin-friction. Moreover, the log-layer that is characteristic of wall-bounded flows was seen to be retained in the particle-laden case but with a much larger Von Kármán ‘constant’. Turbulent intensities in the normal and spanwise directions were reduced whereas the streamwise turbulent intensity was found to be amplified by the presence of coarse particles.

The inelastic collisions are mainly responsible for retaining turbophoresis in case particles with high Stokes response-time are used, and a flattening of the mean particle velocity distribution. These interactions also gave rise to the occurrence of dynamic self-organization of the embedded particles in coherent swarms.

## References

- [1] Armenio, V., Piomelli, U., and Fiorotto, V. 1999 Effect of the subgrid scales on particle motion. *Phys. Fluids* **11**, 3030 (1999).
- [2] Armenio, V., and Fiorotto, V. 2001 The importance of the forces acting on particles in turbulent flows. *Phys. Fluids* **13**, 2437 (2001).
- [3] Bagchi, P., and Balachandar, S. 2003 Effect of turbulence on the drag and lift of a particle. *Phys. Fluids* **15**, 3496-3513.
- [4] Delnoij, E., Kuipers, J.A.M., and van Swaaij, W.P.M. 1999 A three-dimensional CFD model for fluid-liquid bubble columns. *Chem. Eng. Sci.* **54**, 2217-2226.
- [5] Elghobashi, S. and Truesdell, G.C. 1993 On the two-way interaction between homogeneous turbulence and dispersed solid particles. I: Turbulence modification. *Phys. Fluids A* **5**, 1790-1801.
- [6] Feng, Z.-G., Michaelides, E.E. 2004 Proteus: a direct forcing method in the simulation of particulate flows. *J. Comp. Phys.*, to appear.
- [7] Ferry, J., Balachandar, S., 2001 A fast Eulerian method for disperse two-phase flow, *Int. J. of Multiphase Flow* **27**, 1199-1226.
- [8] Geurts, B.J., Kuerten, J.G.M. 1993 Numerical aspects of a block-structured flow solver. *J.Eng.Math.* **27**:293
- [9] Geurts, B.J. 2003 *Elements of direct and large-eddy simulation*. Edwards Publishing Inc. ISBN: 1-930217-07-2,
- [10] Geurts, B.J., Vreman, A.W., 2006. Dynamic self-organization in particle-laden turbulent channel flow. *Int. J. Heat Fluid Flow*, **27**, 945-954.
- [11] Goldschmidt, M.J.V., Beetstra, R. and Kuipers, J.A.M., Comparison of the kinetic theory of granular flow with 3D hard-sphere discrete particle simulations, 2002 *Chem. Eng. Sci.* **57**, 2059-2075.
- [12] Gore, R.A., and Crowe, C.T. 1989 Effect of particle size on modulating turbulence intensity. *Int. J. Multiphase flow* **15**, 279-285.
- [13] Hinze, J.O.: 1975. *Turbulence: An Introduction to its Mechanism and Theory*. New York: McGraw-Hill
- [14] Van der Hoef, M.A., van Sint Annaland M., Deen N.G., Kuipers, J.A.M. 2008 Numerical simulation of fluid-solid fluidized beds: a multiscale modeling strategy. *Ann. Rev. Fluid Mech.* **40**, 47-70.
- [15] Hoomans, B.P.B., Kuipers, J.A.M., Briels, W.J., and van Swaaij, W.P.M. 1996 Discrete particle simulation of bubble and slug formation in a two-dimensional fluid-fluidized bed: A hard-sphere approach. *Chem. Eng. Sci.* **51**, 99-118.
- [16] Hoomans, B.P.B. 1999 *Granular dynamics of fluid-solid two-phase flows*. PhD-Thesis, University of Twente.
- [17] Howard, R.J.A., Sandham, N.D. 2000 Simulation and modeling of a skewed turbulent channel flow. *Flow Turbulence and Combustion* **65**, 83-109.
- [18] Kuerten, J.G.M. 2006 Subgrid modeling in particle-laden channel flow *Phys. Fluids* **18**, 025108.
- [19] Kuerten, J.G.M., and Vreman, A.W. 2005 Can turbophoresis be predicted by large-eddy simulation? *Phys. Fluids* **17**, 011701, 2005
- [20] Kulick, J.D., Fessler, J.R., and Eaton, J.K. 1994 Particle response and turbulence modification in fully developed channel flow. *J. Fluid Mech.* **277**, 109-134.
- [21] Lakehal, D., Smith, B.L., and Milelli, M. 2002 Large-eddy simulation of bubbly turbulent shear flows. *J. Turbulence* **3**, 25.

- [22] Marchioli, C., Giusti, A., Salvetti, M.V., and Soldati, A. 2003 Direct numerical simulation of particle wall transfer and deposition in upward turbulent pipe flow. *Int. J. of Multiphase Flow* **29**, 1017-1038.
- [23] Mathiesen, V., Solberg, T., and Hjertager, B.H. 2000 An experimental and computational study of multi-phase flow behavior in a circulating fluidized bed. *Int. J. Multiphase Flow* **26**, 387-419.
- [24] Maxey, M.R., and Riley, J. 1983 Equation of motion for a small rigid sphere in a turbulent fluid flow. *Phys. Fluids* **26**, 883.
- [25] Moin, P., Kim, J. 1982. Numerical investigation of turbulent channel flow. *J. Fluid Mech.*, **118**, 341.
- [26] Moran, J.C., and Glicksman, L.R. 2003 Mean and fluctuating fluid phase velocities inside a circulating fluidized bed. *Chem. Eng. Science* **58**, 1867-1878.
- [27] Moser, R. D., J. Kim, and N. N. Mansour. 1999. Direct numerical simulation of turbulent channel flow up to  $Re_\tau = 590$ . *Phys. Fluids* **11**, 943-945.
- [28] Nicoud, F., and Ducros, F. 1999 Subgrid-scale stress modeling based on the square of the velocity gradient tensor. *Flow, Turbulence and Combustion* **62**, 183-200.
- [29] Nieuwland, J.J. 1995 *Hydrodynamic modeling of fluid-solid two-phase flows*. PhD-Thesis, University of Twente.
- [30] Piomelli, U., and Balaras, E. 2002 Wall-layer models for large-eddy simulations. *Ann. Rev. Fluid Mech.* **34**, 349.
- [31] Pope, S.B. 2000 *Turbulent flows*, Cambridge University Press.
- [32] Powers, J.M. 2004 Two-phase viscous modeling of compaction of granular materials. *Phys. Fluids* **16**, 2975-2990.
- [33] Reynolds, O. 1895 On the dynamical theory of incompressible viscous fluids and the determination of the criterion. *Phil. Trans.* **186**, 123.
- [34] Righetti, M., and Romano, G.P. 2004 Particle-fluid interactions in a plane near-wall turbulent flow. *J. Fluid Mech.* **2004**, **505**, 93-121.
- [35] Sagaut, P. 2001 *Large eddy simulation for incompressible flows*, Springer Verlag.
- [36] Squires, K.D., and Simonin, O. 2002 Recent advances and perspective of DNS and LES for dispersed two-phase flow. *Proceedings of the 10th workshop on two-phase flow predictions*, Merseburg, 152-163.
- [37] Tryggvason, G., Bunner, B., Esmaeeli, A., Juric, D., Al-Rawahi, N., Tauber, W., Han, J., Nas, S., and Jan Y.-J. 2001 A front-tracking method for the computations of multiphase flow. *J. Comp. Phys.* **169**, 708-759.
- [38] Tsuji, Y., Morikawa, Y., and Shiomi, H. 1984 LDV measurements of an air-solid two-phase flow in a vertical pipe. *J. Fluid Mech.* **139**, 417-434.
- [39] Verstappen, R.W.C.P., and Veldman, A.E.P. (2003) Symmetry-preserving discretization of turbulent flow. *J. Comp. Phys.* **187**, 343-368.
- [40] Vreman, A.W., Geurts, B.J., Deen, N.G., Kuipers, J.A.M., Kuerten, J.G.M.: 2009. Two- and four-way coupled Euler-Lagrangian large-eddy simulation of turbulent particle-laden channel flow, *Flow, Turbulence and Combustion*, **82** 47-71
- [41] Vreman, B., Geurts, B., and Kuerten, H. 1996 Comparison of numerical schemes in large-eddy simulation of the temporal mixing layer. *Int. J. Num. Meth. Fluids* **22**, 297.
- [42] Vreman, A.W. 2004 An eddy-viscosity model for turbulent shear-flow: algebraic theory and applications. *Phys. Fluids* **16**, 3670-3681.
- [43] Yamamoto, Y., Potthoff, M., Tanaka, T. Kajishima, T., and Tsuji, Y. 2001 Large-eddy simulation of turbulent fluid-particle flow in a vertical channel: effect of considering inter-particle collisions. *J. Fluid Mech.* **442**, 303-334.
- [44] Wang, Q. and Squires, K.D. 1996 Large eddy simulation of particle deposition in a vertical turbulent channel flow. *Int. J. Multiphase Flow* **22**, 667.
- [45] Young, J., Leeming, A. 1997. A theory of particle deposition in turbulent pipe flow, *J. Fluid Mech.* **340**, 129-159.
- [46] Zhang, D.Z. and Prosperetti, A. (1997). Momentum and energy equations for disperse two-phase flows and their closure for dilute suspensions. *Int. J. Multiphase Flow* **23**, 425-453.

---

## *ERCOFTAC Workshops and Summer Schools*

---

### **ERCOFTAC Workshops, Conferences - 2014**

<b>Title</b>	<b>Location</b>	<b>Date</b>	<b>Coordinators</b>	<b>Organiser</b>
TURBINTERMARS 2014 International conference on turbulence and interactions in Marine Systems	Trieste, Italy	18-20/11/2014	Armenio, V.	SIG5

### **ERCOFTAC Summer Schools, Courses – 2014**

<b>Title</b>	<b>Location</b>	<b>Date</b>	<b>Coordinators</b>	<b>Organiser</b>
Summer School on Advanced Instability Methods for Complex Flows	Sao Carlos, Brazil	15-19/09/2014	Hanifi, A.	SIG33

---

**Mathematical Methods and Tools in Uncertainty Management and Quantification**

**4-5 Nov 2014, AREVA, Paris, France**

Uncertainty quantification is a new paradigm in industrial analysis and design as it aims at taking into account the presence of numerous uncertainties affecting the behaviour of physical systems. Dominating uncertainties can be either be operational (such as boundary conditions) and/or geometrical resulting from unknown properties, such as tip clearances of rotating fan blades or from manufacturing tolerances. Other uncertainties are related to models, such as turbulence or combustion should also be considered, or to numerical related errors.

Whether bringing a new product from conception into production or operating complex plant and production processes, commercial success rests on careful management and control of risk in the face of many interacting uncertainties. Historically, chief engineers and project managers have estimated and managed risk using mostly human judgment founded upon years of experience and heritage. As the 21st century begins to unfold, the design and engineering of products as well as the control of plant and process are increasingly relying on computer models and simulation. This era of virtual design and prototyping opens the opportunity to deal with uncertainty in a systematic formal way by which sensitivities to various uncertainties can be quantified and understood, and designs and processes optimized so as to be robust against such uncertainties. After several successful Courses on the applications of UQ.

ERCOFTAC decided, based on requests from many participants, to focus the present Course on the mathematical methodologies of UQ, enabling the participants to develop an in-depth understanding of the main methods such as: spectral, including polynomial chaos methods; methods of moments and Monte-Carlo methodologies.

**Lecturers**

- Olivier Le Maître - Visiting Professor, Duke University Department of Mechanical Engineering and Materials Science, Durham, NC - Directeur de Recherche, CNRS Laboratoire d'Informatique pour la Mécanique et les Sciences de l'Ingénieur, Orsay, France
- Gilbert Rogé, Dr. Dassault Aviation & HDR University Pierre et Marie Curie Paris, France
- Mike Giles, Professor of Scientific Computing at Oxford University Professorial Fellow in Mathematical Finance at St Hugh's College
- Charles Hirsch, Prof. Em. Vrije Universiteit Brussel & President, Numeca Int.

**Best Practice For Engineering CFD III (3rd delivery)**

**26-27 Nov 2014, CMT-Motores, Valencia, Spain**

This course is targeted at relatively new and improving CFD analysts in engineering industries and consultancies. It provides the knowledge to effect a step-change in the accuracy and reliability of CFD practices across a range of engineering applications relevant to the power generation, aerospace, automotive, built environment and turbomachinery sectors - amongst others.

The course is directly relevant to engineering applications of CFD for single-phase, compressible and incompressible, steady and unsteady, turbulent flows, with and without heat transfer. Much of the content will also be relevant to even more complex engineering applications.

The main focus will be on RANS applications, but an introduction to the special considerations required by LES and hybrid methods is also given.

The course provides the means for CFD analysts to significantly enhance their use of commercial and open-source CFD software for engineering applications. In particular, it provides guidance on best practices and highlights common pitfalls to be avoided.

**Lecturers**

- Prof. Charles Hirsch, Em. Vrije Universiteit Brussel & President, Numeca Int., Belgium
- Prof. Kemo Hanjalic, TU Delft, The Netherlands
- Prof. Dominique Laurence, UM IST, Manchester, UK, EDF, Chatou, France
- Prof. Michael Leschziner, Imperial College, London, UK
- Prof. Wolfgang Rodi, Karlsruhe Institute of Technology, Germany

**Registration - Dr Richard Seoud**  
**richard.seoud-ieo@ercoftac.org**



Announcement for 32<sup>nd</sup> series of Short Courses  
on

**Modelling and Computation of Multiphase Flows**  
**Part I: Bases**  
**Part IIA: New Reactor Systems and Methods**  
**or**  
**Part IIB: Computational Multi-Fluid Dynamics (CMFD)**  
**Part III: CMFD with Commercial Codes**

*Zurich, Switzerland, 09-13 February 2015*

*Hosted by the  
Swiss Federal Institute of Technology (ETH)  
in Zurich, Switzerland.*

Multiphase flows and heat transfer with phase change are of interest to researchers, scientists and engineers working in a multitude of industries. Courses similar to this one have been offered at ETH-Zurich continuously since 1984. Over the years, the courses have continuously evolved, reflecting ongoing progress and developments. This year the schedule has been again expanded by the addition of extra lectures in Parts II to further reinforce the CMFD aspects of the modules.

The courses are organized in a modular form as an intensive introduction for persons having basic knowledge of fluid mechanics, heat transfer, and numerical techniques (introductory tutorial texts are e-mailed to the participants before the course), but also serve as advanced courses for specialists wishing to obtain the latest information.

**Part I, Bases**, covers the common background material and emphasises the latest modelling and computational aspects of multiphase flows. A tutorial text is e-mailed to the participants before the course to introduce the very basic concepts and fill any basic gaps in their background, so that they can participate in the best possible way.

**Part IIA, New Reactor Systems and Methods**, covers multiphase flow topics of particular interest to the nuclear industry. Some of the most recently proposed advanced reactor designs and the main multiphase phenomena of importance are treated. The state-of-the-art and beyond in modelling and simulation methods (including CFD and CMFD applications) for core design and accident analysis is introduced. An article introducing Light Water Reactors, will be e-mailed as tutorial material for non-nuclear specialists to the participants before the course.

**Part IIB, Computational Multi-Fluid Dynamics (CMFD)**, reflects the growing interest in the application of CFD techniques to *multi*-phase flows and covers the most common computational techniques. The introductory chapters from a book authored by Tryggvason, Scardovelli and Zaleski will be emailed to the participants in Part IIB to prepare them for the lectures.

**Part III, CMFD with Commercial Codes**, is attached to both Parts IIA and IIB. The participants will hear commercial code developers discuss their products for both nuclear and other applications.

**Course language: English**

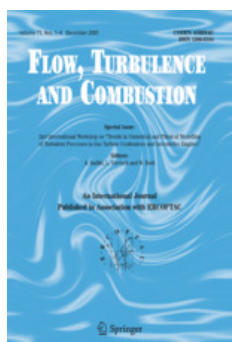
**Lecturers:** S. Banerjee, D. Bestion, M.L. Corradini, G. Hetsroni, G.F. Hewitt, D. Lakehal, Simon Lo, B. Niceno, H.-M. Prasser, G. Tryggvason, S.A. Vasquez, G. Yadigaroglu and S. Zaleski.

For further information contact by e-mail:

shortcourse@lke.mavt.ethz.ch

Internet: <http://www.lke.mavt.ethz.ch/news-and-events/events/short-course-mpf.html>

[ ETH ML K 14, Sonneggstrasse 3, CH-8092 Zurich, Switzerland. Tel. +41-44 632.88 21 ]



RECENT TABLE OF CONTENTS OF FLOW TURBULENCE AND COMBUSTION

AN INTERNATIONAL JOURNAL PUBLISHED BY SPRINGER  
IN ASSOCIATION WITH ERCOFTAC

EDITOR-IN-CHIEF: K. HANJALIĆ

EDITORS: J.J. CHEN, M. REEKS, W. RODI, L. VERVISCH

HONORARY EDITOR: J.C.R HUNT

FOUNDING EDITOR: F. NIEUWSTADT

**VOLUME 93, NUMBER 2, SEPTEMBER 2014**

**Linear Eddy Mixing Model Studies of High Karlovitz Number Turbulent Premixed Flames**

*S. Srinivasan I S. Menon*

**Parametric Analysis of Excited Round Jets - Numerical Study**

*A. Tyliczszak I B.J. Geurts*

**Experimental Study on Bubble Movement Characteristics during Underwater Pyrotechnic Combustion**

*J. Li I H. Guan I D. Song I Q. Wang I J. Du*

**Fuel Composition Effects on Flame Stretch in Turbulent Premixed Combustion: Numerical Analysis of Flame-Vortex Interaction and Formulation of a New Efficiency Function**

*S. Bougrine I S. Richard I O. Colin I D. Veynante*

**Effects of Differential Diffusion on Predicted Autoignition Delay Times Inspired by  $H_2/N_2$  Jet Flames in a Vitiated Coflow Using the Linear Eddy Model**

*D. Frederick I J.Y. Chen*

**Large Eddy Simulations of a Small-Scale Flameless Combustor by Means of Diluted Homogeneous Reactors**

*C. Locci I O. Colin I J.-B. Michel*

**LES Modeling of the Impact of Heat Losses and Differential Diffusion on Turbulent Stratified Flame Propagation: Application to the TU Darmstadt Stratified Flame**

*R. Mercier I P. Auzillon I V. Moureau I N. Darabiha I O. Gicquel I D. Veynante I B. Fiorina*

**VOLUME 93, NUMBER 3, OCTOBER 2014**

**Recent Advances in Turbulent Combustion**

*Guest Editors: Assaad Masri and Epaminondas Mastorakos*

**Preface**

*A.R. Masri I E. Mastorakos*

**Large Eddy Simulation of Air Entrainment and Mixing in Reacting and Non-Reacting Diesel Sprays**

*C. Gong I M. Jangi I T. Lucchini I G. D'Errico I X.-S. Bai*

**Simulation of Dilute Acetone Spray Flames with LES-CMC Using Two Conditional Moments**

*S. Ukai I A. Kronenburg I O.T. Stein*

**Investigation of Lifted Flame Propagation Under Pulsing Conditions Using High-Speed OH-LIF and LES**

*V.N. Prasad I M. Juddoo I A. Kourmatzis I A.R. Masri*

**Topology and Brush Thickness of Turbulent Premixed V-shaped Flames**

*S. Kheirkhah I Ö.L. Gülder*

**Scalar Dissipation Rate Transport in the Context of Large Eddy Simulations for Turbulent Premixed Flames with Non-Unity Lewis Number**

*Y. Gao I N. Chakraborty I N. Swaminathan*

**Linear-Eddy Model Formulated Probability Density Function and Scalar Dissipation Rate Models for Premixed Combustion**

*H.P. Tsui I W.K. Bushe*

**Large Eddy Simulation and Extended Dynamic Mode Decomposition of Flow-Flame Interaction in a Lean Premixed Low Swirl Stabilized Flame**

*H. Carlsson I C. Carlsson I L. Fuchs I X.S. Bai*

**Investigation of the Dynamic Response of Swirling Flows Based on LES and Experiments**

*F. Biagioli I T. Lachaux I S. Narendran*

## ERCOFTAC Special Interest Groups

### 1. Large Eddy Simulation

Salvetti, M.V.  
University of Pisa, Italy.  
Tel: +39 050 221 7262  
Fax: +39 050 221 7244  
mv.salvetti@ing.unipi.it

### 4. Turbulence in Compressible Flows

Dussauge, Jean-Paul  
IUSTI, Marseille  
jean-paul.dussauge  
@polytech.univmrs.fr

### 5. Environmental Fluid Mechanics

Armenio, V.  
Universit di Trieste, Italy.  
Tel: +39 040 558 3472  
Fax: +39 040 572 082  
armenio@dica.units.it

### 10. Transition Modelling

Dick, E.,  
University of Ghent, Belgium.  
Tel: +32 926 433 01  
Fax: +32 926 435 86  
erik.dick@ugent.be

### 12. Dispersed Turbulent Two Phase Flows

Sommerfeld, M.  
Martin-Luther University, Germany.  
Tel: +49 346 146 2879  
Fax: +49 346 146 2878  
martin.sommerfeld@iw.uni-halle.de

### 14. Stably Stratified and Rotating Flows

Redondo, J.M.  
UPC, Spain.  
Tel: +34 934 017 984  
Fax: +34 934 016 090  
redondo@fa.upc.edu

### 15. Turbulence Modelling

Jakirlic, S.  
Darmstadt University of Technology,  
Germany.  
Tel: +49 615 116 3554  
Fax: +49 615 116 4754  
s.jakirlic@sla.tu-darmstadt.de

### 20. Drag Reduction and Flow Control

Choi, K-S.  
University of Nottingham, England.  
Tel: +44 115 951 3792  
Fax: +44 115 951 3800  
kwing-so.choi@nottingham.ac.uk

### 24. Variable Density Turbulent Flows

Anselmet, F.  
IMST, France.  
Tel: +33 491 505 439  
Fax: +33 491 081 637  
anselmet@irphe.univ-mrs.fr

### 28. Reactive Flows

Pfitzner, M.  
Universität der Bundeswehr München,  
Germany.  
Tel: +49 (0) 8960 042 103  
Fax: +49 (0) 8960 042 116  
michael.pfitzner@unibw.de

### 32. Particle Image Velocimetry

Stanislas, M.  
Ecole Centrale de Lille, France.  
Tel: +33 320 337 170  
Fax: +33 320 337 169  
Michel.Stanislas@ec-lille.fr

### 33. Transition Mechanisms, Prediction and Control

Hanifi, A.  
FOI, Sweden.  
Tel: +46 855 503 197  
Fax: +46 855 503 397  
ardeshir.hanifi@foi.se

### 34. Design Optimisation

Giannakoglou, K.  
NTUA, Greece.  
Tel: +30 210 772 1636  
Fax: +30 210 772 3789  
kgianna@central.ntua.gr

### 35. Multipoint Turbulence Structure and Modelling

Cambon, C.  
ECL Ecully, France.  
Tel: +33 472 186 161  
Fax: +33 478 647 145  
claudc.cambon@ec-lyon.fr

### 36. Swirling Flows

Braza, M.  
IMFT, France.  
Tel: +33 534 322 839  
Fax: +33 534 322 992  
braza@imft.fr

### 37. Bio-Fluid Mechanics

Poelma, C.  
Delft University of Technology, Holland.  
Tel: +31 152 782 620  
Fax: +31 152 782 947  
c.poelma@tudelft.nl

### 38. Micro-thermofluidics

Borhani, N.  
EPFL, Switzerland.  
Tel: +41 216 933 503  
Fax: +41 216 935 960  
navid.borhani@epfl.ch

### 39. Aeroacoustics

Bailly, C.  
Ecole Centrale de Lyon, France.  
Tel: +33 472 186 014  
Fax: +33 472 189 143  
christophe.bailly@ec-lyon.fr

### 40. Smoothed Particle Hydrodynamics

Le Touze, D.  
Ecole Centrale de Nantes, France  
Tel: +33 240 371 512  
Fax: +33 240 372 523  
David.LeTouze@ec-nantes.fr

### 41. Fluid Structure Interaction

Longatte, E.  
EDF, France.  
Tel: +33 130 878 087  
Fax: +33 130 877 727  
elisabeth.longatte@edf.fr

### 42. Synthetic Models in Turbulence

Nicolleau, F.  
University of Sheffield, England.  
Tel: +44 114 222 7867  
Fax: +44 114 222 7890  
f.nicolleau@sheffield.ac.uk

### 43. Fibre Suspension Flows

Lundell, F.  
The Royal Institute of Technology,  
Sweden.  
Tel: +46 87 906 875  
fredrik@mech.kth.se

### 44. Fundamentals and Applications of Fractal Turbulence

Fortune, V.  
Université Pierre et Marie Curie, France.  
Tel: +33 549 454 044  
Fax: +33 549 453 663  
veronique.fortune@lea.univ-poitiers.fr

### 45. Uncertainty Quantification in Industrial Analysis and Design

Lucor, D.  
d'Alembert Institute, France.  
Tel: +33 (0) 144 275 472  
didier.lucor@upmc.fr

## ERCOFTAC Pilot Centres

### Alpe - Danube - Adria

Steiner, H.  
Inst. Strömungslehre and  
Wärmeübertragung  
TU Graz, Austria  
kristof@ara.bme.hu

### Belgium

Geuzaine, P.  
Cenaero,  
CFD Multi-physics Group,  
Rue des Frères Wright 29,  
B-6041 Gosselies,  
Belgium.  
Tel: +32 71 919 334  
philippe.geuzaine@cenaero.be

### Brasil

Rodriguez, O.  
Department of Mechanical Engineering,  
Sao Carlos School of Mechanical  
Engineering,  
Universidade de Sao Paulo,  
Brasil.  
oscarmhr@sc.usp.br

### Czech Republic

Bodnar, T.  
Institute of Thermomechanics AS CR,  
5 Dolejskova,  
CZ-18200 Praha 8,  
Czech Republic.  
Tel: +420 224 357 548  
Fax: +420 224 920 677  
bodnar@marian.fsik.cvut.cz

### France - Henri Bénard

Cambon, C.  
Ecole Centrale de Lyon.  
LMFA, B.P. 163,  
F-69131 Ecully Cedex,  
France.  
Tel: +33 4 72 18 6161  
Fax: +33 4 78 64 7145  
claudc.cambon@ec-lyon.fr

### France South

Braza, M.  
IMF Toulouse,  
CNRS UMR - 5502,  
Allée du Prof. Camille Soula 1,  
F-31400 Toulouse Cedex, France.  
Tel: +33 534 322 839  
Fax: +33 534 322 992  
Braza@imft.fr

### France West

Danaila, L.  
CORIA, University of Rouen,  
Avenue de l'Université BP12,  
76801 Saint Etienne du Rouvray  
France.  
Tel: +33 232 953 702  
luminita.danaila@coria.fr

### Germany North

Gauger, N.R.  
Computational Mathematics  
Group  
RWTH Aachen University  
Schinkelstr. 2  
D-52062 Aachen, Germany  
Tel: +49 241 80 98 660  
Fax: +49 241 80 92 600  
gauger@mathcces.rwth-aachen.de

### Germany South

Becker, S.  
Universität Erlangen, IPAT  
Cauerstr. 4  
91058 Erlangen  
Germany  
Tel: +49 9131 85 29451  
Fax: +49 9131 85 29449  
sb@ipat.uni-erlangen.de

### Greece

M. Founti.  
National Tech. University Of Athens,  
School of Mechanical Engineering,  
Lab. of Steam Boilers and  
Thermal Plants,  
Heron Polytechniou 9,  
15780 Zografou, Athens, Greece  
Tel: +30 210 772 3605  
Fax: +30 210 772 3663  
mfou@central.ntua.gr

### Iberian East

Oñate, E.  
Universitat Politècnica de Catalunya,  
Edificio C-1, Campus Norte,  
Gran Capitan s/n,  
E-08034 Barcelona,  
Spain.  
Tel: +34 93 401 6035  
Fax: +34 93 401 6517  
onate@cimne.upc.es

### Iberian West

Theofilis, V.  
Research Professor of Fluid Mechanics  
School of Aerospace Engineering  
Technical University of Madrid (UPM)  
Tel: +34 91 336 3298  
Fax: +34 91 336 3295  
vassilios.theofilis@upm.es

### Italy

Rispoli, F.  
Tel: +39 064 458 5233  
franco.rispoli@uniroma1.it  
Borello, D.  
Tel: +39 064 458 5263  
domenico.borello@uniroma1.it  
Sapienza University of Rome,  
Via Eudossiana, 18  
00184 Roma, Italy

### Netherlands

Van Heijst, G.J.  
J.M. Burgerscentrum,  
National Research School for Fluid  
Mechanics,  
Mekelweg 2,  
NL-2628 CD Delft, Netherlands.  
Tel: +31 15 278 1176  
Fax: +31 15 278 2979  
g.j.f.vanheijst@tudelft.nl

### Nordic

Wallin, S.  
Swedish Defence Research Agency FOI,  
Information and Aeronautical Systems,  
S-16490 Stockholm,  
Sweden.  
Tel: +46 8 5550 3184  
Fax: +46 8 5550 3062  
stefan.wallin@foi.se

### Poland

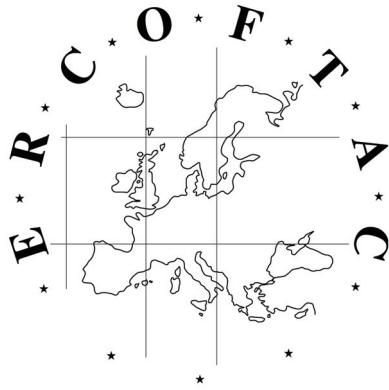
Rokicki, J.  
Warsaw University of Technology,  
Inst. of Aeronautics & Applied  
Mechanics,  
ul. Nowowiejska 24,  
PL-00665 Warsaw, Poland.  
Tel: +48 22 234 7444  
Fax: +48 22 622 0901  
jack@meil.pw.edu.pl

### Switzerland

Jenny, P.  
ETH Zürich,  
Institute of Fluid Dynamics,  
Sonneggstrasse 3,  
8092 Zürich, Switzerland.  
Tel: +41 44 632 6987  
jenny@ifd.mavt.ethz.ch

### United Kingdom

Standingford, D.  
Zenotech Ltd.  
University Gate East, Park Row,  
Bristol, BS1 5UB  
England.  
Tel: +44 117 302 8251  
Fax: +44 117 302 8007  
david.standingford@zenotech.com



# Best Practice Guidelines for Computational Fluid Dynamics of Dispersed Multi-Phase Flows

## Editors

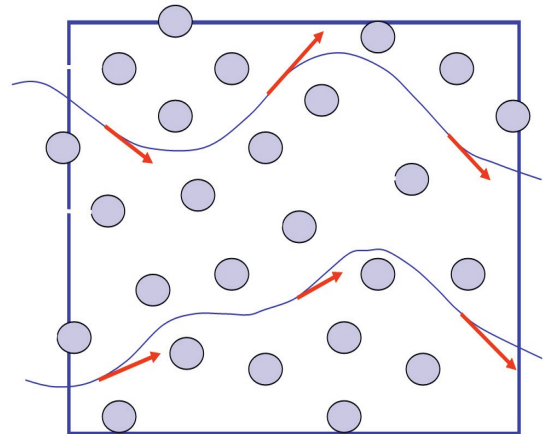
Martin Sommerfeld, Berend van Wachem  
&  
René Oliemans

The simultaneous presence of several different phases in external or internal flows such as gas, liquid and solid is found in daily life, environment and numerous industrial processes. These types of flows are termed multiphase flows, which may exist in different forms depending on the phase distribution. Examples are gas-liquid transportation, crude oil recovery, circulating fluidized beds, sediment transport in rivers, pollutant transport in the atmosphere, cloud formation, fuel injection in engines, bubble column reactors and spray driers for food processing, to name only a few. As a result of the interaction between the different phases such flows are rather complicated and very difficult to describe theoretically. For the design and optimisation of such multiphase systems a detailed understanding of the interfacial transport phenomena is essential. For single-phase flows Computational Fluid Dynamics (CFD) has already a long history and it is nowadays standard in the development of air-planes and cars using different commercially available CFD-tools.

Due to the complex physics involved in multiphase flow the application of CFD in this area is rather young. These guidelines give a survey of the different methods being used for the numerical calculation of turbulent dispersed multiphase flows. The Best Practice Guideline (BPG) on Computational Dispersed Multiphase Flows is a follow-up of the previous ERCOFTAC BPG for Industrial CFD and should be used in combination with it. The potential users are researchers and engineers involved in projects requiring CFD of (wall-bounded) turbulent dispersed multiphase flows with bubbles, drops or particles.

## Table of Contents

1. Introduction
2. Fundamentals
3. Forces acting on particles, droplets and bubbles
4. Computational multiphase fluid dynamics of dispersed flows
5. Specific phenomena and modelling approaches
6. Sources of errors
7. Industrial examples for multiphase flows
8. Checklist of 'Best Practice Advice'
9. Suggestions for future developments



Copies of the Best Practice Guidelines can be acquired electronically from the ERCOFTAC website:

[www.ercoftac.org](http://www.ercoftac.org)

Or from:

ERCOFTAC (CADO)  
PO Box 53877  
London, SE27 7BR  
United Kingdom

Tel: +44 203 602 8984

Email: [magdalena.jakubczak@ercoftac.org](mailto:magdalena.jakubczak@ercoftac.org)

The price per copy (not including postage) is:

ERCOFTAC members

First copy	Free
Subsequent copies	75 Euros
Students	75 Euros

Non-ERCOFTAC academics	140 Euros
Non-ERCOFTAC industrial	230 Euros
EU/Non EU postage fee	10/17 Euros